

Electronic Thesis and Dissertation Repository

4-20-2022 11:00 AM

Static liquefaction and critical state mechanics of gold mine tailings subjected to different stress paths

Amir reza Fotovvat, *The University of Western Ontario*

Supervisor: Sadrekarimi, Abouzar, *The University of Western Ontario*

A thesis submitted in partial fulfillment of the requirements for the Doctor of Philosophy degree in Civil and Environmental Engineering

© Amir reza Fotovvat 2022

Follow this and additional works at: <https://ir.lib.uwo.ca/etd>



Part of the [Geotechnical Engineering Commons](#)

Recommended Citation

Fotovvat, Amir reza, "Static liquefaction and critical state mechanics of gold mine tailings subjected to different stress paths" (2022). *Electronic Thesis and Dissertation Repository*. 8477.
<https://ir.lib.uwo.ca/etd/8477>

This Dissertation/Thesis is brought to you for free and open access by Scholarship@Western. It has been accepted for inclusion in Electronic Thesis and Dissertation Repository by an authorized administrator of Scholarship@Western. For more information, please contact wlsadmin@uwo.ca.

Abstract

The mechanisms through which mine tailings fail have been the interests of many studies recently. In this series of studies, the flow liquefaction and instability behavior of gold mine tailings were examined within the framework of critical state soil mechanics. In the first study, the behavior of a gold mine tailings in stress paths involving extensional consolidation or shearing in extension was evaluated. Monotonic tests were carried out on isotropically and K_0 -consolidated samples to assess the effect of stress-induced anisotropy and mode of shearing on the static liquefaction characteristics tailings. In the second study, the drained instability of two gold mine tailings under lateral stress relief was investigated. Constant deviator stress (CDS) unloading tests were performed using a triaxial apparatus to simulate instability imposed by unloading in a drained condition. Several field failures have been associated to similar mechanisms. Different techniques were employed to determine the onset of instability in CDS tests and important affecting parameters were assessed. In the third study, the effect of the presence of different percentages of non-plastic fines on the static liquefaction behavior of a given gold mine tailings was examined. The variability of fines content during compaction of mine waste and deposition of tailings slurries, even in a single tailings impoundment, highlights the possible consequences of tailings' gradation change and fine particles presence on the behavior of such materials. In the fourth study, the capability of a critical state-based model, NorSand model, in replicating the behavior of two gradations of a gold mine tailings was investigated. The purpose was to simulate liquidation susceptibility to tailings. The ability of the model was evaluated in a numerical model of a tailings dam.

Keywords

Static Liquefaction, Instability, Mine tailings, Triaxial testing, Critical state, Effect of fines content, Extensional shearing

Summary for Lay Audience

Mining industries are important to modern societies these days that provide vital mineral products and energy resources. Their by-product wastes, mine tailings, are usually stored in isolated conditions as deposits in impoundments under water behind dams to prevent them from exposure to atmospheric oxidation. However, these materials are prone to failure since they are usually deposited in loose and saturated conditions. Flow liquefaction is a known mechanism that can trigger these failures. To study the strength characteristics and behaviors of these materials, laboratory experimentation such as triaxial testing on reconstituted samples is a common method. However, these tests are usually carried out in a conventional way due to its simplicity and versatility, which includes consolidating samples isotropically (the simplest procedure of consolidation) and then loading (shearing) them in compression. In the first section, it is argued this is not necessarily the loading history applied on a soil element. The consolidation can be anisotropic, either by extension or compression, as well shearing, that can happen through extensive loading or compressive. These “stress-path” were applied on the tailings specimens and their behaviors were studied. Another triggering mechanics is lateral confinement relief. This can happen because of water table raise, snow melt, erosion, etc. As such, within the second part, special stress-paths were employed to simulate these conditions, and to study the instability behavior of tailings subjected to them. Also, particle segregation and separation can result in different gradations fabricated from a given mine tailings with different amounts of non-plastic fines. The difference in fines content can highly affect the behavior of these materials. Therefore, in the third part, this effect was studied through testing on different mixtures. Replicating the behavior of tailings using numerical methods, is crucial in design and analyzing geo-structures built from these materials. A critical state-based model called NorSand has been shown to perfectly capture the behavior of granular materials with liquefaction susceptibility. However, its capability in modeling tailings has faced challenges especially due to the distinctive magnitudes of parameters for tailings. In the fifth part, the feasibility of using this constitutive model in simulating tailings dams was assessed.

Co-Authorship Statement

This thesis has been prepared in accordance with an Integrated-Article format thesis stipulated by the School of Graduate and Postdoctoral Studies at the University of Western Ontario and has been co-authored as:

Chapter 2: Instability of a Gold Mine Tailings Subjected to Different Stress Paths

All experimental work was completed by Amir reza Fotovvat under the supervision of Dr. Abouzar Sadrekarimi. A peer-reviewed journal paper co-authored by Amir reza Fotovvat and Abouzar Sadrekarimi was published in the ASCE “Journal of Geotechnical and Geoenvironmental Engineering”.

Chapter 3: Instability of Gold Mine Tailings subjected to Undrained and Drained Unloading Stress Paths

All experimental work was completed by Amir reza Fotovvat under the supervision of Dr. Abouzar Sadrekarimi. A conference paper co-authored by Amir reza Fotovvat, Abouzar Sadrekarimi, and Michael Etezzad was accepted and presented in “Tailings and Mine Waste 2021 conference”. A peer-reviewed journal paper co-authored by Amir reza Fotovvat, Abouzar Sadrekarimi, and Michael Etezzad was accepted in “Géotechnique”.

Chapter 4: Effect of non-plastic fines content on the static liquefaction behavior of a gold mine tailings

All experimental work was completed by Amir reza Fotovvat under the supervision of Dr. Abouzar Sadrekarimi. A paper co-authored by Amir reza Fotovvat and Abouzar Sadrekarimi will be submitted to a peer-reviewed journal.

Chapter 5: Numerical modeling of a tailings impoundment using NorSand constitutive model

All numerical work was completed by Amir reza Fotovvat under the supervision of Dr. Abouzar Sadrekarimi.

Acknowledgments

First and foremost, I would like to thank my supervisor, Dr. Abouzar Sadrekarimi from the Department of Civil and Environmental Engineering at Western University for his consistent guidance, support and assistance throughout the progress of this research and methodology. The assistance of Laboratory Technician Melodie Richards as well as fellow graduate researchers Mr. Shayan Hashemi, Mr. Hamed Behzadipour and Mr. Ronit Ganguly is greatly acknowledged and appreciated. Financial support provided by the Ontario Center of Innovation (OCI), Golder Associates, and Natural Sciences and Engineering Research Council of Canada (NSERC) are highly appreciated.

Table of contents

Abstract.....	ii
Summary for Lay Audience.....	iii
Co-Authorship Statement.....	iv
Acknowledgments.....	v
Table of contents.....	vi
List of Tables	x
List of Figures	xi
Nomenclature	xviii
Chapter 1	1
1 Introduction.....	1
1.1 Typical properties of gold mine tailings	3
1.2 Effect of different loading paths	8
1.3 Instability in drained conditions.....	12
1.4 Effect of fines content.....	14
Chapter 2.....	19
2 Instability of a Gold Mine Tailings Subjected to Different Stress Paths	19
2.1 Abstract.....	19
2.2 Introduction.....	20
2.3 Terminology.....	23
2.4 Experimental Program	25
2.4.1 Material tested.....	25
2.4.2 Testing apparatus	26
2.4.3 Sample preparation	28
2.4.4 Saturation	29

2.4.5	Consolidation	29
2.4.6	Shearing	30
2.4.7	Test program	31
2.5	Results and Discussion	34
2.5.1	Effect of preparation method	34
2.5.2	Effect of loading direction	35
2.5.3	Post-liquefaction friction angle.....	39
2.5.4	Critical State Line	40
2.5.5	Undrained shear strengths.....	41
2.5.6	Triggering friction angle.....	45
2.5.7	Brittleness and Pore Pressure Generation	47
2.5.8	Comparisons with Natural Soils and Other Tailings	50
2.6	Summary	56
2.7	Acknowledgments.....	57
Chapter 3	58
3	Instability of Gold Mine Tailings subjected to Undrained and Drained Unloading Stress Paths	58
3.1	Abstract.....	58
3.2	Introduction.....	59
3.3	Experimental Procedure.....	62
3.3.1	Material tested.....	62
3.3.2	Triaxial Apparatus	65
3.3.3	Specimen Preparation	66
3.3.4	Saturation	69
3.3.5	Consolidation	69
3.3.6	Shearing	70

3.4	Results.....	74
3.4.1	Critical State Line	80
3.4.2	Undrained instability.....	83
3.4.3	Instability in CDS tests	86
3.4.4	Effect of unloading rate	93
3.4.5	Comparison of instability stress ratios from CDS and undrained tests	96
3.4.6	Effect of void ratio	101
3.4.7	Correlations with the State Parameter.....	103
3.4.8	Practical significance	109
3.5	Conclusions.....	110
3.6	Acknowledgments.....	112
Chapter 4	113
4	Effect of Non-Plastic Fines on the Instability Behavior of a Gold Mine Tailings.....	113
4.1	Abstract.....	113
4.2	Introduction.....	114
4.3	Experimentation	116
4.3.1	Tested tailings	116
4.3.2	X-Ray diffraction analysis	117
4.3.3	SEM images	118
4.3.4	Sample preparation	119
4.3.5	Testing apparatus	120
4.3.6	Saturation and Consolidation.....	120
4.3.7	Shearing	121
4.4	Results and discussion	123
4.4.1	Undrained stress paths	123
4.4.2	Liquefaction triggering and post-liquefaction strengths.....	126

4.4.3	Liquefaction severity	129
4.4.4	Critical states.....	129
4.4.5	Effective stress unloading.....	135
4.4.6	Effect of FC.....	137
4.4.7	Effect of stress path.....	139
4.4.8	Effect of unloading rate	140
4.5	Conclusion	142
Chapter 5	143
5	Numerical modeling of a tailings impoundment using NorSand constitutive model	143
5.1	Introduction.....	143
5.2	Validation of the numerical method	146
5.2.1	Geometry and meshing of Fundao tailings dam model	147
5.2.2	Model parameters for Fundao tailings dam’s simulation	147
5.2.3	Results of the Fundao tailings dam’s simulations.....	150
5.3	Modeling of a tailings dam	154
5.3.1	Geometry and meshing	154
5.3.2	Constitutive model selection and parameters	155
5.4	Results and discussions.....	161
5.4.1	Developing the dam in accordance with its construction history	161
5.4.2	Evaluation of failure	169
5.5	Conclusion	175
Chapter 6	177
6	Conclusions.....	177
References	180
Curriculum Vitae	201

List of Tables

Table 2-1: Summary of TxC and TxE tests on the gold tailings of this study.....	33
Table 3-1: Index properties of gold tailings used in this study.....	63
Table 3-2: Summary of the undrained and drained TxC tests of this study	72
Table 3-3: Specifications of the constant deviator stress tests on Q and O tailings	73
Table 4-1: Summary of triaxial compression tests on tailings mixtures with different FC ..	122
Table 4-2: Summary of the CDS tests carried out in this study.....	123
Table 5-1: NorSand model's parameters	145
Table 5-2: Elastic and Mohr-Coulomb parameters for Fundao tailings dam analysis	149
Table 5-3: NorSand parameters used for the deposited sands in Fundao tailings dam analysis	149
Table 5-4: Measured and calibrated values for NorSand model.....	160
Table 5-5. Elastic and Mohr-Coulomb parameters.....	161

List of Figures

Figure 1-1: Variation of mode of shearing along a failure plane beneath a sloping ground Sadrekarimi (2016).	9
Figure 2-1: Change of shearing direction under an embankment during construction and embankment raising	22
Figure 2-2: Reversal in shearing direction following embankment extension	22
Figure 2-3: The (a) ESP of a limited flow liquefaction behavior (ICU 1); (b) stress-strain of a limited flow liquefaction behavior (ICU 1)	24
Figure 2-4: Average particle-size distribution of the gold tailings used in this study	25
Figure 2-5: SEM images of the gold mine tailings particles at: (a) $\times 983$, (b) $\times 300$, (c) $\times 300$, and (d) $\times 100$ magnifications	26
Figure 2-6: Schematic layout of the triaxial system	27
Figure 2-7: Modifications of the triaxial setup for extension testing.....	31
Figure 2-8: Formation of shear bands in EKEU tests at p'_c of (a) 335 kPa and (b) 117 kPa..	32
Figure 2-9: Comparison of stress paths from ICU tests on specimens prepared by dry deposition (DD), moist tamping (MT) and slurry deposition (SD)	34
Figure 2-10: The comparison of the results of two duplicate samples with the same initial densities tested through stress path of ICU1	35
Figure 2-11: Stress paths (a) and stress-strain behaviors (b) of tailings specimens subjected to CKCU and CKEU shearing	37
Figure 2-12: Stress paths (a) and stress-strain behaviors (b) of tailings specimens subjected to ICU and IEU shearing.....	38

Figure 2-13: Stress paths (a) and stress-strain behaviors (b) of tailings specimens subjected to EKEU and EKCU shearing.....	39
Figure 2-14: Critical state lines established from the triaxial tests of this study	41
Figure 2-15: Variations of (a) $s_u(\text{yield})/\sigma'_{1c}$ and (b) $s_u(\text{liq})/\sigma'_{1c}$ with e_c based on the triaxial tests of this study.....	43
Figure 2-16: Variations of (a) $s_u(\text{yield})/\sigma'_{1c}$ and (b) $s_u(\text{liq})/\sigma'_{1c}$ with ψ_{cs} based on the triaxial tests of this study.....	44
Figure 2-17: Variations of ϕ'_{yield} with (a) e_c and (b) ψ_{cs} from the triaxial tests of this study..	47
Figure 2-18: Comparisons of I_B and $r_{u,\text{max}}$ from the triaxial tests of this study with empirical trends proposed by Sadrekarimi (2020) for specimens consolidated in (a) compression, and (b) extension. Numbers in parentheses show K_C values of Sadrekarimi (2020) trends	49
Figure 2-19: Variations of I_B with $r_{u,\text{yield}}$ for different loading directions from the triaxial experiments of this study	50
Figure 2-20: Comparison of CSLs of Ottawa sand Sadrekarimi (2009), Monterey No. 0 sand Riemer and Seed (1997), a clayey sand Georgiannou (1988), Lagunillas sandy silt Zlatovic and Ishihara (1997), and Merriespruit gold tailings (Fourie and Papageorgiou 2001; Fourie and Tshabalala 2005) with those of this study.....	52
Figure 2-21: Comparisons of (a) $s_u(\text{yield})/\sigma'_{1c}$ and (b) $s_u(\text{liq})/\sigma'_{1c}$ from the triaxial compression tests of this study with those for a clayey sand Georgiannou (1988), Ottawa sand Sadrekarimi (2009), Lagunillas sandy silt Zlatovic and Ishihara (1997), and Merriespruit gold tailings (Fourie and Papageorgiou 2001; Fourie and Tshabalala 2005)....	53
Figure 2-22: Comparisons of $s_u(\text{yield})/\sigma'_{1c}$ and $s_u(\text{liq})/\sigma'_{1c}$ from isotropically-consolidated triaxial extension tests of this study with those for Monterey No. 0 Riemer and Seed (1997) and Kawagishi-Cho Yoshimine et al. (2001) sands.....	54
Figure 2-23: Comparisons of ϕ'_{yield} from (a) triaxial compression and (b) isotropically-consolidated triaxial extension tests of this study with those mobilized in Ottawa Sadrekarimi	

(2009), Monterey No. 0 Riemer and Seed (1997), and Kawagishi-Cho Yoshimine et al. (2001) sands, a clayey sand Georgiannou (1988), Lagunillas sandy silt Zlatovic and Ishihara (1997), and Merriespruit gold tailings (Fourie and Papageorgiou 2001; Fourie and Tshabalala 2005)	55
Figure 3-1: Stress path of an undrained triaxial compression test on an isotropically-consolidated	59
Figure 3-2: Average particle-size distributions of the gold tailings used in this study.....	63
Figure 3-3: SEM images of coarse sand (a, b) and fine (c, d) gold tailings	64
Figure 3-4: Photos of the specimen preparation procedure: (a) membrane-lined mold, (b) specimen tamping with a graduated rod, (c) completed specimen after removing the mold, (d) specimen in the triaxial cell mounted on the loading frame	68
Figure 3-5: Undrained (a) stress paths and (b) stress-strain behaviors of QIU specimens.....	75
Figure 3-6: Undrained (a) stress paths and (b) stress-strain behaviors of QK _o U specimens..	76
Figure 3-7: Undrained (a) stress paths and (b) stress-strain behaviors of OIU specimens....	77
Figure 3-8: Undrained (a) stress paths and (b) stress-strain behaviors of OK _o U specimens.	79
Figure 3-9: (a) deviator stress and (b) volumetric strains versus axial strain of drained TxC tests on each tailings	80
Figure 3-10: Critical state lines of Q and O tailings in the (a) stress path, and (b) e-log(p') planes (IU: isotropically-consolidated undrained test; AU: anisotropically-consolidated undrained test; ID: isotropically-consolidated drained test)	83
Figure 3-11: Variations of (a) $s_u(\text{yield})$ with σ'_{1c} ; and (b) $s_u(\text{yield})/\sigma'_{1c}$ with e_c for both $K_c = 1$ and $K_c > 1$ specimens of Q tailings. Numbers in parentheses indicate η_c	85
Figure 3-12: Variations of (a) $s_u(\text{yield})$ with σ'_{1c} , and (b) $s_u(\text{yield})/\sigma'_{1c}$ with e_c for both $K_c = 1$ and $K_c > 1$ specimens of O tailings. Numbers in parentheses indicate η_c	86

Figure 3-13: CDS stress paths on Q tailings.....	87
Figure 3-14: Variations of ε_a and ε_{vol} with $\eta = q/p'$ in CDS tests: (a) QCDS 1, (b) QCDS 6, and (c) QCDS 9.....	90
Figure 3-15: Changes of $\partial^2 W$ with η in undrained triaxial tests: (a) QK _o U1, (b) QK _o U4, and (c) OK _o U2.....	92
Figure 3-16: (a) stress paths and (b) axial strain rates of CDS tests on Q tailings with different du_e/dt	95
Figure 3-17: (a) stress paths and (b) axial strain rates of CDS tests on O tailings with different du_e/dt	96
Figure 3-18: Comparison of undrained and CDS stress paths on Q tailings consolidated to different p'_c and η_c	98
Figure 3-19: Comparison of undrained and CDS tests on O tailings consolidated to different η_c	100
Figure 3-20: Effect of η_c on η_{IL} for both Q and O tailings.....	101
Figure 3-21: Effect of e_c on η_{IL} in (a) Q and (b) O tailings.....	102
Figure 3-22: Variation of (a) $s_u(\text{yield})/\sigma'_{1c}$ and (b) $s_u(\text{liq})/\sigma'_{1c}$ with ψ_{cs} from undrained triaxial tests on Q and O tailings. Numbers in parentheses are η_c of anisotropically-consolidated (AU and K _o U) tests.....	105
Figure 3-23: Variations of η_{IL} with ψ_{cs} from the triaxial tests of this study on (a) Q and (b) O tailings.....	107
Figure 3-24: Variations of modified (a) yield and (b) post-liquefaction strength ratios with ψ_{cs}	108
Figure 3-25: Variations of $\eta_{IL}-\eta_c^4$ with ψ_{cs} in TxC tests on (a) Q and (b) O tailings.....	109
Figure 4-1: Particle size distributions the gold tailings used in this study.....	116

Figure 4-2: Effect of FC on e_{max} and e_{min} of tailings	117
Figure 4-3: XRD analysis of the gold mine tailings tested in this study	118
Figure 4-4: SEM images of tailings particles at magnifications of: (a) 300x; (b) 500x; (c) 800x.....	119
Figure 4-5: Stress paths of (a) isotropically and (b) anisotropically consolidated tailings specimens	125
Figure 4-6: Stress paths of dry pluviated tailings specimens at different FC	126
Figure 4-7: Effect of FC on (a) $s_u(yield)/\sigma'_{1c}$, (b) $s_u(liq)/\sigma'_{1c}$, and (c) ϕ'_{yield} of tailings specimens at different FC	128
Figure 4-8: Brittleness index of IU and K_oU tests on specimens with different FC.....	129
Figure 4-9: Changes of ϕ'_{PT} with FC from both isotropically- and anisotropically-consolidated specimens of this study	131
Figure 4-10: CSLs of tailings with different FC	132
Figure 4-11: Effect of FC on Γ_{cs} and λ_{cs} of tailings examined in this study.....	133
Figure 4-12: Variations of (a) $s_u(yield)/\sigma'_{1c}$ and (b) $s_u(liq)/\sigma'_{1c}$ with ψ_{cs} in isotropically-consolidated specimens.....	134
Figure 4-13: Variations of (a) $s_u(yield)/\sigma'_{1c}$ and (b) $s_u(liq)/\sigma'_{1c}$ with ψ_{cs} in anisotropically-consolidated specimens.....	135
Figure 4-14: Variations of ϕ'_{yield} with ψ_{cs} for different tailings mixtures of this study.....	135
Figure 4-15: Stress path of a CDS test on a specimen with FC = 5% (CDS5-1)	137
Figure 4-16: (a) ϵ_a versus mobilized ϕ' and (b) mobilized ϕ' versus ϵ_{vol} for test CDS5-1	137
Figure 4-17: (a) the mobilization of friction angle (ϕ'_{mob}) with volumetric strain (ϵ_{vol}) and (a) axial strain (ϵ_a) rate in CDS tests with different FC.....	139

Figure 4-18: Variations of ϕ'_{yield} mobilized in the CDS tests with (a) e_c and (b) ψ_{cs}	139
Figure 4-19: Comparisons of ϕ'_{yield} mobilized in IU, K_oU and CDS tests on specimens with FC of (a) 5%, (b) 25%, (c) 50%, and (d) 84%	140
Figure 4-20: ε_a versus time in CDS tests with different unloading rates ($\Delta u_e/\Delta t$) for FC = 5%, and FC = 84%	141
Figure 4-21: ϕ'_{mob} versus ε_{vol} in CDS tests with different unloading rates ($\Delta u_e/\Delta t$) for (a) FC = 5%, and (b) FC = 84%	142
Figure 5-1. Geometry of the dam's profile	147
Figure 5-2. Shear modulus of different materials (Morgenstern et al. 2016)	148
Figure 5-3. Horizontal displacement contours for the entirely elastic model obtained by (a) this study and (b) Morgenstern et al. (2016).....	151
Figure 5-4: Horizontal displacement contours for the second model including NorSand constitutive model for sand tailings obtained by (a) this study and (b) Morgenstern et al. (2016).....	152
Figure 5-5. X/Y displacement vectors of the second model.....	153
Figure 5-6. Comparisons of horizontal displacement trends at El. 856 m for (a) the first entirely elastic model and (b) the second model including NorSand model for the tailings	154
Figure 5-7: Geometry and materials of the modeled dam	155
Figure 5-8: Particle size distribution curves of fine and coarse tailings	156
Figure 5-9: Critical state lines of the two gradations of the tailings	157
Figure 5-10: Shear wave velocities of the coarse and fine tailings.....	158
Figure 5-11: Calibration of NorSand model for the fine mixture: (a) stress paths of undrained TxC at $p'_c=200$ and 300 kPa kPa; (b) stress-strain of undrained TxC at $p'_c=200$ and 300 kPa	159

Figure 5-12: Calibration of NorSand model for the coarse tailings: (a) stress paths of undrained TxC at $p'_c=200$ and 300 kPa; (b) stress-strain of undrained TxC at $p'_c=200$ and 300 kPa.....	159
Figure 5-13. The horizontal displacement contours of (a) 3 rd raising, (b) 5 th raising, (c) 8 th raise and (d) the final raise.....	164
Figure 5-14. Horizontal Displacements at the end of construction Robertson et al. (2019) (section 1-1)	165
Figure 5-15. X/Y displacement vectors at the end of construction (a) over all look, (b) downstream compressive deformations, and (c) upstream extensional deformations.....	166
Figure 5-16: Contours of shear stresses distribution of this study.....	167
Figure 5-17: Contours of η/M_{tc} of (a) this study and (b) Robertson et al. (2019) (section 1-1)	168
Figure 5-18. Yielding zones (colored yellow) of the model at the end of the construction .	169
Figure 5-19. Factor of safety of the dam at the end of its construction	169
Figure 5-20. FOS of the model with zero pressure head above water level and in undrained condition	170
Figure 5-21. (a) x-displacement, (b) factor of safety and (c) the yielding zones of the dam after applying 15 cm deformation on its face and zeroing the suction above the water level	172
Figure 5-22. (a) Shear stress distribution contours and (b) η/M_{tc} contours of the dam after applying 15 cm deformation on its face and zeroing the suction above the water level	173
Figure 5-23. Factor of safety against pore water pressure ratio, R_u calculated from Slope/w analyses.....	174
Figure 5-24. Critical slip surfaces associated with R_u values of (a) 0.1, (b) 0.2, (c) 0.3, and (d) 0.4.....	175

Nomenclature

B	Skempton's pore pressure parameter
C_U	Coefficient of uniformity
D	Specimen's diameter
D_r	Relative density
D_{rc}	Relative density after consolidation
D_{50}	Average particle size
dp'	Increment in mean effective stress
dq	Increment in deviator stress
dt	Increment in time
du_e	Increment in pore water pressure
$d\gamma$	Increment in shear strain
$d\varepsilon_{vol}$	incremental change in volumetric strain
$d\varepsilon_{ij}$	Increment in strain tensor
$d\sigma'_1$	incremental change in effective major principal stress
$d\sigma'_3$	incremental change in effective minor principal stress
$d\bar{\sigma}_{ij}$	Increment in stress tensor
d^2W	Second-order work
e	Void ratio
e_c	Consolidation void ratio
e_f	Specimen's final void ratio
e_{max}	Maximum void ratio
e_{min}	Minimum void ratio
FC	Fines content
G	Shear modulus
G_s	Specific gravity
H	Specimen's height
H_o	Plastic hardening modulus
H_ψ	Change in hardening modulus with ψ

I_B	Brittleness index
I_r	Dimensionless shear rigidity
K	Principal stress ratio
K_C	Principal stress ratio after anisotropic consolidation
K_o	Laterally confined principal stress ratio
M	Stress ratio at critical state
K	Principal stress ratio
N	Volumetric coupling coefficient
p'	Mean effective stress
p'_c	Mean effective stress after consolidation
q	Deviator stress
q_c	Deviator stress after consolidation
$s_u(yield)$	Peak undrained strength
$s_u(liq)$	Lowest post-liquefaction undrained strength
t	Time
u_e	Pore water pressure
V_s	Shear wave velocity
W_S	Specimen's dry weight
W_W	Specimen's wet weight
γ	Shear strain
Γ	CSL's reference void ratio
ε_a	Axial strain
ε_r	Radial strain
ε_{vol}	Volumetric strain
η	Deviator stress ratio of q/p'
η_c	After-consolidation deviator stress ratio
η_{cs}	Critical state deviator stress ratio
η_{IL}	Deviator stress ratio at the triggering of instability
λ	CSL's slope in e - $\log(p')$ plane
ν	Poisson's ratio
σ'_v	Effective vertical stress

σ'_{vc}	Effective vertical stress after consolidation
σ'_1	Effective major principal stress
σ'_3	Effective minor principal stress
σ'_{1c}	Effective major principal stress after consolidation
σ'_{3c}	Effective minor principal stress after consolidation
ϕ'	Effective friction angle
ϕ'_{cs}	Critical state effective friction angle
ϕ'_{PT}	Phase transformation effective friction angle
χ_{tc}	Dilatancy constant in TxC
ψ	State parameter
ψ_{cs}	Critical state parameter
ω_f	Specimen's final water content

Chapter 1

1 Introduction

Nowadays extractive mining industries are crucial components of modern societies and to the world economy, that provide vital mineral products due to the increasing demand of metal and energy resources. Additionally, mining industries are of considerable importance for employment opportunities on global and local scales. However, as a consequence of such industrial activities, a large amount of mining waste is being produced on a daily basis. Once the mining sites are excavated, the resultant mixture is processed to extract the valuable components, which are generally only a small portion of the total mined material in volume. The remaining voluminous unusable material is considered as a mining waste. Mine tailings, by definition, are mixtures of crushed rock and processing fluid left over from the extraction of valuable minerals, deposited in slurry form.

It is an accepted practice to store mine tailings in isolated conditions as deposits in impoundments under water behind dams in order to prevent them from exposure to atmospheric oxidation (Kossoff et al. 2014). However, these dams fail frequently on a global scale. LePoudre (2015) has explored tailings dam failures during the past few decades and indicated that 2 to 5 major tailings dam failures occur annually. Considering approximately 3500 tailings dam worldwide, annual rate of failure is 1:700 to 1:750, according to statistics gathered by LePoudre (2015). Soil flow liquefaction has been recognized as the cause of many of many geotechnical structures such as tailings dams. Liquefaction flow failures of mine tailings due to monotonically – increasing and dynamic shearing loads have been described in several different studies in the literature (Olson 2002; Fourie and Tshabalala 2005; Muhammad 2013; Morgenstern et al. 2016; Robertson et al. 2020). Such failures have drastic consequences from both economical and environmental points of views given the large area impacted by such flow slides and as an enormous volume of mine waste releases which contains potentially toxic elements and hazardous contaminants (Lottermoser 2010).

One of the most recent mine tailings dam failures occurred on January 25th, 2019 at Vale S.A.'s Córrego do Feijão Iron Ore Mine ("Dam I"). Robertson et al. (2020) have studied this failure extensively. This dam was located at north-east of Brumadinho, in the state of Minas Gerais, Brazil. Due to a collapse of the dam, which occurred in less than 10 seconds, 9.7 cubic meters tailings flowed (which was reported to be approximately 75% of the stored tailings) out of the dam in less than 5 minutes. The failure mechanism was captured thoroughly by high quality video images taken by cameras installed in front of and behind the dam. A slope failure commenced within the dam starting from the dam crest. The crest dropped and the area above the toe region bulged outwards. Followed by that, the failure extended across most of the dam and the surface of the dam broke apart, resulting in the collapse of the slope of the dam. As a result, more than 250 people perished. The failure was triggered by a critical combination of several mechanisms including a high water level (due to heavy rainfall, low permeable fine tailings, and insufficient drainage), loss of suction and reduced strength of tailings above the water table following a heavy rainfall, high shear stresses under its steep slopes, and ongoing internal creep (Robertson et al. 2020).

Another disastrous tailings dam failure occurred in Brazil on November 5th 2015 in which the Fundão iron tailings dam in the state of Minas Gerais collapse (Morgenstern et al. 2016). The failure resulted in 30 million cubic meters of mine waste and water releasement (61% of the impoundment's content) and a fatality of seventeen villagers in a nearby town as well as extensive environmental damages by polluting the local water system (Agurto-Detzel et al. 2016). As described by Morgenstern et al. (2016), a chain of unfortunate circumstances initiated a liquefaction flow slide at the dam's left abutment. In particular, lateral extrusion of soft compressible slimes under construction loading induced an effective stress reduction, lateral deformation, and liquefaction of the overlying loose sand tailings, which were highly saturated due to limited drainage and a clogged drainage blanket. Additional shocks by a series of three low-magnitude earthquakes just hours preceding the failure further accelerated the flowslide event.

Fourie and Tshabalala (2005) described the Merriespruit gold tailings dam failure in Virginia, South Africa as a result of erosion, overtopping and heavy rainfalls-induced

steepening, that caused reduction in effective stress. As a result, in February 1994, 600,000 m³ of waste tailings were released, killing seventeen people, destroying 280 houses and affecting areas over a distance of more than two kilometers. Failure of a Tar Island dyke built of oil sand tailings in August 1974, in northern Alberta is another example of a tailings dam failure as a consequence of rapid construction described by Mittal and Hardy (1977). Dobry and Alvarez (1967) reported the release of 2×10⁶ tons of tailings and more than 200 deaths due to several El Cobre tailings dams' failures throughout central Chile caused by an earthquake in March 1965. Another tailings dam failure triggered by an earthquake occurred in Hokkaido, Japan in 1968 which is described by Ishihara et al. (1990). There are many other liquefaction triggered flow failure cases of tailings dams described in the literature.

Considering the failures of tailings dams, it is of great importance to understand the fundamentals of liquefaction phenomena and instability concepts in analysis and design of earth structures made of tailings. Whether the tailings responds in a dilative or contractive manner for a given initial state, depends upon the preparation method, the loading mode, stress history and the drainage condition (Vaid and Sivathayalan 2000); and in laboratory settings, specimens with contractive behaviors under triaxial compression may not be so in simple shearing (Al-Tarhouni et al. 2011); and even a dilative soil in compression, becomes completely susceptible to static liquefaction. The soil structure and inherent fabric in preparation method of reconstituted samples has a significant effect on the mechanical behavior of tailings (Chang et al. 2011). Given these controversies and concerning the lack of research with the emphasis on the instability behavior of gold tailings, this study aims to examine all of these effects for gold mine tailings.

1.1 Typical properties of gold mine tailings

The conventional method of deposition of tailings as a slurry in dammed impoundments rises a significant risk in terms of static liquefaction and flow failure because of tailings high degree of saturation and loose deposition. Various researchers focused on studying the shearing behavior and liquefaction of gold mine tailings (Fourie and Papageorgiou

2001; Qiu and Segó 2001; Fourie and Tshabalala 2005; Al-Tarhouni et al. 2011; Chang et al. 2011; Schnaid et al. 2013).

Gold mine tailings are generally classified as sandy silt or clayey silt with zero cohesion and very little plasticity (McPhail and Wagner 1987; Vermeulen 2007). Qiu and Segó (2001) studied the physical and engineering properties of several mine tailings including a gold mine tailings from Echo Bay's Lupin Mines with a fines content of 81.3%. They report a rather stable behavior with limited strain softening of slurry deposited tailings samples in isotropically-consolidated undrained triaxial compression tests.

With an interest in evaluating the potential of liquefaction and deriving the CSL of the Merriespruit gold tailings from south Africa, Fourie and Papageorgiou (2001) performed a series of undrained triaxial compression tests. The moist-tamped tailings specimens demonstrated high potential to static liquefaction. However, Fourie and Papageorgiou (2001) were unable to establish a unique CSL because of the variation in fines content of the tailings. Later, Fourie and Tshabalala (2005) determined different CSLs for Merriespruit gold tailings samples for various percentages of fines content. They also investigated the role of anisotropic consolidation by carrying out a series of undrained triaxial compression tests on anisotropically consolidated specimens. The latter specimens exhibited a more brittle shearing behavior than the isotropically consolidated samples. Higher yield stress ratios were also found in the anisotropically consolidated samples compared to those in the isotropically consolidation tailings specimens. Because of this difference, they recommended anisotropically-consolidated triaxial tests to determine shear strength for stability analysis of tailings dam.

To reduce liquefaction potential of loose tailings, Al-Tarhouni et al. (2011) evaluated the shearing behavior and liquefaction of low plastic thickened gold tailings (with a fines content of 70%) in monotonic and cyclic direct simple shear tests. The thickening method involves dewatering tailings to a water content near their shrinkage limit to enhance matric suction and raise the effective stress within the tailings. This allows stacking thickened tailings at steeper slopes and stabilized under their own weight. Despite potential disadvantages, such as a higher risk of oxidation and acid drainage due to the

absence of a water cover, and remobilization due to seismic loadings, this method alleviates seepage related problems. The laboratory specimens were prepared by two methods including a wet method where tailings were mixed with a certain amount of bleed water and a dry-wet method in which wet tailings were allowed to dry once placed in the simple shearing mold. They measured a friction angle of 27.5° at phase transformation. Although no unique relationship was found between shear strength and void ratio; the normalized shear strength exhibited a consistent trend with consolidation pressure and void ratio. No clear CSL could be established based on their tests due to large scatter in data. They also reported a positive influence of desiccation on increasing the cyclic resistance of the gold tailings.

With respect to the importance of the effect of fabric upon the laboratory preparation methods and the resultant particle arrangement on the mechanical behavior of mine tailings, Chang et al. (2011) carried out an experimental program on moist tamped and slurry deposited samples of a gold tailings. The samples were obtained from the ERPM Dam No. 4 in Johannesburg located in South Africa. SEM (scanning electron microcopy) microscope images showed that none of the two preparation methods were successful in replicating the in-situ fabric and behavior of the undisturbed tailings samples. Nevertheless, the slurry-deposited samples were able to mimic the in-situ behavior relatively better than the moist-tamped specimens. Their experiment included ICU triaxial tests on tailings samples representing three different locations of the impoundment, with three different gradations: Pond, middle beach and upper beach which contained about 90%, 50% and 30% fine content, respectively. Only the tailings samples corresponding to pond showed a small plasticity. Chang et al. (2011) also observed that the coefficient of consolidation was 2 to 3 times higher in case of moist tamping than the undisturbed and slurry deposited samples. Although the different fabrics reached a unique stress ratio at the critical state, a unique CSL was not achieved, and it was concluded that the CSL depends on the fabric and soil characteristics. Static liquefaction was reported to be highly influenced by the preparation technique. While a strain softening behavior followed by hardening was observed for the undisturbed and slurry deposited samples, a completely contractive behavior was attained in some moist tamped specimens.

With regard to the mode of shear, Schnaid et al. (2013) performed a series of drained and undrained triaxial tests under monotonic shearing load in both compression and extension modes. The tested gold tailings with an average fines content of 43% were obtained from a waste disposal plant located in Bahia state in Northeast Brazil. Laboratory specimens were prepared by moist tamping due to its simplicity and ease in reproducing high void ratios. While specimens consolidated to low stresses (< 200 kPa) exhibited strong strain-softening and instability in triaxial compression tests, the instability behavior was suppressed at higher consolidation stresses (> 200 kPa) because of lower void ratios and denser fabric. Concerning evaluating the extension shearing mode, the samples were consolidated anisotropically. The anisotropic consolidation was done along the K_0 line while σ'_3/σ'_1 was considered to be equal to $1 - \sin\phi' = 0.45$. The drained shearing was accomplished by reducing the vertical stress and holding the lateral stress constant. The drained tests indicated contractive behavior. Undrained tests were performed by holding the vertical stress constant and increasing the lateral confining stress. The undrained tests exhibited positive excess pore water pressure and complete collapse as they liquefied with zero effective stress. A unique and curved CSL was established based on both the compression and extension tests. This suggests that the CSL is unique regardless of the magnitude of the principal stress. The nonlinearity of the CSL also indicates a constant state parameter does not exist for the material along its NCL. Their results proved that state parameters lower than 0.1 represented stable conditions, while full liquefaction occurs at state parameters around 0.3. The $\psi = 0.1$ was chosen as the limit for the onset of instability.

Mine tailings are generally classified as sandy silt to clayey silt in terms of gradation. However, when tailings are used for dam construction the geotechnical (and environmental) properties of the material become important to know in order to build safe embankments. A major problem is that the production process creates angular particles at a size similar to clay, slit and fine sand, which do not behave in the same way as natural geological material Jantzer et al. (2008). It is unclear if similar results of studies on the static liquefaction of sands can be true for gold tailings, that are silty sand with platy fines Vermeulen (2007). Tailings are artificial material and are a by-product of

rock crushing and the behavior of tailings material upon loading is different as compared to natural soil materials. (Johansson 1990; Bhanbhro 2014; Jantzer et al. 2008). While natural material has been tested and described extensively, tailings properties raise new questions. The angularity of tailings may be one important concern. On the other hand, the lack of post-deposition compaction mechanisms and the electrical interaction among the finer particles generally entail loose in-situ arrangements; which, combined with full saturation and static/dynamic rapid loading, can lead to the generation of pore pressures that eventually liquefy the material Sottile et al. (2019). Thus, quantifying the material contractiveness is of paramount importance for practical engineering purposes. The tailings are also composed of different minerals and chemicals remaining from the refining process that can affect the mechanical behavior.

However, soil mechanics principles can be applicable to predict the tailings behavior upon loading. In relation to natural soil of equivalent gradation in general, the properties of tailings such as shear strength, permeability Vanden Berghe et al. (2009) and particle shapes Rodriguez (2013) are different. Tailings particles are more angular as compared to natural soils Rodriguez (2013) and are therefore likely to have influence on the mechanical properties Cho et al. (2004).

According to Cho et al. (2004), decrement in sphericity (i.e., increment in angularity) for a given gradation, leads to increment in extreme void ratios (e_{\max} and e_{\min}) and void ratio interval ($I = e_{\max} - e_{\min}$); increment in compressibility under zero lateral strain loading (C_c); increment in constant volume critical state friction angle (ϕ'_{cs}); and increment in the critical state line intercept (Γ) (and a weak effect on the slope (λ)).

As stated by Cho et al. (2004) “the relevance of grain size and grain size distribution in soil behavior is extensively recognized in soil classification systems, such as the USCS. While particle shape is overlooked in current classification guidelines, it emerges as a determining parameter in soil behavior. It is recommended that particle shape be assessed and explicitly documented as part of every soil characterization exercise.”

Shuttle and Jefferies (2010), have stated that different material properties than the typical range of values for regular soils have been measured for tailings. According to them,

recent experimental measurements have revealed relatively very high values of critical stress ratios or friction angles (ϕ'_{cs}); or diverging values of the dilatancy parameter (χ_{tc}). Tailings have slightly higher effective friction angle (3-5°) than natural granular materials; this is because of high angularity (Vick 1990; Mittal and Morgenstern 1975). Vick (1990) further indicates that tailings are more compressible as compared to natural soils of equivalent grains, due to their grading characteristics, loose depositional state and high angularity.

The stress concentration at edges during shear probably leads to further crushing and higher resistance to shear. Crushing and grinding creates particles that are much more angular than natural grains. Because of saturation and the lack of cohesion, the placement of an undisturbed tailings sample in a triaxial test device is difficult to carry out, thus making representative laboratory testing on tailings difficult. When the silt content is high, however, tailings behavior combines aspects from clay-like and sand-like materials; it resembles clay behavior in terms of low hydraulic conductivity, and sand behavior in terms of having the strength controlled by particle contacts; entailing dilative/contractive behavior depending on the void ratio e and mean effective stress Sottile et al. (2019).

One main difference between tailings dams and water retention dams is that tailings dams are raised in stages or continuously as the impoundment is filled up with tailings along with mining production Vick (1990). This deference highlights the importance of different scenarios of loading combinations.

Therefore, understanding the geotechnical properties of tailings (i.e., shear strength; density and hydraulic conductivity) are important factors to be considered while designing and analyzing a tailings dam. Characterization of the mechanical response of tailings is also important for calibrating constitutive models to capture key aspects of such materials' behavior by geotechnical engineers Jefferies and Been (2016).

1.2 Effect of different loading paths

The possible influence of alternative stress modes rather than compression on the behavior of loose granular material has been explored and reported in several studies

(Chung 1985; Vaid and Thomas 1995; Finge et al. 2006; Finge et al. 2006; Doanh et al. 1997; Gennaro et al. 2004). As illustrated by Sadrekarimi (2016) and shown in Figure 1-1, along a potential failure surface beneath a sloping ground, mode of shear varies as a result of variations in the principal stress directions from compression at the crest, to simple shearing, and ultimately extension near the toe, corresponding to the angle of the failure plane to the horizon, θ , of $\theta > 15^\circ$, $-15^\circ \leq \theta \leq 15^\circ$ and $\theta < -15^\circ$, respectively.

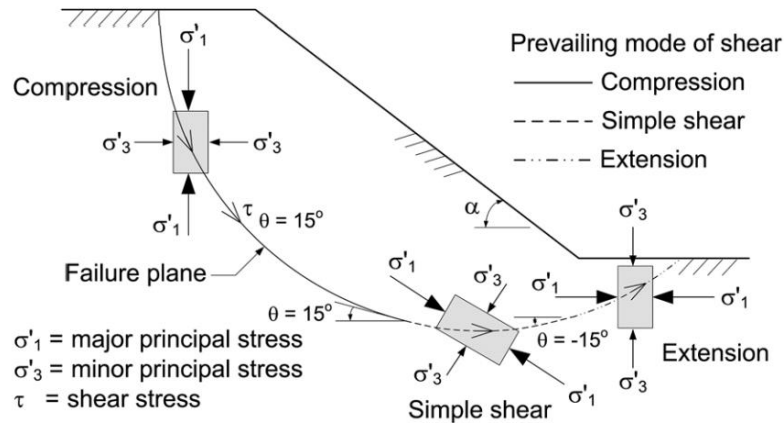


Figure 1-1: Variation of mode of shearing along a failure plane beneath a sloping ground Sadrekarimi (2016).

The comparison between the responses of soil in simple shearing mode and triaxial compression (TxC) and triaxial extension (TxE) has been of interest to investigate. Vaid and Thomas (1995) and Gens (1982) reported identical steady state friction angles for sands under undrained triaxial extension and compression shearing. Bishop (1971), Miura and Toki (1982), Gennaro et al. (2004), Chang et al. (1982) and Doanh et al. (1997) reported differences in behaviors of sands sheared in undrained conditions by triaxial compression and triaxial extension, such as unequal critical state angles of friction, different volumetric strains, peak, and post – liquefaction undrained strengths for given consolidation history and void ratio. As suggested by Chung (1985), the inherent fabric anisotropy in loose sands can be accounted for the primary cause of the differences in sands behaviors in different shearing modes. Inherent anisotropy is referred to the microstructural changes developed at the end of a K_0 consolidation. Stress-induced

anisotropy on the other hand, is another type of anisotropy which is a result of application of stress after the completion of K-consolidation process (Finge et al. 2006).

By an experimental study on Fraser Delta sand, Vaid and Sivathayalan (1996) showed that the potential for liquefaction depends on the stress paths during loading. They found out the most susceptible mode for static liquefaction is extension, while the least is compression. The results from simple shearing mode lied closer to extension than to compression. They measured friction angles mobilized at the peak shear stress in simple shearing and triaxial extension were noted to be approximately equal and about 10 degrees less than what was obtained from triaxial compression. Vaid and Sivathayalan (1996) observed that effective stress conditions at phase transformation in simple shear lie along a straight line passing through the origin. This line was found to be close to that derived from triaxial compression tests by Vaid and Thomas (1995). They also observed the same friction angles at the critical and the phase transformation states in both undrained compression and extension shearing. Vaid and Sivathayalan (1996) found that the simple shear and triaxial PT friction angles were almost the same and independent of the void ratio, confining stress and loading mode. In addition, they that observed increasing confining pressure at a constant void ratio, promotes the contractiveness of sand under simple shearing mode. A similar conclusion was made by Vaid and Thomas (1995) for triaxial compression; while, according to Vaid and Thomas (1995), increasing confining pressure decreases the contractiveness in triaxial extension. Gens (1982) has reported the same friction angles at critical state for both extension and compression.

Gennaro et al. (2004) studied the undrained behavior of Hostun sand and their findings indicated lower slopes of failure and PT lines in extensionally sheared samples than of those sheared in compression. Gennaro et al. (2004) also showed that under monotonic compression, the undrained response is controlled by phase transformation, and the mechanical behavior is stable and dilatant; while, subjected to undrained extension shearing, the material is unstable and contractive, and liquefaction-induced instability occurs. These findings appeared to be in line with the conclusions made by Chang et al. (1982) as they showed for a given range of densities, samples subjected to compression loading tend to be more dilative than those undergoing extension shearing.

Anisotropic consolidation induces stress - induced anisotropy in yielding stresses (IMAM et al. 2002). The influence of anisotropy during the consolidation process on instability line (IL) has been investigated by Doanh et al. (1997). They showed the instability line of a compressible sand under an undrained condition is highly influenced by the anisotropic consolidation process such that in compression shear, a higher slope of instability line is obtained by a greater anisotropic consolidation level, but a reverse trend is observed for extension. Also, they observed larger mobilized undrained shear strengths in compression than of what was obtained from extension in both isotropic and anisotropic cases. This dependency of the instability line on anisotropic consolidation level indicates that the instability line is not an intrinsic characteristic as the critical state. It is stated by IMAM et al. (2002) that if an anisotropic consolidation is applied at a stress ratio smaller than the peak stress ratio of an isotropic undrained ESP (effective stress path), the stress at the peak would not be affected. However, a higher stress ratio would cause an increment in peak shear stress during an undrained shearing in the direction of the anisotropic consolidation, and a decrement in the opposite direction.

The increment in strain – softening behavior, or brittleness, of anisotropically consolidated specimens of sands during an undrained shearing has been explained by Sadrekarimi (2016). According to him, the induced shear stress during a K – consolidation decreases the potential of pore water pressure generation. This happens due to densification and soil particles interlocking, imposed by the anisotropic consolidation, that leads to a larger effort to surmount the yield undrained strengths.

An important parameter for undrained stability analysis and evaluating the potential of flow liquefaction occurrence is undrained shear strength of soils following liquefaction flow failures (Sadrekarimi 2013a). For designing large geotechnical structures, such as mine tailings impoundments, the undrained post – liquefaction shear strength is a necessary parameter for stability analysis. The yield strength ratio, $s_u(\text{yield})/\sigma'_{1c}$, can be used to estimate the undrained shear strength prior to the commencement of undrained instability and liquefaction by knowing the major principle stress (Olson and Stark 2003a). The minimum undrained shear strength mobilized in a liquefaction failure flow is termed the undrained critical shear strength or $s_u(\text{critical})$ by Terzaghi et al. (1996). Olson

and Stark (2002) have used a different term, $s_u(\text{liq})$, as according to them, the infield conditions may violate the constant volume condition. Sadrekarimi (2020) has used $s_u(\text{liq})$ to include both $s_u(\text{critical})$ in strain-softening behavior and $s_u(\text{PT})$ for limited liquefaction behaviors. These two terms are used interchangeably in this proposal. Other researchers have normalized yield and critical state undrained shear strengths with respect to various consolidation stresses (Hanzawa 1980, Ishihara 1993, Vaid and Sivathayalan 1996, Olson and Stark 2003; Sadrekarimi and Olson 2011). Vaid and Sivathayalan (1996) found no unique relationship between void ratio, and steady – state and phase transformation strengths ($s_u(\text{PT})$ if response is limited liquefaction, and $s_u(\text{critical})$ or $s_u(\text{SS})$ if steady state) for static liquefaction in simple shearing mode. Instead, they found different relationships at each confining stress level. They investigated the existence of a relationship between normalized $s_u(\text{critical})$ with respect to the confining pressure and e_c . A noticeable scatter was noted in their plotted results; however, they suggested this relationship as an approximation for estimating $s_u(\text{critical})$ based on e_c for a given confining pressure.

Chapter 2 of this study investigates the undrained instability and liquefaction behavior of gold mine tailings by conducting monotonic TxC and TxE tests on isotropically and K_σ -consolidated tailings specimens in order to assess the effect of stress-induced anisotropy and mode of shearing. The experimental results are analyzed within the framework of critical state mechanics to characterize the triggering of instability and undrained shear strength of tailings samples.

1.3 Instability in drained conditions

A specific type of stress path can be employed to simulate the conditions in which a slow lateral stress relief or an increment of pore pressure due to water infiltration occurs at a constant applied shear stress in drained conditions. This stress path is termed drained constant shear stress (CSS) by Brand (1981) and investigated by a few studies (Anderson and Riemer 1995; Zhu and Anderson 1998; Lourenço et al. 2011). Many cases of field failures of mine tailings dams as a result of snowmelt, ground water table rising, heavy rainfalls and irrigation have been associated to this type of stress paths (Harp et al. 1990; Anderson and Sitar 1995; Olson et al. 2000; Leroueil 2001). These types of unloading

can trigger instability under fully drained conditions followed by an abrupt increment of axial and volumetric strains and eventually a complete failure. In such cases, as reported by Eckersley (1990), the generation of excess pore water pressure is a consequence of soil elements failure due to static loadings instead of the cause of the failure. These stress paths consist of a conventional drained shearing part followed by an unloading part with a decrement of mean effective stress while the deviator stress remains constant.

In case of undrained response of loose granular deposits, instability commencement point can be interpreted as the initiation of strain softening or the reduction in deviator stress. Contrariwise, in drained constant shear stress path, $s_u(\text{yield})$ is never exceeded. Hence, another criterion might be required to explain the onset of instability of porous materials subjected to such stress-paths. Drucker (1957) incorporated the second-order derivative of work per volume to formulate the instability postulate generally for materials. In this sense, a material is stable as long as the second increment of plastic work, meaning the scalar product of the stress increment and plastic strain increment, remains non-negative. The formulation is as below:

$$d^2W = d\sigma_{ij} \cdot d\varepsilon_{ij}^p \quad [1-1]$$

Where $d\sigma_{ij}$ is the increment of stress tensor, $d\varepsilon_{ij}^p$ is the increment of plastic strain tensor, and d^2W is the second-order of work. Hill's stability Hill (1958) guarantees stability a little beyond the condition given by Drucker as it incorporates the second-order of work including both elastic and plastic strains increment. Although, according to the argument by Li and Dafalias (2000), it may be assumed that all the work is plastic. This assumption is for simplicity and as the elastic strains are negligible compared to the plastic strains at large strains.

With respect to the variable nature of rates of erosion or water infiltration in reality, the rate of unloading, $\Delta\sigma_3/dt$, in experimental programs can be various. Different studies have used different unloading rates in their experimental simulations. Anderson and Sitar (1995) used a small rate of 0.017 kPa/min, Lade and Pradel (1990) used 0.1 kPa/min and Dong et al. (2016) employed a rate of 1 kPa/min. Some studies have examined and reported the possible influence of changing this rate on the drained instability behavior.

Chu et al. (2012) changed the unloading rate in their drained constant shear stress tests on Singapore sand from 1 kPa/min to 5 kPa/min and reported a negligible effect on the commencement of instability points. Gajo et al. (2000) carried out drained CSS tests on Huston sand and reported a slight effect in terms of a small decrement in the stress ratio at which instability begins by increasing the rate of $\Delta\sigma_3/dt$ from 0.13 kPa/min to 2.5 kPa/min. They attributed this decrement in instability onset stress ratio to the lack of pore water pressure dissipation as a result of a faster rate of confining pressure reduction. On the other hand, Rabbi et al. (2019) observed a significant difference in the occurrence of onset of instability of Yellow sand by changing the unloading rate from 0.2 kPa/min to 5 kPa/min. They concluded the stress ratio at the onset of instability increases by decreasing the reduction rate. As a possible explanation, they accounted for the presence of 10% fine content in their observation. Overall, it is noted that no consensus has been reached regarding the effect of the rate of unloading on the drained instability behavior and further investigation is needed.

Static liquefaction and instability of two different gold mine tailings are investigated in this study in Chapter 3 through undrained and constant-deviator stress unloading triaxial compression tests. The primary goals of this study are to examine three different approaches (strain rate, volumetric strain, energy) for identifying the triggering of instability in CDS tests. Furthermore, stress ratios (i.e., friction angle) mobilized at the triggering of instability from CDS and undrained shear tests are compared. A unified framework based on the critical state theory for determining the triggering of instability in two gold mine tailings from CDS and undrained tests are established. At the end, the effects of void ratio, effective stress, initial stress ratio, and unloading rate on the triggering of instability in gold tailings are studied.

1.4 Effect of fines content

The after-effects of tailings' gradation change and fine particles presence on the behavior of such materials has been a concern in the literature. Studies such as Seed (1987) and Pitman et al. (1994) suggest that fines provide a better resistance against liquefaction for sands. Carraro et al. (2009) tested Ottawa sand with up to 15% either non-plastic silt or

kaolin clay through isotropically consolidated drained triaxial compression tests. They showed that adding the nonelastic silt resulted in increasing both peak and critical state friction angles and more dilative behavior compared to that of a clean sand. However, for very loose states, more contractive response was observed by adding the silt. On the other hand, addition of kaolin clay to the host sand led to decrement in the mentioned friction angles and more contractiveness for all the states.

On the other hand, there are indications that loose sands containing non-plastic fines up to a certain amount, existing in both natural and man-made deposits such as tailings dams, are more susceptible and prone to earthquake-induced large deformations or flow failures (Zlatović and Ishihara 1995; Lade and Yamamuro 1997; Thevanayagam 1998; Ni et al. 2004). Verdugo and Ishihara (1996) showed that relative contractiveness of sands, an indication for the intrinsic potential of liquefaction, increases by adding fines. Yamamuro and Lade (1997), Wang and Sassa (2000), Fourie et al. (2001), Naeini and Baziar (2004), de Alba and Ballesterro (2008) and Belkhatir et al. (2011) showed the presence of fines less than 30% increases the liquefaction susceptibility of sands. For example, Lade and Yamamuro (1997) performed undrained triaxial compression tests on Ottawa and Nevada sands with varying amounts of non-plastic silts and showed that the fines create a very compressible particle structure in soils. This increment in the potential of liquefaction continues up to a threshold and afterwards, remains constant with respect to relative density. Enomoto (2019) observed that this threshold is about 50% non-plastic “DL clay” silt added to silica sand No. 6 as the host sand. They used undrained triaxial compression tests, both cyclic followed by monotonic loading, and monotonic tests without precedent cyclic loading on reconstituted wet-tamped samples. Similar reversal behavior was also observed by Monkul et al. (2017) using undrained monotonic triaxial compression and Papadopoulou and Tika (2008) by undrained and drained monotonic triaxial compression tests. Huang and Huang (2007) performed a series of monotonic and cyclic triaxial compression tests on both undisturbed and reconstituted (moist tamping and water sedimentation) samples of Yuan Lin soil with fines contents ranging from 18, 43 and 89%. They emphasized on the importance of the existence of soft minerals on the mechanical behavior of their soil. However, the cyclic resistance ratio of their both reconstituted and natural specimens decreased all the way with increasing FC without

showing any reversal. They concluded this observation indicates that a threshold in FC may not be universal for all sand-silt mixtures. Kwa and Airey (2017) measured the resistance of metallic ores with varying fines, 18, 28, 40 and 60%, to liquefaction using monotonic (drained and undrained) and cyclic (undrained) compression triaxial tests. The 18% fines containing ores with the densest condition showed the highest resistance to liquefaction by resisting the higher number of cycles for any CSR.

Ni et al. (2004) demonstrated a downward translation of CSL in $e-p'$ plane due to addition of non-plastic fine to a clear sand. This conclusion is in agreement with the findings of Murthy et al. (2007). They performed undrained triaxial compression tests on clean sand and silty sands with 5%-15% non-plastic silt contents. Owing to this problem, Torres-Cruz and Santamarina (2020) have studied the change in the location of the critical state line of Platinum tailings due to the change in FC. They demonstrated that three different mixtures of the tailings with FC=10%, FC=30% and FC=81% exhibited three different critical state lines in the plane of $e-p'$ in such wise that the mixture containing 30% fines by weight was found to have the lowest interception in this plane, while the FC=10% appeared to be above the other gradations, and the gradation containing 81% fines, was placed in the middle. Naeini and Baziar (2004) conducted a series of monotonic and dynamic triaxial compression tests on Ardebil sand. The percentage of fines in their reconstituted samples (prepared by both moist tamping and water sedimentation techniques) varied from 0% to 100%. They prepared their water sedimented samples through repeated stepwise depositions, each step including dropping predetermined amount of soil into de-aired water followed by a length of time. Their results illustrated that the critical state line of the soil moves downward by increasing silt content up to 30%, and by experiencing a reversal, starts to shift upward after this limit. The results of the study of Kwa and Airey (2017) shows that the CSLs of metallic ores shifted upwards to looser conditions all the way with increasing fines content from 18 to 60%, parallel to each other. This movement was without observing any particular FC relating to a threshold. They attributed this observation to the lack of a clear distinction between the fine and coarse portions of their well-graded under-study material.

In addition to the global void ratio and relative density, two other density parameters have been introduced regarding the effect of fines. Global void ratio is by definition the ratio of the volume of voids over the volume of solids. However, skeleton and intergranular void ratios are defined to treat the volume occupied by the fines as they were void spaces. Carraro et al. (2009) concluded that using skeleton and intergranular void ratios may not be suitable for explaining the mechanical behavior of sands containing different types of fines since they do not take the intrinsic microstructural characteristics and plasticity of the fines into account.

The reconstituted specimen preparation technique has a strong influence on the stress – strain response of the samples. The widely used methods include wet sedimentation (i.e., water pluviation), moist tamping, slurry deposition, and dry pluviation. Water sedimentation is suitable to simulate the field conditions of many soil types such as alluvial, lacustrine and marine deposits that deposit through water in nature Ghionna and Porcino (2006), or hydraulic fills that are built by man. However, according to Kuerbis and Vaid (1988) this preparation methods results in fines-coarse segregation for sands containing fines, such that the coarse fraction sediment at the bottom, grading upwards to fines. Moist tamping is superior as it produces particle structures that can show the liquefaction response whereas water pluviated samples cannot at the same soil state Vaid et al. (1999). the Ishihara (1993) has indicated the benefits of moist tamping method in terms of homogeneity and the possibility of having very loose structures. According to Jefferies and Been (2015) this method minimizes strain-localization in the samples. Huang and Huang (2007) witnessed that among moist tamping and wet sedimentation, neither created weaker structures. They related this observation to the mineral content in their Yuan Lin soil samples.

Regarding the issue of particle segregation and separation, different mixtures fabricated from a given gold mine tailings with different amounts of non-plastic fines were tested using triaxial apparatus in this study. The results will be presented and discussed in Chapter 4 with a concentration on the characteristics of the monotonic undrained responses of the tailings such as static liquefaction behavior and instability of the material.

Chapter 2

2 Instability of a Gold Mine Tailings Subjected to Different Stress Paths

2.1 Abstract

Static liquefaction of mine tailings has been the interest of many studies as these materials are generally deposited in a loose condition and stored at high saturation ratios. Yet few researchers have investigated the behavior of mine tailings in stress paths involving extensional consolidation or shearing in extension. In this study, the results of a set of experiments aimed at investigating the static liquefaction behavior of saturated loose gold mine tailings samples in triaxial compression and extension shear tests are described. Monotonic tests are carried out on isotropically and K_0 -consolidated samples to assess the effect of stress-induced anisotropy and mode of shearing on the instability and critical state behaviors of tailings. The comparison of undrained extension and compression shearing behaviors of samples consolidated to similar densities and stress conditions show a profound difference in their undrained shearing responses. This is attributed to the angular shapes of tailings particles which amplify the effects of particle orientation and sample fabric, as well as microstructural changes induced by different loading paths. Post-liquefaction and yielding undrained shear strengths and effective friction angles from different modes of consolidation and shearing are examined. In both undrained compression and extension tests, tailings samples exhibit a limited liquefaction behavior after yielding, followed by a strain-hardening (dilative) behavior. Differences in tailings behavior under different loading directions and anisotropic stresses indicate the importance of considering the effects of these phenomena on the stability analysis of mine tailings dams.

2.2 Introduction

It is an accepted practice to store mine tailings in submerged impoundments behind dams to prevent them from exposure to atmospheric oxidation (Kossoff et al. 2014). However, these dams have failed frequently on a global scale. (LePoudre 2015) has summarized tailings dam failures during the past few decades and indicates that 2 to 5 major tailings dam failures occur annually. Considering approximately 3500 tailings dams worldwide, the annual rate of failure is 1:700 to 1:750, according to statistics gathered by LePoudre (2015). Flow liquefaction has been recognized as the primary failure mechanism for most of these failures. Liquefaction flow failure of mine tailings due to monotonically – increasing shear loads have been described in several different studies (Fourie and Tshabalala 2005; Morgenstern et al. 2016; Robertson et al. 2020). Such failures have had damaging economical and environmental consequences given the large areas impacted by such flowslides and the enormous volume of released mine waste. One of the most recent mine tailings dam failures occurred on January 25th 2019, at Vale S.A.’s Córrego do Feijão Iron Ore Mine (“Dam I”) in the state of Minas Gerais, Brazil. In less than 5 minutes, 9.7×10^6 m³ of tailings ($\approx 75\%$ of the stored tailings) was released out of the dam and the flowing tailings killed more than 250 people. The failure was triggered by a critical combination of several mechanisms including a high water level (due to heavy rainfall, low permeable fine tailings, and insufficient drainage), loss of suction and reduced strength of tailings above the water table following a heavy rainfall, high shear stresses under its steep slopes, and ongoing internal creep (Robertson et al., 2020). An earlier failure also occurred in Brazil on November 5th 2015 in which the Fundão iron tailings dam in the state of Minas Gerais collapsed (Morgenstern et al. 2016), releasing 30×10^6 m³ of mine waste ($\approx 61\%$ of the impoundment’s content) and perishing 17 villagers in a nearby town (Agurto-Detzel et al. 2016). As described by Morgenstern et al. (2016), a chain of unfortunate circumstances initiated a liquefaction flow slide at the dam’s left abutment. In particular, lateral extrusion of soft compressible slimes under construction loading induced an effective stress reduction, lateral deformation, and liquefaction of the overlying loose sand tailings which were highly saturated due to limited drainage and a clogged drainage blanket.

Additional shocks by a series of three low-magnitude earthquakes just hours preceding the failure further accelerated the flowslide event.

Gold mine tailings generally have little cohesive strength and plasticity (McPhail and Wagner 1987; Vermeulen 2007) which is conducive to their strain-softening and liquefaction behavior (Qiu and Sego 2001; Chang et al. 2011; Fourie and Papageorgiou 2001; Schnaid et al. 2013; Riveros and Sadrekarimi 2020). Furthermore, stress-induced anisotropy (Doanh et al. 1997; Fourie and Tshabalala, 2005; Bahadori et al. 2008; Jafarzadeh et al. 2008; Shahsavari Goughari 2012; Keyhani and Haeri 2013; Lashkari et al. 2017) and differences in mode of shearing (Vaid and Thomas 1995; Vaid and Sivathayalan 1996; Gennaro et al. 2004; Doanh et al. 1997) can result in significance changes to the shearing strength and stress-strain behavior of soils and mine tailings. Liquefaction susceptibility and strain-softening potential of specimens subjected to TxE are also found (e.g., Vaid and Sivathayalan 1996; Gennaro et al. 2004, Boukpeti et al. 2002; Altun and Goktepe 2006) to be greater than those in TxC tests.

In light of the many failures of tailings dams, it is important to understand tailings shearing behavior subjected to complex loading histories that include both compression and extension consolidation and undrained shearing modes in the analysis and design of earth structures made of such materials. The variation of principal stress direction with respect to a curved failure plane leads to different modes of consolidation and shearing. Therefore, TxC alone cannot represent the undrained strength and shearing behavior along the entire potential failure surface (Vaid et al. 1990). As illustrated in Figures 1 and 2, the shearing mode beneath a tailings dam could vary from compression just under the crest to extension near the toe. During an embankment construction (Figure 2-1), sediments which are anisotropically consolidated in compression (i.e. drained compression shearing) would be sheared in compression under the embankment's crest at A (CKCU), and in extension at the outskirts of the embankment at B (CKEU). Raising of an existing embankment would exert additional extensional loading at B (EKEU) which has undergone extensional consolidation during embankment construction. Further extension of an embankment (e.g., from a starter dyke to a full dam, or constructing a

berm) as in Figure 2-2 could reverse the loading direction at B from extension to compression shearing (EKCU).

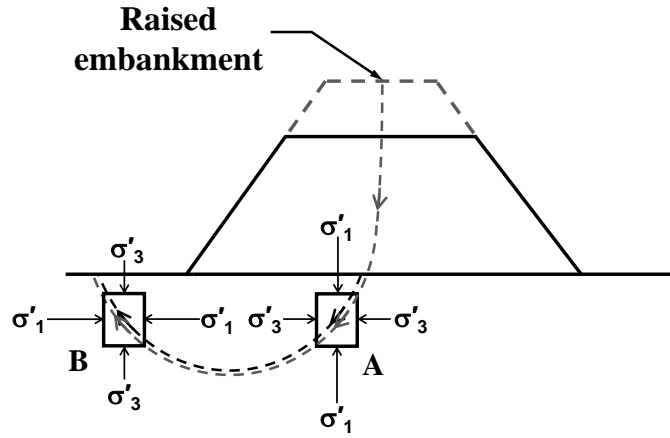


Figure 2-1: Change of shearing direction under an embankment during construction and embankment raising

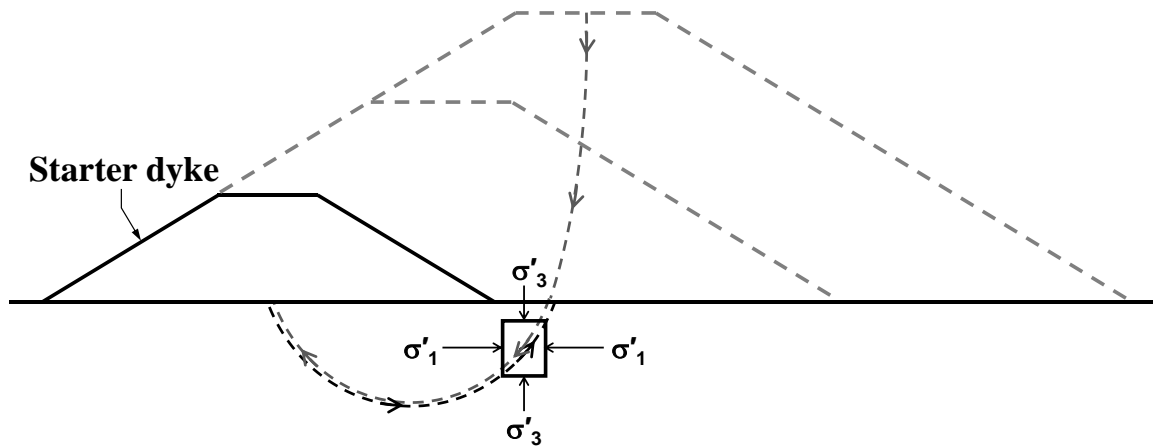


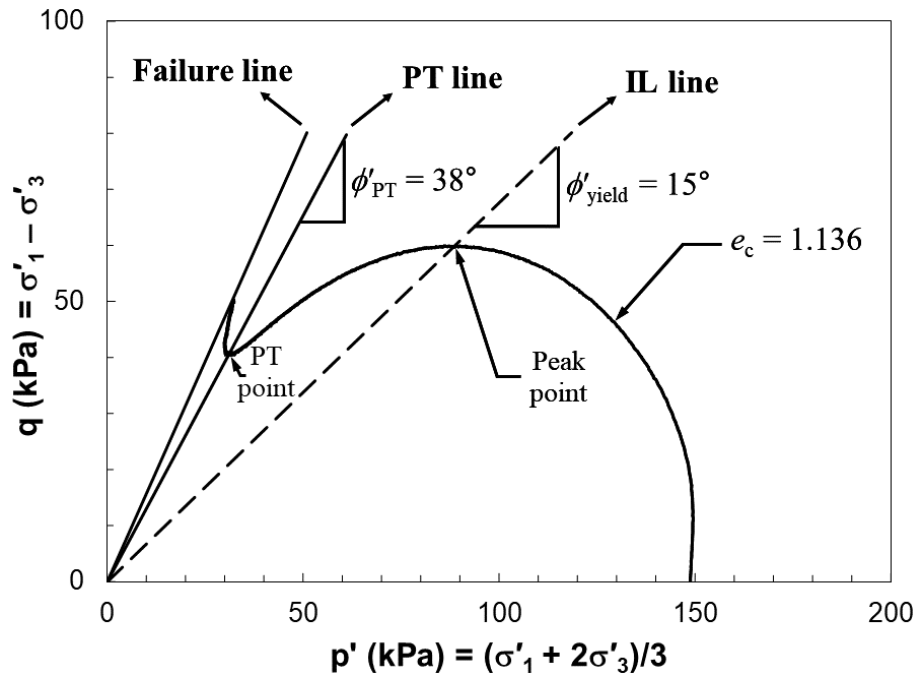
Figure 2-2: Reversal in shearing direction following embankment extension

This paper investigates the undrained instability and liquefaction behavior of gold mine tailings by conducting monotonic TxC and TxE tests on isotropically and K_0 -consolidated tailings specimens in order to assess the effect of stress-induced anisotropy and mode of shearing. The experimental results are analyzed within the framework of

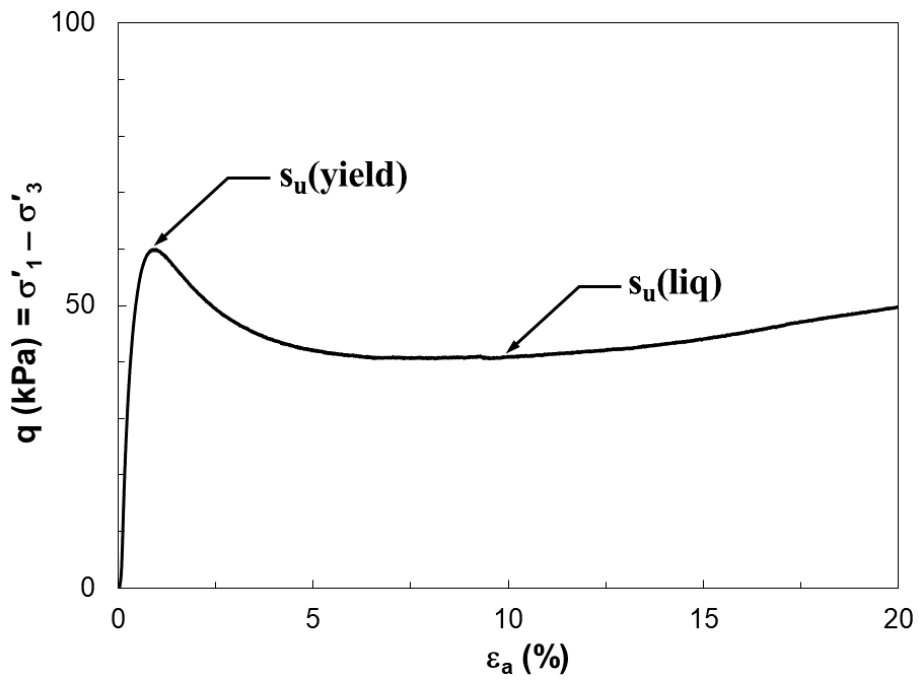
critical state mechanics to characterize the triggering of instability and undrained shear strength of tailings samples.

2.3 Terminology

Some of the most widely used terminology throughout this paper are described below. Figure 3 illustrates the effective stress path (ESP) from an undrained triaxial compression (TxC) test on a loose gold mine tailings specimen carried out in this study. According to this figure, during undrained shearing, the deviator stress reaches a peak which is the triggering condition for the subsequent strength loss and static flow liquefaction. The peak deviator stress corresponds to the undrained yield strength, or $s_u(\text{yield})$ (Terzaghi et al. 1996) at which undrained instability is triggered. Strain-softening and static liquefaction failure follow the triggering of instability where large plastic strains are generated in the tailings specimen (Chu et al. 2003). The instability line (IL) is drawn through the peak points of undrained stress paths at a given void ratio but at different effective confining pressures for a given contractive soil (Lade 1992; Chu et al. 2003). This line separates potentially unstable stress states from stable conditions (Lade 1992). The minimum undrained shear strength reached after the triggering of instability is called the post-liquefaction strength, $s_u(\text{liq})$. Alarcon-Guzman et al. (1988) called the type of strain softening which is followed by strain hardening a quasi-steady state (QSS). The termination of strain softening in a QSS behavior (i.e. limited flow liquefaction) occurs by a turnaround of the ESP at a phase transformation (PT) point according to Ishihara et al. (1975). A unique line is associated with limited liquefaction, similar to the critical state line associated with flow liquefaction, that passes through the origin and the PT points. These terms will be used throughout this paper since the tailings used in the current study mostly show a QSS behavior.



(a)



(b)

Figure 2-3: The (a) ESP of a limited flow liquefaction behavior (ICU 1); (b) stress-strain of a limited flow liquefaction behavior (ICU 1)

2.4 Experimental Program

2.4.1 Material tested

Gold mine tailings from a mine site in Quebec, Canada were used in the experiments of this study. Particle size distribution of the tailings were determined according to the ASTM D422 standard procedure as shown in Figure 2-4, indicating a fines content of 17% by weight. Maximum and minimum void ratios of respectively 0.68 and 1.08 and a specific gravity (G_s) of 2.75 were also measured following ASTM D4253, ASTM D4254, and ASTM D854-14 standard methods, respectively. SEM (scanning electron microscope) images of tailings particles in Figure 2-5 suggest angular to subangular particle shapes and rough surface textures. The mineralogical composition of tailings was identified using X-ray diffraction (XRD) analysis, indicating the prevalence of quartz, albite, clinocllore, ferroan, and glycolated minerals.

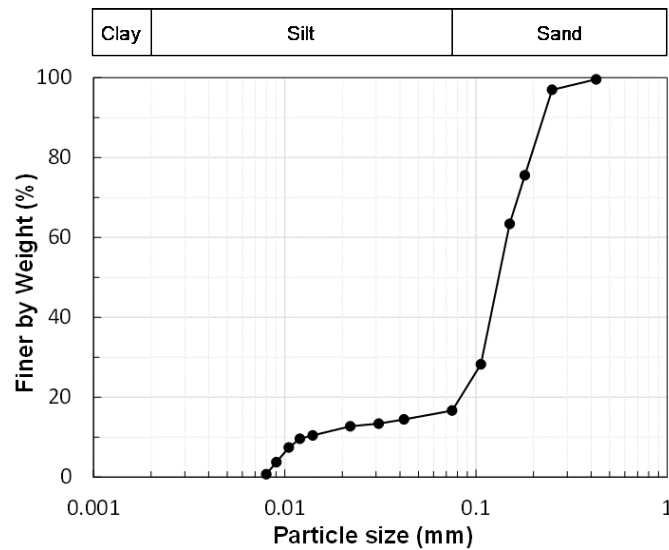
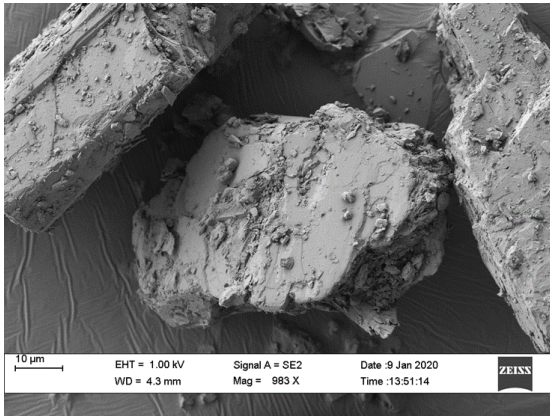
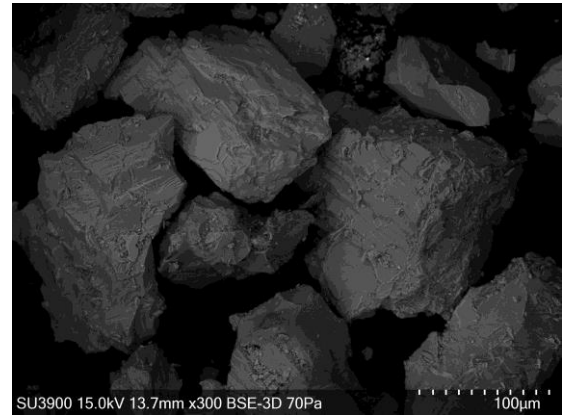


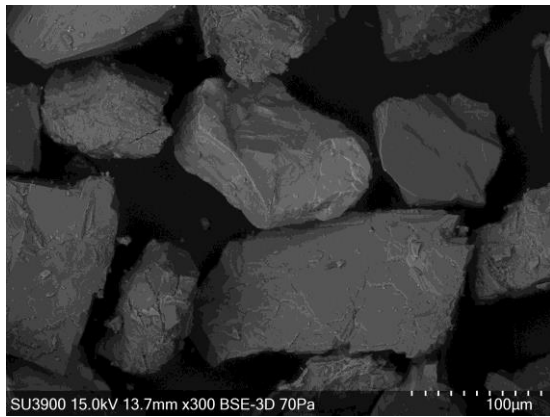
Figure 2-4: Average particle-size distribution of the gold tailings used in this study



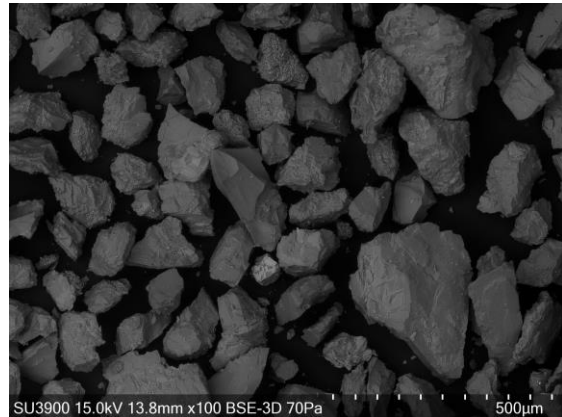
(a)



(b)



(c)



(d)

Figure 2-5: SEM images of the gold mine tailings particles at: (a) $\times 983$, (b) $\times 300$, (c) $\times 300$, and (d) $\times 100$ magnifications

2.4.2 Testing apparatus

A computer-controlled stress path triaxial testing system manufactured by GeoTac Trautwein (USA) was used in this study. A schematic layout of the triaxial system is shown in Figure 2-6. The system consists of a uniaxial loading frame, two electromechanical pressure pumps and a distributed data acquisition and control system

(DDAC). The two pressure pumps are used to supply and monitor the specimen's pore water and cell fluid pressures and volumes with volumetric capacities of 170 ml and 75 ml, respectively. Each pump is equipped with high resolution pressure transducers with a pressure capacity of 2,068 kPa and an accuracy of 0.1% full-scale (FS). A separate pressure transducer is mounted on the triaxial cell and connected to the bottom of the specimen to measure specimen's pore water pressure with a pressure capacity of 1,370 kPa. The uniaxial loading frame is used to apply axial compression and extension to the triaxial specimen via an electromechanical force actuator. The deviatorory load is recorded by a submerged internal load cell located above the top specimen cap with a capacity of 2,224 N and an accuracy of 0.025%FS. The axial deformation of the sample is measured externally using a linear variable differential transformer (LVDT) with an accuracy of 0.002 mm. The electronic control system allows a closed-loop control of specimen volume change, deformation, fluid pressures, and axial load. GeoTac's versatile TestNet software was used for data acquisition and controlling the loading frame and pressure pumps during consolidation and shearing. Data conversion hardware is placed very close to sensor locations where analog signals are converted to digital signals.

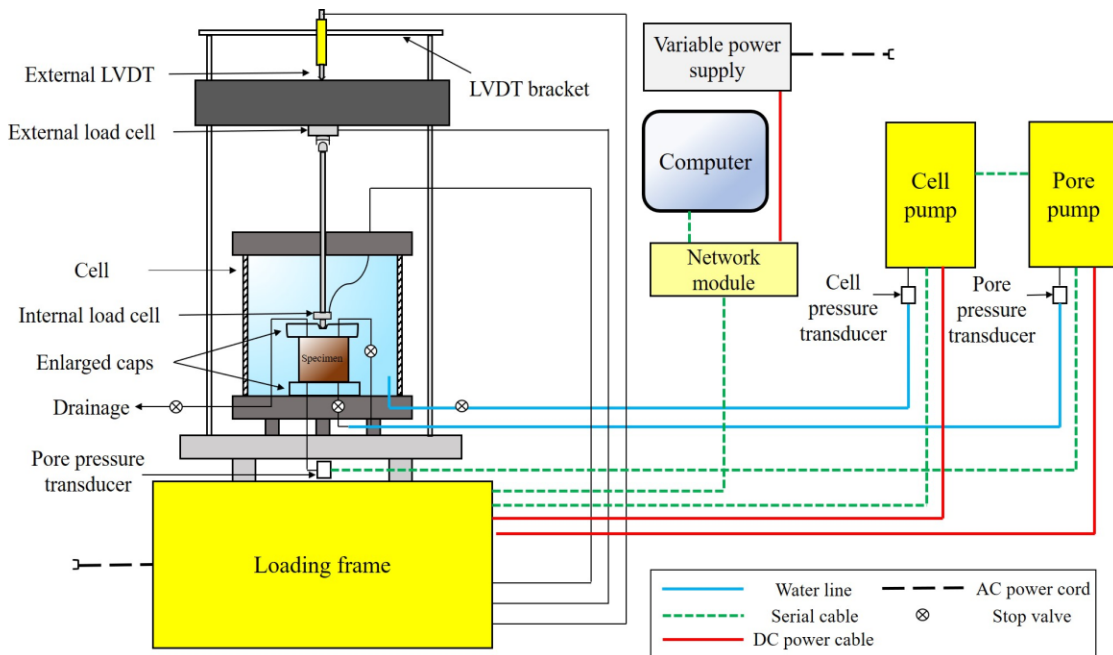


Figure 2-6: Schematic layout of the triaxial system

2.4.3 Sample preparation

Moist tamping using Ladd's under compaction method (Ladd 1978) was used here to prepare reconstituted tailings specimens. The specimens were prepared in four layers by tamping a certain mass of tailings with a moisture content of 5% at predefined heights in an aluminum split mold. The inside circumference of the mold was lined with a 0.3 mm thick latex membrane secured by a pair of O-rings at the bottom cap. The MT method was adopted for its simplicity and ease in reproducing high void ratios that are difficult to reach with dry deposition and slurry deposition techniques (Schnaid et al. 2013). Specimen uniformity was examined in a loose specimen by taking small plug samples of tailings from several layers after completing the tests and measuring and comparing the void ratios. The void ratio variation of these plug samples was within ± 0.006 (i.e., an average variation of 0.4%), confirming the uniformity of the tailings specimen.

To elucidate the impact of preparation method in controlling the initial void ratio, a limited number of triaxial tests were also carried out on specimens reconstituted by dry deposition and slurry deposition. Dry deposited (DD) specimens were prepared by pouring dry tailings into the specimen mold using a funnel with its spout kept above the tailings surface at a nearly zero drop height to form loose specimens. The funnel was gently raised in a circular motion as tailings particles were poured into the mold. This resulted in specimens with consolidation void ratios (e_c) of 0.937 to 0.905. For comparison, three moist tamped (MT) specimens were prepared with e_c (0.933 to 0.900) similar to those of the DD specimens and consolidated isotropically to confining pressures (p'_c) of 150, 300 and 400 kPa. These specimens were prepared to demonstrate the difference in shearing behavior between DD and MT preparation techniques. Two slurry-deposited (SD) specimens were also formed at $e_c = 0.914$ and 0.942 by thoroughly mixing tailings and water in a bottle. The suspended tailings were then transferred through a tube from the bottle to the specimen mold using a peristaltic pump. The supernatant water was then siphoned out using a syringe.

All specimens were prepared with equal height (H) and diameter (D) of 70 mm. The resulting $H/D = 1$ would reduce bulging at large strains and allow a uniform specimen deformation throughout shearing (Colliat-Dangus et al. 1988; Rowe and Barden 1964). Although the effect of other H/D values was not examined in this study, Lade et al. (1987) show nearly the same stress – strain behaviors, friction angles, and volumetric strain responses in specimens of a fine silica sands with $H/D = 1$ and 2.65. The effect of end restraint was minimized using two layers of lubricated latex sheets on the specimen caps as well as enlarged caps (90 mm in diameter) for compression testing. After filling the mold, the top cap was placed on the tailings surface and the membrane was folded on the top cap and secured with another pair of O-rings. A small suction of about 7-10 kPa was applied to stabilize the sample before removing the split mold. The triaxial cell was then assembled and filled with silicone oil to protect the internal load cell from electrical shortcuts. The vacuum pressure was slowly released and replaced by a seating cell pressure of 10 kPa.

2.4.4 Saturation

Saturation of the samples was accomplished in two stages. At first, CO₂ gas was circulated through the samples followed by flushing with about 5 pore volumes of deaired water. Back pressure saturation procedure, recommended by Bishop and Henkel (1962), was then followed until a pore pressure parameter, B, of 0.98 or higher was achieved. Volume change associated with saturation was determined by freezing the specimen after shearing and measuring the final void ratio and total weight of the specimen.

2.4.5 Consolidation

Following saturation, specimens were consolidated either isotropically or anisotropically. Isotropic consolidation was carried out by applying equal vertical (σ'_{1c}) and horizontal (σ'_{ec}) effective stresses on the specimen, while anisotropic K_0 -consolidation was achieved

by carefully controlling the increments of axial (ϵ_a) and volumetric (ϵ_{vol}) strains of the specimen via a computer-controlled feedback system to induce $d\epsilon_a/d\epsilon_{vol} = 1$ and thus a zero radial strain (ϵ_r). This technique is also used by numerous other studies (Mesri and Hayat 1993; Chu and Wanatowski 2008; Wanatowski et al. 2009; Guo 2010; Santana and Candeias 2015) to induce K_o -consolidation. Average effective stress ratios of $K_o = \sigma'_{3c}/\sigma'_{1c}$ of 0.57 in consolidation by compression, and 0.59 in consolidation by extension were measured in the anisotropically-consolidated specimens. The K_o values for each type of consolidation showed a slight decrement with decreasing e_c , and the average K_o values are reported above. The volume of the specimen was measured during consolidation to calculate e_c . The applied consolidation stresses were maintained for about two hours to allow complete excess pore pressure dissipation and primary consolidation prior to shearing.

2.4.6 Shearing

Following consolidation, the specimens were sheared in an undrained or a drained condition at an axial strain rate of 5%/hr up to $\epsilon_a = 25\%$. The undrained condition was imposed by closing the drainage valves and measuring the shear-induced pore pressure by a pore pressure transducer. During drained shearing the drainage valves were open and connected to the pore pressure pump to maintain the constant backpressure applied for saturation. The submerged internal load cell was used to measure the deviator stress on the specimen. For extensional shearing, a special cap was manufactured to screw and lock the axial loading rod into the top cap, and the bottom triaxial platen was clamped to the loading frame to prevent lifting of the triaxial cell. These modifications are illustrated in Figure 2-7.

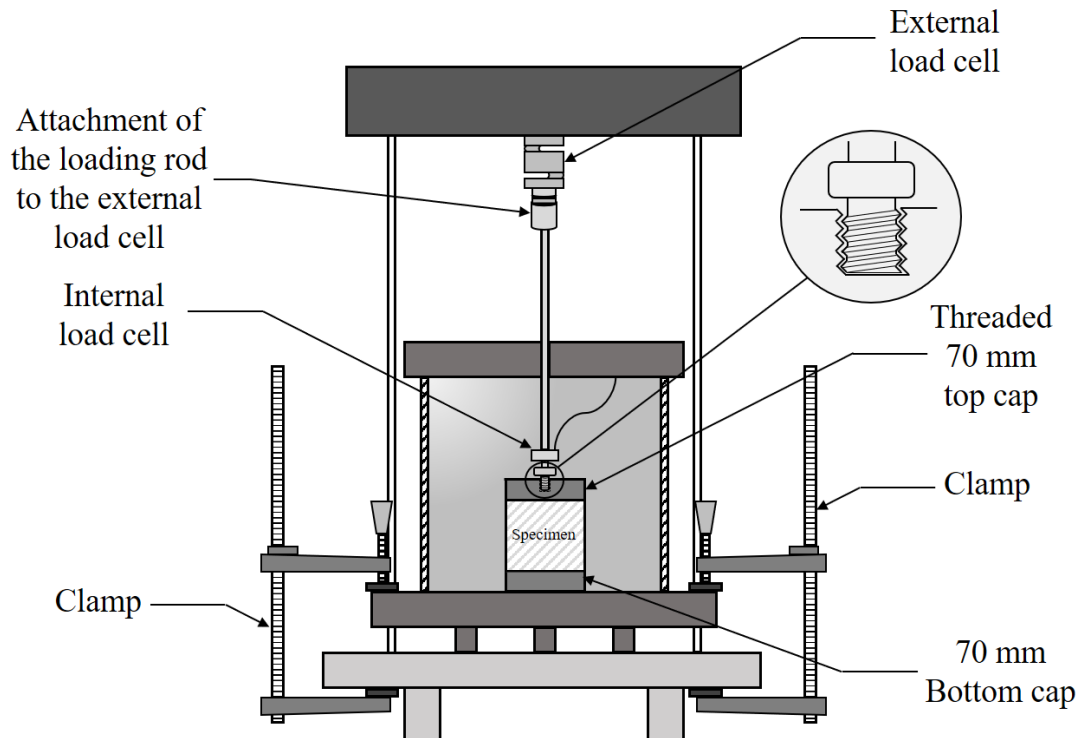


Figure 2-7: Modifications of the triaxial setup for extension testing

2.4.7 Test program

Table 2-1 summarizes the triaxial experiments carried out on the gold mine tailings in this study. Each test is labeled as ICD, ICU, IEU, CKCU, CKEU or EKEU where the first letters identify the consolidation type (I: isotropic; CK: anisotropic compression; EK: anisotropic extension), the middle letter shows the shearing direction (C: compression; E: extension), and the last letter indicates the drainage condition during shearing (D: drained; U: undrained). For example, CKCU describes a TxC test on a sample which is anisotropically consolidated in compression and sheared in undrained compression. A limited number of EKEU tests are presented here as all such tests dilated and didn't liquefy. Furthermore, as shown in Figure 2-8, multiple conjugated shear bands formed in specimens consolidation and shear in extension (EKEU tests). This was particularly significant at $p'_c > 100$ kPa, resulting in a complete rupture of these specimens. This was followed by a sharp rise in shear-induced pore pressure and loss of effective confinement at which point the experiment had to be terminated. As a result, the

complete stress paths of EKEU tests are presented only for specimens consolidation to $p'_c < 100$ kPa (Tests No. 1 to 3 in Table 2-1). In addition to the tests summarized in Table 2-1, several ICU tests were performed to assess different preparation methods including: three DD specimens consolidated to $e_c = 0.937, 0.928, 0.905$ at $p'_c = 150, 300, 400$ kPa, and two SD specimens consolidated to $e_c = 0.942, 0.914$ at $p'_c = 150, 300$ kPa.



Figure 2-8: Formation of shear bands in EKEU tests at p'_c of (a) 335 kPa and (b) 117 kPa

Table 2-1: Summary of TxC and TxE tests on the gold tailings of this study

Test #	Test ID	p'_c (kPa)	K_0	e_c^a	$\phi'_{yield}{}^b$ (°)	$\phi'_{cs}{}^c$ (°)	$\Psi_{cs}{}^d$
1	EKEU1	21	0.59	1.279	17		0.083
2	EKEU2	49	0.59	1.211	20	25	0.060
3	EKEU3	96	0.59	1.158	21		0.043
4	EKEU4	140	0.59	1.125	-	-	-
5	EKEU5	260	-	1.116	-	-	-
6	EKEU6	335	-	1.080	-	-	-
7	CKEU1	75	0.57	1.204	13		0.147
8	CKEU2	141	0.57	1.140	14		0.123
9	CKEU3	246	0.57	1.099	17		0.115
10	CKEU4	328	0.57	1.074	18	34	0.111
11	CKEU5	436	0.57	1.040	18		0.094
12	CKEU6	495	0.57	1.038	18		0.100
13	CKEU7	551	0.57	1.025	19		0.091
14	CKCU1	75	0.57	1.174	20		0.116
15	CKCU2	139	0.57	1.109	21		0.089
16	CKCU3	243	0.57	1.049	21	38	0.065
17	CKCU4	303	0.57	1.04	21		0.070
18	CKCU5	316	0.57	1.022	22		0.054
19	CKCU6	362	0.57	0.983	21		0.038
20	ICU1	150	1	1.136	15		0.121
21	ICU2	300	1	1.058	18	38	0.087
22	ICU3	400	1	1.036	19		0.083
23	ICU4	150	1	0.933	-		-
24	ICU5	300	1	0.919	-	-	-
25	ICU6	400	1	0.900	-		-
26	IEU1	150	1	1.168	10		0.078
27	IEU2	300	1	1.100	14	18	0.047
28	IEU3	400	1	1.077	15		0.040
29	ICD1	100	1	1.092	-	-	-
30	ICD2	200	1	1.067	-	-	-
31	ICD 3	250	1	1.043	-	-	-
32	ICD 4	250	1	1.040	-	-	-
33	EKCU	119	0.58	1.15	-	-	-

^a consolidation void ratio; ^b friction angle at the onset of instability; ^c critical state friction angle; ^d state parameter

2.5 Results and Discussion

2.5.1 Effect of preparation method

The stress paths of ICU tests carried out to examine the effect of sample preparation are shown in Figure 2-9. Although specimens prepared by neither method show strain-softening behavior, the MT specimens undergo greater p' reductions and pore pressure generation than DD and SD specimens. Particle suspension during slurry deposition prevented the formation of a liquefiable fabric, resulting in a strongly dilative shearing behavior. Whereas the honey-comb metastable fabric of MT specimens experienced more severe structural degradation during undrained shearing. Because of their relatively higher liquefaction susceptibility, moist-tamping was selected to study the undrained instability and liquefaction potential of tailings in this study.

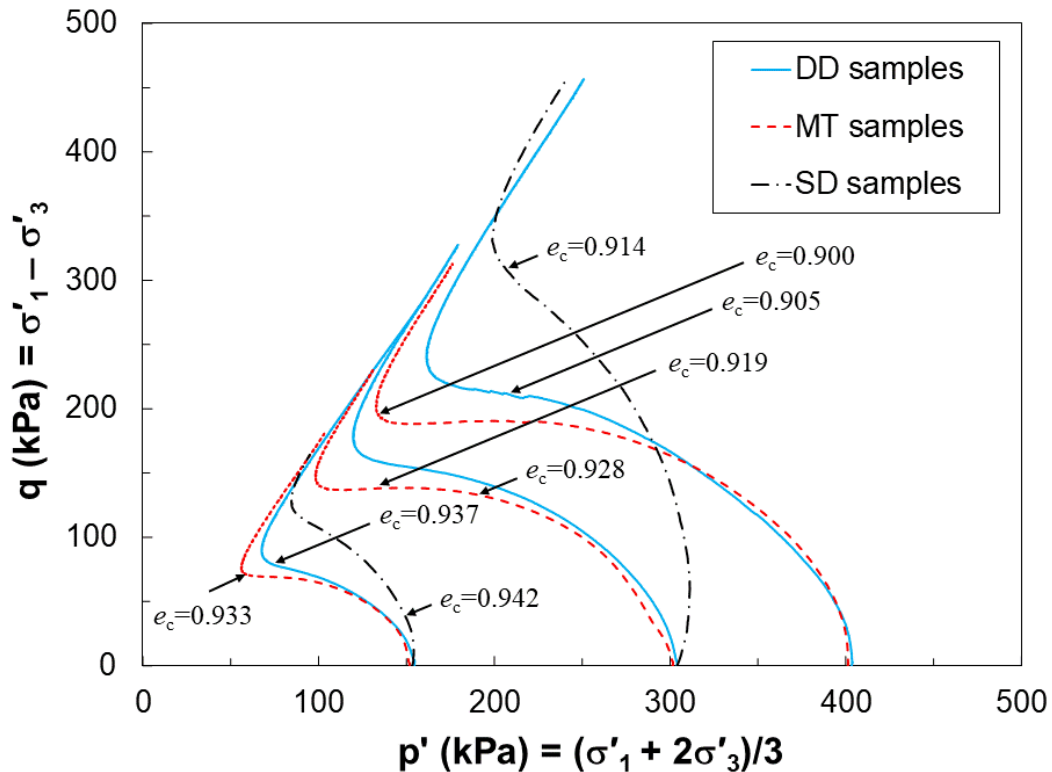


Figure 2-9: Comparison of stress paths from ICU tests on specimens prepared by dry deposition (DD), moist tamping (MT) and slurry deposition (SD)

Additionally, in order to examine the reproducibility of test results, an identical sample to the one tested under ICU1 stress path was created and sheared. The results are demonstrated in the figure below. This figure shows the consistency between the tests results in all stress ratios upon shearing and further demonstrates the reproducibility in the testing methodology.

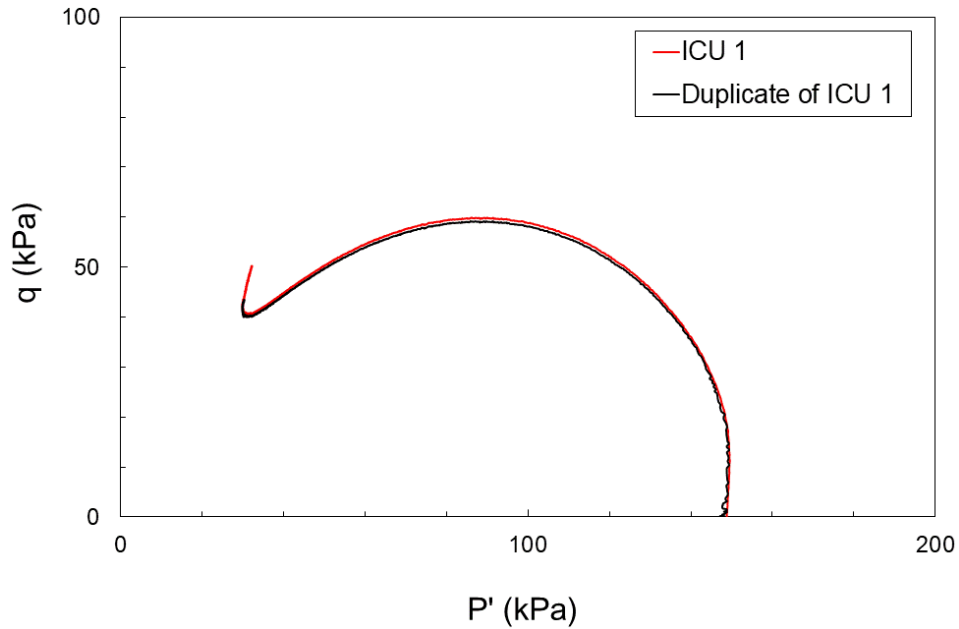
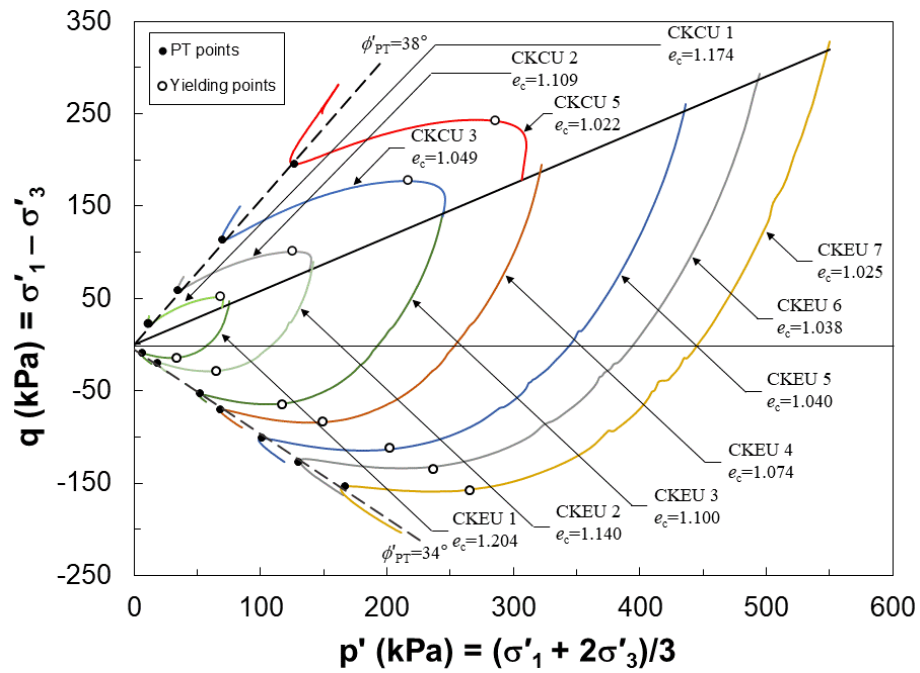


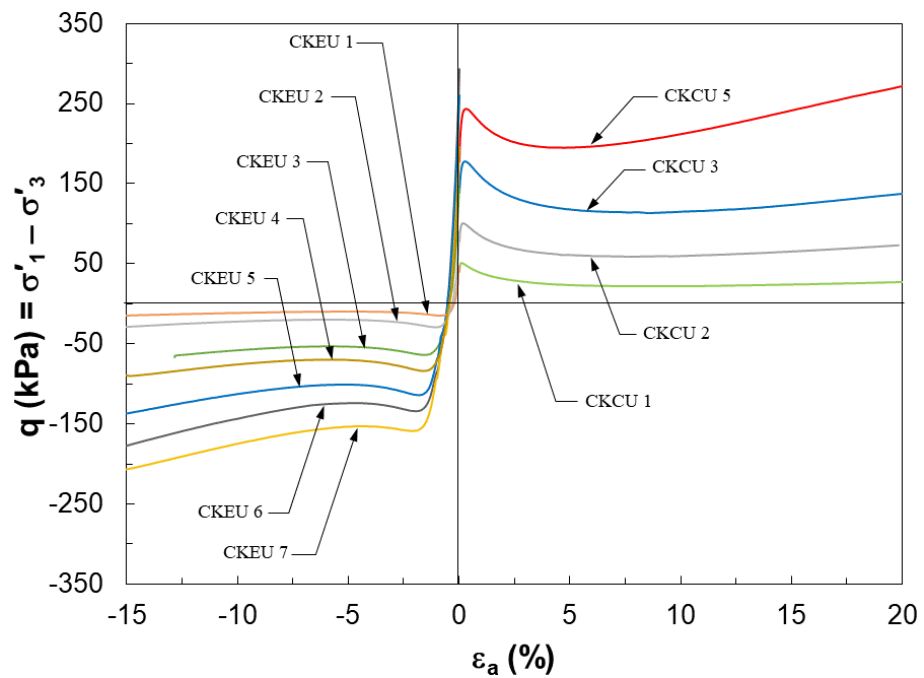
Figure 2-10: The comparison of the results of two duplicate samples with the same initial densities tested through stress path of ICU1

2.5.2 Effect of loading direction

Figure 2-11 to Figure 2-13 present the stress paths and stress – strain behaviors of the triaxial tests conducted in this study. As illustrated in these figures, while specimens subjected to ICU, CKCU, CKEU, and EKCU tests exhibit limited-liquefaction or dilative behavior, continuous strain-softening occurs in those under sustained extensional shear in IEU and EKEU tests. These observations are in line with those made by Vaid and Sivathayalan (1996), Gennaro et al. (2004), Boukpeti et al. (2002), and Altun and Goktepe (2006) in which samples subjected to compression loading tended to be less contractive than those undergoing extension.

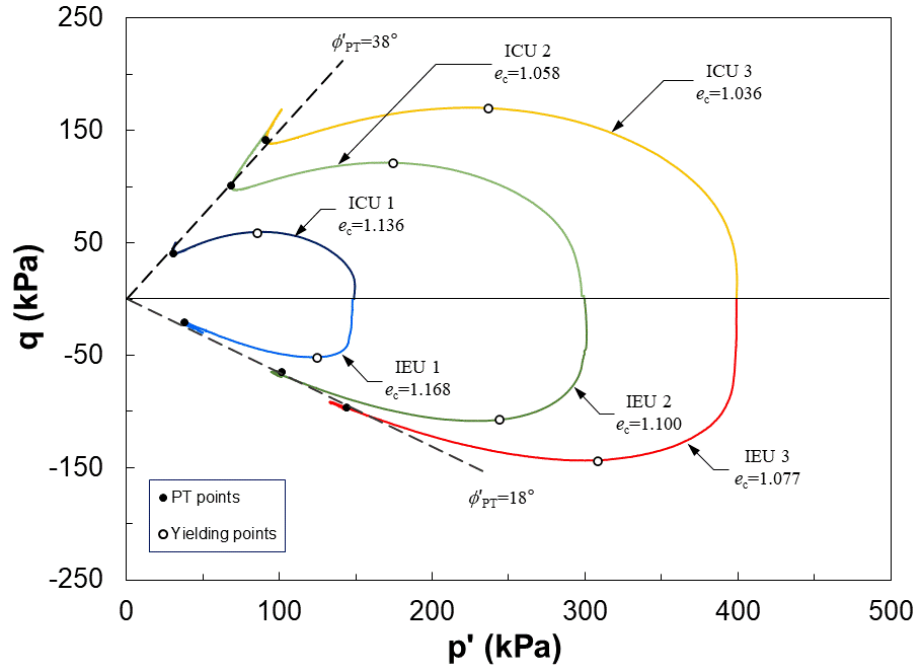


(a)

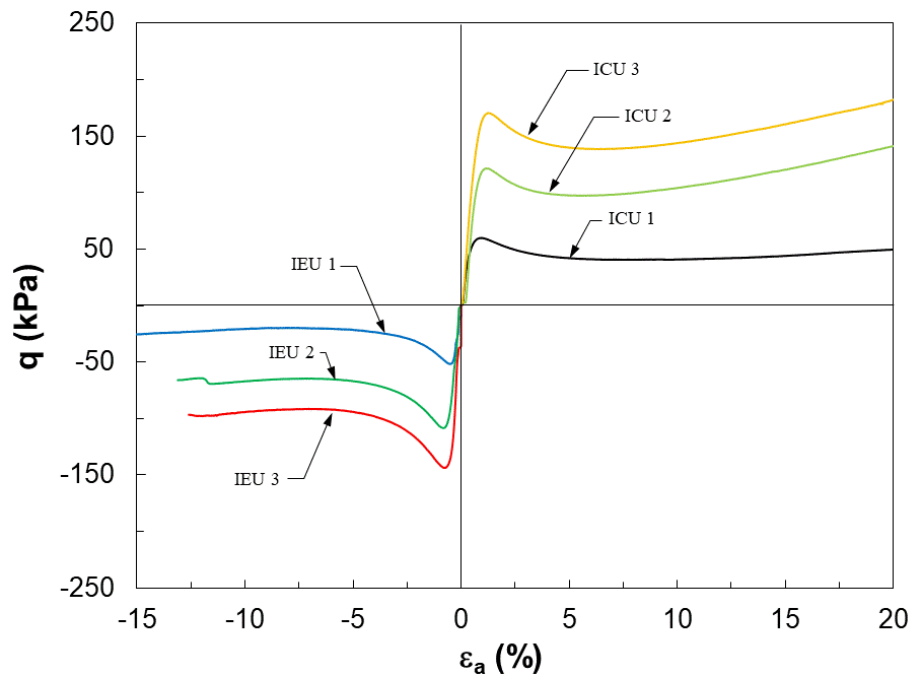


(b)

Figure 2-11: Stress paths (a) and stress-strain behaviors (b) of tailings specimens subjected to CKCU and CKEU shearing

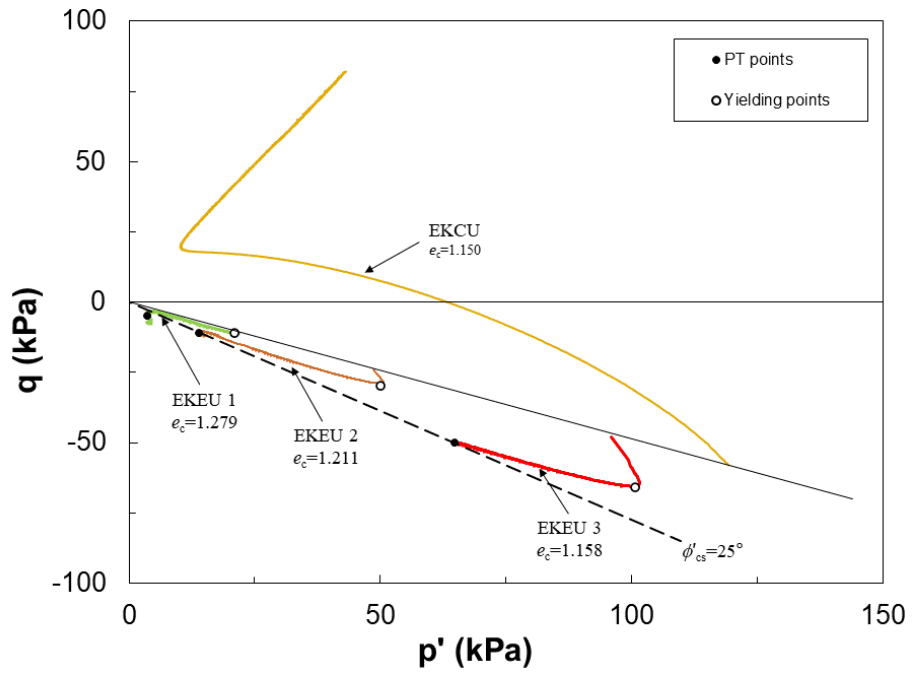


(a)

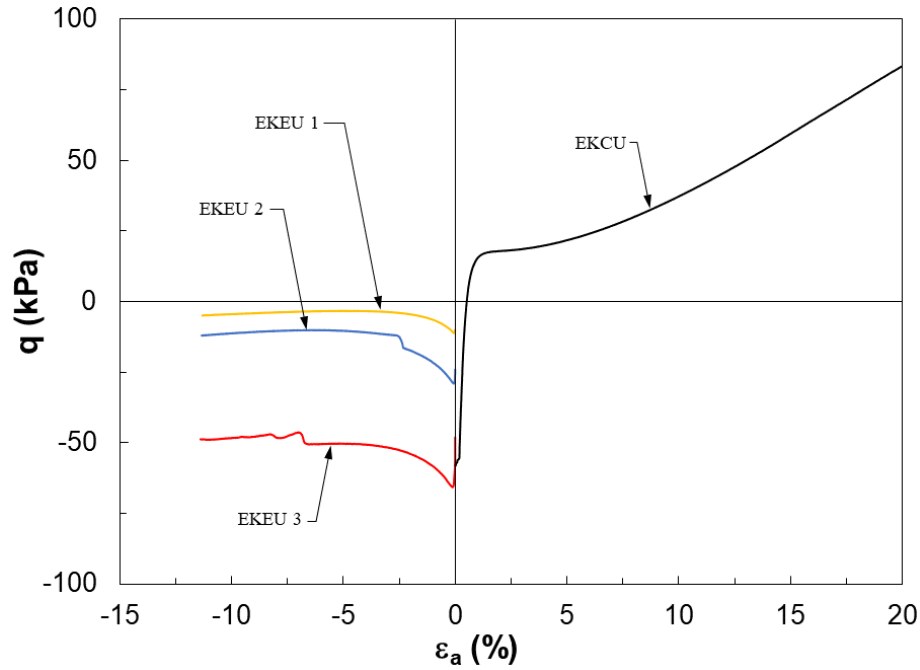


(b)

Figure 2-12: Stress paths (a) and stress-strain behaviors (b) of tailings specimens subjected to ICU and IEU shearing



(a)



(b)

Figure 2-13: Stress paths (a) and stress-strain behaviors (b) of tailings specimens subjected to EKEU and EKCU shearing

2.5.3 Post-liquefaction friction angle

Friction angles mobilized at phase transformation (ϕ'_{PT}) and critical (ϕ'_{cs}) states are also indicated in the stress paths of Figure 2-11 to Figure 2-13. As shown in these figures, higher ϕ'_{PT} were produced in compression loading compared to extension (e.g., 38° in ICU vs. 18° in IEU) for the same consolidation histories (i.e., ICU vs. IEU or CKCU vs. CKEU). This is consistent with the lower K_o of specimens consolidated anisotropically in compression (average $K_o = 0.57$) than those in extension (average $K_o = 0.59$). In extension shearing, higher ϕ'_{PT} were also mobilized in anisotropically-consolidated specimens (CKEU, EKEU) compared to those under isotropic (IEU) consolidation. These suggest a non-unique ϕ'_{PT} which depends on the loading direction. In compression (e.g., ICU, CKCU, & CKEU tests), the ultimate friction angle increased beyond ϕ'_{PT} due to dilation following phase transformation.

2.5.4 Critical State Line

Critical state is defined as the state at which a soil continues to deform under constant shear stress, constant effective stress and constant void ratio (Taylor 1948; Casagrande 1936; Roscoe et al. 1958). Figure 2-14 presents the critical state lines (CSL) projected in the $e - \log(p')$ space from both drained and undrained triaxial compression and extension tests. Critical state points were taken at the end of shearing for specimens exhibiting completely strain-softening behavior while for those showing limited liquefaction behavior the phase transformation points were selected. According to Figure 2-14, ICU, ICD, CKCU and CKEU tests, which exhibited limited liquefaction behavior, show a unique CSL. Whereas, a separate CSL is established from IEU and EKEU tests which experienced strain-softening without any strain-hardening behavior. The difference in CSLs can be associated with differences in mode of shearing, consolidation path, non-uniform void redistribution (Ayoubian and Robertson 1998), and post-liquefaction behavior (limited liquefaction vs complete liquefaction) of specimens used to determine each CSL. It is difficult to identify the precise differentiating mechanism as even the loosest specimens exhibited limited liquefaction behavior when subjected to ICU, CKCU, CKEU, or EKEU loading paths. Different critical states lines under compression and extension loadings have also been observed by others for Monterey No. 0 (Riemer and Seed 1997), Toyoura (Yoshimine et al. 1998) and Cambria (Yamamuro and Lade 1996) sands.

Note that static liquefaction is defined as the reduction in undrained shear strength following a peak resistance at $s_u(\text{yield})$. This is the same as Hill's second order work postulate of instability. According to Hill (1958), instability occurs when the second order work increment becomes negative. In the majority of stress paths obtained in the triaxial tests, instability occurred according to the abovementioned criterion. The subsequent strain-hardening observed following a phase transformation point in some of the experiments was likely due to specimen boundary conditions as described by Garga and Zhang (1994). In a field setting, once instability is triggered, sliding inertia, grain collision and the turbulent nature of the ensuing flowslide will produce an undrained

strain-softening shearing condition and suppress the strain-hardening response following the minimum $s_u(\text{liq})$.

The state parameter (ψ_{cs}) is defined (Been and Jefferies 1985) as the difference between e_c and the void ratio on the CSL at p'_c . This is widely used to determine liquefaction susceptibility, assess the degree of looseness of a sand, and constitutive modeling. Table 2-1 summarizes ψ_{cs} determined using the CSL corresponding to each loading path.

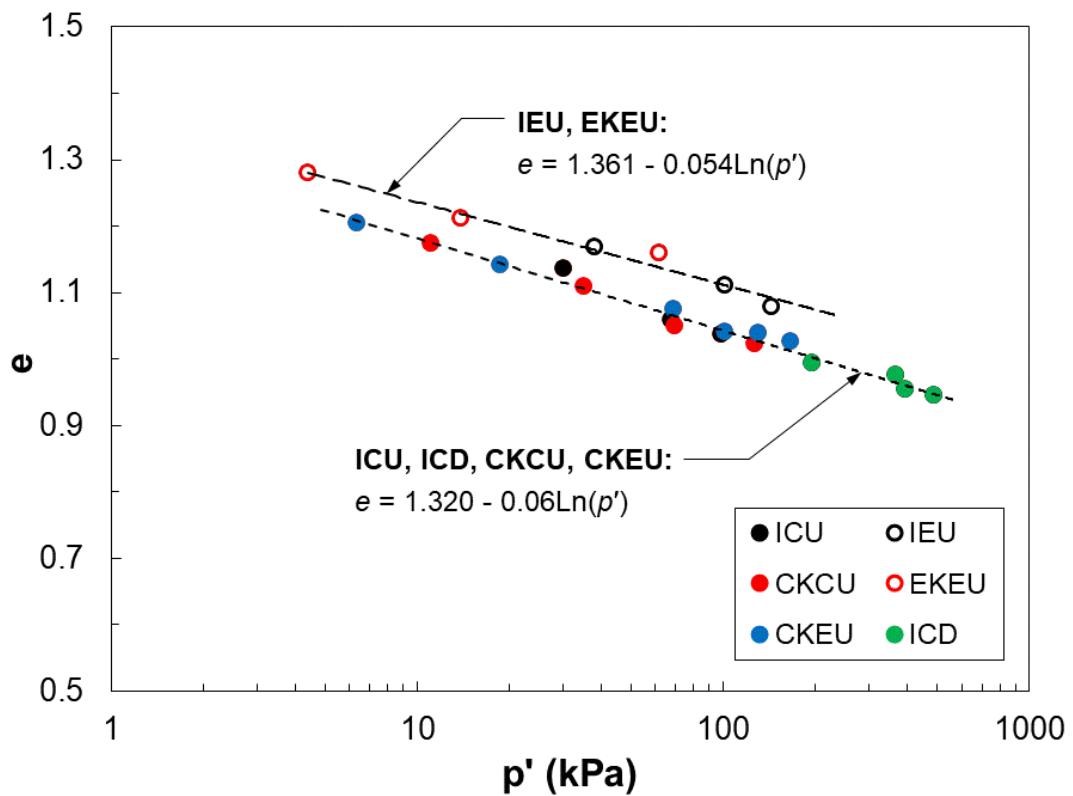


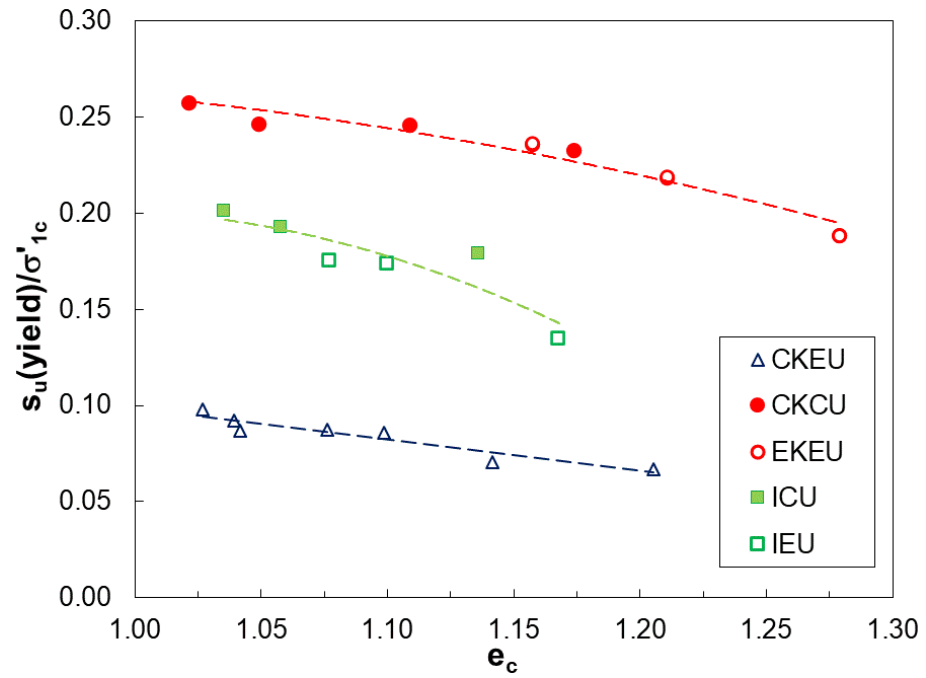
Figure 2-14: Critical state lines established from the triaxial tests of this study

2.5.5 Undrained shear strengths

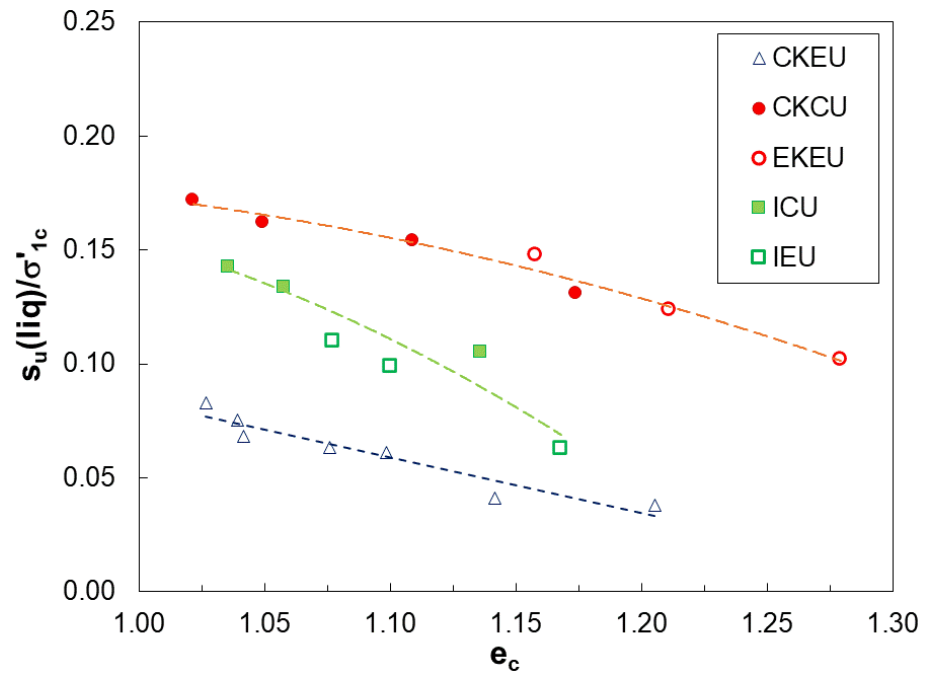
The undrained yield strength, $s_u(\text{yield})$, is the peak shear strength mobilized just prior to the triggering of strain-softening and undrained instability (Olson and Stark 2003b) and $s_u(\text{liq})$ is the minimum undrained shear strength produced following liquefaction flow failure (Terzaghi et al. 1996). For designing large geotechnical structures, such as mine

tailings impoundments, the undrained yield, $s_u(\text{yield})$, and post-liquefaction, $s_u(\text{liq})$, shear strengths are used respectively for determining the occurrence of instability and post-liquefaction stability analyses (Sadrekarimi 2016). Deviator stresses (q) corresponding to $s_u(\text{yield})$ and $s_u(\text{liq})$ are identified in the stress paths of Figure 2-11 to Figure 2-13. These strength parameters are often normalized with respect to the initial effective vertical stress to account for the effect of overburden pressure and depth in stability analysis (Olson and Stark 2003a). Accordingly, $s_u(\text{yield})$ and $s_u(\text{liq})$ are normalized here by the major principal stress after consolidation (σ'_{1c}), which corresponds to the vertical or the horizontal consolidation stress applied on specimens consolidated in compression (CKCU, ICU, CKEU) and extension (IEU, EKEU), respectively.

Figure 2-15 and Figure 2-16 show the variations of $s_u(\text{yield})/\sigma'_{1c}$ and $s_u(\text{liq})/\sigma'_{1c}$ with respectively e_c and ψ_{cs} from the triaxial tests of this study. Similar to Al-Tarhouni et al. (2011), who studied the shearing behavior of another gold tailings in direct simple shear tests, the results show unique trends with e_c (in Figure 2-15) or ψ_{cs} (in Figure 2-16) for each direction of consolidation and shearing. The ranges of the measured strength ratios in these figures are also in good agreement with those reported by the several other studies (Hanzawa 1980; Ishihara 1993; Vaid and Sivathayalan 1996; Olson and Stark 2003a; Sadrekarimi and Olson 2011; Omar and Sadrekarimi 2015). For example, Olson and Stark (2003a) reported $s_u(\text{yield})/\sigma'_{1c} = 0.29 - 0.42$ and $s_u(\text{liq})/\sigma'_{1c} = 0.02 - 0.22$ based on a collected database of ICU tests on 46 sands, silty sands and sandy silts. Been and Jefferies (1985) obtained $s_u(\text{yield})/\sigma'_{1c} = 0.21 - 0.51$ in ICU tests on Kogyuk sand. ICU tests on moist-tamped specimens of Toyoura sand further showed $s_u(\text{yield})/\sigma'_{1c} = 0.21 - 0.34$ and $s_u(\text{liq})/\sigma'_{1c} = 0.21 - 0.28$ (Ishihara 1993). $s_u(\text{yield})/\sigma'_{1c} = 0.11-0.27$ and $s_u(\text{liq})/\sigma'_{1c} = 0.23-0.41$ were reported by Hanzawa (1980) for Valgrinda, Sengenyama, and Kisarazu sands in ICU triaxial compression tests. Olson and Mattson (2008) further reported $s_u(\text{yield})/\sigma'_{1c} = 0.18-0.43$ (ICU) and $0.11-0.24$ (IEU) and $s_u(\text{liq})/\sigma'_{1c} = 0.01-0.23$ (ICU) and $0.01-0.11$ (IEU) by updating the triaxial testing database of Olson and Stark (2003a).

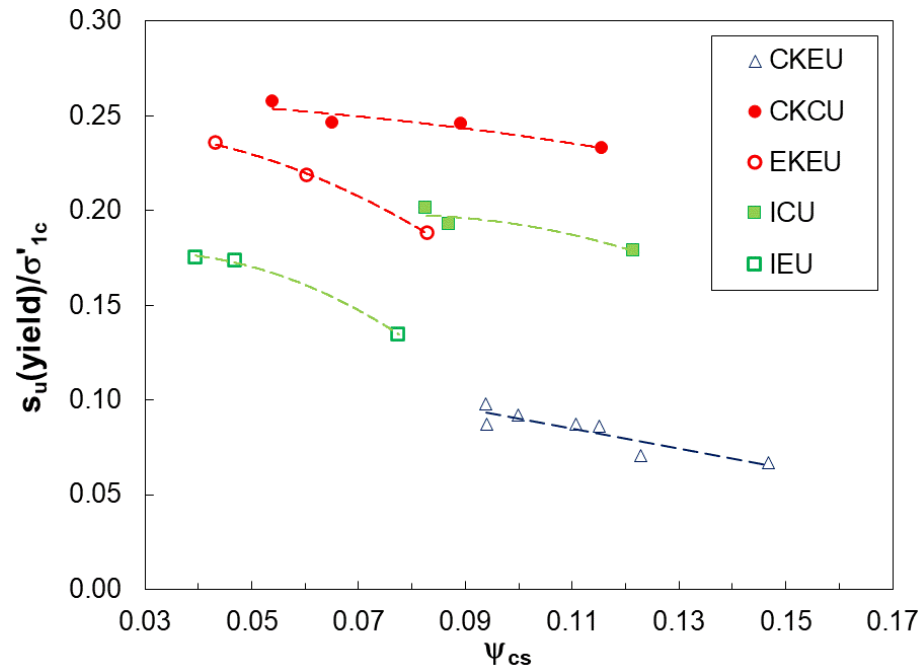


(a)

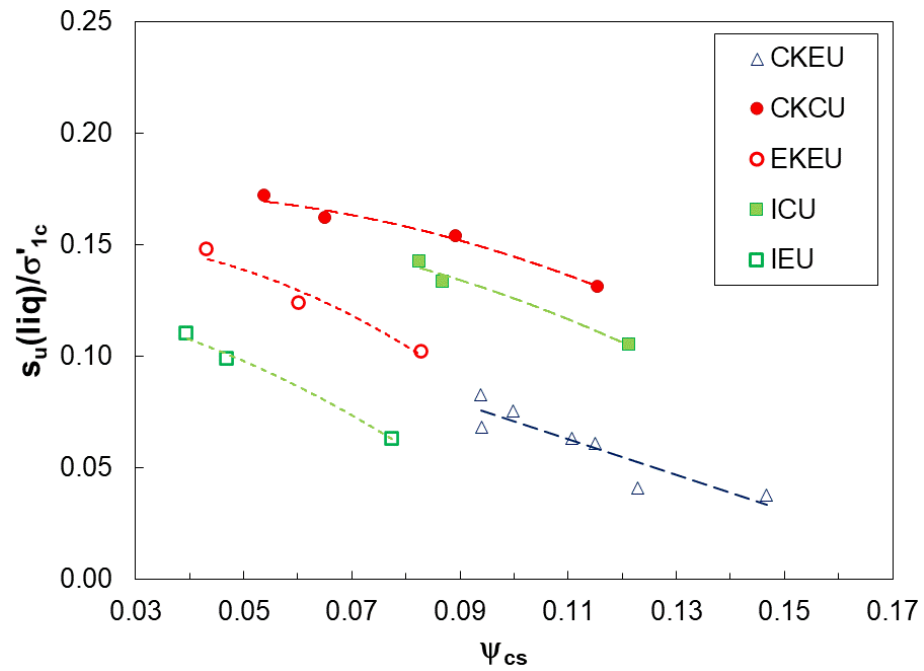


(b)

Figure 2-15: Variations of (a) $s_u(\text{yield})/\sigma'_{1c}$ and (b) $s_u(\text{liq})/\sigma'_{1c}$ with e_c based on the triaxial tests of this study



(a)



(b)

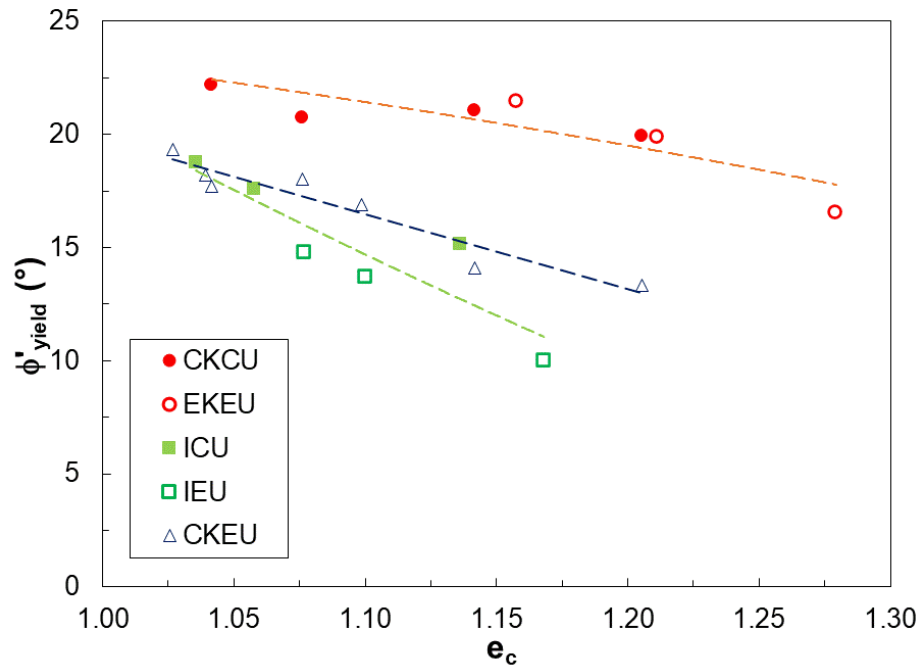
Figure 2-16: Variations of (a) $s_u(\text{yield})/\sigma'_{1c}$ and (b) $s_u(\text{liq})/\sigma'_{1c}$ with ψ_{cs} based on the triaxial tests of this study

Figure 2-15 and Figure 2-16 particularly demonstrate the significance of stress-induced anisotropy. The largest undrained strength ratios were developed in specimens consolidated anisotropically and then shear in the same direction (i.e., CKCU & EKEU tests), while the lowest strength ratios ($s_u(\text{yield})/\sigma'_{1c} = 0.067\text{--}0.098$, $s_u(\text{liq})/\sigma'_{1c} = 0.038\text{--}0.083$) occur in CKEU tests where specimens were consolidated anisotropically in compression and sheared in the opposite direction in extension. As noted earlier, all EKEU tests showed dilative behavior and we could not determine $s_u(\text{yield})$ and $s_u(\text{liq})$ from these tests. The higher shear strengths of the CKCU and EKEU tests can be attributed to the interlocking of tailings particles following anisotropic consolidation which is further reinforced during shearing in the same direction of anisotropic consolidation, resulting in a reduced potential for pore water pressure generation (Sadrekarimi 2016). The opposite occurs in CKEU tests where the interlocked particles in compression are unlocked by extension shearing. Strength ratios from isotropically-consolidated specimens (ICU and IEU) fall between the above limits from anisotropically-consolidated tests when plotted against their void ratios. The same observations can be made when strength ratios are plotted versus ψ_{cs} corresponding to each CSL. Quite interestingly, specimens consolidated and sheared in the same direction (CKCU and EKEU) exhibit the same trend with e_c (in Figure 2-15). However, for each trend, relatively lower $s_u(\text{yield})/\sigma'_{1c}$ and $s_u(\text{liq})/\sigma'_{1c}$ are measured in extension shearing than in compression. The angular shapes of tailings particles (see Figure 2-5) may have formed an anisotropic fabric with a preferred particle orientation, inducing higher shear strengths in compression than those in extension loading.

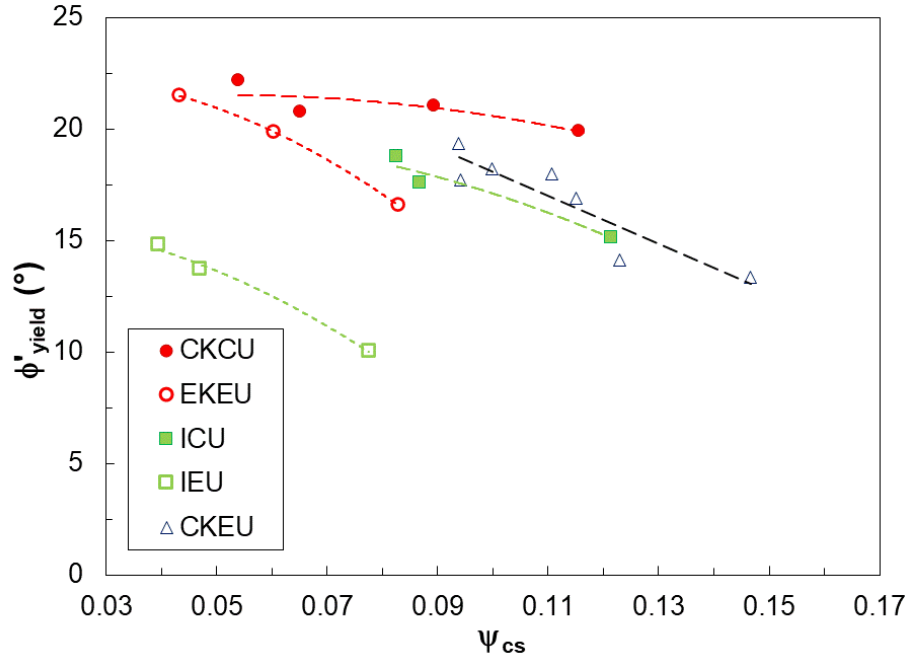
2.5.6 Triggering friction angle

In addition to $s_u(\text{yield})$, the triggering of instability can be determined using the instability line slope or the yield friction angle, ϕ'_{yield} , as demonstrated in Figure 2-3. These are found from the stress path plots of Figure 2-11 to Figure 2-13 by connecting peak points to the origin. Figure 2-17 shows descending trends of ϕ'_{yield} with e_c and ψ_{cs} from the triaxial tests of this study. Similar to $s_u(\text{yield})/\sigma'_{1c}$, higher ϕ'_{yield} were mobilized in specimens consolidated and sheared in the same direction (i.e., CKCU and EKEU tests)

than those undergoing stress reversal (i.e., CKEU tests). Nevertheless, both stress paths resulted in ϕ'_{yield} somewhat greater than those from isotropically-consolidated tests (ICU and IEU tests) because of the effect of anisotropic consolidation. Same as the undrained shear strengths, relatively larger ϕ'_{yield} were produced in compression loading (CKCU, ICU) than in extension (CKEU, IEU) in tests with parallel or opposite consolidation and shearing directions. The lower strength parameters (yielding friction angles and undrained shearing strengths) of the samples in extension than compression loading could be explained in terms of the orientation of principal stresses with respect to particle fabric and depositional direction. Since the particles are angular instead of completely spherical, they might be oriented upon samples preparation and shearing in such way with respect to the direction of principal stresses that result in less strength in extension. Note that the somewhat different ranking of ϕ'_{yield} in Figure 2-17(b) is an artifact of the different CSLs (see Figure 2-14) used to determine ψ_{cs} in compression (CKCU, ICU) and in extension (EKEU, IEU).



(a)



(b)

Figure 2-17: Variations of ϕ'_{yield} with (a) e_c and (b) ψ_{cs} from the triaxial tests of this study

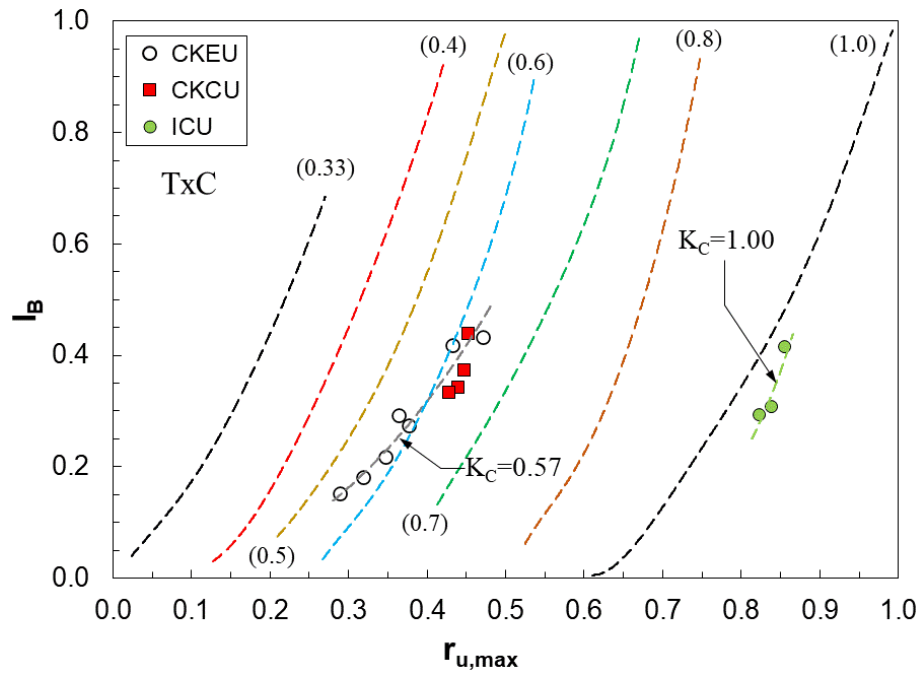
Note that the above figures show only a limited number of the EKEU tests which exhibited uniform deformation and shearing before a complete rupture. At high deviator stresses induced during anisotropic consolidation, samples subjected to a EKEU stress path bifurcated into multiple localized shear bands and were not suitable as an element test for measuring strength parameters.

2.5.7 Brittleness and Pore Pressure Generation

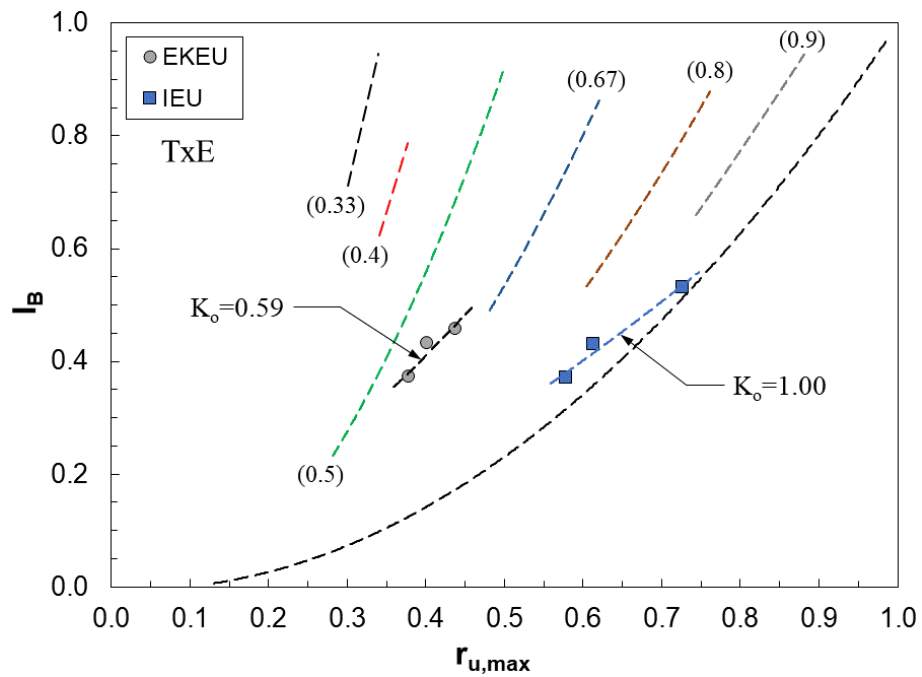
Different stress paths of Figure 2-11 to Figure 2-13 show different degrees of strain softening and strength loss. The amount of undrained strength loss is quantified here by the undrained brittleness index (Bishop 1973), $I_B = [s_u(yield) - s_u(liq)]/s_u(yield)$. For strain-hardening specimens $I_B = 0$ (non-brittle), and for highly contractive loose

specimens with low $s_u(\text{liq})$, I_B approaches 1.0. A higher I_B indicates a more severe flow liquefaction failure which could travel a longer distance.

In cohesionless soils, such as the gold tailings examined in this study, undrained shear strength depends on the amount of shear-induced pore pressure (Δu) and therefore a rising Δu would induce undrained strength loss. Based on this hypothesis, Sadrekarimi (2020) proposed unique relationships between I_B and the maximum excess pore pressure ratio, $r_{u,\max} = \Delta u/\sigma'_{1c}$ for compression, extension, and simple shear modes based on an extensive database of laboratory tests. These are compared with the pairs of I_B and $r_{u,\max}$ from the triaxial tests of this study in Figure 2-18 for compression and extension shearing modes. As shown in this figure, I_B and $r_{u,\max}$ of this study are closely located to the average relationships proposed by Sadrekarimi (2020) for the corresponding principal stress ratios (K_C). These figures further show that a certain degree of strain-softening and I_B can be induced more easily at a lower $r_{u,\max}$ in anisotropically-consolidated samples (CKCU, EKEU) than those subjected to isotropic stresses (ICU, IEU). The lower $r_{u,\max}$ is likely because of the stiffer fabric and interlocked particles of anisotropically consolidated specimens. For a given $r_{u,\max}$, specimens subjected to extension shearing (IEU & EKEU) exhibit greater I_B than those in compression (ICU, CKCU). In summary, anisotropic consolidation and undrained extensional shearing promote brittleness and undrained instability.



(a)



(b)

Figure 2-18: Comparisons of I_B and $r_{u,max}$ from the triaxial tests of this study with empirical trends proposed by Sadrekarimi (2020) for specimens consolidated in (a)

compression, and (b) extension. Numbers in parentheses show K_C values of Sadrekarimi (2020) trends

Besides $r_{u,max}$, a different $r_{u,yield}$ is introduced here which characterizes Δu produced at the triggering of instability. Figure 2-19 shows increasing trends of I_B with rising $r_{u,yield}$ from the results of this study. This is interesting as it suggests that the behavior of a saturated tailings prior to instability can reflect its post-liquefaction behavior and strain-softening. The slightly negative $r_{u,yield}$ in EKEU tests is due to the small reduction of Δu during the early shearing ($\epsilon_a < 1\%$) of these specimens as indicated in the stress paths of Figure 2-13a. This likely occurs because of the initially dilative behavior of these specimens at relatively low p'_c (< 100 kPa) which is then overcome by strain-softening and contractive behavior induced by shearing in extension. An initial Δu reduction was also observed by Doanh et al. (1997) in TxE tests.

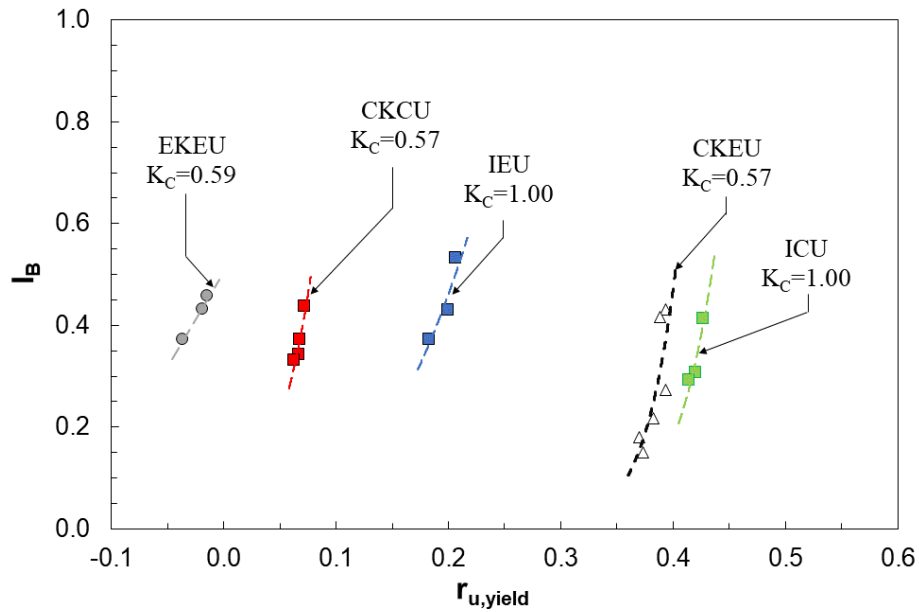


Figure 2-19: Variations of I_B with $r_{u,yield}$ for different loading directions from the triaxial experiments of this study

2.5.8 Comparisons with Natural Soils and Other Tailings

The observed reductions of $s_u(\text{yield})/\sigma'_{1c}$, $s_u(\text{liq})/\sigma'_{1c}$, and ϕ'_{yield} with increasing e_c or ψ_{cs} in Figure 2-15 to Figure 2-17 are not unique to the gold tailings of this study. The distinguishing characteristics and shearing behavior of these tailings are subsequently highlighted in the following paragraphs by comparing their CSL, $s_u(\text{yield})/\sigma'_{1c}$, $s_u(\text{liq})/\sigma'_{1c}$ and ϕ'_{yield} with those of several fine sands (Georgiannou 1988; Riemer and Seed 1997; Yoshimine et al. 2001; Sadrekarimi 2009), silt (Zlatovic and Ishihara 1997), and another gold tailings (Fourie and Papageorgiou 2001; Fourie and Tshabalala 2005). These include Ottawa (FC = 0%; D_{50} = 0.52 mm), Monterey No. 0 (FC = 0%; D_{50} = 0.35 mm), Kawagishi-Cho (FC = 1.4%; D_{50} = 0.32 mm) sands, a clayey sand (FC = 20 to 35%; plasticity index = 25%; clay content \approx 12%), Lagunillas sandy silt (FC = 74%; D_{50} = 0.05 mm), and Merriespruit gold tailings (FC = 0 & 20%; D_{50} = 0.12 mm). As demonstrated in Figure 2-20, CSLs of Merriespruit gold tailings locate around those from the triaxial tests of this study. However, likely because of their more angular particle shapes, both tailings present looser critical states than those of fine sands and silts compared in Figure 2-20. The notably steeper CSL of the clayey sand emerges from the more compressible fabric induced by the clay particles.

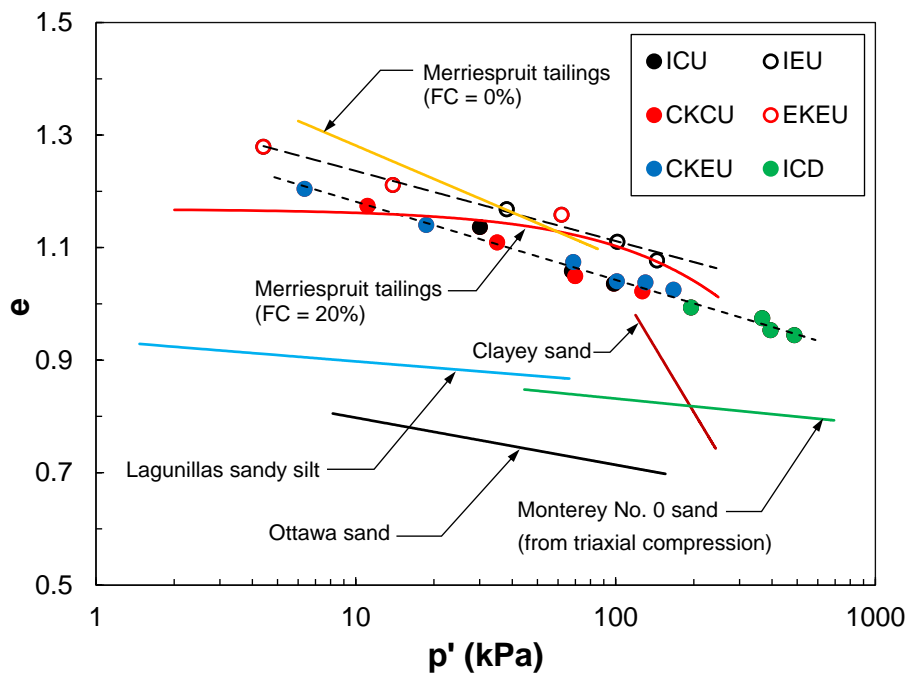
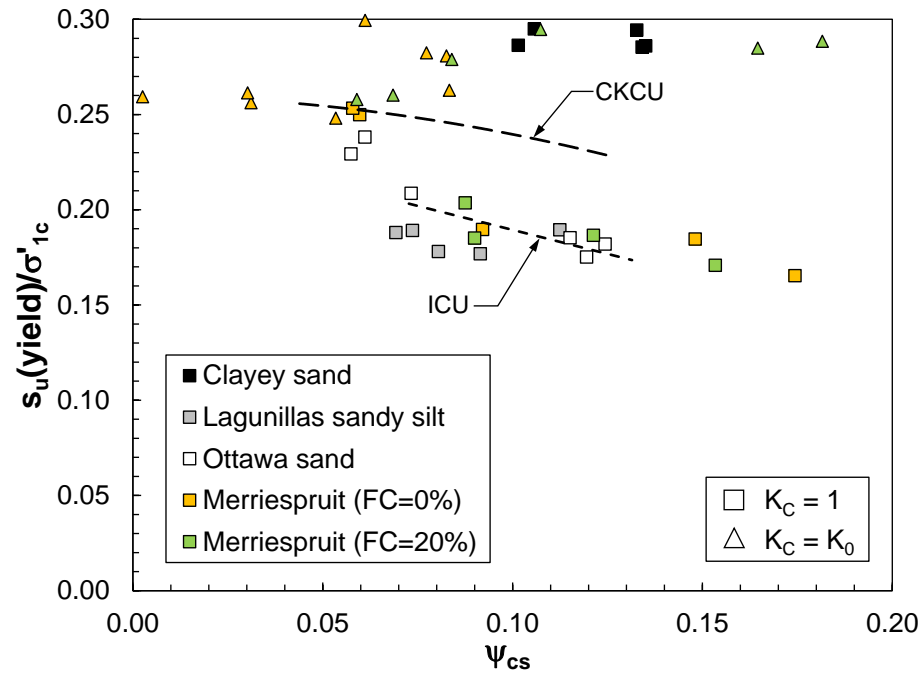
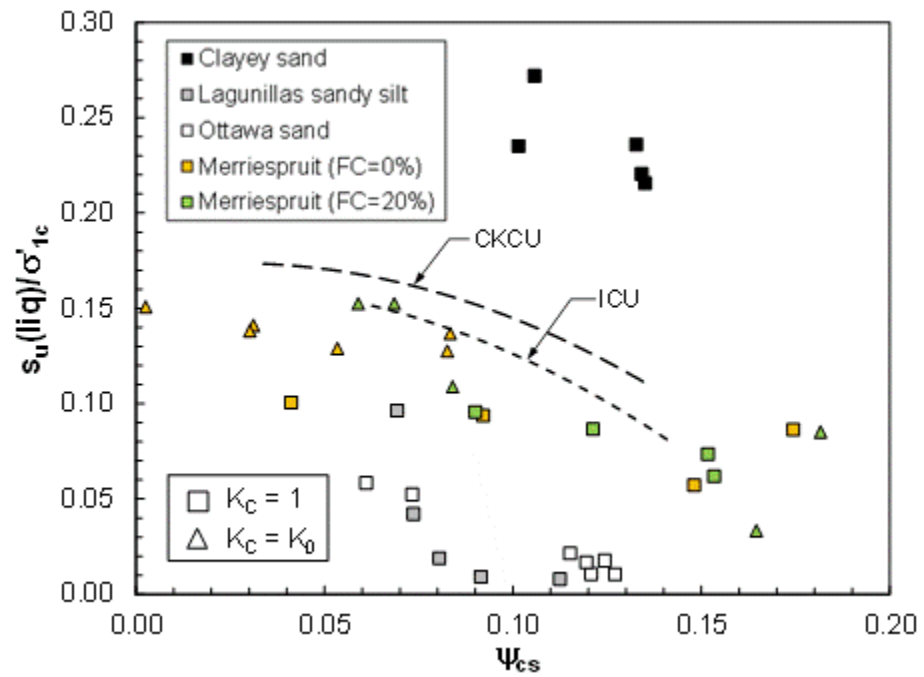


Figure 2-20: Comparison of CSLs of Ottawa sand Sadrekarimi (2009), Monterey No. 0 sand Riemer and Seed (1997), a clayey sand Georgiannou (1988), Lagunillas sandy silt Zlatovic and Ishihara (1997), and Merriespruit gold tailings (Fourie and Papageorgiou 2001; Fourie and Tshabalala 2005) with those of this study

Undrained yield and post-liquefaction strength ratios of these materials are also compared in Figure 2-21 and Figure 2-22 for compression and extension modes of loading, respectively. These comparisons are made based on ψ_{cs} to incorporate differences in consolidation stresses and e_c among different studies. According to Figure 2-21, $s_u(\text{yield})/\sigma'_{1c}$ of Ottawa sand and Merriespruit tailings are close to the $s_u(\text{yield})/\sigma'_{1c} - \psi_{cs}$ trend from the ICU triaxial tests of this study, while those of the Lagunillas sandy silt show slightly lower values. Except for the clayey sand, tailings examined here achieved relatively higher $s_u(\text{liq})/\sigma'_{1c}$ for a given ψ_{cs} than those of the sand, silt, and other gold tailings compared in Figure 2-21 (b) in compression, while those developed in Figure 2-22 during extensional loading were within the ranges of Monterey No. 0 and Kawagishi-Cho sands' $s_u(\text{liq})/\sigma'_{1c}$ values. In both compression and extension, $s_u(\text{yield})/\sigma'_{1c}$ and $s_u(\text{liq})/\sigma'_{1c}$ of this study display generally steeper reductions with increasing ψ_{cs} compared to those of the other materials in Figure 2-21 and Figure 2-22.



(a)



(b)

Figure 2-21: Comparisons of (a) $s_u(\text{yield})/\sigma'_{1c}$ and (b) $s_u(\text{liq})/\sigma'_{1c}$ from the triaxial compression tests of this study with those for a clayey sand Georgiannou (1988), Ottawa

sand Sadrekarimi (2009), Lagunillas sandy silt Zlatovic and Ishihara (1997), and Merriespruit gold tailings (Fourie and Papageorgiou 2001; Fourie and Tshabalala 2005)

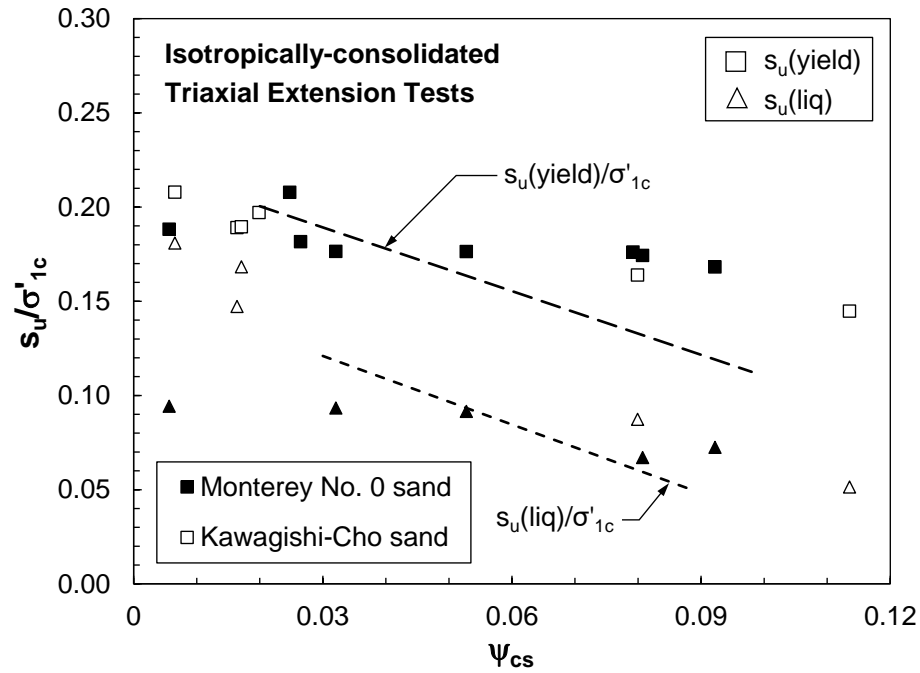
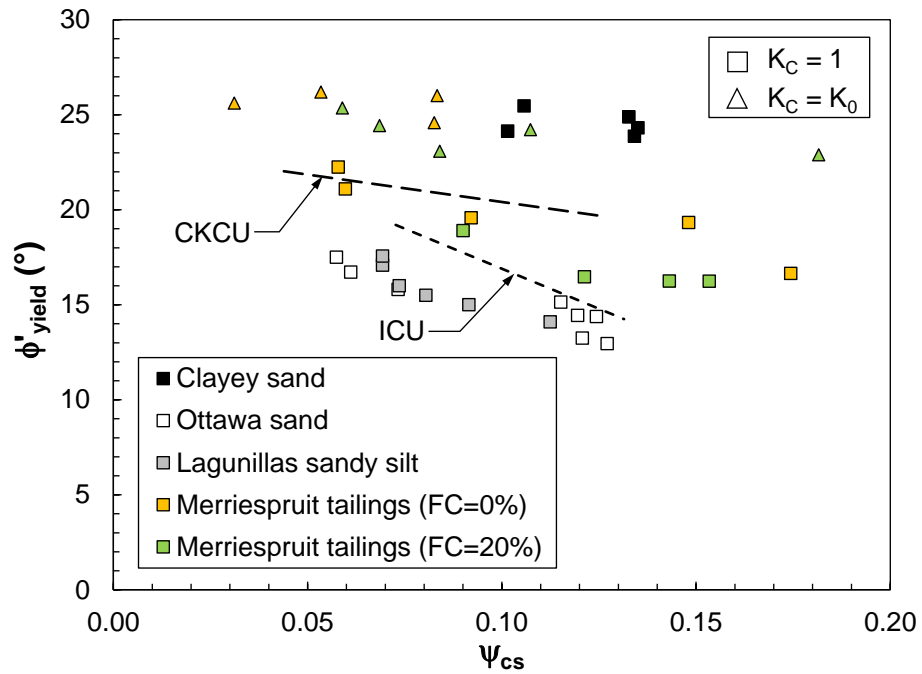
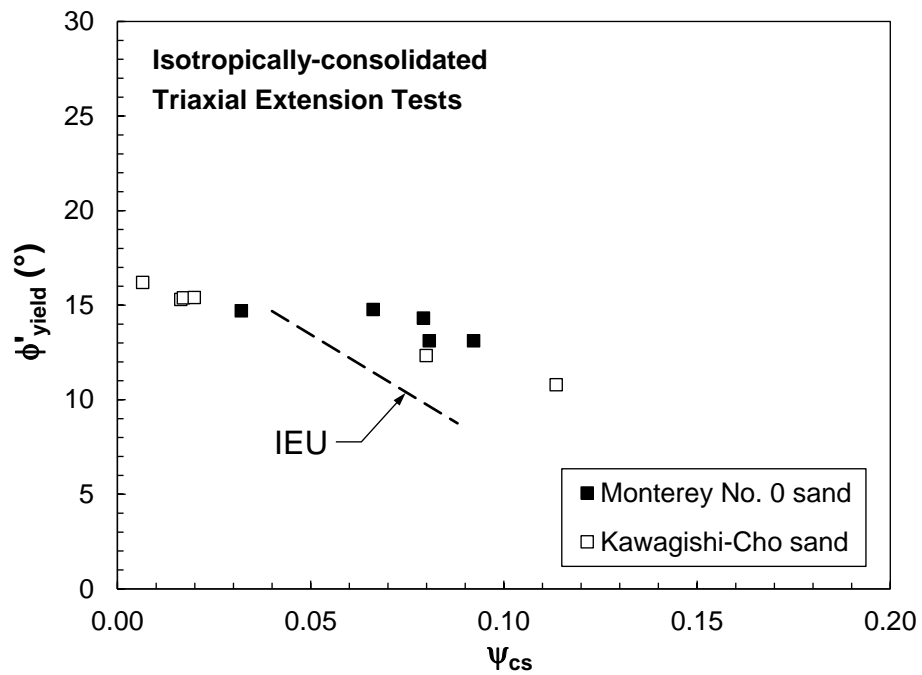


Figure 2-22: Comparisons of $s_u(yield)/\sigma'_{1c}$ and $s_u(liq)/\sigma'_{1c}$ from isotropically-consolidated triaxial extension tests of this study with those for Monterey No. 0 Riemer and Seed (1997) and Kawagishi-Cho Yoshimine et al. (2001) sands

The triggering of instability further occurred in the tailings specimens of this study at ϕ'_{yield} higher than those of Ottawa sand and Lagunillas sandy silt in compression, but generally lower than those mobilized in Monterey No. 0 and Kawagishi-Cho sands under extensional loading in Figure 2-23. In contrary, both undrained i.e., $s_u(yield)/\sigma'_{1c}$ and $s_u(liq)/\sigma'_{1c}$, and drained (ϕ'_{yield}) strength parameters of the clayey sand are markedly higher than those of this study likely because of the presence of clay particles.



(a)



(b)

Figure 2-23: Comparisons of ϕ'_{yield} from (a) triaxial compression and (b) isotropically-consolidated triaxial extension tests of this study with those mobilized in Ottawa

Sadrekarimi (2009), Monterey No. 0 Riemer and Seed (1997), and Kawagishi-Cho Yoshimine et al. (2001) sands, a clayey sand Georgiannou (1988), Lagunillas sandy silt Zlatovic and Ishihara (1997), and Merriespruit gold tailings (Fourie and Papageorgiou 2001; Fourie and Tshabalala 2005)

Although, similar to the triaxial tests of this study, anisotropic K_o -consolidation resulted in increased undrained (in Figure 2-21) and drained (in Figure 2-23) strength parameters of Merriespruit tailings, these specimens exhibit relatively higher values of ϕ'_{yield} than those of this study in both isotropic and anisotropic (K_o) consolidation according to Figure 2-23. In summary, the instability and liquefaction behaviors of gold tailings, both of this study and Merriespruit mine, are different than those of natural sands and silts. This is likely associated with the more angular shapes of tailings particles and their peculiar mineralogical composition.

2.6 Summary

Instability and critical state behavior of a gold mine tailings under compression and extension modes of shearing were examined in this study. Most specimens were prepared by moist tamping because of the higher liquefaction potential of such specimens compared to those prepared by pluviation through air or deposited as a slurry. Difference in the behavior type (limited liquefaction vs complete liquefaction) led to separate critical state lines (CSL) in specimens subjected to different modes of shearing, with a slightly looser CSL from specimens sheared only in extension compared those sheared in compression.

Undrained triggering and post-liquefaction shear strength ratios (normalized by the consolidation vertical stress) as well as friction angles at the triggering of instability decreased with increasing consolidation void ratio and critical state parameter in both modes of shearing. These strength parameters were found to be greater in specimens consolidated anisotropically and then shear in the same direction (i.e., CKCU, EKEU) compared those subjected to isotropic consolidation or undergoing loading reversal from

consolidation to shearing (i.e., CKEU tests). This was attributed to the enhanced interlocking and stiffer fabric of particles shearing and consolidated in the same direction compared to when they were disengaged by a change in the loading direction. Friction angles mobilized at phase transformation were also found to be a function of the loading direction and increased from 18° to 38° in respectively extension and compression loadings for the same consolidation mode.

Tailings specimens subjected to undrained extensional shearing exhibited lower undrained strength ratios and friction angles, as well as higher brittleness compared to those sheared in compression. Unique trends were found between brittleness index (I_B) and the maximum excess pore pressure ratio ($r_{u,max}$) for specimens subjected to a certain consolidation and shearing direction. For a given shearing mode, these trends indicated relatively lower $r_{u,max}$ generation in anisotropically-consolidated specimens compared to those subjected to isotropic consolidation for inducing a certain I_B . In summary, loading direction in consolidation and shearing were observed to have profound effects on the mobilized friction angle, critical state line, brittleness and undrained shear strengths of tailings and this should be accounted for in analyzing the occurrence of liquefaction and stability of tailings dams.

It was finally demonstrated that gold tailings often present looser (i.e., located at higher void ratios) CSLs and higher instability and post-liquefaction shear strengths than those of natural sands and silts.

2.7 Acknowledgments

The authors gratefully acknowledge the financial support from Natural Sciences and Engineering Research Council of Canada (NSERC) that supported the work described in this paper.

Chapter 3

3 Instability of Gold Mine Tailings subjected to Undrained and Drained Unloading Stress Paths

3.1 Abstract

The drained instability of two gold mine tailings under lateral stress relief is investigated in this study. This type of failure is important as it has been associated with the flow liquefaction failure of several tailings dams. Constant deviator stress (CDS) unloading tests were performed using a triaxial apparatus to examine instability imposed by unloading in a drained condition. In the laboratory tests, instability was induced by enforcing a constant deviator stress while simultaneously reducing the mean effective stress. This reduction was attained via an external mechanism such as reducing the cell pressure or raising specimen's pore pressure. Stress paths and shear strengths of CDS tests were compared with undrained triaxial tests on comparable specimens which were anisotropically-consolidated to the same initial stress ratios of the CDS tests. Several techniques were employed to determine the onset of instability in CDS tests. The effects of unloading rate and initial stress ratio on the behavior and the triggering of instability in CDS tests were further investigated. It was observed that specimens consolidated to the same void ratios and initial stress ratios undergo instability at similar stress ratios or friction angles in both CDS and undrained shear tests. This suggests that the instability characteristic of tailings prone to stress relief can be predicted using undrained triaxial tests on anisotropically-consolidated specimens. Critical states and state parameters of specimens subjected to CDS and unloading stress paths were also compared and analyzed.

Keywords: Static liquefaction, Instability, Triaxial test, Mine tailings, Undrained strength

3.2 Introduction

When a saturated loose (“contractive”) granular soil is subjected to undrained shear loading, excess pore water pressure would be generated resulting in a decrease of mean effective stress. This is illustrated through the stress path of an undrained triaxial compression (TxC) test on an Ottawa sand (Omar and Sadrekarimi 2015) in **Figure 3-1**.

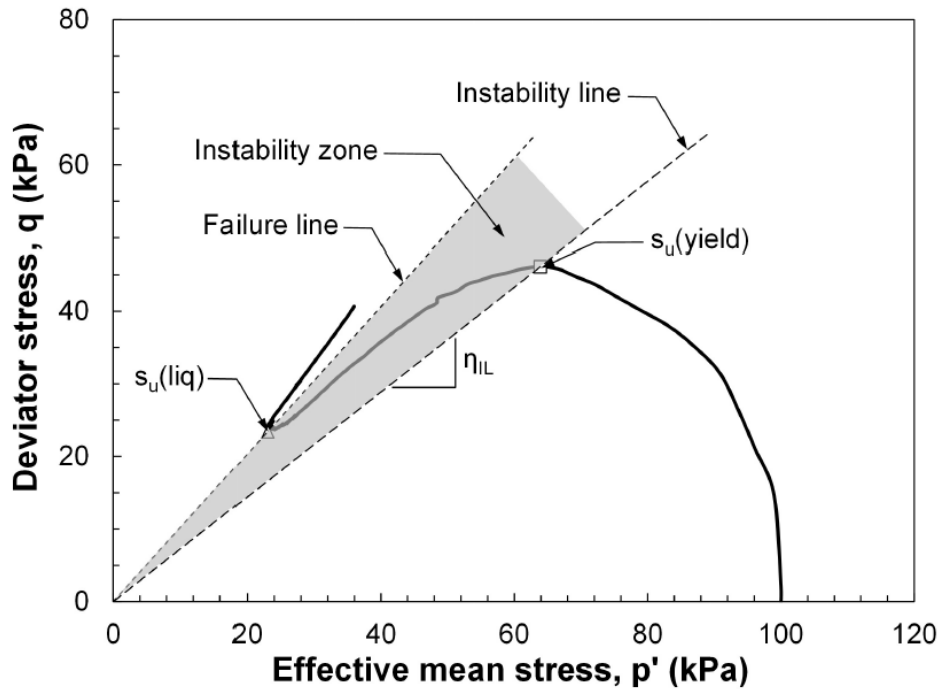


Figure 3-1: Stress path of an undrained triaxial compression test on an isotropically-consolidated specimen of loose Ottawa sand (Omar and Sadrekarimi 2015)

In this experiment, the deviator stress increases at first, reaching a peak undrained strength at $s_u(\text{yield})$, and then drops following the triggering of instability to a lowest post-liquefaction undrained strength, $s_u(\text{liq})$. The undrained instability of a loose specimen is also called “static liquefaction” failure (Terzaghi et al. 1996) or “flow liquefaction” failure. As shown in Figure 3-1 the instability line is the locus of $s_u(\text{yield})$ connecting to the origin in the stress path diagram (Chu et al. 2003). The instability region is the stress states between the instability line and the critical state line Lade (1992). Chu et al. (2012) describes a “chain of snowball effect” when the stress path

enters the instability zone in an undrained condition; suggesting that excess pore water pressure is generated as a result of plastic yielding. Large plastic strains are generated rapidly following the occurrence of instability. Undrained instability as described above can only occur in loose cohesionless soils in which sufficient shear-induced pore pressure can be generated to drive the stress path to instability.

Instability may also occur under a drained shearing condition when the total stress is reduced or the pore water pressure is increased by an external mechanism, resulting in a reduction of effective stress at a constant shear stress. This could be imposed for example by a rainfall, snowmelt, rise in phreatic surface, or lateral stress relief (Harp et al. 1990; Anderson and Sitar 1995; Olson et al. 2000; Leroueil 2001). A loose fabric and a constant-volume (i.e., undrained) condition are not required for this type of instability, which has made this phenomenon more challenging to predict. Several researchers (Anderson and Riemer 1995; Gajo et al. 2000; Zhu and Anderson 1998; Lourenço et al. 2011; Chu et al. 2012; Dong et al. 2016; Cherif Taiba et al. 2018; Rabbi et al. 2019; Riveros and Sadrekarimi 2020) have studied the behavior of soil specimens under the aforementioned stress path in constant deviator stress (CDS) or constant shear stress (CSS) unloading triaxial or direct simple shear tests. These studies have generally found that the deviator stress ratio at the triggering of instability ($\eta_{IL}=q/p'$) decreases with increasing consolidation void ratio (e_c) or a decrease in density. For example, Cherif Taiba et al. (2018) examined the instability of Fontainebleau sand mixed with 0 to 30% low plastic fines. Their results indicated that η_{IL} increased with increasing the size of particles or decreasing the coefficient of uniformity (CU) and e_c of the sand-silt mixtures.

Chu and Wanatowski (2008) further found little effect of anisotropic consolidation and initial deviator stress (q_c) on the triggering of instability, while others (Prisco et al. 1995; Doanh et al. 1997; Dong et al. 2016; Fourie and Tshabalala 2005; Gajo et al. 2000; Kato et al. 2001; Lade 1993; Rabbi et al. 2018; Wanatowski et al. 2010) have reported increased η_{IL} as well as an earlier onset of instability with anisotropic consolidation. Through a series of TxC tests on moist-tamped specimens of a silty sand, Rabbi et al. (2018) found that η_{IL} not only increased with decreasing e_c and increasing effective

consolidation pressure (p'_c), but also distinctly higher η_{IL} were mobilized in anisotropically-consolidated specimens than those produced in specimens subjected to isotropic stresses. Gajo et al. (2000) examined several factors affecting the instability of loose Hostun sand in drained stress-controlled triaxial tests. They found that instability was largely affected by pre-shearing and initial density, with a negligible effect of the loading path (i.e., constant deviator stress vs constant effective mean pressure). Wanatowski et al. (2010) studied the effect of the initial deviator stress ratio, $\eta_c=q_c/p'_c$, on the instability of a marine-dredged silica sand in plane strain CDS tests. They observed that the time to instability increased and the rate of axial displacement dropped with decreasing η_c . A lower q_c also required a greater amount of effective stress reduction and volumetric dilation to instability in CDS triaxial tests carried out by Dong et al. (2016) on moist-tamped specimens of Toyoura sand. Nevertheless, the same η_{IL} was mobilized irrespective of differences in q_c and p'_c .

Observations indicate that effective stress unloading at a constant deviator or shear stress can trigger instability in laboratory settings under a fully drained condition followed by a sharp increment of axial and volumetric strains and eventually a complete failure.

Static liquefaction and instability of two different gold mine tailings are investigated in this study through undrained loading and constant-deviator stress unloading triaxial compression tests. Mine tailings, by definition, are mixtures of crushed rock and processing fluid left over from the extraction of valuable minerals. Storing mine tailings in dammed impoundments has gained widespread acceptance (Kossoff et al. 2014). However, flow liquefaction failure and the subsequent collapse of mine tailings dams has resulted in large financial losses, environmental damages, and loss of lives in the past few decades (Morgenstern et al. 2016 and Robertson et al. 2020). More research is accordingly needed to fully understand tailings liquefaction behavior under different stress paths and implement mitigative measures.

The primary goals of this study are to: 1) examine three different approaches (strain rate, volumetric strain, energy) for identifying the triggering of instability in CDS tests, 2) compare stress ratios (i.e., friction angle) mobilized at the triggering of instability (η_{IL})

from CDS and undrained shear tests, 3) establish a unified framework based on the critical state theory for determining the triggering of instability in two gold mine tailings from CDS and undrained tests, and 4) investigate the effects of void ratio, effective stress, initial stress ratio, and unloading rate on the triggering of instability in gold tailings.

3.3 Experimental Procedure

3.3.1 Material tested

Fine and coarse tailings materials from two undisclosed gold mine sites across Ontario (O) and Quebec (Q) were used in this study. Average gradations and index properties of both tailings, determined following ASTM standard procedures, are summarized in Figure 3-2 and Table 3-1.

ASTM D4253 (ASTM, 2006a) and ASTM D4254 (ASTM, 2006b) standard procedures for measuring the maximum (e_{\max}) and the minimum (e_{\min}) void ratios are not applicable for the Ontario tailings because of their high fines content, FC (>15%). Nevertheless, to provide an estimate of the expected void ratio ranges, ASTM D4254 was used to measure e_{\max} of both tailings. For consistency, e_{\min} of both tailings was determined using the ASTM D1557 (ASTM, 2012) modified compaction procedure, which does not have the FC limitation of the ASTM D4253 method. These extreme void ratios were, however, not used for any other purposes (e.g., determining relative density) throughout this chapter.

X-ray diffraction analyses indicated that both tailings are composed of quartz, albite, chlorite, and trace bismuth gold minerals, with the fine O tailings also including Illite. As shown in Figure 3-2, the Q tailings is a silty sand with FC \approx 17% while the O tailings is a silt with FC \approx 84%. The fine silt particles in both tailings were found to be non-plastic.

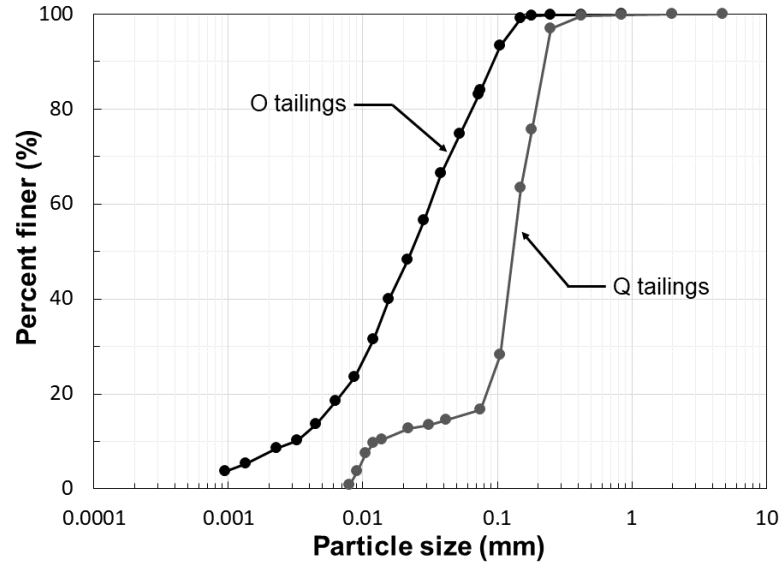


Figure 3-2: Average particle-size distributions of the gold tailings used in this study

Table 3-1: Index properties of gold tailings used in this study

Tailings	Maximum void ratio (e_{max})	Minimum void ratio (e_{min})	Specific gravity (G_s)	FC (%)
O tailings	2.08	0.62	2.72	84
Q tailings	1.18	0.68	2.75	17

SEM (scanning electron microscope) images of the tailings particles are shown in Figure 3-3, which indicate angular to subangular particle shapes. These figures further show rough surface textures of the coarse sand Q tailings, while those of fine O tailings are rather smooth.

A more quantitative description of the particles shown in Figure 3-3 can be stated using the definitions given by Cho et al. (2004). According to them, sphericity (also eccentricity or platiness) refers to the global form of the particle and reflects the similarity between the particle’s length, height, and width. Roundness (angularity) describes the scale of major surface features. Also, convexity is a measure of compactness of a particle. Using the method analyzed by Cho et al. (2007), the sphericity of the Q tailings particles was obtained to be 0.7 while their roundness ranged between

0.4-0.5. Their convexity parameter fell between 0.93 to 0.96. For the sand particles of O tailings however the sphericity was less than Q tailings, about 0.5 as well as the roundness parameter, which was also lower, about 0.3. The convexity was between 0.94-0.96. For the platy-shaped fines, the sphericity was observed to be very low, about 0.3, and the roundness was 0.1 (completely platy). The compactness, or convexity, parameter for the fines of O tailings was in the range of 0.91-0.93.

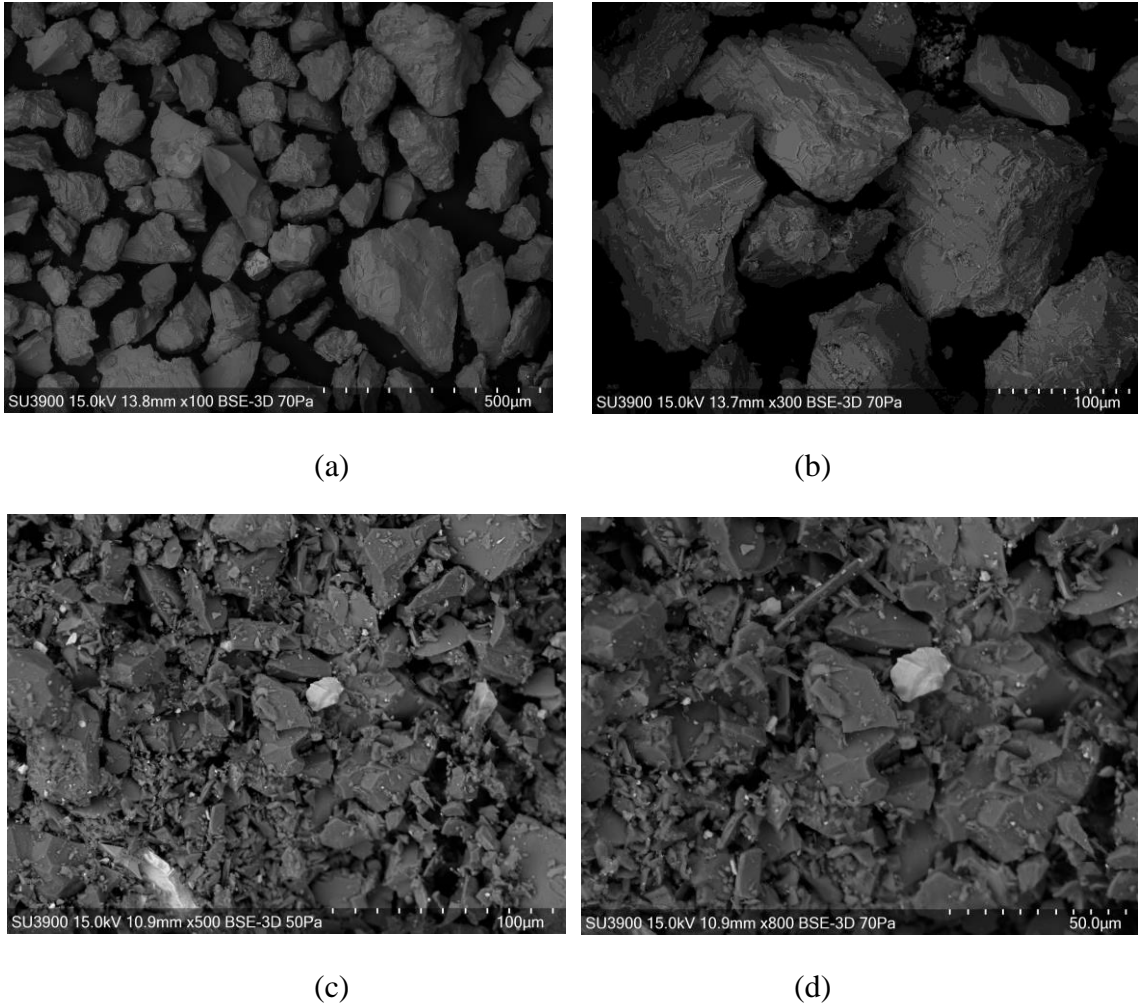


Figure 3-3: SEM images of coarse sand (a, b) and fine (c, d) gold tailings

3.3.2 Triaxial Apparatus

Monotonic triaxial compression tests were carried out using a computer-controlled stress path triaxial testing system manufactured by GeoTac Trautwein (USA).

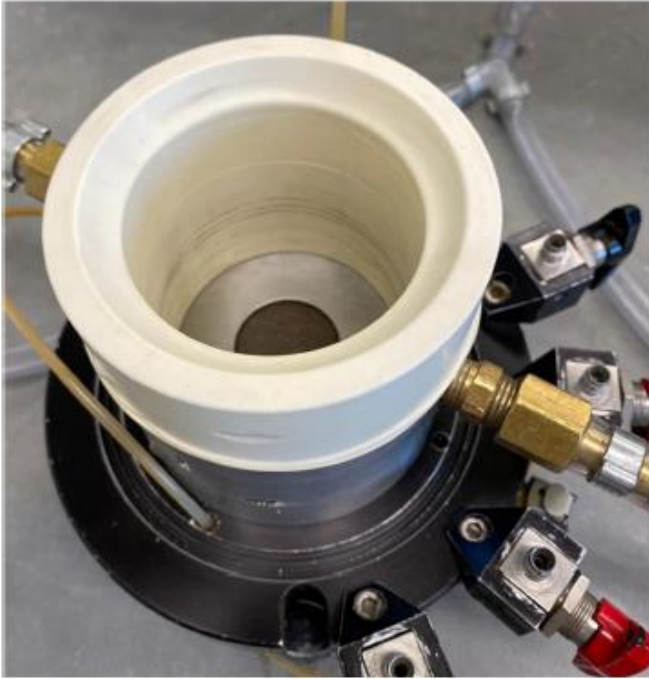
The triaxial setup included a 10 kN servo-controlled uniaxial loading frame, internal and external load cells, three pressure transducers, an LVDT, a distributed data acquisition and control system (DDAC) and two electromechanical pressure pumps.

The cell fluid and the specimen's pore water pressures and volumes are measured and controlled by two electromechanical pumps with volumetric capacities of 75 mL (for the specimen's pore water) and 170 mL (for the cell fluid). Each pressure pump is equipped with an electrical pressure transducer which can measure fluid pressure up to 2,070 kPa inside the pump at a resolution of 2.1 kPa. A third pressure transducer with a capacity of 1,370 kPa, mounted on the triaxial cell, measures the specimen's pore water pressure. Manufacturer calibrations were verified and confirmed for these pressure transducers by connecting them to a single pressure pump and cross-checking their measurements at several pressure increments. An internal load cell with a capacity of 2,224 N, installed above the specimen on the loading piston, is used to measure the deviator stress applied on the specimen without the effects of shaft friction and uplift. The internal load cell was recalibrated using known dead weights prior to the experimental program. The axial deformation of the specimen is measured by a high resolution linear variable differential transformer (LVDT) at a resolution of 0.002 mm as well as a digital encoder embedded in the loading frame. Specimen 113 volume change is also measured by one of the electromechanical pressure pumps at a resolution of 0.01 mL. A data logger with a maximum sampling frequency of 1 Hz included with the triaxial loading frame is used for data acquisition and real-time monitoring of the experiments. The computer-controlled data acquisition and control systems allows conducting a wide range of triaxial stress paths including laterally-confined K_0 -consolidation. The servo-controlled electromechanical loading frame was used to compress the sample or adjust the ram movement during confining stress reduction in CDS tests to maintain a constant deviator stress.

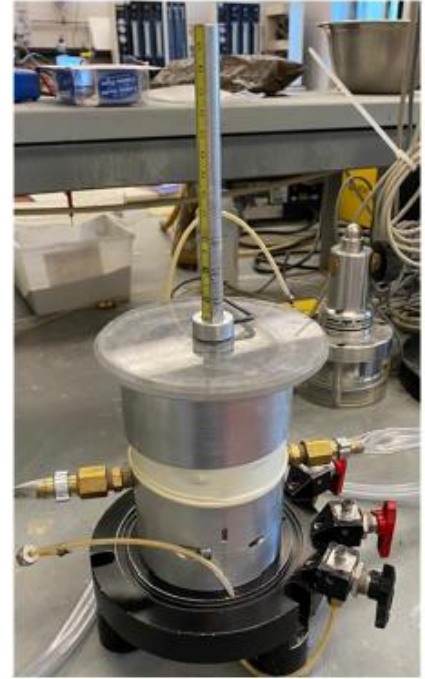
3.3.3 Specimen Preparation

Specimens of both tailings were reconstituted by moist-tamping according to the undercompaction technique introduced by Ladd (1978). This method was adopted due to its simplicity, easy control of initial void ratio Schnaid et al. (2013), and creating a relatively uniform density throughout the specimen (Sladen et al. 1985; Al-Tarhouni et al. 2011). Specimen uniformity was confirmed in this study by taking small plug samples with pre-determined volumes along the height of several frozen specimens of both Q and O tailings and weighing the mass of tailings in each container. Void ratio variations of ± 0.005 (i.e., $\pm 0.4\%$ change) and ± 0.008 (i.e., $\pm 0.6\%$ change) were found in coarse (Q) and fine (O) tailings, respectively. These small variations indicate the high degree of uniformity of the tailings specimens prepared in this study.

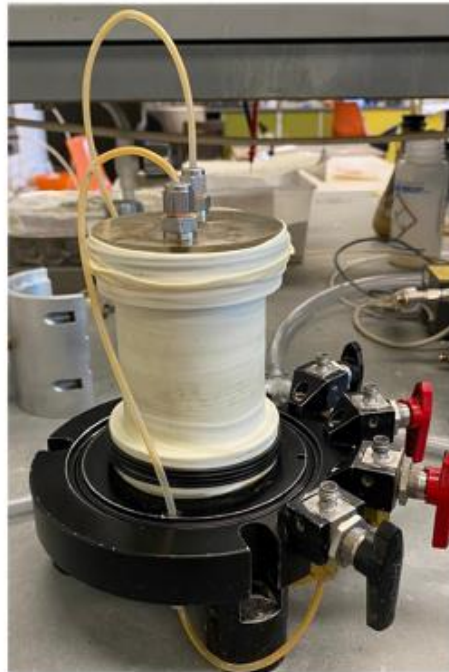
The enhanced strain-softening of moist-tamped specimens (Qiu and Sego 2001; Fourie and Tshabalala 2005; Chang et al. 2011; Schnaid et al. 2013) also facilitated investigating the instability and static liquefaction behavior of tailings in this study as the loosest possible specimens prepared by air pluviation and slurry deposition exhibited strain hardening behavior and did not liquefy. It has been shown that specimens with $H/D = 1$ experience more uniform deformation and reduced bulging at large shear strains (Foray et al. 1998; Rowe and Barden 1964). Specimens of 70 mm in height (H) and diameter (D) were prepared by tamping moist tailings in a 70 mm aluminum split mold. Figure 3-4 shows several photos of the specimen preparation procedure. As illustrated in Figure 3-4(a), a latex membrane lined the internal circumference of the aluminum mold.



(a)



(b)



(c)



(d)

Figure 3-4: Photos of the specimen preparation procedure: (a) membrane-lined mold, (b) specimen tamping with a graduated rod, (c) completed specimen after removing the mold, (d) specimen in the triaxial cell mounted on the loading frame

Lubricated end platens with a diameter of 20 mm larger than that of the specimen (70 mm) were used to minimize end friction and allow free expansion of the specimen during shearing (Omar and Sadrekarimi 2015). A specially designed split mold was constructed and utilized for accommodating the enlarged platens for specimen preparation. The contact friction between the end platens and the specimen was minimized through two sheets of 0.3 mm thick latex discs separated by a very thin smear of high vacuum silicone grease. The latex discs were trimmed to the specimen diameter with a central hole cut to the diameter of the porous stone to allow drainage. An additional layer of silicon grease was smeared on the rubber discs to provide a smooth and frictionless sliding on the end platens.

3.3.4 Saturation

Following sample preparation, the top cap was placed on the specimen and the membrane was folded over the top cap. The specimens were subsequently saturated by first circulating CO₂ gas through them for about 20 minutes, followed by flushing with several pore volumes of deaired water until no air bubbles were visible in the specimen or the drainage tubes. A backpressure saturation procedure recommended by Bishop and Henkel (1962) was followed by simultaneously increasing the cell and the pore water pressures until a pore pressure ratio, $B = \Delta u / \Delta \sigma_3$, of at least 0.98 was achieved.

To determine the volume change during saturation, the specimens were frozen after each test and their final void ratios (e_f) and total weights were measured. For this procedure, the drainage valves were first closed, and the cell fluid was drained. This created a small vacuum (negative pore pressure) and stabilized the specimen form. The acrylic cell wall was then lifted off and the specimen assembly including the platens, membrane, and drainage lines were carefully placed in a chest freezer for 24 hours. The specimen was then removed from the freezer, the end caps were carefully detached from the frozen tailings, and the latex membrane was cut and removed by a scissor. The frozen tailings along with any particles sticking to the membrane or the specimen caps were brushed and placed in a pan and weighed to determine the specimen's wet weight (W_w). The pan (containing the tailings) was subsequently placed in an oven at a temperature of around 60°C for 24 hours. The weight of dried tailings (W_s) was then measured and used for the calculation of specimens' final water content, $\omega_f = (W_w - W_s) / W_s$. This was finally used for determining $e_f = \omega_f G_s$ of the saturated specimens. By measuring volume changes during shearing (for drained tests) and consolidation, specimens' void ratio after saturation was backcalculated.

3.3.5 Consolidation

Following saturation, tailings specimens were consolidated under either isotropic (IC) or anisotropic (AC) stresses. Various principal stress ratios, $K_c = \sigma'_{3c} / \sigma'_{1c} = 0.3$ to 0.6, were

applied during anisotropic consolidation where σ'_{3c} and σ'_{1c} are the minor and the major principal consolidation stresses, respectively. A number of specimens were also consolidated under a laterally-confined (K_o) condition. This was accomplished by maintaining equal volumetric (ϵ_{vol}) and axial (ϵ_a) strains, and therefore imposing a zero radial strain, $\epsilon_r = (\epsilon_{vol} - \epsilon_a)/2 = 0$, during consolidation. Lateral stress ratios ($K_o = \sigma'_{3c}/\sigma'_{1c}$) of 0.57 and 0.55 were produced in respectively coarse (Q) and fine (O) tailings at the end of consolidation. The applied consolidation stresses were maintained for about two hours to allow complete excess pore pressure dissipation and primary consolidation prior to shearing.

3.3.6 Shearing

Following consolidation, specimens of each tailings were subjected to: A) undrained shearing, B) drained shearing, and C) constant-deviator stress unloading (CDS) stress paths. In the undrained tests, specimen drainage valves were closed and axial deformation was applied at a strain rate of 5%/hour following the ASTM D4767-11 (ASTM 2011) standard procedure to ensure pore pressure equalization throughout the specimen. To determine the critical state lines and friction angles of the tailings, several drained tests were also carried out at a strain rate of 5% on both tailings by maintaining the backpressure during shearing (e.g., zero excess pore pressure). These tests were conducted on very loose specimens such that their final states would be close to the critical state line without strain localization and shearing banding associated with the shearing of dilative specimens.

A stress-controlled procedure was employed in the CDS tests, where the effective confining pressure (p') was reduced by slowly pumping water into the specimen and increasing the pore pressure (u_e) at different rates of $du_e/dt = 0.1, 0.2, 0.5, 1, 2, 3$ kPa/min. Because of the slow injection of water into the specimen, pore pressure equalized quickly. This was confirmed by a pressure transducer connected to the specimen which showed similar pore pressure increments as those applied by the pressure pump. A constant q_c was maintained during this process by carefully adjusting the axial

load applied by the triaxial loading frame. Changes in volume and height of the specimen were monitored to calculate ε_{vol} and ε_a , which were later used for interpreting the CDS test results and determining the onset of instability. The majority of the undrained shear tests were performed on isotropically-consolidated ($K_c = 1.0$) specimens, while the CDS tests commenced from an initial stress ratio, $\eta_c = q_c/p'_c$, induced during consolidation. Testing characteristics including the initial deviator stress, $q_c = \sigma'_{1c} - \sigma'_{3c}$, mean confining pressure, p'_c , η_c and void ratio (e_c) of each specimen following consolidation are summarized in Table 3-2 and Table 3-3. These correspond to the beginning of unloading for the CDS tests in Table 3-3.

Supplementary undrained tests were performed on specimens consolidated to the same η_c as the CDS tests to assess the role of η_c on the occurrence of instability by different stress paths. These specimens were isotropically consolidated, and then subjected to conventional drained shearing to achieve η_c . For calculating the major principal stress, the specimen's cross-sectional area was corrected based on the right circular cylinder method. Because of the relatively small D_{50} of the tailings used in this study, membrane penetration was negligible and was not corrected for.

Table 3-2: Summary of the undrained and drained TxC tests of this study

Tailings	Test ID	Consolidation	Shearing	p'_c ^a (kPa)	e_c	D_{rc} (%)	η_c ^b	η_{IL} ^c
Coarse (Q)	QIU1	Isotropic	Undrained	150	1.136	9	0.00	0.63
	QIU2			200	1.091	21	0.00	0.68
	QIU3			300	1.058	25	0.00	0.70
	QIU4			400	1.036	29	0.00	0.72
	QID1	Anisotropic (K_o)	Drained	90	1.092	18	0.00	-
	QID2			175	1.067	22	0.00	-
	QID3			190	1.043	27	0.00	-
	QID4			230	1.040	28	0.00	-
	QK _o U1	Anisotropic (K_c)	Undrained	75	1.174	1	0.59	0.75
	QK _o U2			138	1.109	14	0.60	0.82
	QK _o U3			243	1.049	26	0.60	0.85
	QK _o U4			316	1.022	32	0.60	0.90
	QAU1 ^d	Anisotropic (K_c)	Undrained	100	1.064	23	0.42	0.77
	QAU2 ^d			200	1.052	26	0.58	0.80
	QAU3 ^d			300	1.053	26	0.54	0.77
	Fine (O)	OIU1	Isotropic	Undrained	160	1.021	73	0.00
OIU2		200			0.992	75	0.00	0.73
OIU3		300			0.947	78	0.00	0.74
OIU4		600			0.840	82	0.00	0.86
OID1		Anisotropic (K_o)	Drained	230	1.005	71	0.00	-
OID2				310	0.958	73	0.00	-
OID3				400	0.838	77	0.00	-
OK _o U1		Anisotropic (K_o)	Undrained	80	1.082	72	0.61	0.91
OK _o U2				160	1.009	74	0.61	0.92
OK _o U3	300			0.947	77	0.61	0.92	

^a p'_c : mean effective stress after consolidation; ^b η_c : deviator stress ratio (q_c/p'_c) after consolidation; ^c η_{IL} : deviator stress ratio at the triggering of instability; ^d $K_c=0.67, 0.58,$ and 0.60 for QAU1, QAU2 and QAU3, respectively.

Table 3-3: Specifications of the constant deviator stress tests on Q and O tailings

Test ID	du_e/dt (kPa/min)	p'_c ^a (kPa)	q_c ^b (kPa)	e_c	D_{rc} (%)	η_c	η_{IL}
QCDS 1		119	50	1.049	26	0.42	0.77
QCDS 2	0.5	133	100	1.051	26	0.75	0.83
QCDS 3 ^c		-	150	-	-	-	-
QCDS 4		238	100	1.042	28	0.42	0.78
QCDS 5	0.5	240	125	1.043	28	0.52	0.79
QCDS 6		259	150	1.044	27	0.58	0.8
QCDS 7		333	100	1.050	26	0.30	0.73
QCDS 8	0.5	357	150	1.048	26	0.42	0.76
QCDS 9		370	200	1.045	27	0.54	0.77
QCDS 10		119	50	0.909	54	0.42	0.99
QCDS 11	0.5	238	100	0.898	56	0.42	1.00
QCDS 12		357	150	0.892	58	0.42	0.98
QCDS 13		119	50	0.780	80	0.42	1.16
QCDS 14	0.5	357	150	0.779	80	0.42	1.14
QCDS 15	0.1	119	50	1.048	26	0.42	0.77
QCDS 16	0.2	119	50	1.036	29	0.42	0.76
QCDS 17	1	119	50	1.052	26	0.42	0.78
QCDS 18	2	119	50	1.047	27	0.42	0.78
QCDS 19	3	119	50	1.045	27	0.42	0.77
OCDS 1		147	50	1.018	73	0.34	0.89
OCDS 2	1	156	95	1.036	72	0.61	0.92
OCDS 3		271	84	1.030	72	0.31	0.86
OCDS 4	1	311	190	0.975	76	0.61	0.92
OCDS 5	0.1	311	190	1.011	73	0.61	0.93
OCDS 6	0.2	311	190	1.027	72	0.61	0.93
OCDS 7	0.5	311	190	1.034	72	0.61	0.91
OCDS 8	2	311	190	1.033	72	0.61	0.92
OCDS 9	3	311	190	1.029	72	0.61	0.94
OCDS 10	0.5	82	50	1.025	72	0.61	0.92
OCDS 11	1	156	95	0.846	85	0.61	1.07
OCDS 12	1	156	95	0.690	94	0.61	1.19

^a p'_c : mean effective stress at the commencement of unloading; ^b q_c : deviator stress at the commencement of unloading; ^c became unstable prior to unloading

3.4 Results

Figure 3-5 and Figure 3-6 demonstrate undrained shearing responses of respectively isotropically- and anisotropically-consolidated specimens of the Q tailings. The stress paths and stress-strain plots in both figures indicate strain-softening (contractive) and instability triggered following $s_u(\text{yield})$, but at much smaller axial strains (ϵ_a) of 0.15-0.4% in the anisotropically-consolidated specimens than $\epsilon_a=1.0-1.4\%$ in the isotropically-consolidated samples. This suggests a stiffer initial shearing response of the anisotropically-consolidated specimens. Strength loss continues until a minimum post-liquefaction undrained strength, $s_u(\text{liq})$. At this point, the specimens experience a phase transformation (Alarcon-Guzman et al. 1988) from strain-softening to strain-hardening behavior with progressively increasing mean confining pressure (p') and deviator stress (q). A friction angle of $\phi'_{\text{PT}} = 38.6^\circ$ was mobilized at the phase transformation (PT) points of the isotropically- and anisotropically-consolidated specimens, indicating the small effect of consolidation history and η_c on ϕ'_{PT} . Similar behaviors are also observed in Figure 3-7 and Figure 3-8 which show the undrained shearing responses of isotropically- (tests OIU1- OIU4) and anisotropically- (tests OK_oU1 – OK_oU3) consolidated specimens of the O tailings. Despite their relatively higher e_c (= 0.716 – 1.049), these specimens also undergo limited liquefaction and phase transformation at $s_u(\text{liq})$ with a corresponding $\phi'_{\text{PT}} = 39.8^\circ$ for both isotropic- and anisotropic-consolidation. In fact, limited liquefaction is a common feature in the shearing of mine tailings (Fourie and Papageorgiou 2001; Qiu and Segoo 2001; Chang et al. 2011). In addition to undrained testing, several drained TxC tests were also conducted on the O and Q tailings specimens, resulting in effective friction angles similar to the ϕ'_{PT} mobilized in each tailings.

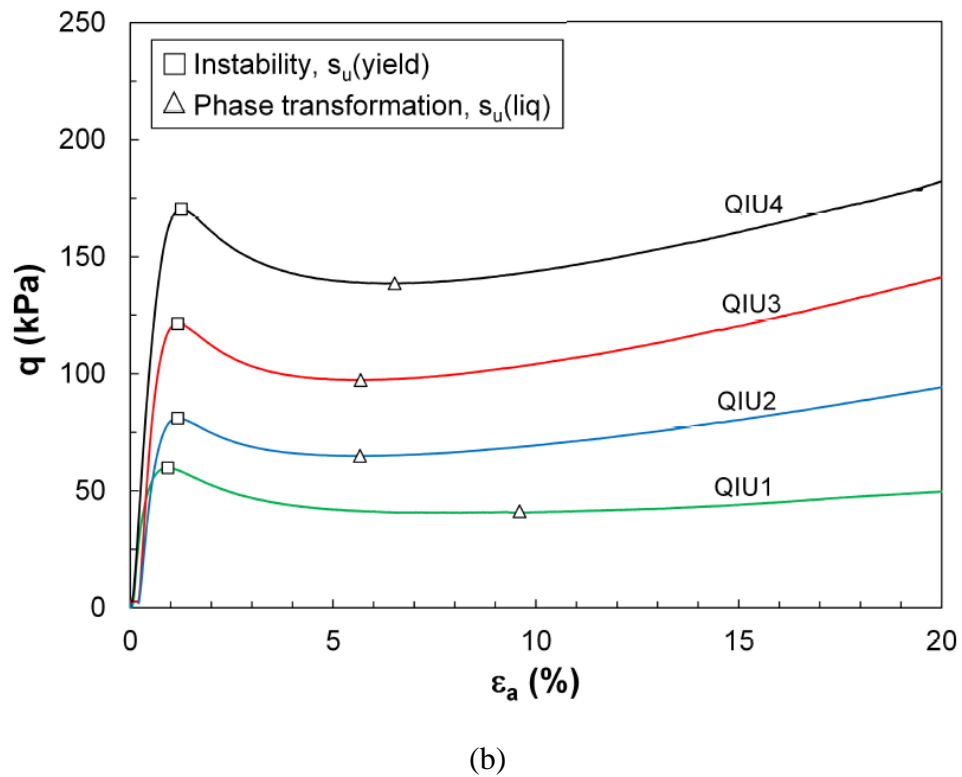
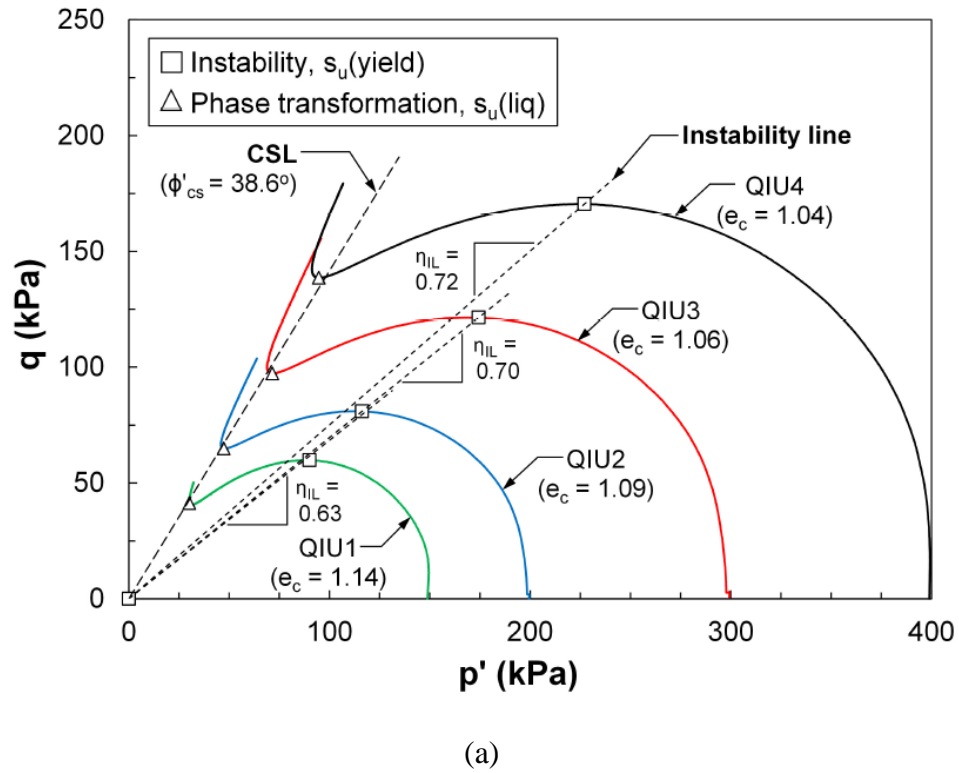
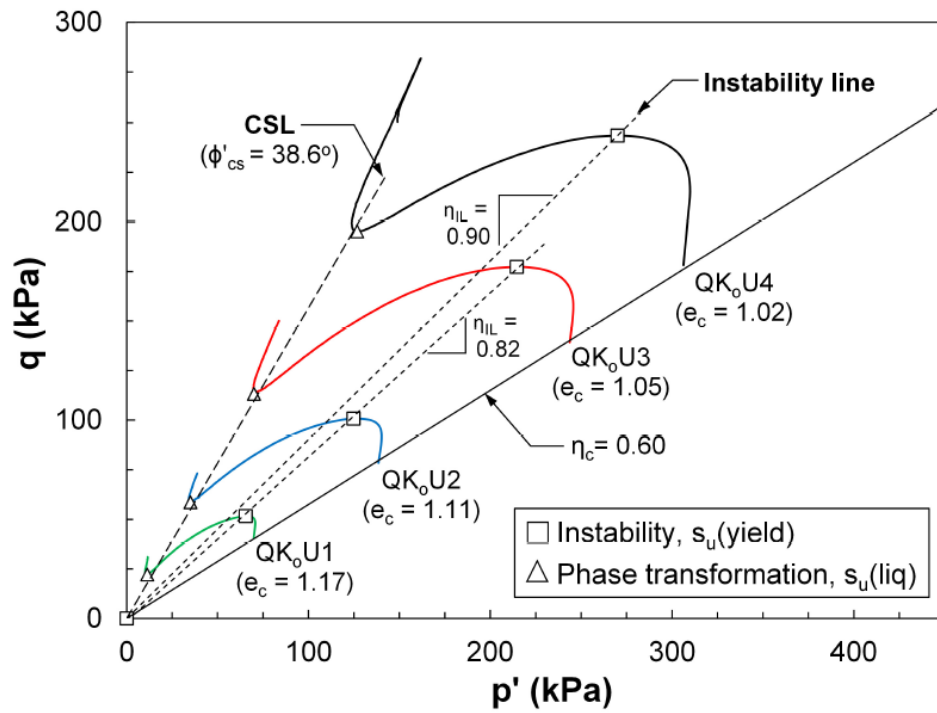
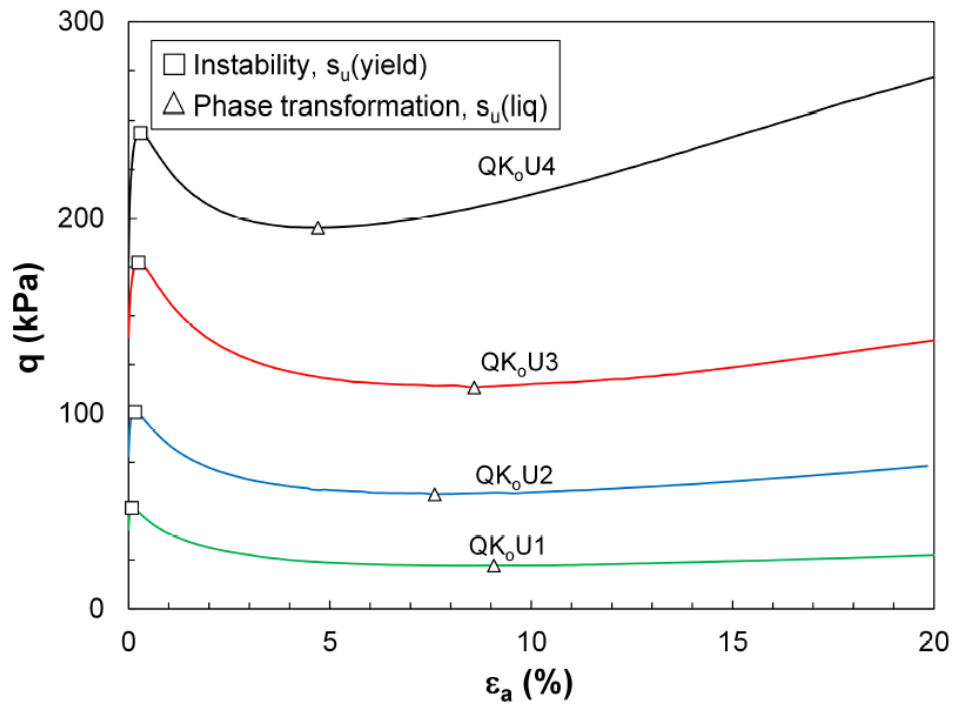


Figure 3-5: Undrained (a) stress paths and (b) stress-strain behaviors of QIU specimens



(a)



(b)

Figure 3-6: Undrained (a) stress paths and (b) stress-strain behaviors of QK₀U specimens

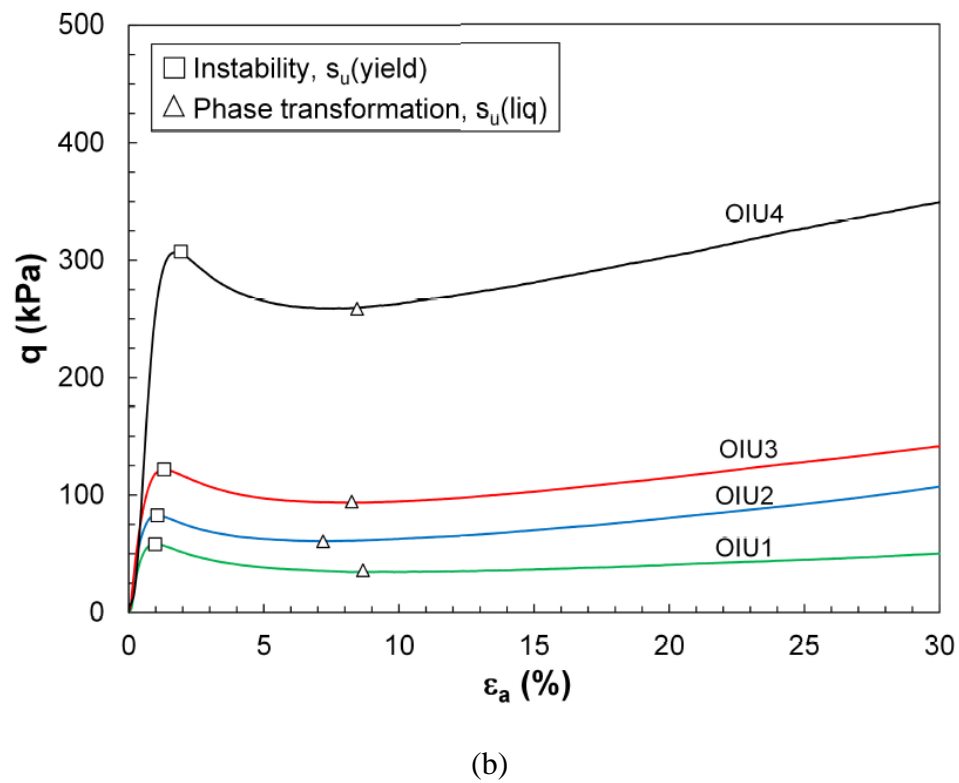
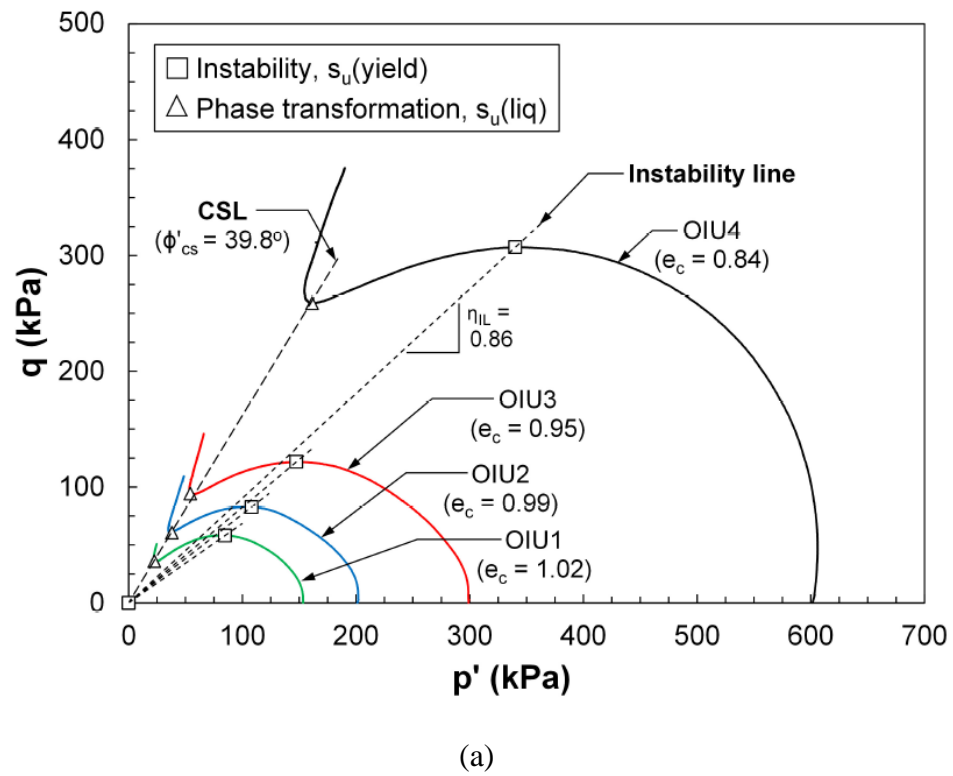
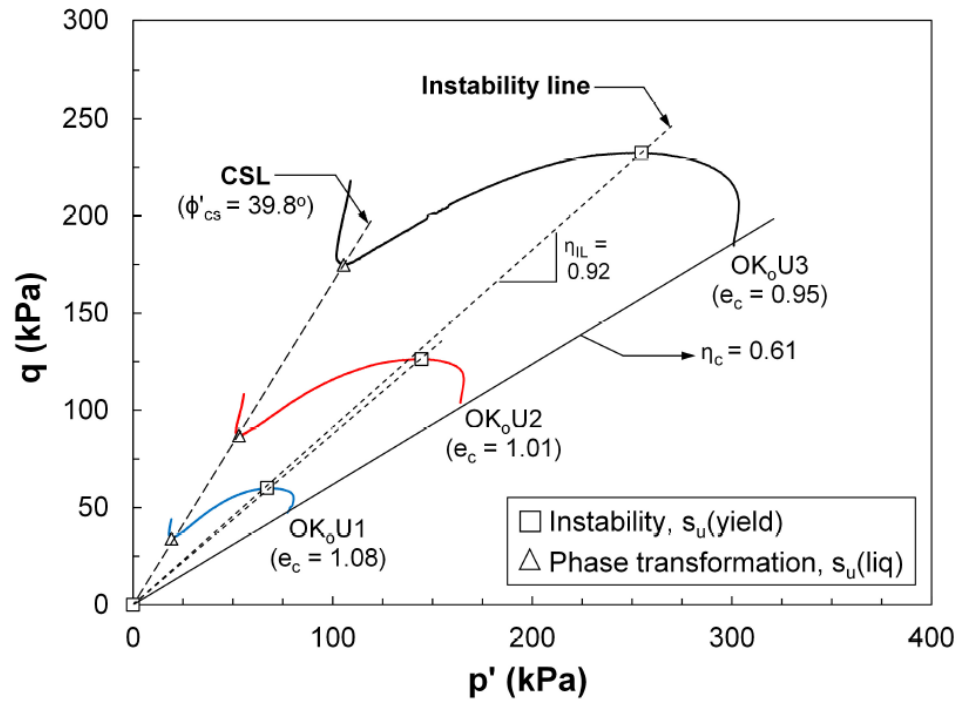
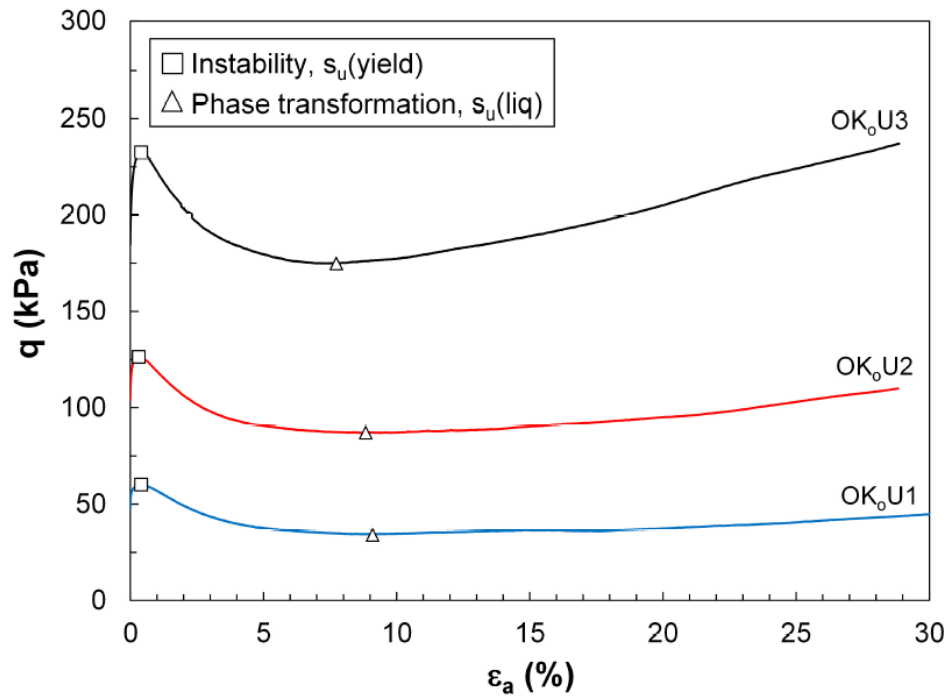


Figure 3-7: Undrained (a) stress paths and (b) stress-strain behaviors of OIU specimens



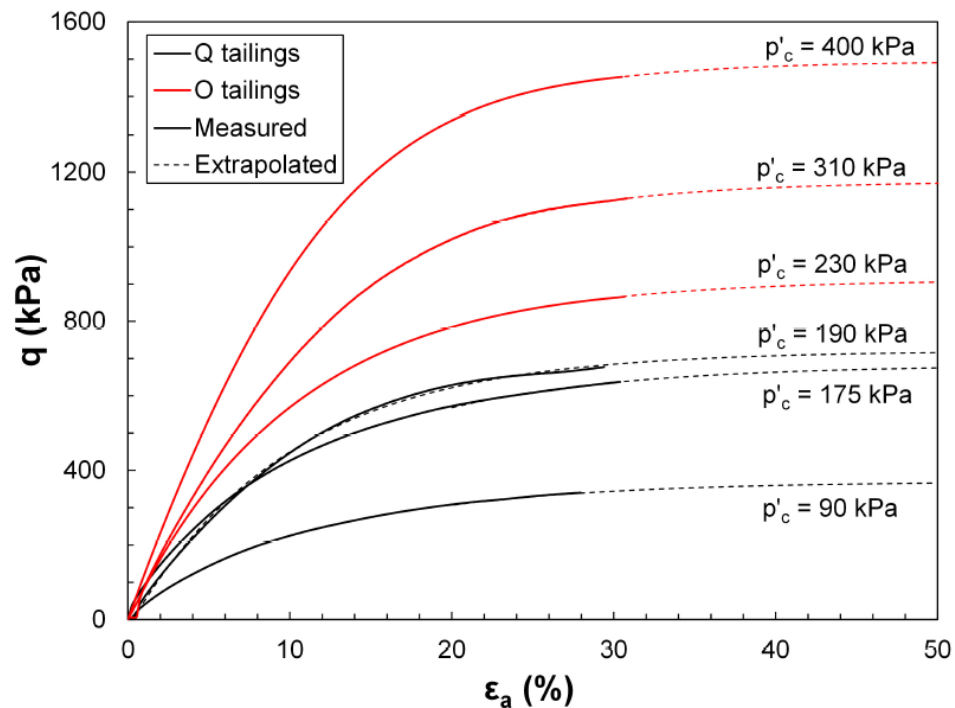
(a)



(b)

Figure 3-8: Undrained (a) stress paths and (b) stress-strain behaviors of OK_oU specimens

Figure 3-9 further shows the deviator stresses and ϵ_{vol} of the supplementary drained TxC tests on isotropically-consolidated specimens of each tailings. Because of their loose fabric, all specimens experienced contractive volume changes amid a rising deviator stress in the drained tests. To avoid stress and strain non-uniformities, TxC tests were not sheared beyond $\epsilon_a=30\%$. As a result of this limitation, the deviator stresses shown in Figure 3-9 continued to rise, although at a reducing rate, until the end of each test. Although ϵ_{vol} of the Q tailings seem to reach asymptotic values, those of tests OID1 and OID2 on the finer O tailings failed to plateau. In these cases, the asymptotic deviator stress and ϵ_{vol} values were determined by extrapolating the best fitted exponential functions to their trends with ϵ_a as illustrated in Figure 3-9. The extrapolation raised the deviator stress and ϵ_{vol} values by average amounts of 4.75% (2.6 to 7.6%) and 3.1% (0.4 to 5.1%), respectively, from their ultimate measured values at end of each test.



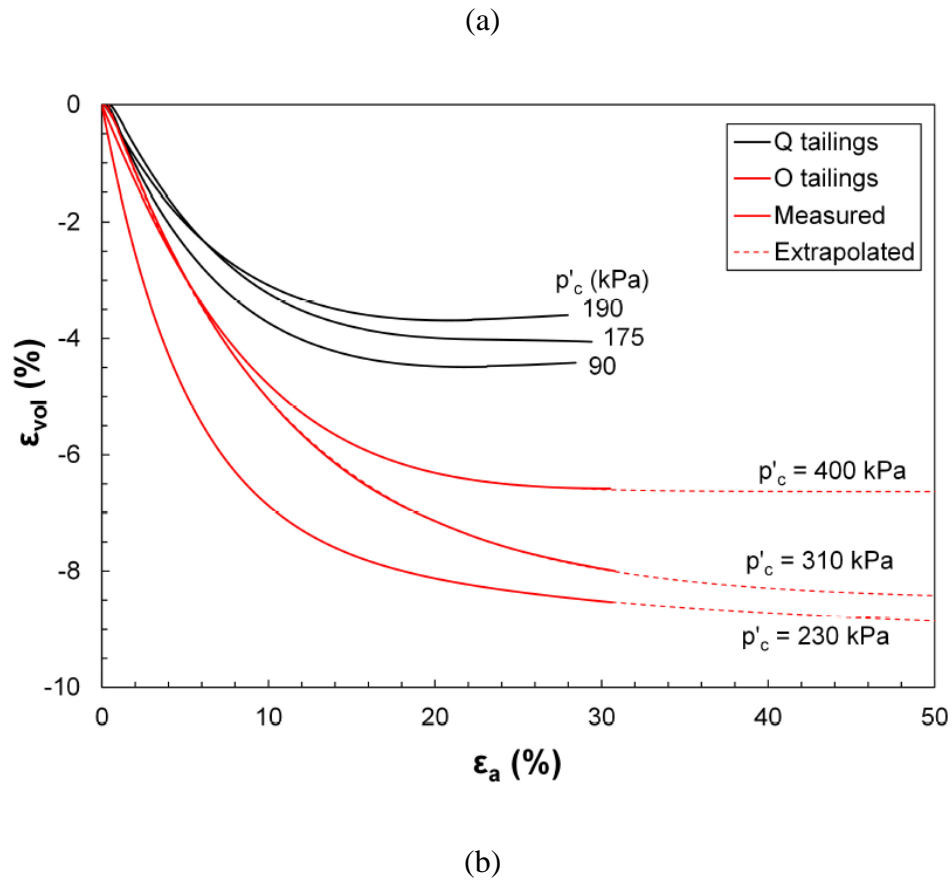


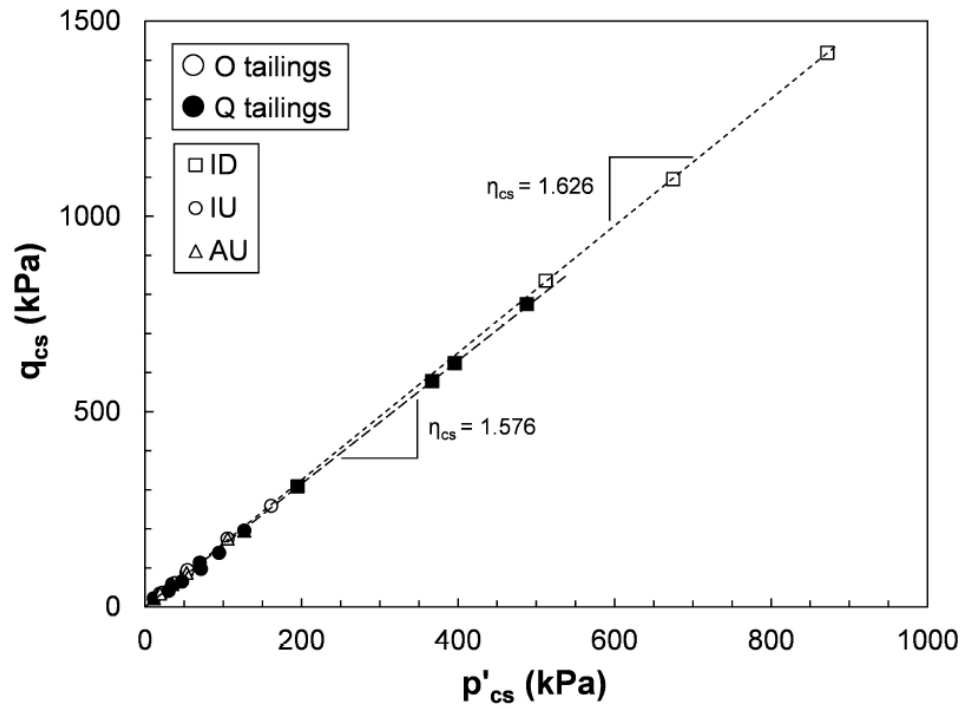
Figure 3-9: (a) deviator stress and (b) volumetric strains versus axial strain of drained TxC tests on each tailings

3.4.1 Critical State Line

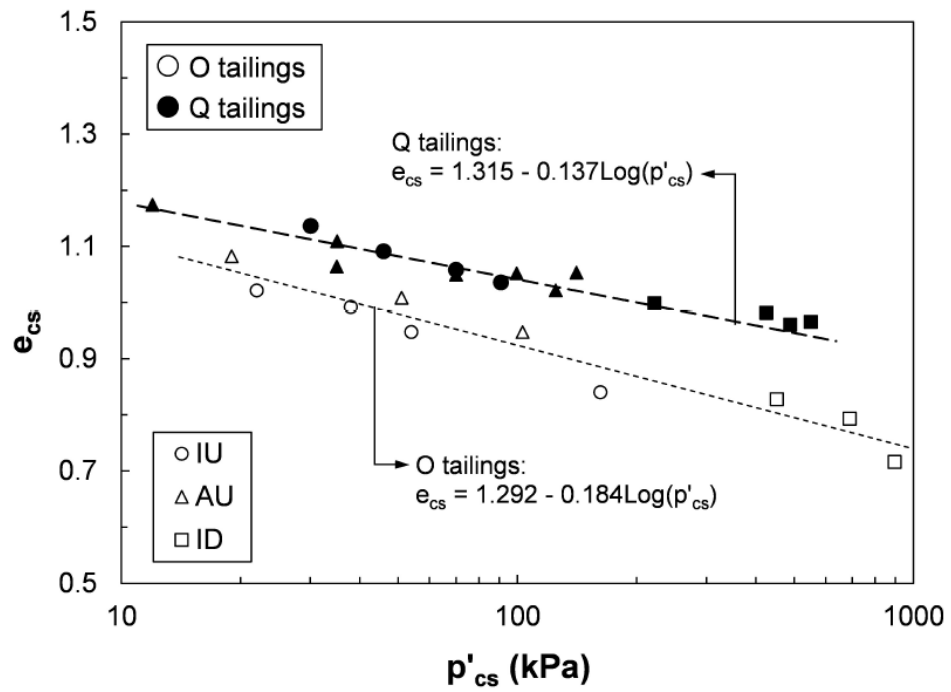
Although the limited liquefaction behaviors of Figure 3-5 to Figure 3-8 don't strictly meet the critical state requirements of constant shear and effective stresses, the post-liquefaction strain-hardening (dilative) responses are often weak and occur following an extended range of nearly constant shear stress at $\epsilon_a > 10 - 15\%$. Accordingly, the phase transformation points constitute distinct states (Alarcon-Guzman et al. 1988; Murthy et al. 2007) which are practically close to the critical states of each tailings. Figure 3-10 demonstrates the critical state lines (CSL) of tailings established from the phase transformation points of the undrained tests as well as the asymptotic states of the drained

TxC tests in both the stress path (q vs. p') and e - $\log(p')$ diagrams. Straight lines, starting from the origin, are fitted to the critical states of each tailings in the stress path diagram. Figure 3-10(a) indicates average deviator stress ratios ($\eta_{cs} = q_{cs}/p'_{cs}$) of 1.626 and 1.576 at the critical states, corresponding to critical state friction angles (ϕ'_{cs}) of 39.8° and 38.6° , for the O and the Q tailings, respectively. The relatively higher ϕ'_{cs} of the O tailings is likely because of the more angular and the higher amount of fines which wedge-in among the sand particles, as also reported by other investigators regarding the effect of non-plastic fines on ϕ'_{cs} (Murthy et al. 2007; Ni et al. 2004; Sladen et al. 1985b).

For each tailings a unique CSL is also obtained in the e - $\log(p')$ plane irrespective of the drainage condition (IU vs ID) and the consolidation history (AU, K_oU , or IU). The relatively greater scatter observed in the critical states of the O tailings is likely associated with their higher FC, making it difficult to prepare uniform specimens compared to those of the Q tailings. The semi-logarithmic relationships fitted to the critical states indicate a relatively denser (located at lower void ratios) and steeper CSL for the O tailings ($\Gamma = 1.292$, $\lambda = 0.08$) compared to that of the Q tailings ($\Gamma = 1.315$, $\lambda = 0.062$). This is likely because of the more compressible and angular shapes of the O tailings particles, as well as the higher FC which fill-in and occupy void spaces among the larger sand grains. In the following paragraphs, the CSLs shown in Figure 3-10(b) are used to determine the state parameter (ψ_{cs}) of each test as the void ratio difference between e_c and the corresponding CSL at p'_c .



(a)



(b)

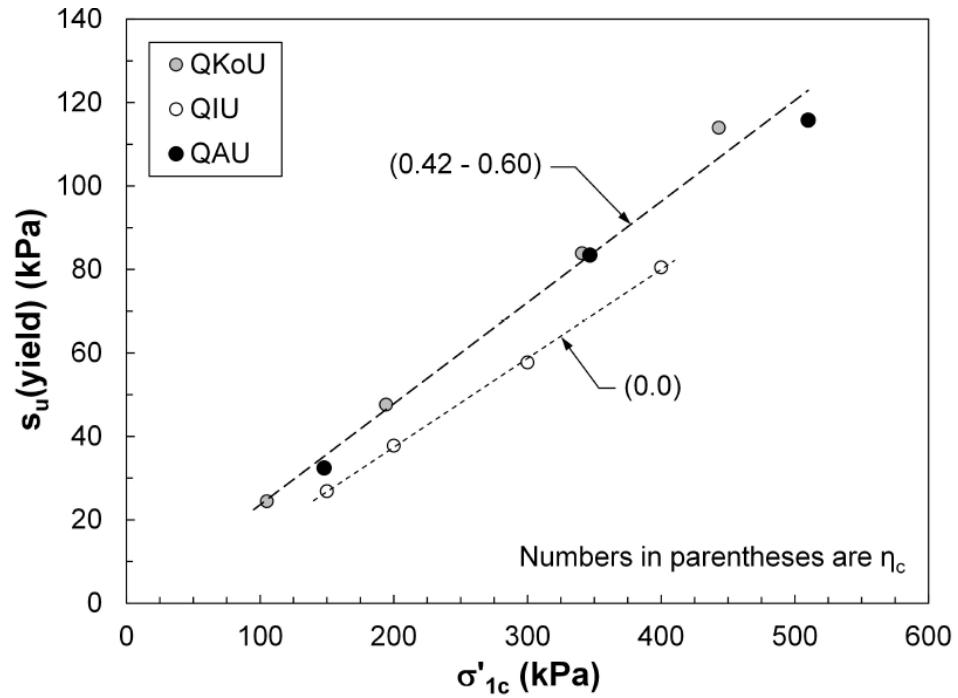
Figure 3-10: Critical state lines of Q and O tailings in the (a) stress path, and (b) e - $\log(p')$ planes (IU: isotropically-consolidated undrained test; AU: anisotropically-consolidated undrained test; ID: isotropically-consolidated drained test)

3.4.2 Undrained instability

In an undrained test, the triggering of instability coincides with $s_u(\text{yield})$, as shown in the stress paths of Figure 3-5 to Figure 3-8, and the instability line (IL) and its slope (η_{IL}) are then established by connecting $s_u(\text{yield})$ to the origin. Similar to several other studies (Baziar and Dobry 1995; Hanzawa 1980; Ishihara 1993; Olson and Mattson 2008; Olson and Stark 2003a; Stark and Mesri 1992; Vaid and Sivathayalan 1996), $s_u(\text{yield})$ and $s_u(\text{liq})$ are normalized here with respect to σ'_{1c} rather than p'_c . This is because σ'_{1c} is nearly the same as the effective vertical stress which can be readily calculated with reasonable accuracy in the field for a known phreatic surface. However, because of the difficulty in measuring the in-situ K_C , there could be some level of uncertainty in estimating the in-situ p'_c , particularly for a sloping ground.

Undrained instability is examined in Figure 3-11 and Figure 3-12 which show linear increases of $s_u(\text{yield})$ with increasing σ'_{1c} and decreasing $s_u(\text{yield})/\sigma'_{1c}$ with increasing e_c for Q and O tailings. Anisotropically-consolidated ($K_C > 1$) tailings samples, however, exhibit greater $s_u(\text{yield})$ and $s_u(\text{yield})/\sigma'_{1c}$, and enhanced strain-softening, compared to those with $K_C = 1$. In fact, $s_u(\text{yield})/\sigma'_{1c}$ increases with increasing stress anisotropy (i.e., rising η_c) in Figure 3-11(b). Improved particle-interlocking during anisotropic consolidation alleviates the potential of pore water pressure generation (Sadrekarimi 2016). A greater effort was thus required to overcome $s_u(\text{yield})$. The measured $s_u(\text{yield})/\sigma'_{1c}$ obtained in the current study are also in good agreement with those reported by other studies, e.g., Olson and Stark (2003), Been and Jefferies (1985), Ishihara (1993), and Hanzawa (1980). For example, based on a collected database of isotropically-consolidated undrained TxC tests on 46 sands, silty sands, and sandy silts, Olson and Stark (2003) reported $s_u(\text{yield})/\sigma'_{1c} = 0.29\text{-}0.42$. Been and Jefferies (1985) obtained $s_u(\text{yield})/\sigma'_{1c} = 0.21\text{-}0.51$ by conducting a series of isotropically-consolidated undrained TxC tests on Kogyuk sand. Ishihara (1993) performed undrained TxC tests on

isotropically-consolidated specimens of moist-tamped Toyoura sand and measured $s_u(\text{yield})/\sigma'_{1c} = 0.21\text{-}0.34$. Hanzawa (1980) also reported $s_u(\text{yield})/\sigma'_{1c} = 0.11\text{-}0.27$, $0.23\text{-}0.41$ and $0.18\text{-}0.32$ for Valgrinda, Sengenama, and Kisarazu sands tested in TxC, respectively.



(a)

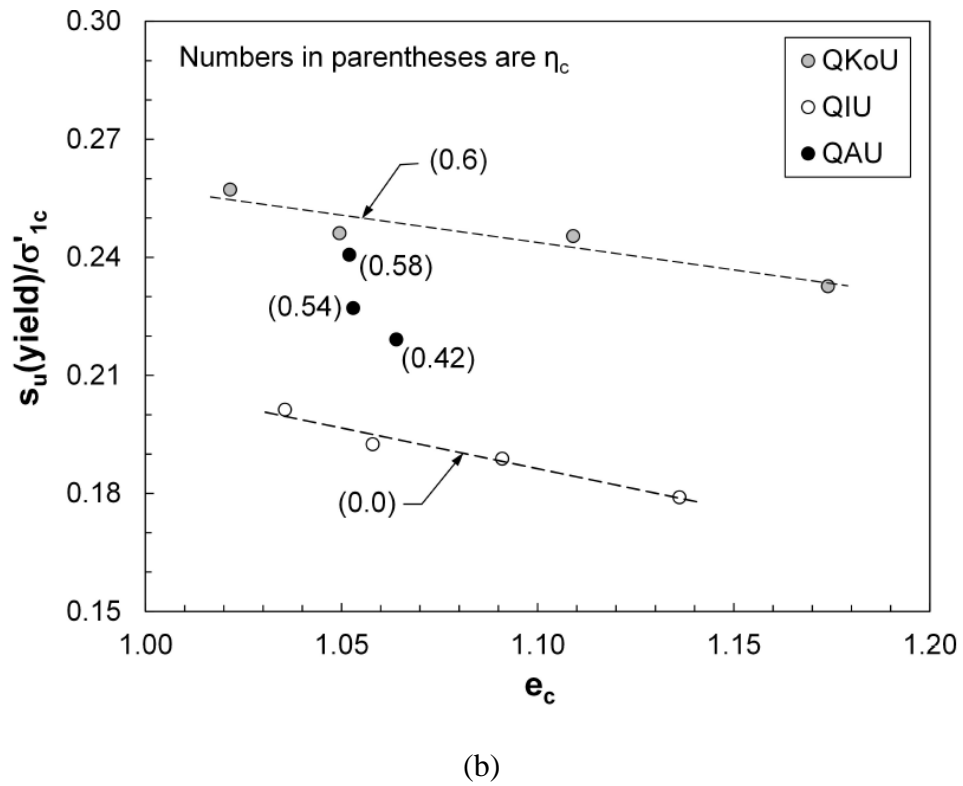
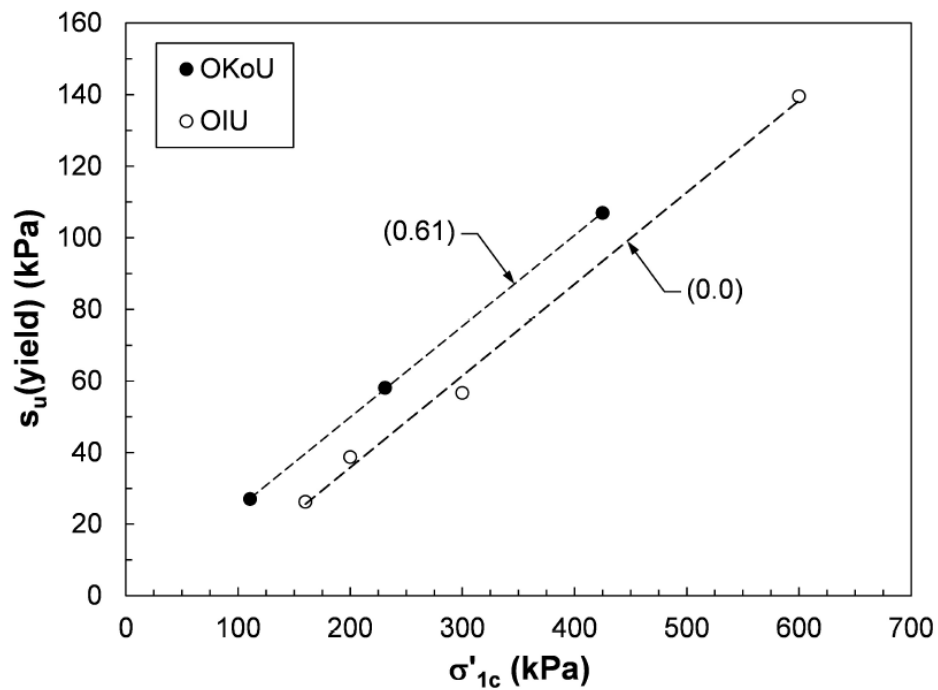


Figure 3-11: Variations of (a) $s_u(\text{yield})$ with σ'_{1c} ; and (b) $s_u(\text{yield})/\sigma'_{1c}$ with e_c for both $K_c = 1$ and $K_c > 1$ specimens of Q tailings. Numbers in parentheses indicate η_c



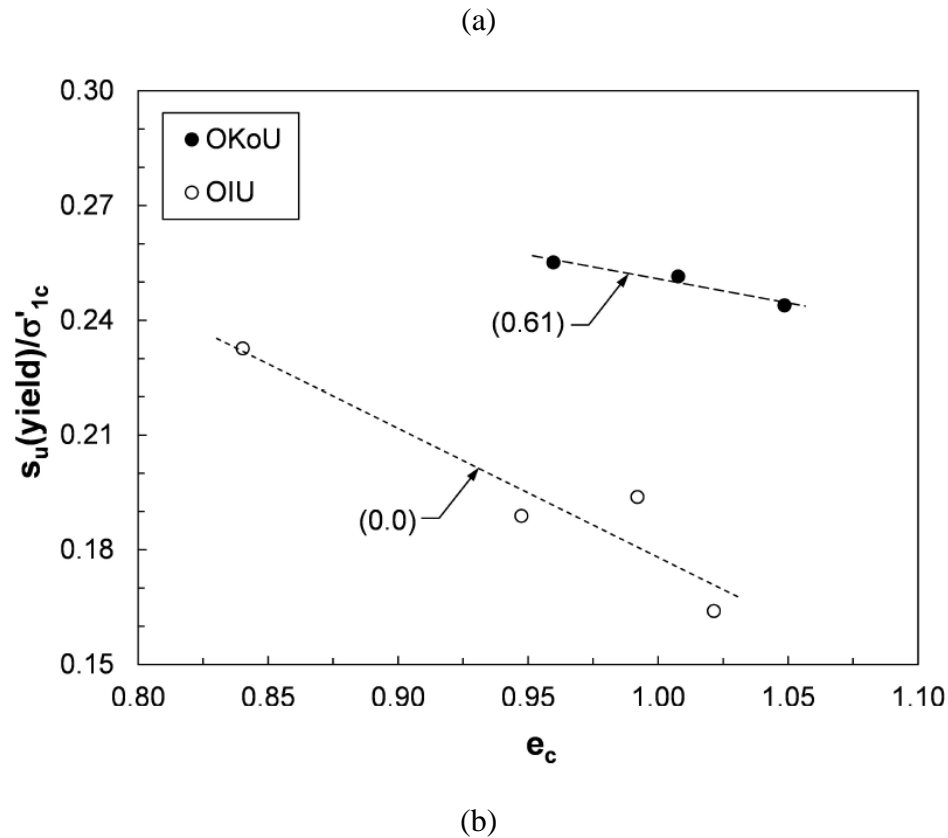


Figure 3-12: Variations of (a) $s_u(\text{yield})$ with σ'_{1c} , and (b) $s_u(\text{yield})/\sigma'_{1c}$ with e_c for both $K_c = 1$ and $K_c > 1$ specimens of O tailings. Numbers in parentheses indicate η_c

3.4.3 Instability in CDS tests

Figure 3-13 demonstrates the stress paths of several CDS test (QCDS1, 6, 9) on the Q tailings specimens. These specimens were first consolidated isotropically and then sheared drained (i.e., anisotropic consolidation) to a certain stress ratio (η_c). Each specimen was subsequently sheared by reducing the effective confining pressure via increasing pore water pressure at a prescribed rate (du_c/dt) of 0.5 kPa/min while maintaining a nearly constant deviator stress by carefully adjusting the axial force applied by the loading frame. Despite the constant q_c up to the instability point, the deviator stress slightly reduced after instability because of the uncontrollable specimen deformation, changes of specimen's cross-sectional area, as well as the limited speed of

the electromechanical jack to keep up with a rapidly collapsing specimen. Similar deviator stress reductions are also observed in CDS tests carried out by other investigators (Anderson and Sitar 1995; Chu et al. 2012; Daouadji et al. 2010; Dong et al. 2016; Gajo et al. 2000; Monkul et al. 2011; Sasitharan et al. 1993; Skopek et al. 1994; Chu and Wanatowski 2008). Although a critical state does not develop in a CDS test, because of the continuously reducing effective stress and void ratio, the post-failure effective stress paths follow the phase transformation or the critical state line established from the undrained shearing tests (IU, K_0U , AU tests).

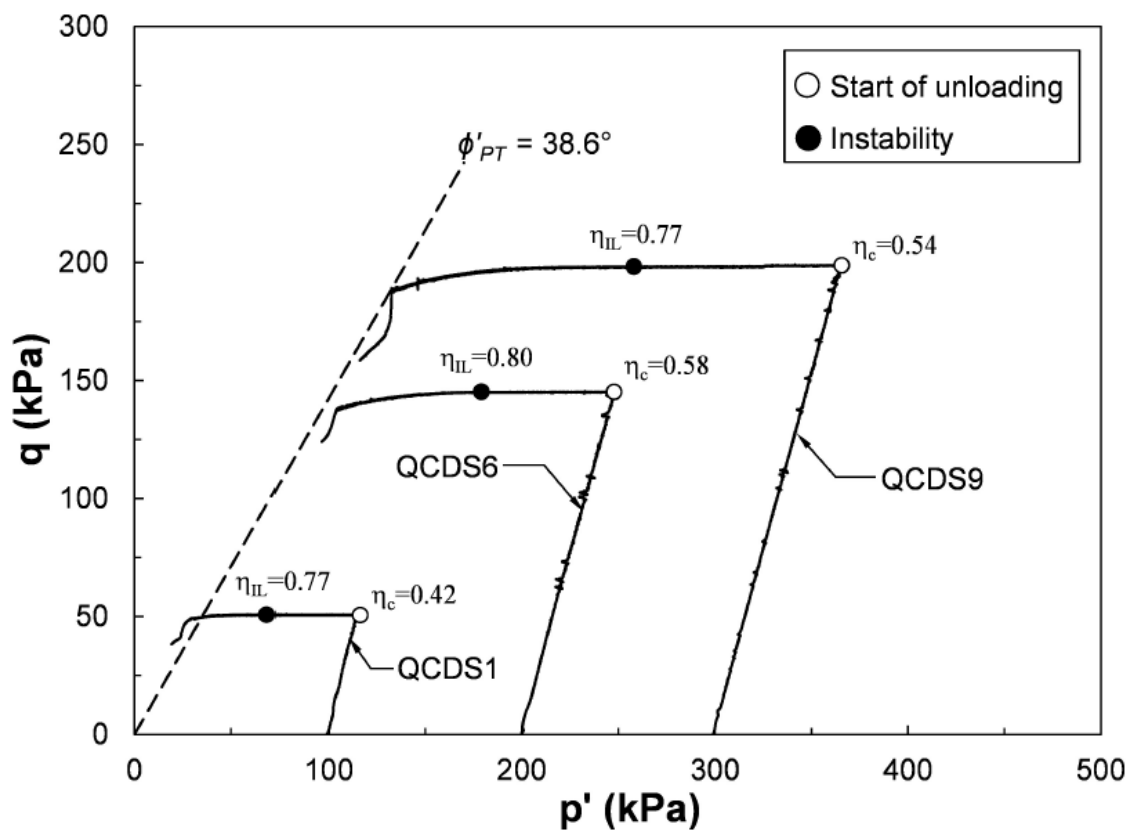


Figure 3-13: CDS stress paths on Q tailings

In contrast to the undrained tests, identifying the occurrence of instability and η_{IL} from a CDS test is not straightforward as no $s_u(\text{yield})$ is developed in a CDS test. In such stress paths, instability is manifested as a runaway-type deformation as described by Chu et al. (2003). Figure 3-14 illustrates that prior to instability axial strain (ϵ_a), which represent

shear strain in triaxial testing, develops slowly in CDS tests QCDS1, QCDS6, and QCDS9. With the reduction of effective confining pressure, the rate of ε_a progressively accelerates and sharply rises as the specimen becomes unstable. However, finding the precise instance of instability based on ε_a is subjective and could occur at any time during the rise of ε_a in Figure 3-14.

Drucker (1957) incorporated the second-order derivative of work per unit volume to formulate a general instability postulate for solid materials. According to this theory, a material is stable if the second differential of plastic work ($\partial^2 W$), i.e., the scalar product of stress ($\partial\sigma$) and plastic strain ($\partial\varepsilon^p$) increments, remains positive as described mathematically below:

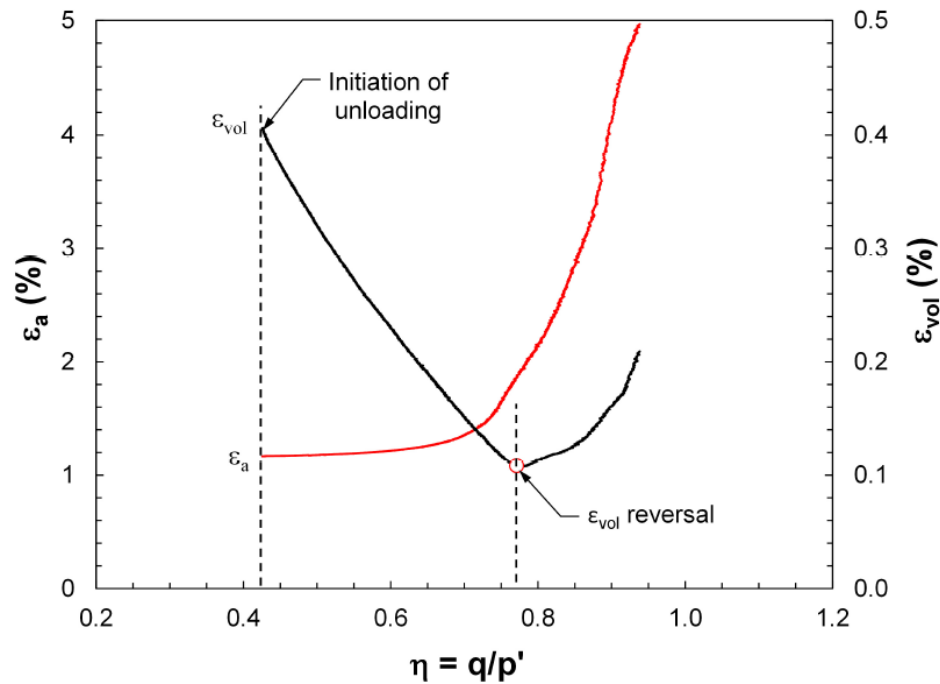
$$\partial^2 W = \partial\sigma \times \partial\varepsilon^p \geq 0 \quad [3-1]$$

By including both elastic and plastic strain increments, Hill (1958) extended the definition of stability to slightly larger strains than in Equation [3-1]. Hill's stability postulate has been used by several studies (Darve and Laouafa 2000; Gajo et al. 2000; Monkul et al. 2011; Dong et al. 2016; Rabbi et al. 2019) to identify the occurrence of instability in laboratory experiments. For a triaxial test, the second-order work increment is written as below:

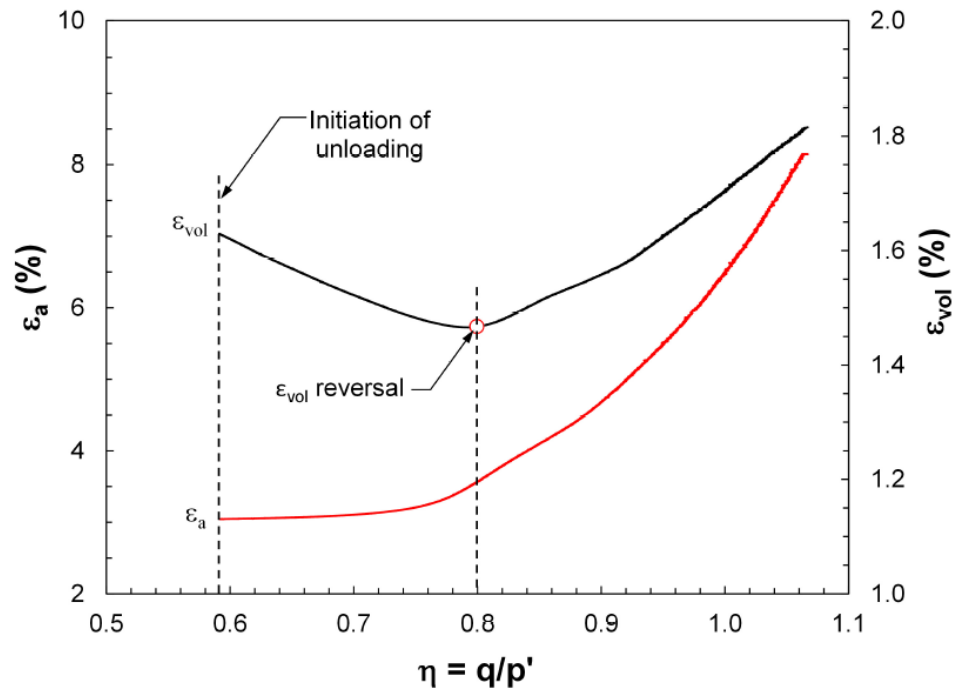
$$\partial^2 W = d\sigma'_1 d\varepsilon_1 + 2d\sigma'_3 d\varepsilon_3 = dp' d\varepsilon_{vol} + dq d\gamma \quad [3-2]$$

Where, σ'_1 and σ'_3 are the major and the minor effective principal stresses, respectively, γ is shear strain, and p' and q are the effective mean and deviator stresses, respectively. Equation [3-2] was used in this study to identify the occurrence of instability ($\partial^2 W < 0$)

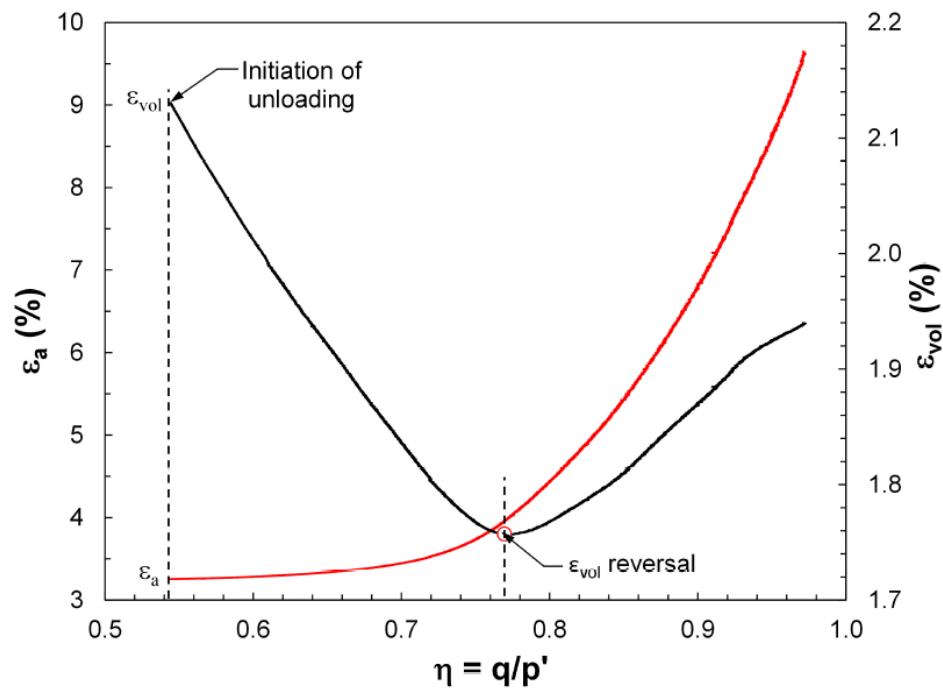
and η_{IL} . In a CDS test, during which a nearly constant deviator stress is maintained ($dq \approx 0$), the second term of Equation [3-2] cancels out. As p' decreases ($dp' < 0$) during CDS shearing, instability ($\partial^2 W < 0$) would arise when the specimen's volumetric strain (ε_{vol}) becomes contractive ($d\varepsilon_{vol} > 0$). This is demonstrated in Figure 3-14 which displays the changes of ε_{vol} and ε_a with the effective stress ratio, $\eta = q/p'$, mobilized during unloading in OCDS1, OCDS6, and OCDS9 tests. During the initial phase of unloading, the specimens expand as the effective confining pressure is reduced. However, the trend of ε_{vol} is reversed and the specimens contract as they become unstable. As shown in Figure 3-14, while the rise of ε_a rate occurs within a range of effective stress ratios ($\eta = q/p'$), the reversal point of ε_{vol} provides the precise value of η_{IL} based on the second-order work increment. This latter approach, using ε_{vol} , is employed throughout this paper to determine the occurrence of instability and η_{IL} from the CDS tests.



(a)



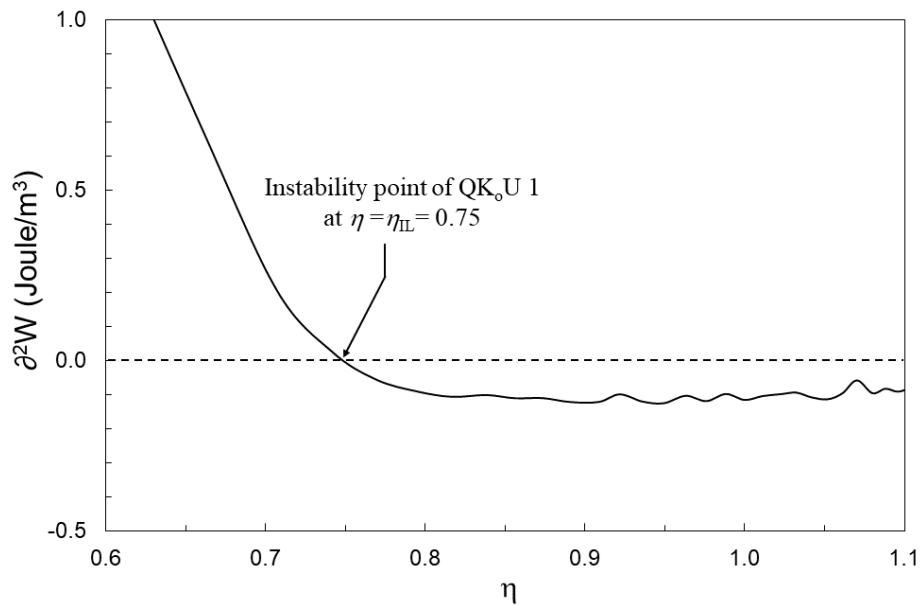
(b)



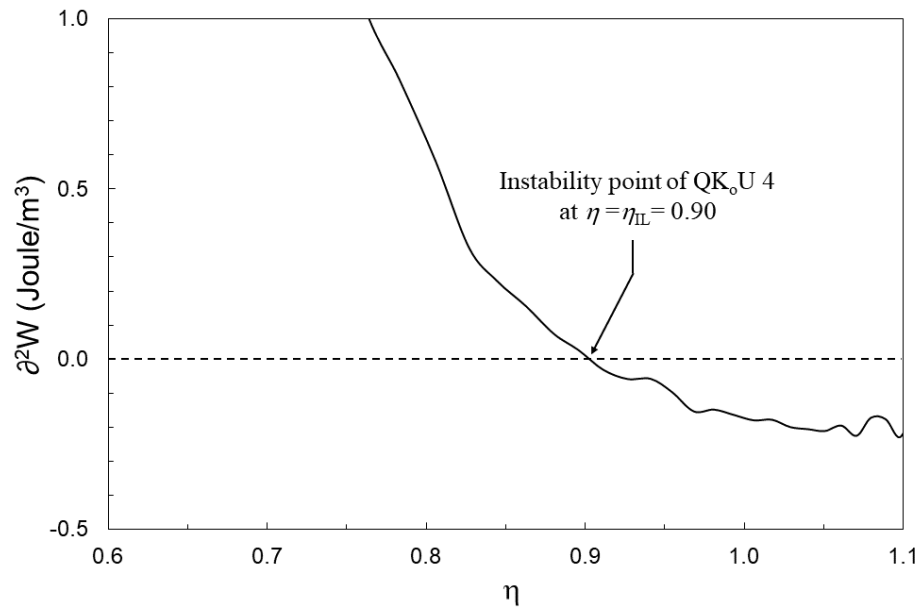
(c)

Figure 3-14: Variations of ε_a and ε_{vol} with $\eta = q/p'$ in CDS tests: (a) QCDS 1, (b) QCDS 6, and (c) QCDS 9

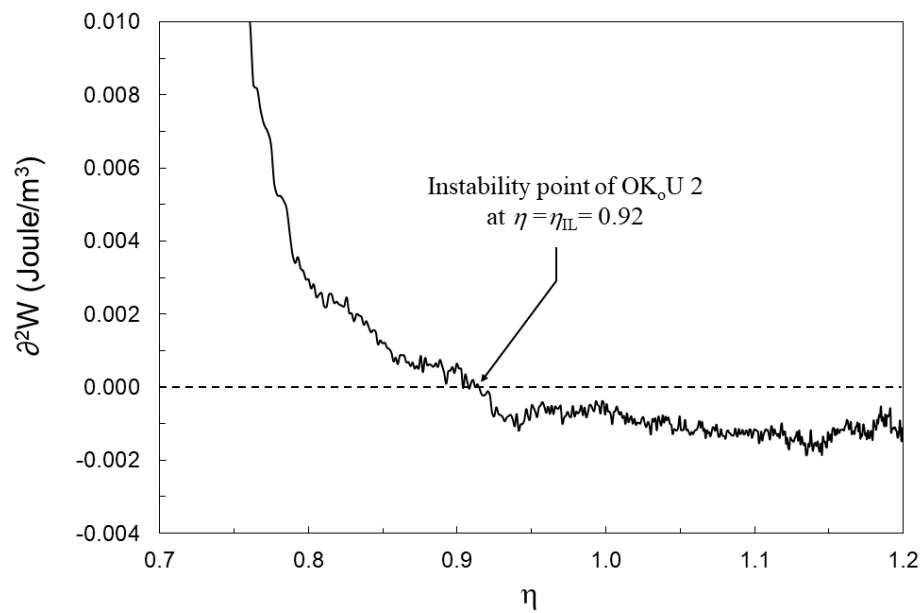
The work approach can also be applied to determine instability in undrained tests. For an undrained condition $d\varepsilon_{vol} = 0$, and hence instability would be triggered when $\partial^2 W = dqdy \leq 0$. This is demonstrated in Figure 3-15 which shows the variations of $\partial^2 W$ with η for several undrained TxC tests carried out in this study. Earlier it was demonstrated in Figure 3-5 to Figure 3-8 that in an undrained test η_{IL} can be established by connecting the peak points of stress paths to the origin. It is shown here that the η_{IL} values obtained from the peak deviator stresses of Figure 3-6 to Figure 3-8 coincide with those determined at $\partial^2 W = 0$ in Figure 3-15.



(a)



(b)



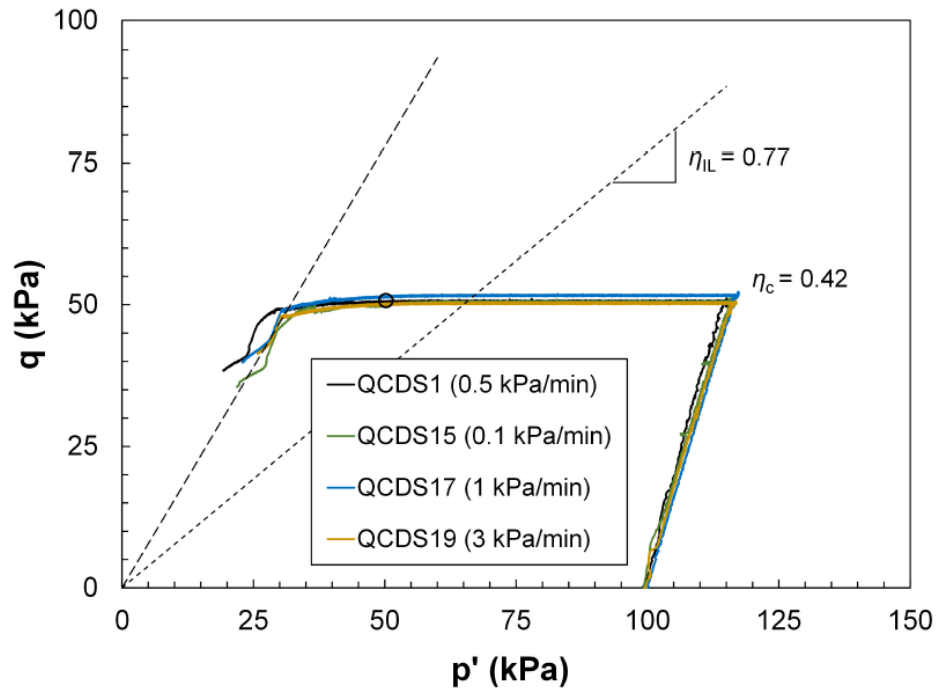
(c)

Figure 3-15: Changes of $\partial^2 W$ with η in undrained triaxial tests: (a) QK_oU1, (b) QK_oU4, and (c) OK_oU2

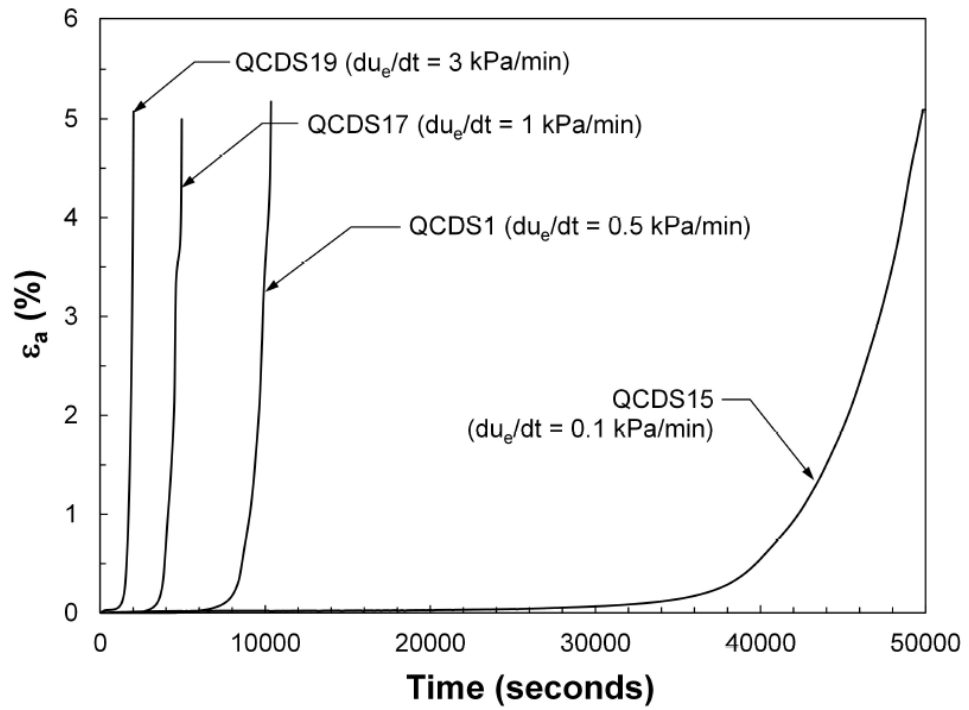
3.4.4 Effect of unloading rate

One of the parameters affecting failure under a CDS stress path is the rate at which the effective stress is reduced. Different studies have used different rates of effective stress unloading to examine the behavior of cohesionless soils under CDS stress paths. For example, Anderson and Sitar (1995) used a slow rate of 0.017 kPa/min, while higher rates of 0.1 and 1.0 kPa/min were applied by Lade and Pradel (1990) and Dong et al. (2016) in their triaxial tests. Several studies have further examined the effect of unloading rate on the drained instability of sands with some researchers observing a negligible effect of unloading rate (i.g. Chu et al. 2012) and others showing a small (Gajo et al. 2000) or a significant (Rabbi et al. 2019) impact. Chu et al. (2012) found the same instability points in drained CDS triaxial tests on Singapore sand with unloading rates of 1 to 5 kPa/min. Gajo et al. (2000) observed a small reduction of η_{IL} as the rate of effective stress reduction was increased from 0.13 to 2.5 kPa/min in drained CDS triaxial tests on Hostun sand. They attributed this decrease to the slower pore water pressure dissipation at faster unloading rates. On the other hand, a more significant reduction of η_{IL} from 0.94 to 0.68 was reported by Rabbi et al. (2019) in CDS triaxial tests on Yellow sand specimens as the unloading rate was raised from 0.2 to 5 kPa/min. Overall, no consensus has been reached regarding the effect of unloading rate on the drained instability behavior of granular materials and in particular mine tailings, warranting further investigation to address this effect.

The effect of unloading rate was examined in this study through several CDS tests on Q (tests QCDS 15 to 19) and O (tests QCDS 5 to 10) tailings carried out with $du_e/dt = 0.1, 0.2, 0.5, 1.0, 2.0$ and 3.0 kPa/min on specimens consolidated to the same $e_c, \eta_c,$ and p'_c . As demonstrated in Figure 3-16 and Figure 3-17, a higher du_e/dt merely shortens the time to instability while η_{IL} are unaffected in both tailings. This indicates that the rate of effective stress reduction has little effect on the triggering of instability, further supporting the observations made by Wanatowski and Chu (2012) and Chu et al. (2012) in plane strain compression tests.

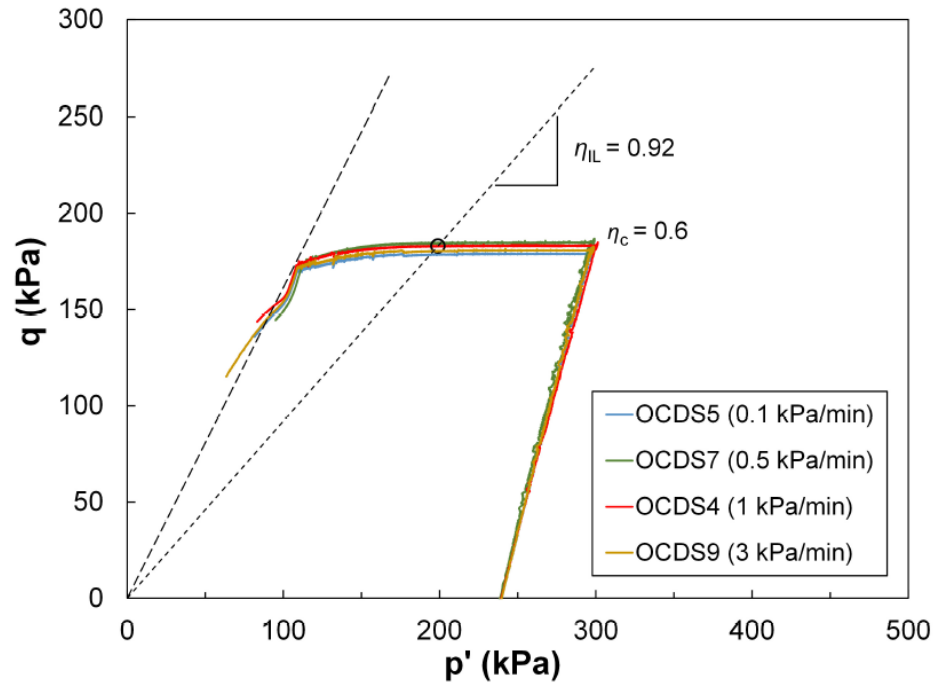


(a)

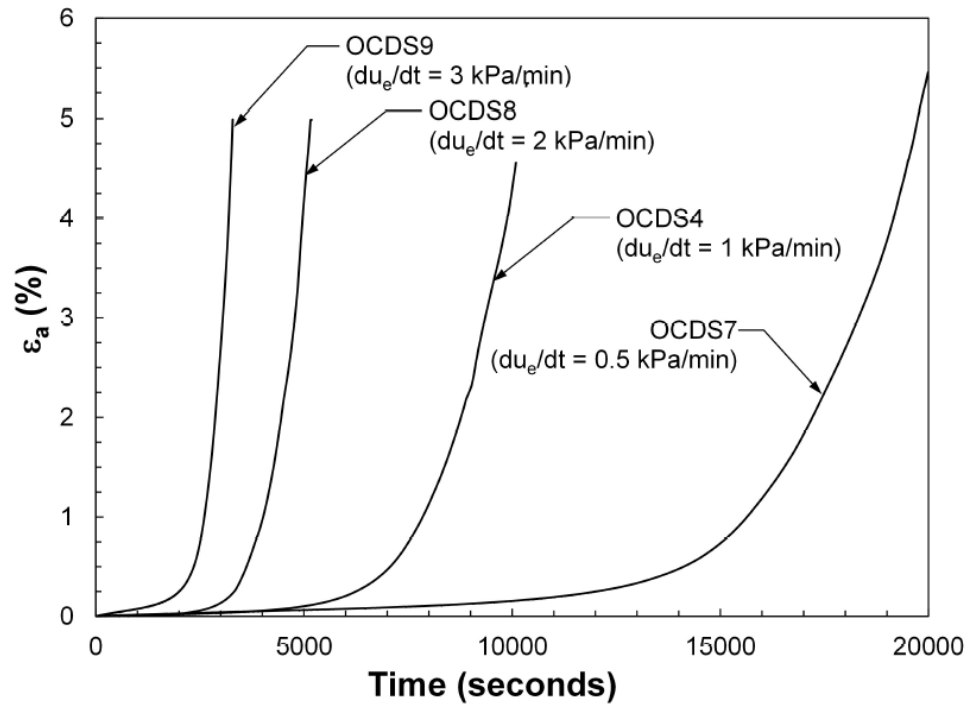


(b)

Figure 3-16: (a) stress paths and (b) axial strain rates of CDS tests on Q tailings with different du_e/dt



(a)



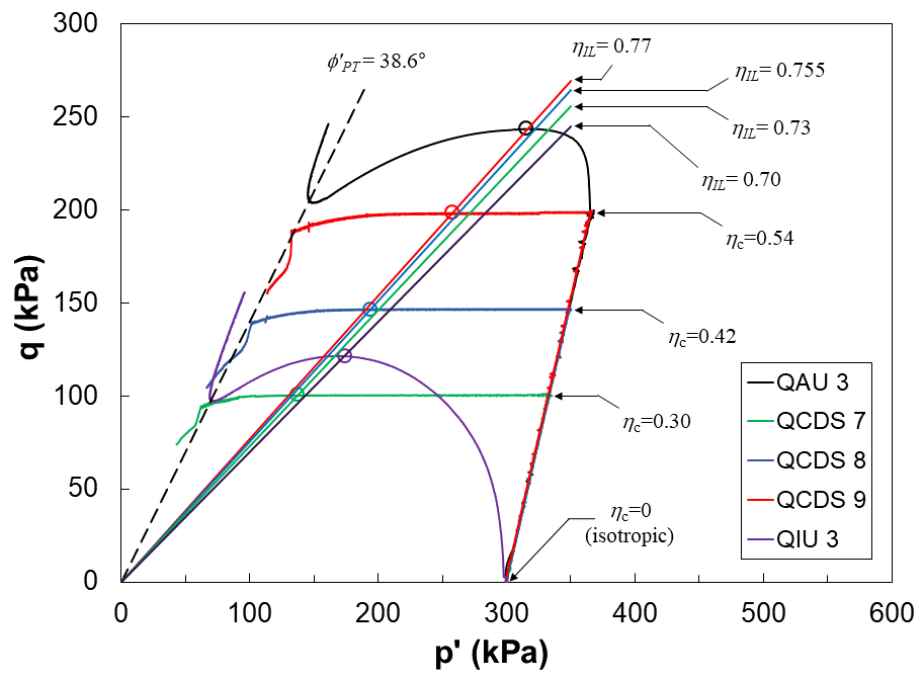
(b)

Figure 3-17: (a) stress paths and (b) axial strain rates of CDS tests on O tailings with different du_e/dt

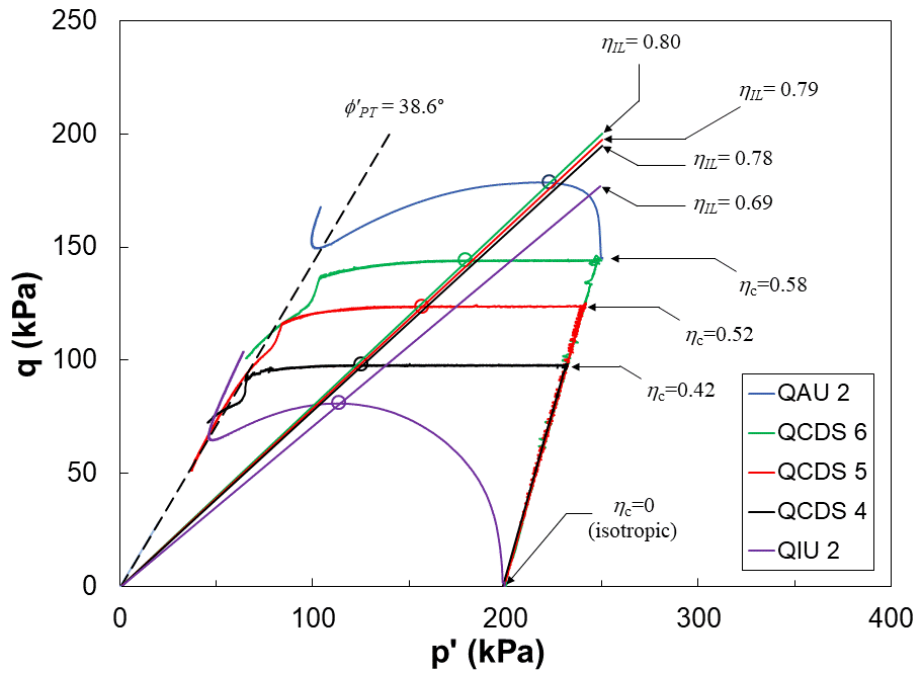
3.4.5 Comparison of instability stress ratios from CDS and undrained tests

Figure 3-18 compares the stress paths of several CDS tests with those from undrained tests on Q tailings consolidated to similar e_c . The undrained tests on each tailings were anisotropically consolidated to the same stresses (p'_c , η_c) as those of the CDS tests. Additional CDS stress paths are demonstrated for other η_c and p'_c (at the end of anisotropic consolidation) values to examine the effect of initial stresses on instability. The onset of instability is shown by a hollow circle for each stress path. These stress paths show the same η_{IL} mobilized in specimens consolidated to the same e_c , p'_c and η_c , irrespective of the stress path (CDS or undrained). Similar observations were also made by other investigators (Chu et al. 2012; Daouadji et al. 2010; Dong et al. 2016; Rabbi et al. 2019) for sandy soils. For example, Chu et al. (2012) carried out a series of TxC tests on moist tamped specimens of Changi sand dredged from the sea. They found that the stress conditions leading to instability under undrained shearing and CDS paths were essentially the same. To model the rise of pore water pressure within a slope, Daouadji et al. (2010) carried out a series of CDS triaxial tests on moist tamped specimens of Hostun S28 sand and obtained the same η_{IL} as those mobilized in undrained TxC tests at the same void ratio. Dong et al. (2016) examined the instability of loose Toyoura sand in CDS and conventional undrained loading TxC tests. The CDS experiments were carried out by lowering the confining pressure at a rate of 1.0 kPa/min while sustaining a constant deviator stress. Similar η_{IL} were measured in the undrained shearing and CDS tests, which also decreased with increasing void ratio. Finally, in comparing the stress paths of CDS and undrained shearing tests on loose Yellow sand samples, Rabbi et al. (2019) indicating that the onset of instability was nearly unaffected by the stress paths starting from the same η_c .

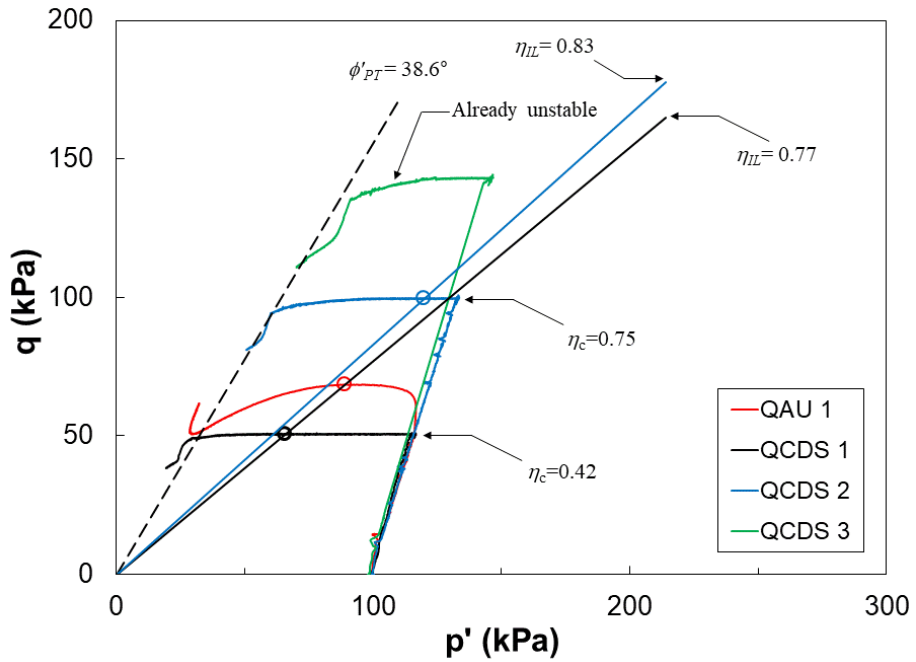
Except for specimen QCDS3 in Figure 3-18 (c), it is further demonstrated that specimens consolidated to lower η_c become unstable at slightly reduced η_{IL} values. For example, as QCDS7 and QCDS 8 were consolidated to relatively lower η_c of respectively 0.30 and 0.42 compared to QCDS9 (with $\eta_c = 0.54$), they became unstable at lower η_{IL} . Specimen QCDS3 was consolidated to $\eta_c = 0.99$ past the instability line and as demonstrated in Figure 3-18 (c) it experienced instant instability upon unloading. A further comparison is made in Figure 3-18 (a) with the isotropically-consolidated ($\eta_c = 0$) undrained test, QIU3, failing at the lowest $\eta_{IL} = 0.70$. Similar inferences can be made from Figure 3-18 (b) and (c).



(a)



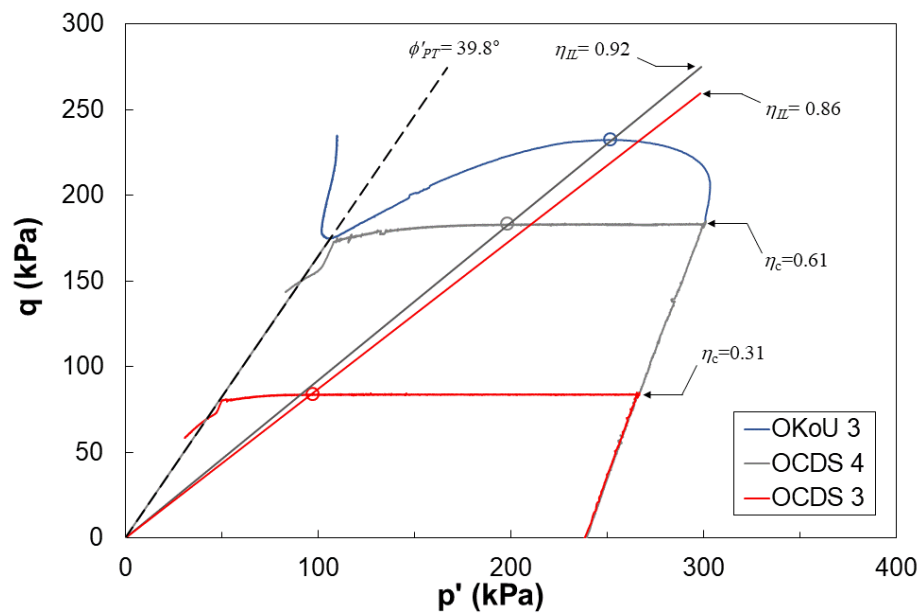
(b)



(c)

Figure 3-18: Comparison of undrained and CDS stress paths on Q tailings consolidated to different p'_c and η_c

Figure 3-19 (a) and (b) further compare stress paths of undrained and CDS tests on O tailings specimens. The anisotropically-consolidated undrained tests (OK_oU2 and OK_oU3) were consolidated under a laterally-constrained (K_o) condition, corresponding to $\eta_c = 0.61$, and compared with CDS tests (OCDS2 and OCDS4) consolidated to the same η_c . Similar to the Q tailings in Figure 3-18, not only the same η_{IL} are mobilized in undrained and CDS tests consolidated to the same p'_c and η_c , but also η_{IL} reduces with decreasing η_c in CDS tests. Although the critical state's definition is not applicable to CDS tests, for both tailings in Figure 3-18 and Figure 3-19, the CDS stress paths reach the same ϕ'_{PT} (38.6° and 39.8° in Q and O tailings, respectively) mobilized in the undrained tests irrespective of differences in p'_c and η_c . The effect of p'_c is assessed in Figure 3-19 (b) by comparing the stress paths of tests OIU1 and OCDS1, consolidated to the same $p'_c = 150$ kPa and $e_c = 1.33$. However, the difference in $\eta_c = (0 \text{ vs. } 0.34)$ led to different $\eta_{IL} = 0.89$ and 0.70 developed in OIU1 and OCDS1, respectively. The above discussion shows the strong effect of η_c on the triggering of instability and static liquefaction of tailings examined in this study.



(a)

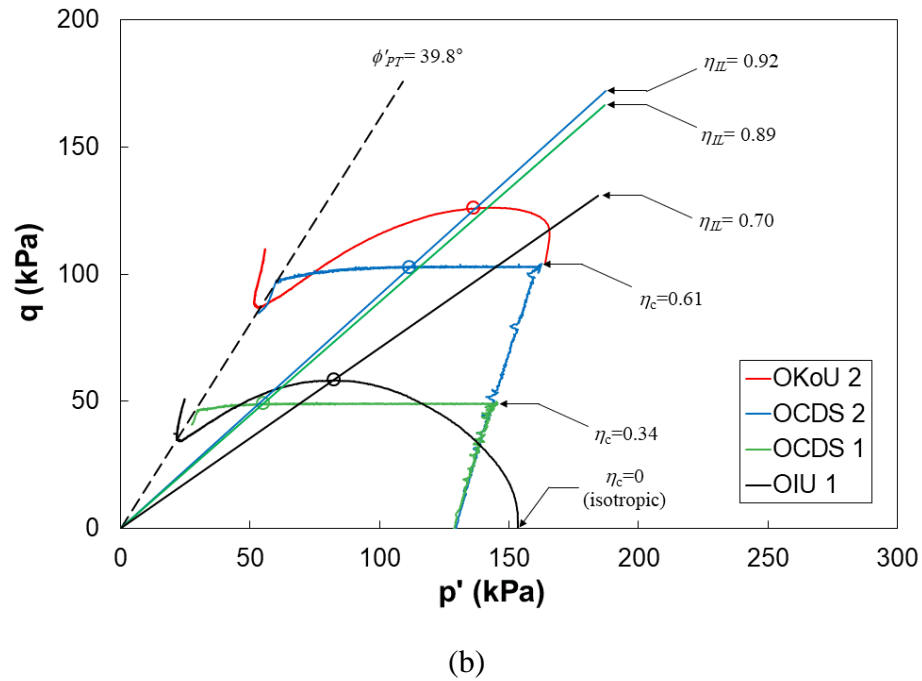


Figure 3-19: Comparison of undrained and CDS tests on O tailings consolidated to different η_c

Figure 3-20 summarizes the effect of η_c based on the CDS and the undrained tests on each tailings. According to this figure, for a given range of e_c (1.251 to 1.353 for O tailings; 1.042 to 1.075 for Q tailings), η_{IL} linearly increases with increasing η_c , with the lowest η_{IL} occurring in isotropically-consolidated triaxial tests ($\eta_c = 0$). Comparatively higher η_{IL} are also mobilized in O tailings than those in Q tailings likely because of their higher FC, denser fabric, and more angular particles (see Figure 3-3).

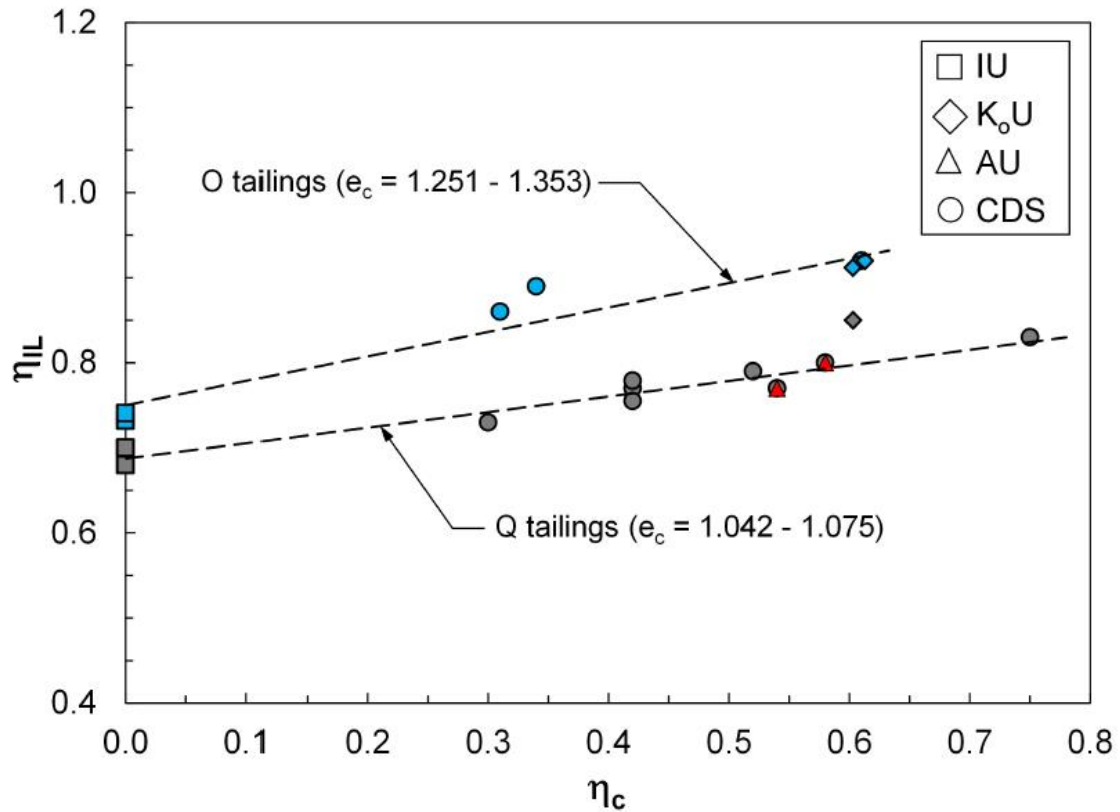
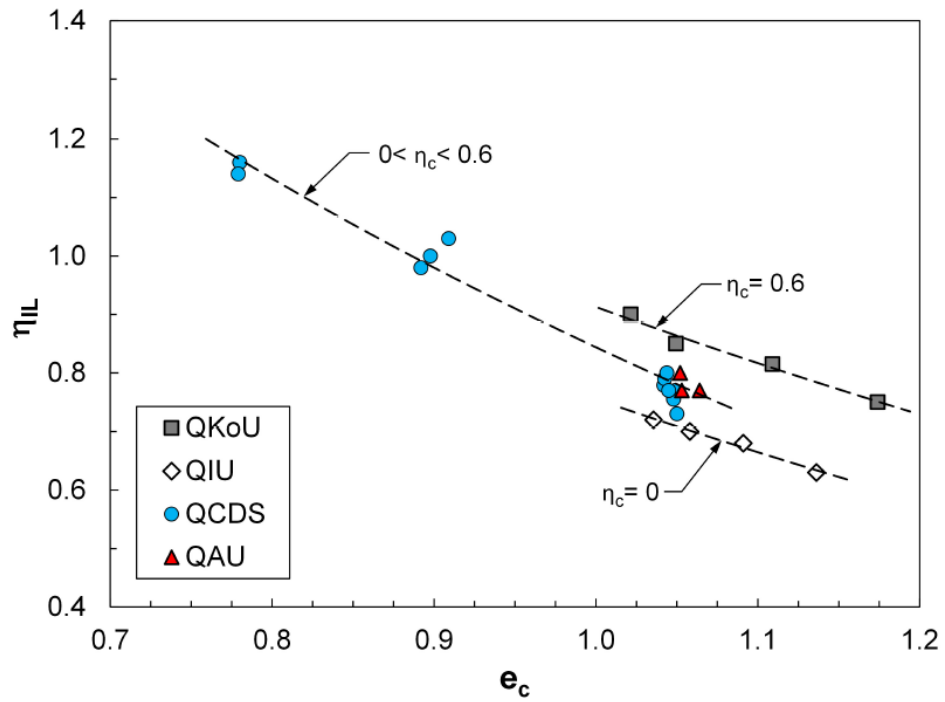


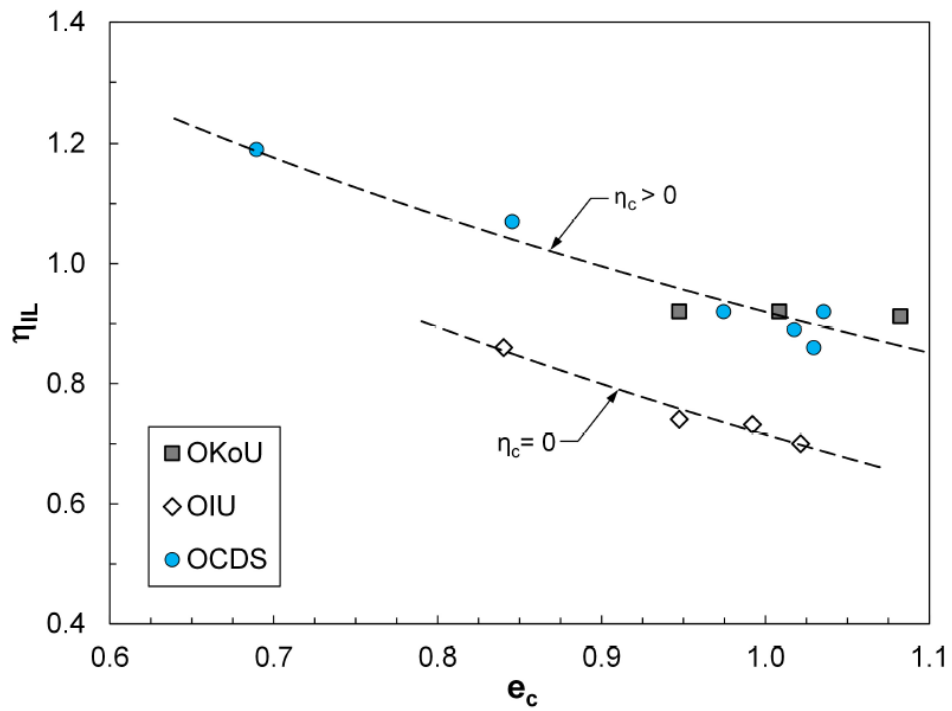
Figure 3-20: Effect of η_c on η_{IL} for both Q and O tailings

3.4.6 Effect of void ratio

The effect of e_c is examined in Figure 3-21 which shows the reductions of η_{IL} with increasing e_c for isotropically- and anisotropically-consolidated specimens of both tailings. Figure 3-21 further indicates higher η_{IL} developed in the anisotropically-consolidated undrained and CDS tests compared to those of the isotropically-consolidated samples. Note that the higher η_{IL} mobilized in K_o -consolidated undrained tests on Q tailings is because of their relatively greater $\eta_c = 0.61$ compared to the corresponding CDS tests (often with $\eta_c = 0.42$), whereas both the K_o -consolidated undrained and the CDS tests on the O tailings were consolidated to the same $\eta_c = 0.61$ and as a result show comparable η_{IL} values. These suggest that for a given η_c , the effect of e_c can be described by the same trend for different stress paths and drainage conditions (CDS vs undrained).



(a)



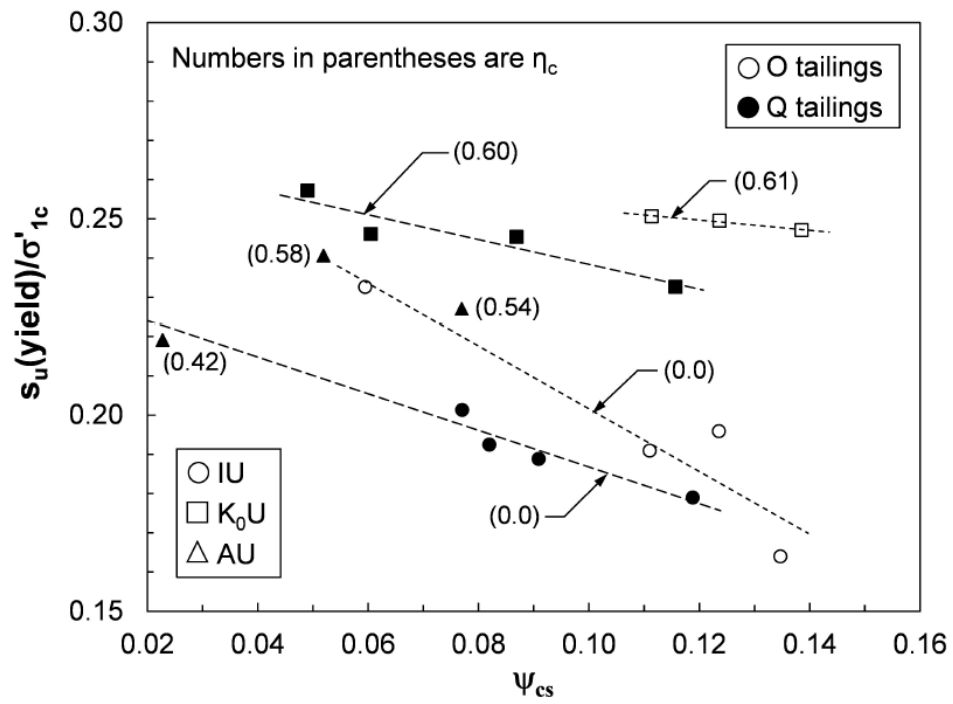
(b)

Figure 3-21: Effect of e_c on η_{IL} in (a) Q and (b) O tailings

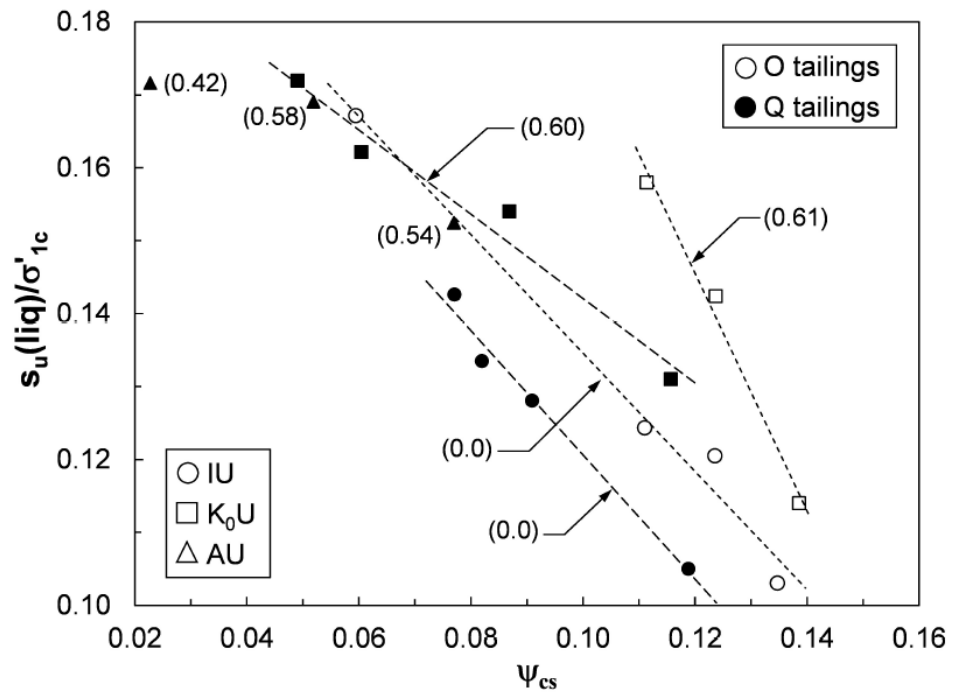
3.4.7 Correlations with the State Parameter

The preceding paragraphs demonstrated the strong effects of e_c and p'_c on the triggering of instability in undrained and CDS tests. The combined effect of e_c and p'_c on $s_u(\text{yield})/\sigma'_{1c}$ and η_{IL} is described here through the state parameter, ψ_{cs} (Been and Jefferies, 1985). Figure 3-22 illustrates linear trends of degrading $s_u(\text{yield})/\sigma'_{1c}$ and $s_u(\text{liq})/\sigma'_{1c}$ with increasing ψ_{cs} for both tailings, with those mobilized in anisotropically-consolidated specimens generally greater than $s_u(\text{yield})/\sigma'_{1c}$ and $s_u(\text{liq})/\sigma'_{1c}$ of the isotropically-consolidated specimens of either tailings. Interestingly, $s_u(\text{yield})/\sigma'_{1c}$ of the O tailings specimen, anisotropically consolidated to $\eta_c = 0.42$, plots along the trendline fitted to the isotropically-consolidated specimens. This is possibly associated with the kinematic hardening behavior and the enlargement of the yield surface of soils once η_c exceeds a certain threshold (Prisco et al. 1995; Doanh et al. 1997; Imam et al. 2002; Kato et al. 2001). In support of Figure 3-22 (a), TxC tests on Hostun RF (Gajo and Piffer 1999; Sacramento River Lee 1965) and Toyoura (Hyodo et al. 1994) sands also indicate that $s_u(\text{yield})/\sigma'_{1c}$ starts to rise only when the level of anisotropic consolidation exceeds a threshold of $\eta_c \approx 0.4$.

Despite the high sensitivity of $s_u(\text{yield})/\sigma'_{1c}$ to η_c observed in Figure 3-11 (b) and Figure 3-22 (b), nearly similar $s_u(\text{liq})/\sigma'_{1c} - \psi_{cs}$ trends are found for anisotropically-consolidated (K_oU and AU) specimens of Q tailings in Figure 3-22 (b). This indicates the trivial effect of anisotropic consolidation on $s_u(\text{liq})/\sigma'_{1c}$, likely because the anisotropic fabric was largely destroyed and remolded at large strains. While $\psi_{cs} > 0$ reflects the loose fabric and the undrained strain-softening response of the tailings specimens, higher $s_u(\text{yield})/\sigma'_{1c}$ and $s_u(\text{liq})/\sigma'_{1c}$ are generally mobilized in the O tailings specimens compared to those of the Q tailings. This is conceivably because of the higher fines content ($\approx 84\%$) and more angular particles of the O tailings.



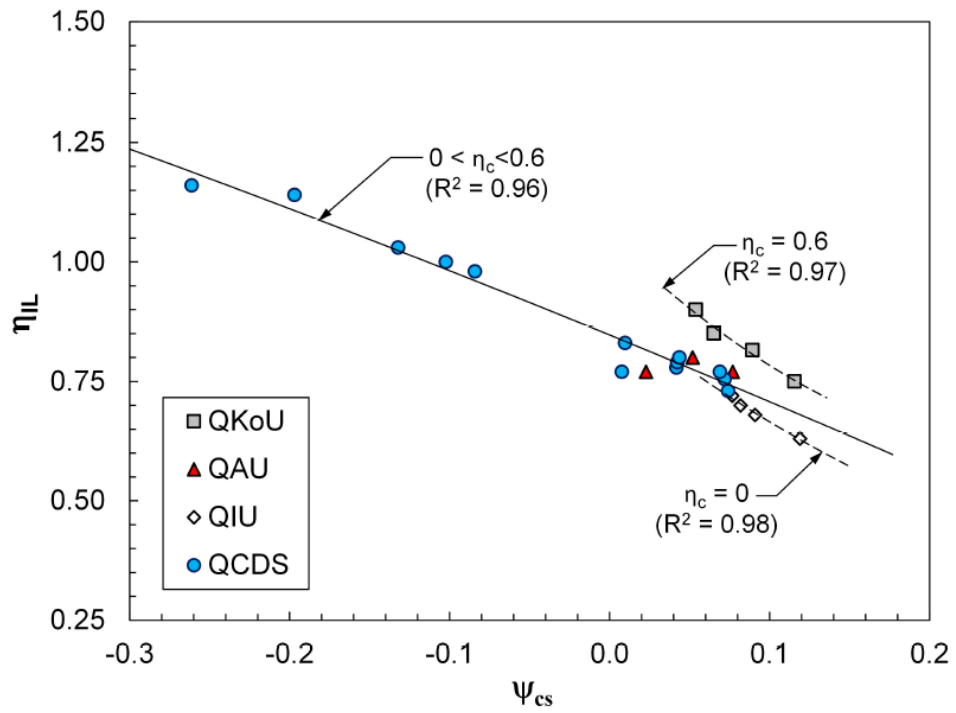
(a)



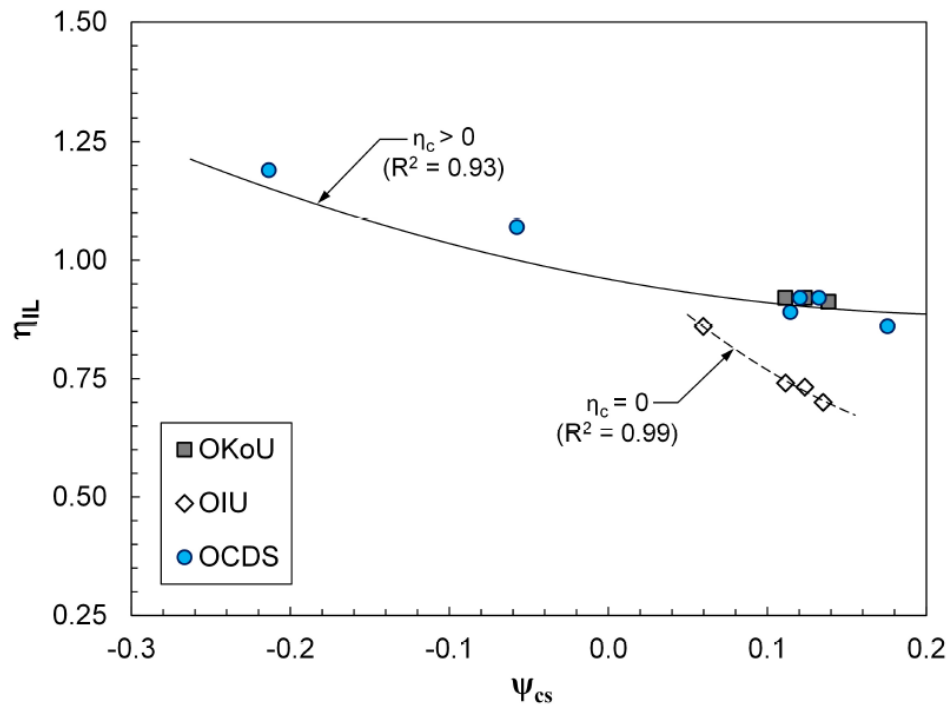
(b)

Figure 3-22: Variation of (a) $s_u(\text{yield})/\sigma'_{1c}$ and (b) $s_u(\text{liq})/\sigma'_{1c}$ with ψ_{cs} from undrained triaxial tests on Q and O tailings. Numbers in parentheses are η_c of anisotropically-consolidated (AU and K_oU) tests

Figure 3-23 finally displays the reduction of η_{IL} with ψ_{cs} based on the undrained and the CDS triaxial tests of this study. Negative ψ_{cs} values correspond to the CDS tests on medium-dense and dense specimens with e_c below the corresponding CSL. According to this figure, depending on the initial stress anisotropy and η_c , certain power functions are fitted to the η_{IL} and ψ_{cs} from CDS and undrained tests on each tailings. The high coefficients of determination, $R^2 (\geq 0.93)$, shown next to each trendline indicate the accuracy of these fits. Similar to Figure 3-23, the larger $\eta_c = 0.60$ of the K_o -consolidated Q tailings has resulted in a slightly higher $\eta_{IL} - \psi_{cs}$ trend than that of the CDS and the undrained triaxial tests consolidated to $\eta_c = 0.42$. Subsequently, the lowest η_{IL} is mobilized in isotropically-consolidated ($\eta_c = 0$) specimens of both tailings. On the other hand, because of the same $\eta_c = 0.61$, η_{IL} values of the CDS and the K_o -consolidated specimens of the O tailings are located along the same trendline. Accordingly, the instability triggering η_{IL} can be predicted through ψ_{cs} for both undrained and CDS loading paths. This suggests that η_{IL} determined from a typical undrained triaxial test can be employed to determine instability under a CDS loading path.



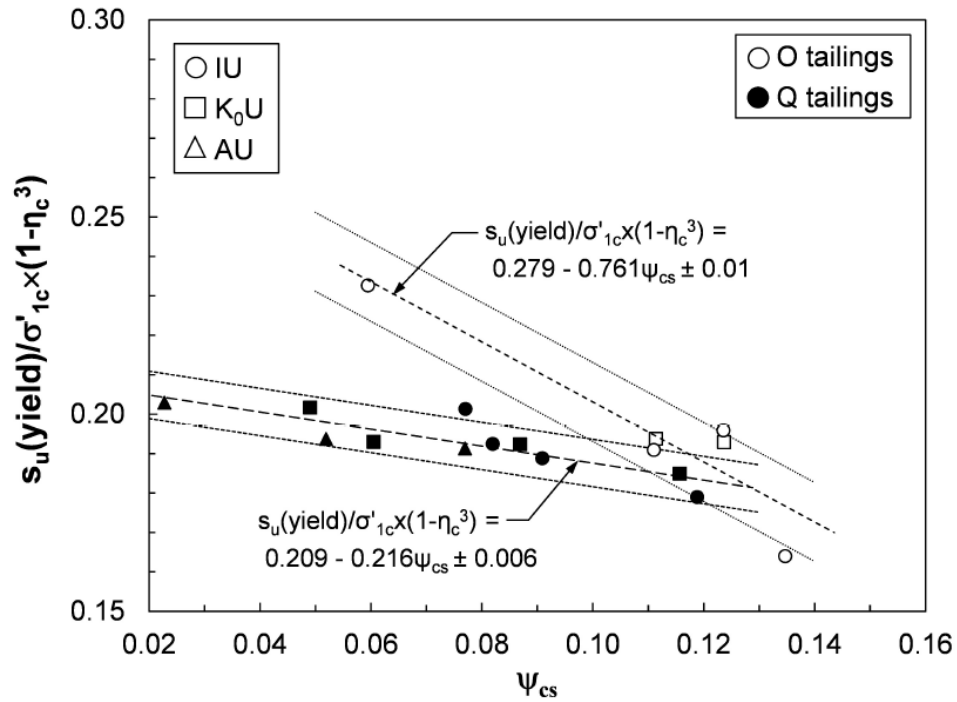
(a)



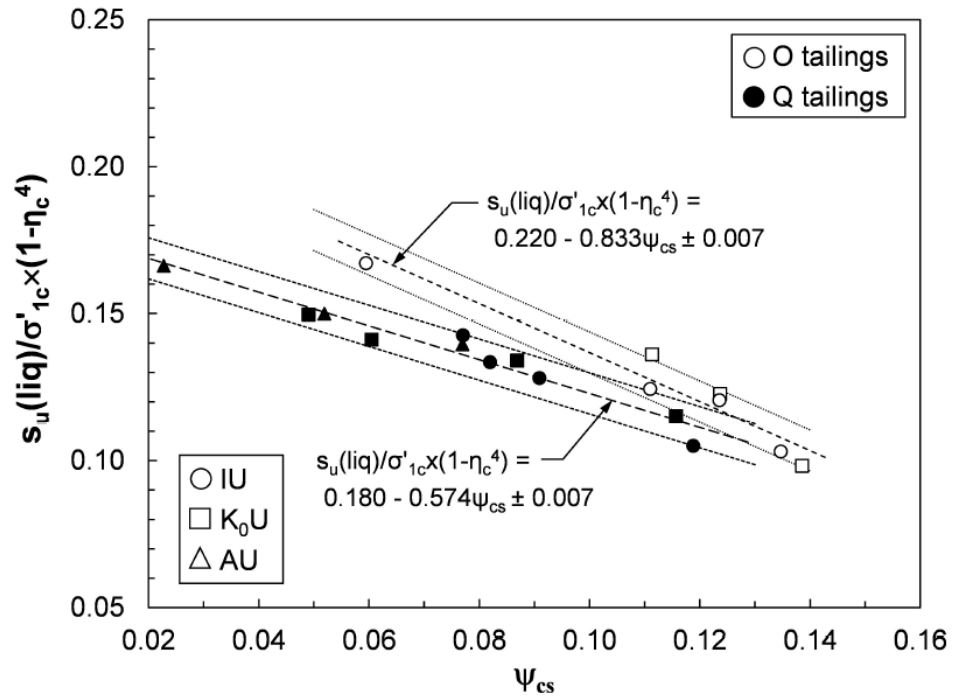
(b)

Figure 3-23: Variations of η_{IL} with ψ_{cs} from the triaxial tests of this study on (a) Q and (b) O tailings

Although ψ_{cs} amalgamates the effects of e_c and p'_c , it failed to provide a unifying relationship with $s_u(\text{yield})/\sigma'_{1c}$, $s_u(\text{liq})/\sigma'_{1c}$ and η_{IL} for different η_c as illustrated in Figure 3-22 and Figure 3-23. Three dimensional regression analyses were subsequently carried out in an effort to include the effect η_c . Modified instability and post-liquefaction shear strengths are introduced in Figure 3-24 and Figure 3-25, showing more consistent and narrower ranges with ψ_{cs} . The modified strength parameters allow distinct trendlines with ψ_{cs} to be established by incorporating η_c as illustrated in Figure 3-24 and Figure 3-25.

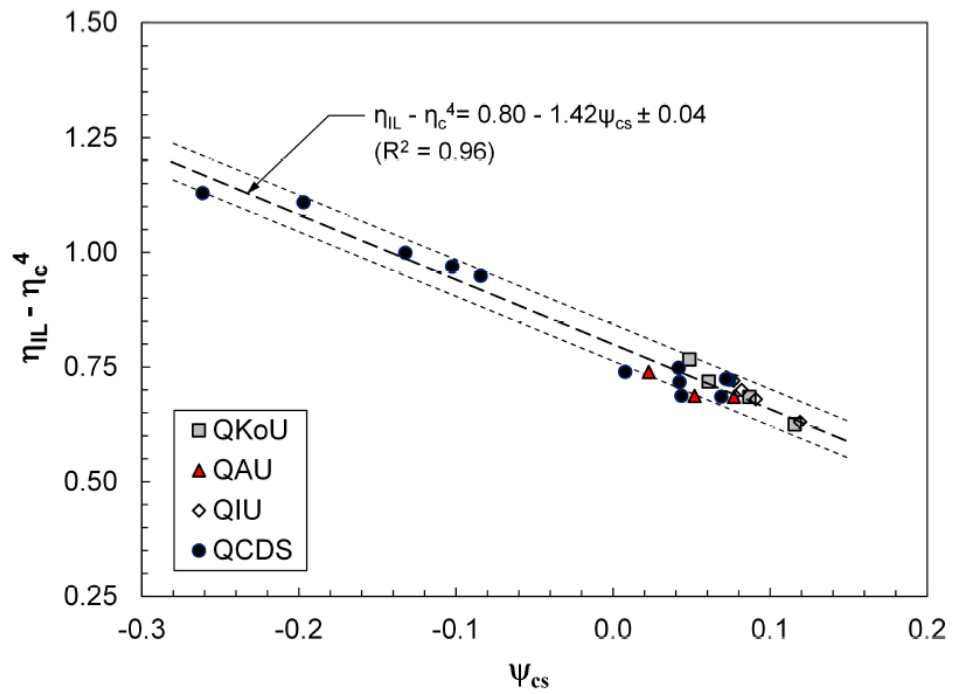


(a)



(b)

Figure 3-24: Variations of modified (a) yield and (b) post-liquefaction strength ratios with ψ_{cs}



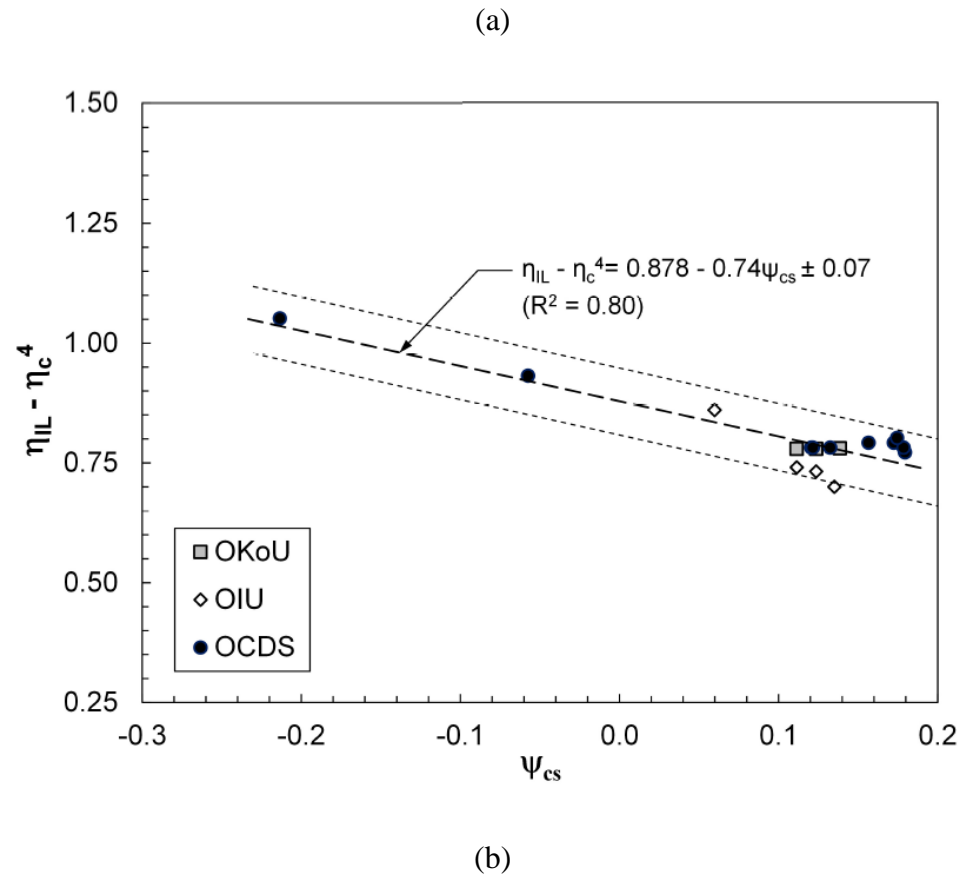


Figure 3-25: Variations of $\eta_{IL} - \eta_c^4$ with ψ_{cs} in TxC tests on (a) Q and (b) O tailings

3.4.8 Practical significance

The CDS testing results presented in this study imply that a tailings dam could fail by not only an increase in external loading (e.g., construction, dam rising, slope steepening), but also a reduction in effective confining pressure. The latter could occur long time after construction through either A) a rise in pore water pressure following for example a heavy rainfall, snowmelt, artesian condition, rise of ground water table, or B) lateral stress relief due to erosion and lateral spreading (Anderson and Sitar 1995; Brand 1981; Leroueil 2001). Figure 3-21 and Figure 3-23 indicate that this could occur at e_c and ψ_{cs} much denser than those at which strain-softening instigates in undrained loading, making such failures particularly critical and challenging for existing tailings dams. The risk of collapse rises with increasing the downstream slope angle as the higher η_c would bring

tailings initial stress state closer to the instability line as shown in Figure 3-18. The sharp rise of ε_a in Figure 3-14 further suggests that once instability is triggered, the failing mass can evolve into a rapidly moving flowslide, as demonstrated by Eckersley (1990) in instrumented model slopes of coking coal stockpiles. Several field failures have been associated to instability due to effective stress unloading at a nearly constant shear stress. For example, based on the backanalysis of the 1907 failure of the Wachusett dam, Olson et al. (2000) suggested that the failure was likely triggered by a monotonic loss of effective stress during the filling of its reservoir as the dam construction had ended for more than three years. More recently, the Fundao (Morgenstern et al. 2016) and the Brumadinho (Robertson et al. 2020) tailings dams experienced massive flow failures in 2015 and 2019, respectively. Both failures occurred long time after construction and the cessation of tailings deposition. As described by their forensic investigation panels, the flow failures were set off by a reduction in effective confining pressure through lateral extrusion of fine tailings beneath the Fundao dam (Morgenstern et al. 2016) and a water level rise in the Brumadinho dam following an intense rainfall (Robertson et al. 2020). The stress path associated with such failures can be simulated in a CDS triaxial test in which the effective confining pressure is reduced at a constant deviator stress. The similar η_{IL} from undrained shearing and CDS tests obtained in Figure 3-21 further suggests that the mechanisms of pre-failure strain-softening and instability are the same. Provided that tailings are consolidated to the same η_c , η_{IL} obtained from an undrained shear test can be used to predict the onset of instability in a CDS path. Several studies (Gennaro et al. 2004; Lo et al. 2008; Vaid and Sivathayalan 2000; Yamamuro and Covert 2001) have observed that the triggering of instability occurs at nearly identical η_{IL} under cyclic and monotonic undrained shearing. Accordingly, η_{IL} of tailings established from the monotonic TxC tests of this study can be potentially used to detect the occurrence of cyclic liquefaction as well.

3.5 Conclusions

The drained instability of coarse and fine gold mine tailings under lateral stress relief and undrained loading paths were examined in this paper through a comprehensive series of

triaxial compression tests. As summarized below, the results address the four objectives of this study as summarized below:

- Instability was observed in tailings specimens subjected to effective stress unloading at a constant deviator stress (CDS) as a rapid increase in shear strain. The triggering of instability was subsequently determined based on the sign of the second-order work increment which provided the same results as that found from the volumetric strain reversal. The rise of axial strain occurred within a range of deviator stress ratios and failed to provide a distinct stress ratio at the triggering of instability. The effective stress paths of these specimens ultimately reached the failure line of the undrained tests. In undrained loading, instability occurred as a reduction in shear resistance following the exceedance of a peak yield strength.
- Irrespective of the stress path and drainage condition, similar deviator stress ratios were mobilized at the triggering of instability in specimens consolidated to the same initial stress anisotropy.
- Among the different parameters examined in this study, density (void ratio) and anisotropic consolidation were found to have the strongest impacts on the onset of instability and static liquefaction with the triggering strength increasing with increasing density and initial deviator stress ratio. This resulted in the anisotropically-consolidated specimens exhibiting greater liquefaction triggering shear strengths compared to the isotropically-consolidated samples. Note that this does not mean that a steeper tailings dam would be more resistant to static liquefaction as the shear stress increment (from the initial to the instability condition) required to triggering instability reduced in anisotropically-consolidated specimens. Furthermore, because of their more angular particle shapes, higher fines content, and denser fabric, greater liquefaction-triggering and post-liquefaction shear strengths were mobilized in the fine tailings than those of the coarse tailings.
- Other than inducing instability within a shorter time period, raising the unloading rate from 0.1 to 3.0 kPa/min had little effect on the CDS stress paths as well as the mobilized

stress ratio at the triggering of instability. For each tailings, trendlines were established between undrained triggering and post-liquefaction shear strength ratios as well as the deviator stress ratio at the triggering of instability with consolidation void ratio (e_c) and the state parameter (ψ_{cs}). Finally, irrespective of the drainage condition and consolidation history, specific critical state lines were determined for each tailings studied here, with that of the fine tailings being denser (at lower void ratios) and steeper than the critical state line of the coarse tailings.

3.6 Acknowledgments

Financial support provided by the Ontario Center of Innovation and Golder Associates are highly appreciated.

Chapter 4

4 Effect of Non-Plastic Fines on the Instability Behavior of a Gold Mine Tailings

4.1 Abstract

The Mine tailings are characterized by a wide range of grain sizes and often with high fines contents (FC). Non-plastic fines in mine tailings fill-in the pore spaces among the coarse particles, and despite increasing tailings density, may or may not contribute to the load bearing capacity and mechanical strength of tailings. The effect of non-plastic fines on the instability behavior of gold mine tailings is examined in this paper. Tailings specimens with FC = 5, 25, 50 and 84% were consolidated isotropically or anisotropically, and subjected to monotonically increasing shearing loads under an undrained condition. The lowest undrained shear strength as well as mobilized friction angles at the triggering of instability, was observed at FC = 25%. The initial deviator stress ratio following anisotropic consolidation was also found to promote liquefaction behavior and strain softening of the tailings specimens during undrained shearing. The principal stress ratio, K_o , at the end of laterally confined anisotropic consolidation, was found to increase from FC of 5% to 25, and then decrease with any more increment in FC. The critical state lines of tailings specimens not only became steeper but also shifted to lower void ratios with increasing FC from 5% to 25%. At higher FC (> 25%), however, these lines reversed course and translated to higher void ratios, suggesting a change of tailings fabric from a sand- to a fines-controlled structure. To examine tailings behavior and instability induced under a drained lateral stress reduction path, a series of triaxial experiments were also carried out by applying an initial deviator stress and then reducing the effective mean pressure while sustaining the initial deviator stress. The CDS tests revealed the same trend of how mobilized instability friction angles change with FC as undrained tests. Effective friction angles at the triggering of instability correspond to the points of volumetric strain reversal from volumetric dilation to contraction.

4.2 Introduction

Static liquefaction failure and instability of mine tailings has emerged as a critical risk to tailings dams around the world. In particular, the upstream method of depositing tailings as a slurry in dammed impoundments rises a significant risk in terms of static liquefaction and flow failure due to the high degree of saturation and loose deposition of tailings. The static liquefaction failure of the Merriespruit gold tailings dam in South Africa in 1994 (Fourie and Papageorgiou 2001) showed tailings can undergo a catastrophic strain-softening behavior and liquefy. Subsequently, several researchers have focused on studying the physical and engineering properties of tailings including their shearing behavior and liquefaction potential (Al-Tarhouni et al. 2011; Chang et al. 2011; Fourie and Papageorgiou 2001; Fourie and Tshabalala 2005; Qiu and Seg0 2001; Schnaid et al. 2013). Gold tailings generally have little cohesive strength and plasticity which is conducive to their strain-softening and liquefaction behavior.

Because of the mineral extraction process, tailings (even from the same mine site) can have a wide range of grain sizes and fines contents (FC), making it difficult to generalize the shearing behavior of tailings. During upstream construction of a mine tailings dam, coarse tailings are typically used to construct a starter dyke and several downstream berms, and then the fine tailings (i.e., FC > 50%) are stored behind them. Variations in the amount of fine particles (< 0.075 mm in diameter) and their plasticity can have a significant impact on the undrained shearing behavior and liquefaction potential of mine tailings. Numerous researchers have studied the effect of fines on instability and static liquefaction behavior of soils including mine tailings. Most of these studies (Amini and Qi 2000; Baziar and Dobry 1995; Fourie and Papageorgiou 2001; Lade and Yamamuro 1997; Ni et al. 2004; Thevanayagam 1998; Thevanayagam et al. 1997; Wang and Sassa 2000; Yang et al. 2006; Zlatović and Ishihara 1995) have reported that the addition of non-plastic fine particles would destabilize a silty sand, resulting in a reduced resistance against liquefaction. For example, Zlatović and Ishihara (1995) examined the effect of non-plastic silt on the monotonic shearing behavior of Toyoura sand ($D_{50} = 0.17$ mm) and found increased contractiveness and excess pore pressure generation as well as reduced

peak and post-liquefaction resistances with the addition of fine particles. Yamamuro and Lade (1998) carried out monotonic undrained triaxial tests on dry deposited specimens of Nevada sand mixed with non-plastic silt particles. Opposite the higher liquefaction susceptibility of clean sands at larger initial confining pressures (p'_c), Yamamuro and Lade (1998) reported a “reverse” behavior of enhanced contractiveness and reduced liquefaction resistance with decreasing p'_c until complete liquefaction to zero effective stress occurred in silty sand specimens consolidation to $p'_c = 25$ kPa. This was associated to the unstable structure and the resulting compaction of silty sands with increasing p'_c which suppressed their undrained strain softening and liquefaction potential at higher p'_c .

Monkul et al. (2017) carried out an extensive series of undrained monotonic triaxial compression tests on three sands with varying amounts of different non-plastic silts and reported a higher static liquefaction potential and reduced liquefaction resistance with increasing FC of up to 25%, irrespective of the sand and silt type or the basis of comparison, being either the loosest possible density, same relative density, or similar void ratios. On the other hand, some other studies (Kuerbis et al. 1988; Ni et al. 2004; Pitman et al. 1994) have found increased liquefaction resistance with increasing FC. For example, in monotonic triaxial tests on slurry-deposited specimens of Brenda mine tailings Kuerbis et al. (1988) observed increased dilative behavior in compression and less contractive behavior in extension loading with the addition of up to 20% Kamloops silt.

As summarized above, FC can have a significant effect on the monotonic shearing behavior and shear strength of cohesionless soils. Nevertheless, studies on the role of FC on the behavior of mine tailings, specimens subjected to anisotropic consolidation, effective stress unloading path, or the liquefaction triggering strength have been limited. This paper presents an extensive laboratory investigation on the instability of gold mine tailings for a wide range of FC and subjected to both undrained and effective stress unloading stress paths. The results are used to analysis the static liquefaction potential, as well as the liquefaction triggering and post-liquefaction strengths of tailings within the framework of critical state soil mechanics.

4.3 Experimentation

4.3.1 Tested tailings

Gold mine tailings collected from a mine site in northern Ontario were used in this study. Figure 4-1 shows the average gradation of in-situ tailings, indicating an average FC = 84% by weight. The fine particles were found to be non-plastic silt.

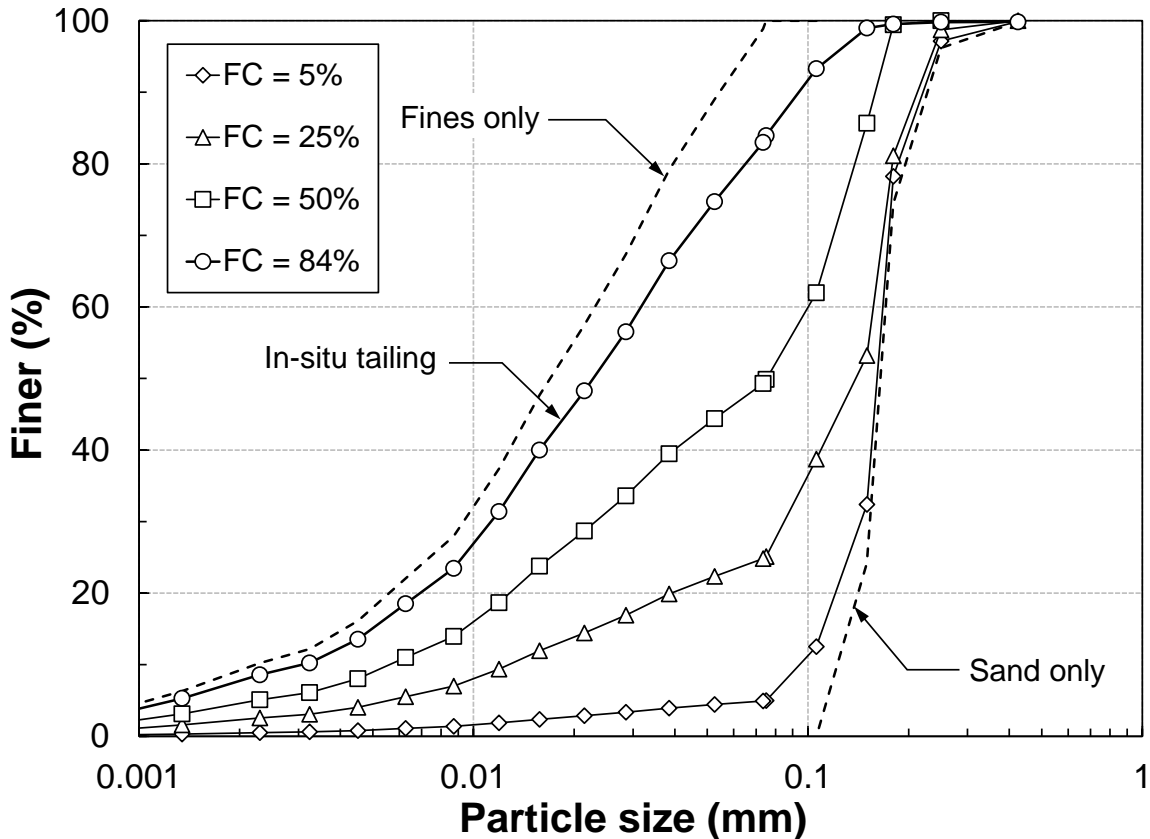


Figure 4-1: Particle size distributions the gold tailings used in this study

Samples with different FC were subsequently reproduced by first separating the sand and the non-plastic fine particles of the as-received tailings and then remixing them with FC = 5%, 25%, and 50% as shown in Figure 4-1. Specific gravity (G_s) as well as the maximum void ratios (e_{max}) of tailings were measured following ASTM D854 (ASTM, 2006a) and ASTM D4254 (ASTM, 2006b) standard procedures. $G_s = 2.66$ and 2.73 were found for the sand and the fine particles, respectively. Minimum void ratios (e_{min}) were however determined using the standard proctor test (ASTM, 2021) and the vibrating

table (ASTM, 2012) methods for $FC > 15\%$ and $FC = 5\%$, respectively following the recommended FC in each procedure. Figure 4-2 presents the variations of e_{min} and e_{max} with FC. With increasing FC, both e_{max} and e_{min} decrease as the voids are progressively occupied with the fine particles until all void spaces are filled (Lade et al. 1998) and the index void ratios reach their minimum values at a threshold $FC = 25$ to 32% . At $FC < 25\%$, the silt particles primarily occupy the pore spaces among the coarser sand particles and result in reduced e_{min} and e_{max} (Lade, et al., 1998). However, with added silt beyond $FC > 25\%$, the fines start to occupy particle contacts, separating the coarse sand particles and increasing void ratios. Tailings fabric subsequently transforms from a sand- to a silt-dominated structure. Similar trends are also reported by several other studies (Papadopoulou and Tika 2008; Park and Santamarina 2017; Torres-Cruz and Santamarina 2020; Zlatović and Ishihara 1995) for sand-silt mixtures.

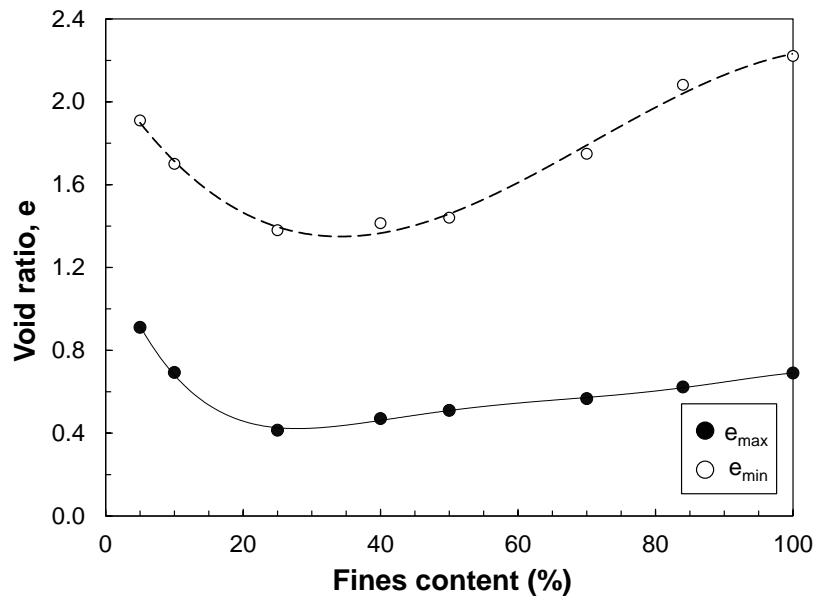


Figure 4-2: Effect of FC on e_{max} and e_{min} of tailings

4.3.2 X-Ray diffraction analysis

Fine-grain tailings minerals and their crystalline structure were further examined using X-ray diffraction (XRD) analysis. Certain minerals with distinct and unique interatomic planes can absorb X-rays of different wavelengths. This makes it possible to filter the emissions of an X-ray tube using Bragg's law and determine their composition (Mitchell

and Soga 2005). According to Figure 4-3, XRD traces of the tailings indicated the presence of Quartz, Illite, and Albite minerals.

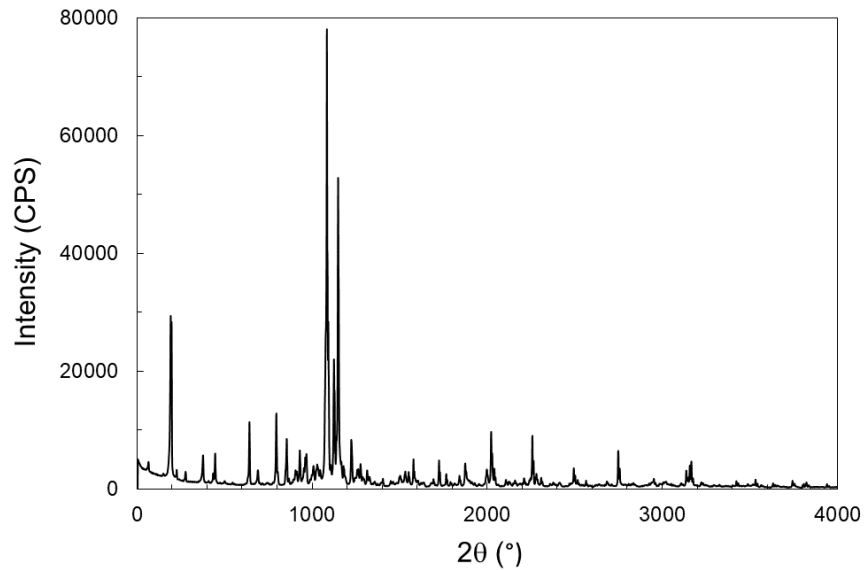
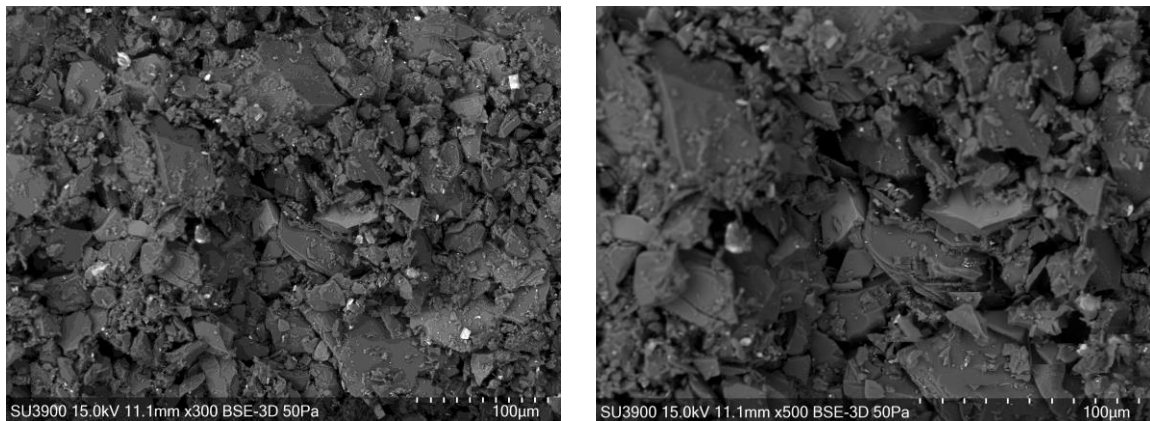


Figure 4-3: XRD analysis of the gold mine tailings tested in this study

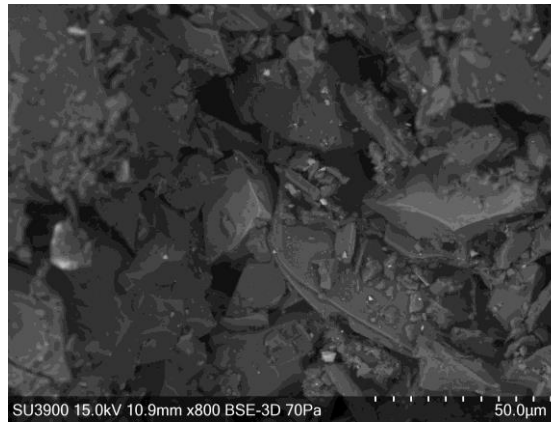
4.3.3 SEM images

Scanning electron microscopic (SEM) images were also taken to determine the shapes of the tailings' particles at their natural fines content (FC = 84%). As illustrated in Figure 4-4, the received tailings are composed of highly-angular to sub-angular coarse grains with relatively smooth surface textures. The fine particles are generally platy.



(a)

(b)



(c)

Figure 4-4: SEM images of tailings particles at magnifications of: (a) 300x; (b) 500x; (c) 800x

4.3.4 Sample preparation

Because of difficulties with undisturbed sampling of mine tailings, their shearing behavior and strength are generally studied based on laboratory-reconstituted specimens. Tailings specimens at different FC were prepared by the undercompaction moist-tamping technique proposed by Ladd (1978). This method allows the preparation of relatively uniform specimens of loose silty sands which would liquefy and undergo strain-softening in undrained monotonic shearing (Ishihara 1993; Thevanayagam et al. 2002; Vaid et al. 1999), whereas specimens prepared by other techniques (e.g., air or water pluviation) could segregate during preparation (Kuerbis and Vaid 1988) or fail to undergo strain-softening and liquefaction in undrained shearing (Høeg et al. 2000; Vaid et al. 1999; Vaid and Thomas 1995).

Specimens were prepared in a latex-lined split mold with equal height and diameter of 70 mm to improve strain uniformity within the specimen at large strains. Lubricated and enlarged end caps were used to minimize the effect of end restraint and induce a uniform specimen deformation during shearing. For moist tamping, tailings were thoroughly

mixed with about 5% moisture (by dry mass of tailings) and tamped in four layers. Four specimens were also prepared by pluviating dry tailings with FC = 5, 25, 50, and 84% through a funnel into the specimen mold to assess the significance of specimen preparation method and fabric. The spout of the funnel was kept very close to the tailings surface to drop particles with a nearly zero height and create the loosest specimens possible with dry pluviation. The funnel was gently raised in a circular motion as tailings particles were poured into the specimen mold. The top cap was then placed on the specimen, and the membrane was folded over the top cap and secured by two O-rings. A small vacuum pressure of 10 kPa was subsequently applied to stabilize the specimen as the split mold was removed and the triaxial cell was filled with silicon oil to protect the internal load cell against electrical shortcuts. The vacuum pressure was gradually replaced by an equal seating pressure after filling the cell.

4.3.5 Testing apparatus

A computer-controlled triaxial testing apparatus manufactured by GeoTac Trautwein (USA) was employed to carry out the triaxial experiments of this study. This apparatus consists of a distributed data acquisition and control system, a uniaxial loading frame, and two electromechanical pressure pumps, allowing a closed-loop control of specimen volume change, deformation, fluid pressures, and axial load. Pressures and volume of fluid in the triaxial cell and in the specimen were controlled by two electromechanical pressure pumps with volumetric capacities of 170 and 75 mL. High-resolution pressure transducers with a capacity of 2,068 kPa were used to measure the fluid pressures in the triaxial cell and the specimen. Axial displacement was applied by an electromechanical force actuator, while the axial deformation of the specimen was measured by an external linear variable differential transformer (LVDT) with an accuracy of 0.002 mm. The axial force (i.e., deviator stress) applied on the specimen was recorded by a 2200 N capacity submerged internal load cell placed over the specimen's top cap.

4.3.6 Saturation and Consolidation

Specimens were saturated by flushing CO₂ gas and deaired water through them, followed by a backpressure saturation process until a B value of at least 0.97 was established. After

saturation, the specimens were consolidated either isotropically or anisotropically in multiple loading stages. Isotropic consolidation was carried out in this study by increasing the cell pressure, while maintaining a constant backpressure. Anisotropic K_0 consolidation was induced by imposing a laterally-confined condition with zero radial strain ($\epsilon_r = 0$) by maintaining equal volumetric ($\epsilon_{vol} = \epsilon_a + 2\epsilon_r$) and axial (ϵ_a) strains during consolidation. Consolidation loads were kept for about 2 hours to complete primary consolidation.

4.3.7 Shearing

After the completion of primary consolidation, the specimens were sheared in a strain-controlled mode at an axial strain rate of 5%/hr up to $\epsilon_a = 30\%$. Undrained and drained shearing were conducted by closing and opening the drainage valves, respectively and monitoring the specimens shear-induced pore water pressure or volume change using the pressure pump. The shearing rate was selected in accordance to ASTM D4767 and D7181 standard procedures to ensure pore pressure equalization in undrained tests or complete dissipation in drained shearing throughout the specimen at failure. Besides the undrained and drained triaxial compression tests, several specimens were subjected to a constant deviator stress unloading (CDSU) stress path. In these tests, the specimens were consolidated anisotropically to $p'_c = (\sigma'_{1c} + 2\sigma'_{3c})/3$, and an initial deviator stress of $q_c = \sigma'_{1c} - \sigma'_{3c}$, corresponding to a deviator stress ratio of $\eta_c = q_c/p'_c$. They were subsequently sheared through a reduction in the effective confining pressure by rising the backpressure applied to the specimen at a rate of $du_e/dt = 1$ kPa/min while maintaining the initial q_c . Several CDSU tests were also conducted by increasing the backpressure at $du_e/dt = 0.5$ and 3 kPa/min to assess the effect of unloading rate on the instability of gold tailings.

Final void ratios were determined by freezing the specimens after each test and measuring their weight and water content. This further allowed the calculation of each specimen's volume change during the flushing and backpressure saturation stages and thus a more accurate determination of the consolidation void ratio (e_c). Because of the small sizes of tailings particles, correction for membrane penetration was negligible while the effect of membrane rigidity was accounted for through a procedure described by

Fukushima and Tatsuoka (1984). Table 4-1 and Table 4-2 summarize the triaxial tests carried out in this study under different stress paths.

Table 4-1: Summary of triaxial compression tests on tailings mixtures with different FC

No.	Test ID*	FC (%)	P'_c (kPa)	e_{cs}	K_o	D_{rc} (%)	ψ_{cs}
1	FC5-IU150		150	1.183	1	72	0.0754
2	FC5-IU200		200	1.169	1	74	0.0572
3	FC5-IU300		300	1.110	1	80	0.0316
4	FC5-KoU85	5	85	1.210	0.56	70	0.0781
5	FC5-KoU170		172	1.160	0.55	75	0.0359
6	FC5-KoU310		310	1.073	0.55	84	0.0005
7	FC5-ID200		300	1.090	1	76	-
8	FC5-ID300		200	1.040	1	80	-
9	FC25-IU150		150	0.662	1	74	0.1198
10	FC25-IU200		200	0.632	1	77	0.1100
11	FC25-IU300		300	0.601	1	81	0.0963
12	FC25-IU500	25	500	0.561	1	85	0.0791
13	FC25-KoU75		75	0.638	0.62	77	0.0644
14	FC25-KoU160		163	0.580	0.61	83	0.0460
15	FC25-KoU290		291	0.540	0.61	87	0.0323
16	FC25-ID200		200	0.510	1	81	-
17	FC25-ID300		300	0.460	1	85	-
18	FC50-IU200		200	0.860	1	69	0.1368
19	FC50-IU300		300	0.830	1	72	0.1204
20	FC50-IU301		500	0.757	1	80	0.0997
21	FC50-KoU80	50	80	0.920	0.60	63	0.1174
22	FC50-KoU170		168	0.820	0.59	74	0.0932
23	FC50-KoU300		302	0.781	0.59	78	0.0740
24	FC50-ID200		200	0.669	1	77	-
25	FC84-IU155		160	1.021	1	73	0.1179
26	FC84-IU200		200	0.992	1	75	0.1125
27	FC84-IU300	84	300	0.947	1	78	0.1027
28	FC84-IU600		600	0.840	1	85	0.0860
29	FC84-KoU78		78	1.049	0.57	71	0.1352

30	FC84-KoU163	163	1.008	0.55	73	0.1174
31	FC84-KoU300	300	0.960	0.55	77	0.1027
32	FC84-ID150	150	0.828	1	73	-
33	FC84-ID300	300	0.793	1	76	-
34	FC84-ID400	400	0.716	1	78	-

* I and Ko in test ID indicate isotropic and anisotropic (Ko) consolidations, respectively;
U and D in tests ID indicate undrained and drained shearing, respectively

Table 4-2: Summary of the CDS tests carried out in this study

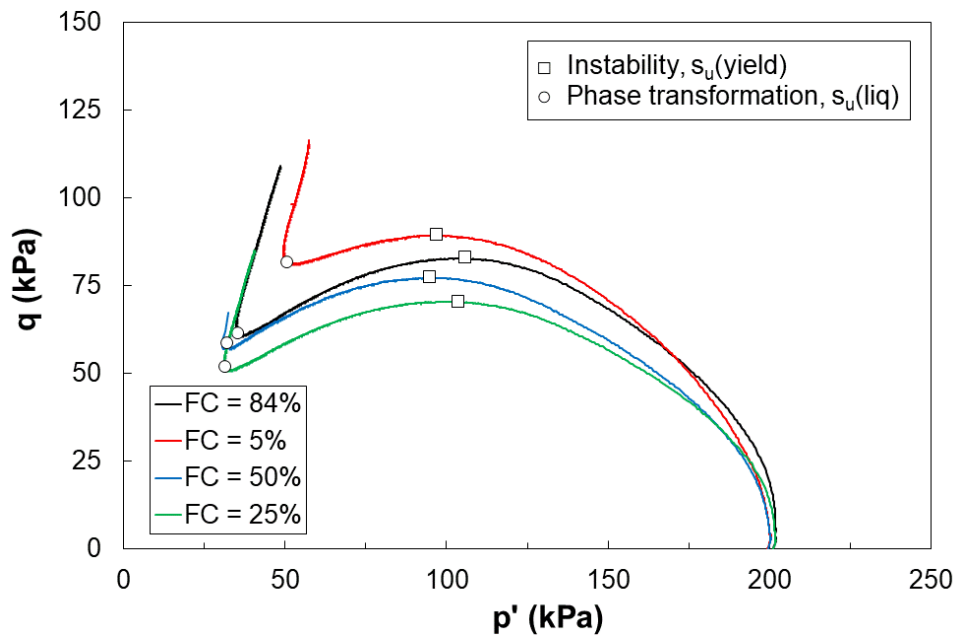
No.	Test ID	FC (%)	du_e/dt (kPa/min)	p'_c (kPa)	q_c (kPa)	η_c	e_c	η_{IL}	D_{rc} (%)	ψ_{cs}
1	CDS 5-1	5	1	174	108	0.62	1.163	0.96	75	0.0556
2	CDS 25-1	25		156	83	0.53	0.584	0.74	82	0.0517
3	CDS 50-1	50		167	92	0.55	0.815	0.89	74	0.0688
4	CDS 84-1	84		169	103	0.61	0.988	0.92	75	0.1033
5	CDS 5-2	5	1	173	107	0.62	0.980	1.05	93	-0.1275
6	CDS 25-2	25		157	83	0.53	0.472	0.85	94	-0.0603
7	CDS 50-2	50		165	91	0.55	0.662	1.07	91	-0.0842
8	CDS 84-2	84		170	104	0.61	0.720	1.12	93	-0.1647
9	CDS 84-3	84	0.5	169	103	0.61	0.970	0.92	76	0.0853
11	CDS 84-4	84	3	169	103	0.61	0.977	0.92	76	0.0923
12	CDS 5-3	5	3	174	108	0.62	1.159	0.95	75	0.2743

4.4 Results and discussion

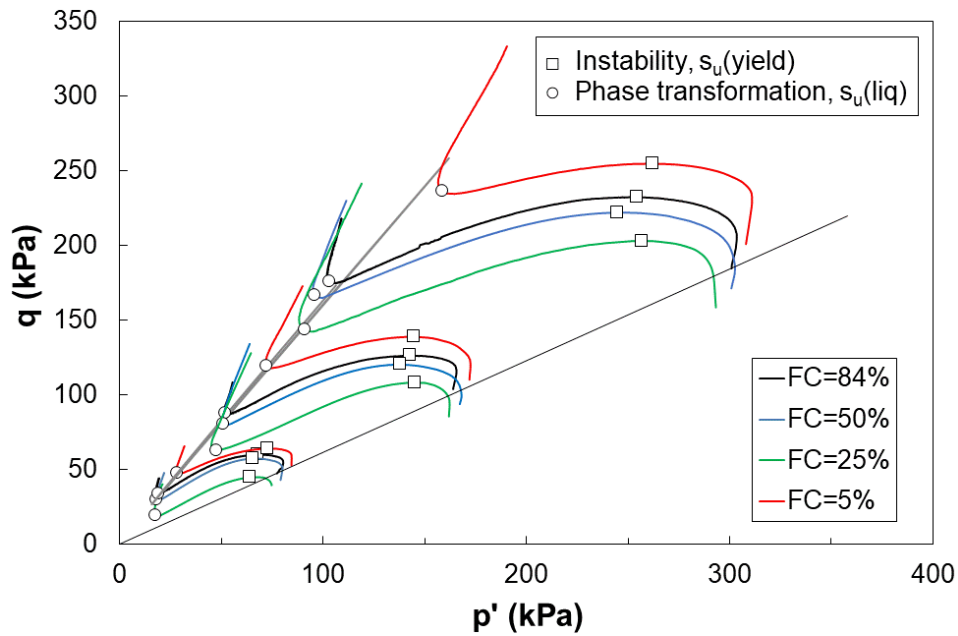
4.4.1 Undrained stress paths

To investigate the effect of fines, three different mixtures were prepared in addition to the as-received tailings (FC = 84%). Figure 6 presents the stress paths of specimens consolidated isotropically ($K_c = 1$) and anisotropically ($K_c = K_o$) to different levels of p'_c . Isotropically-consolidated undrained and drained shear tests are labeled with IU and ID, while K_oU indicates an undrained test on a K_o -consolidated specimen. All specimens exhibited undrained instability and strain-softening following a peak undrained strength at $s_u(\text{yield})$. However, they subsequently underwent strain-hardening following limited

liquefaction behavior (Alarcon-Guzman et al. 1988) and a minimum undrained post-liquefaction shear strength, $s_u(\text{liq})$. The strain-softening behavior is however enhanced with increasing p'_c from 150 to 300 kPa. Friction angles of $\phi'_{PT} = 37.2^\circ$ to 39.8° were also mobilized at the phase transformation (Ishihara et al. 1975) points in these specimens. As indicated in Figure 4-5, irrespective of p'_c and K_c , increasing FC from 5% to 25% first promoted strain softening, and resulted in reduced values of $s_u(\text{yield})$ and $s_u(\text{liq})$. These strength parameters were, however, increased with additional fines in FC = 50 & 84% specimens, but didn't reach those of the clean (FC = 5%) tailings. The initial reduction and the subsequent rises of $s_u(\text{yield})$ and $s_u(\text{liq})$ with FC in fact follow the trends of e_{max} and e_{min} with FC shown in Figure 4-2.



(a)



(b)

Figure 4-5: Stress paths of (a) isotropically and (b) anisotropically consolidated tailings specimens

Figure 4-6 further shows stress paths of the four dry pluviated specimens which were isotropically consolidated to relative densities ($D_{rc} = 70 - 78\%$) values very close to those of their moist-tamped counterparts ($D_{rc} = 70 - 77\%$) for each FC. Despite the comparable D_{rc} values, none of these specimens experienced strain-softening and instability similar to the moist-tamped specimens of Figure 6. This demonstrates the significance of specimen preparation method and tailings fabric in inducing instability and static liquefaction. Accordingly, many studies (Bobei et al. 2009; Chien et al. 2002; Daouadji et al. 2010; Fourie and Tshabalala 2005; Khoa et al. 2006; Matiotti et al. 1995; Pitman et al. 1994; Reid et al. 2018; Riveros and Sadrekarimi 2020), including this study, have used moist-tamped specimens for investigating static liquefaction and instability behavior of cohesionless soils.

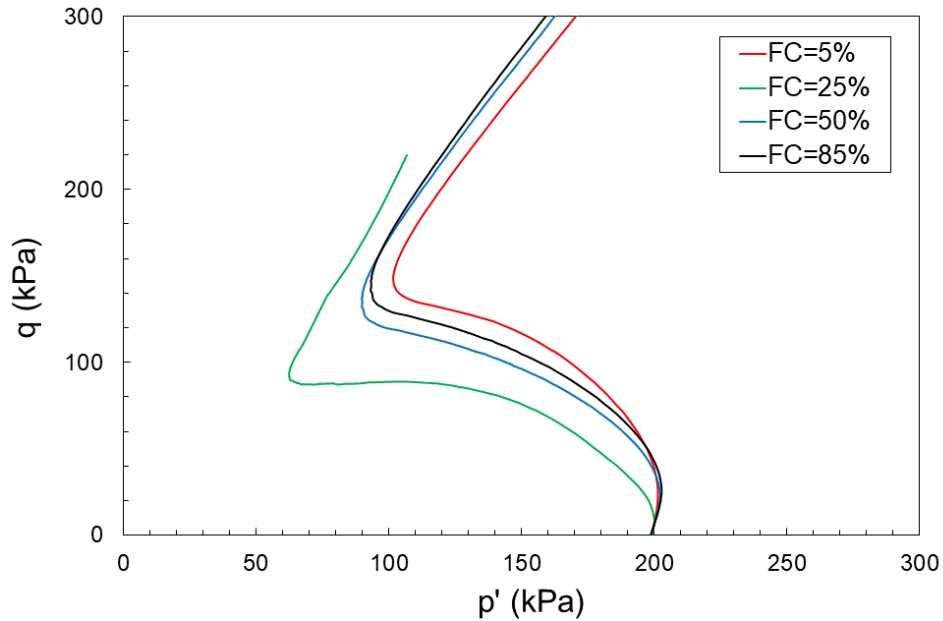


Figure 4-6: Stress paths of dry pluviated tailings specimens at different FC

4.4.2 Liquefaction triggering and post-liquefaction strengths

Liquefaction potential and shear resistance of cohesionless soils is primarily affected by their density and void ratio. As $s_u(\text{yield})$ is developed in undrained shearing, it is primarily applicable to analyze liquefaction under an undrained loading condition. The yield friction angle (ϕ'_{yield}) mobilized at $s_u(\text{yield})$, however, provides a more comprehensive assessment of static liquefaction and instability under different stress paths (Riveros and Sadrekarimi 2019). This was established from the undrained stress paths by connecting $s_u(\text{yield})$ to the origin. Figure 4-7 shows the general trends of increasing $s_u(\text{yield})/\sigma'_{1c}$, $s_u(\text{liq})/\sigma'_{1c}$, and ϕ'_{yield} with decreasing e_c of tailings specimens mixed with different amounts of fines and subjected to either isotropic ($K_C = 1$) or anisotropic ($K_C = K_0$) consolidation. The undrained strengths are normalized with respect to the effective vertical stress, i.e., σ'_{1c} in triaxial compression testing, to account for the effect of overburden pressure. The trends shown in Figure 4-7 suggest that stress-densification of tailings with depth and overburden pressure would result in an increased resistance against instability and a lower liquefaction potential.

Besides e_c , the liquefaction triggering and post-liquefaction strengths of tailings in this study are also affected by K_C and FC. According to Figure 4-7, both undrained, $s_u(\text{yield})/\sigma'_{1c}$ and $s_u(\text{liq})/\sigma'_{1c}$, and drained (ϕ'_{yield}) strengths drop to their minimum values as FC rises from 5 to 25%. This reduction is primarily associated with the metastable fabric formed by the silt grains as they cushion among the coarse particles and provide partial support of the coarse grain skeleton. Upon undrained loading, the silt grains move into the void spaces among the sand particles, inducing volumetric contraction and excess pore pressure in undrained shearing. According, silty tailings would be more susceptible to liquefaction flow failure than clean tailings sands at comparable void ratios. These strength parameters however increase with further rises of FC to 50% and 84% but fail to reach those of the clean (FC = 5%) specimens at a given e_c . With increasing FC to 50% and 84%, the fines not only dominate the tailings fabric but also produce a wider gradation, both of which improve tailings strength and reduce their liquefaction potential.

Similar effects of FC are also reported by several other researchers (Naeini and Baziar 2004; Thevanayagam 1998; Thevanayagam et al. 2002). For example, based on undrained triaxial compression tests on an Ottawa sand, Thevanayagam et al. (2002) found enhanced instability and reduced shear strength with increasing the amount of non-plastic fines for a given void ratio. These trends were however reversed with reduced contractive behavior and higher shear strengths as FC exceed a threshold amount. In undrained triaxial compression tests, Naeini and Baziar (2004) observed that the peak and the residual undrained strengths of Ardebil sand mixed with a non-plastic silt reached their minimum values at FC = 35%. However, those of the pure silt were still weaker than $s_u(\text{yield})$ and $s_u(\text{liq})$ of the clean sand, similar to the observations made in this study.

Figure 4-7 further highlights the effect of anisotropic consolidation. While $s_u(\text{yield})/\sigma'_{1c}$ of the K_o -consolidated specimens are notably higher than those of the isotropically-consolidated specimens, the effect of anisotropic consolidation was substantially lower for $s_u(\text{liq})/\sigma'_{1c}$ and ϕ'_{yield} . As reflected in Table 4-1, changes of the lateral stress coefficient (K_o) in these experiments with increasing FC mirrors that of ϕ'_{yield} . According to these numbers, the average K_o increases from 0.55 to 0.61 with increasing FC from 5% to 25%, but then progressively drops to 0.59 and 0.55 at FC = 50% and 84%, respectively. This

similarity can be explained by the Jaky's equation (i.e., $K_o = 1 - \sin \phi'$) which indicates an inverse relationship between K_o and the effective friction angle (ϕ').

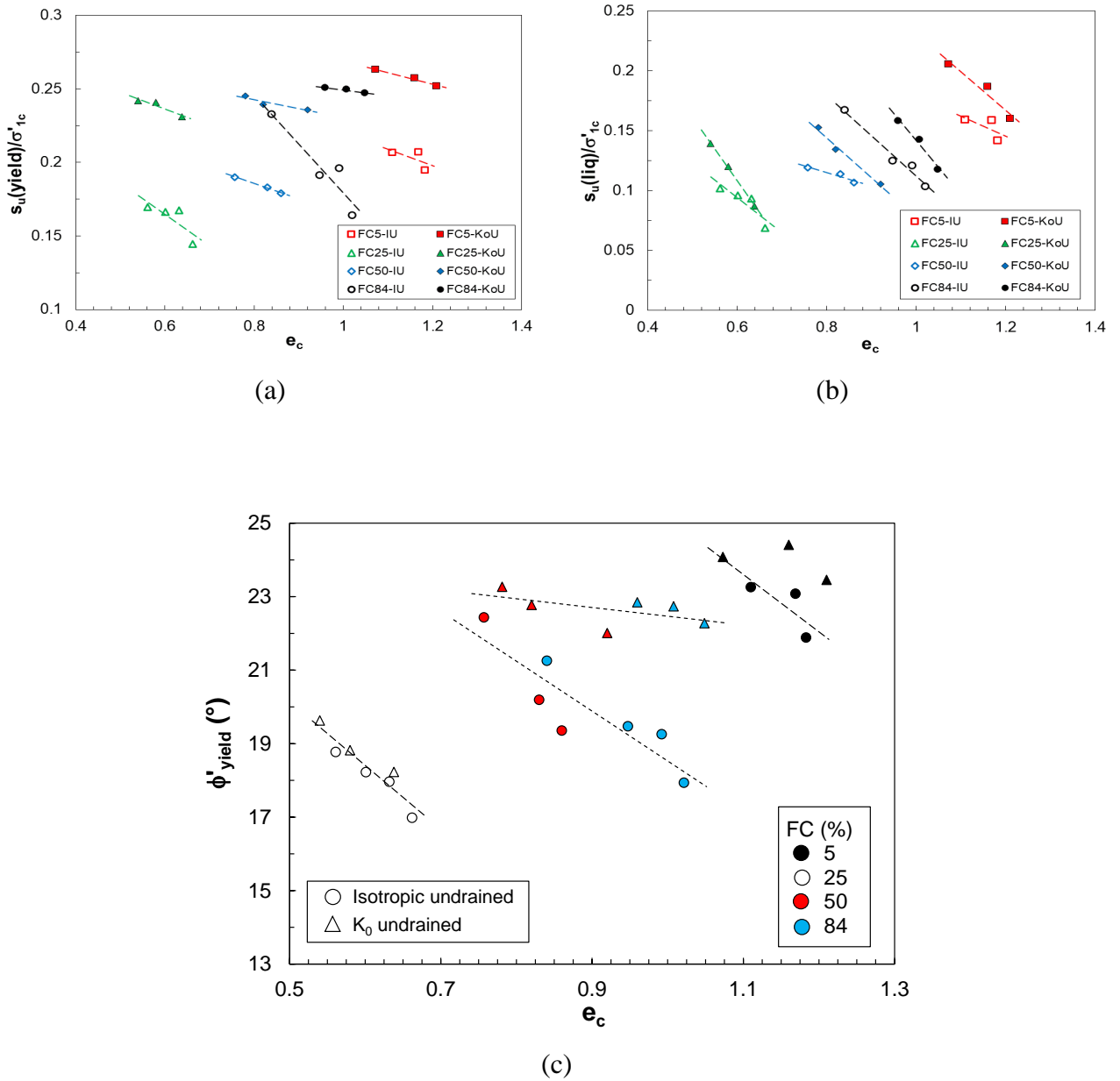


Figure 4-7: Effect of FC on (a) $s_u(\text{yield})/\sigma'_{1c}$, (b) $s_u(\text{liq})/\sigma'_{1c}$, and (c) ϕ'_{yield} of tailings specimens at different FC

4.4.3 Liquefaction severity

Static liquefaction in undrained loading results from the rapid collapse and loss of shear strength. Accordingly, the severity of liquefaction can be characterized based on the amount of strength reduction from $s_u(\text{yield})$ to $s_u(\text{liq})$. This is described by the brittleness index, I_B (Bishop 1973) shown in Figure 4-8. According to this figure, the lowest I_B occurs in tailings with $FC = 5\%$ and rises with increasing FC to 25% . This is associated with the weaker and unstable structure of silty tailings as the amount of fines at $FC = 25\%$ were inadequate to form a structure of their own and primarily floated within the voids or at the contacts among the coarse sand particles with little contribution to the shear strength and stability of the tailings specimens. However, with further rises of FC to 50 and 84% , I_B and hence the severity of liquefaction decreased as the fines dominated the tailings fabric and began contributing to the load bearing network of the tailings specimens.

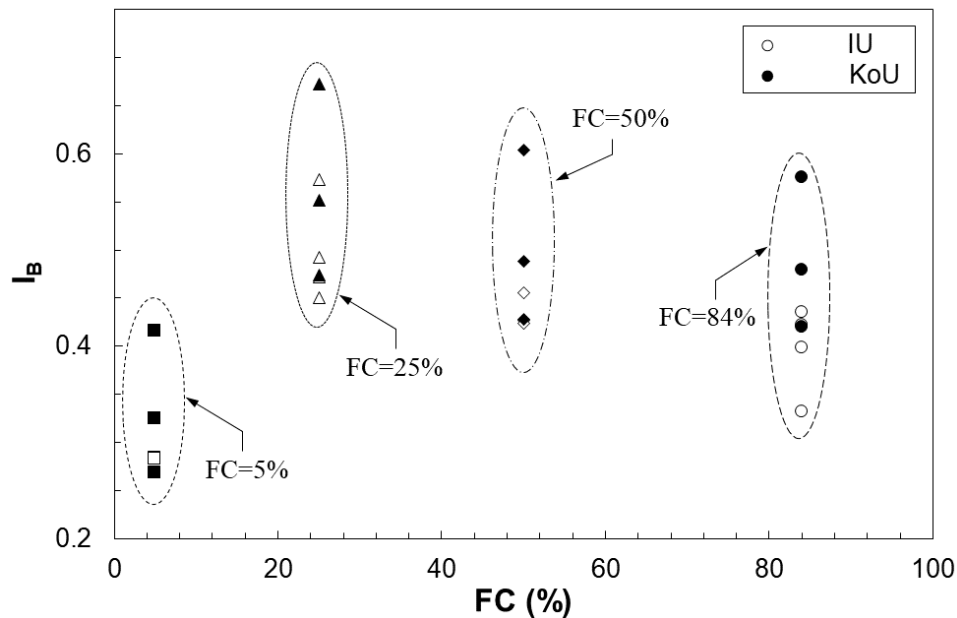


Figure 4-8: Brittleness index of IU and KoU tests on specimens with different FC

4.4.4 Critical states

The results of the undrained triaxial tests conducted in the study are used to establish the critical states of different tailings mixtures. The central idea of the critical state

framework is establishing a unique combination of effective stress and void ratio at the end of shearing, irrespective of the loading history or the stress path (Roscoe et al. 1958). As strain-softening was followed by a post-liquefaction strain-hardening behavior in most specimens of this study (see Figure 4-6), the phase transformation points of the undrained stress paths were treated as the critical states. A similar approach was taken by several other researchers for establishing critical states (Castro 1969; Baziar and Dobry 1995; Sladen et al. 1985).

Critical state friction angle

Figure 4-9 shows the variations of friction angle mobilized at phase transformation (ϕ'_{PT}) with FC from both isotropically- and anisotropically-consolidated specimens of the gold tailings examined here. Similar ϕ'_{PT} were mobilized in specimens subjected to isotropic and anisotropic (K_o) consolidation. As shown in Figure 4-9, ϕ'_{PT} slightly drops from 39.4° to 37.2° with increasing FC from 5 to 25% but then rises to 39.8° with further increase of FC to 84%. The latter trend is analogous to the rise of the critical state friction angle (ϕ'_{cs}) with FC reported by other investigators (Sladen et al. 1985; Salgado et al. 2000; Chu and Leong 2002; Bouckovalas et al. 2003; Carraro et al. 2003; Ni et al. 2004; Murthy et al. 2007), likely because of the more angular and platy shapes of the fine tailings particles which can wedge in among the sand grains. For example, Murthy et al. (2007) reported 1, 5 and 14% increases of ϕ'_{cs} as FC increased from 0 to 5, 10, and 15%. A 2.5% increase of the average ϕ'_{cs} was observed by Ni et al. (2004) with the addition of 9% non-plastic crushed silica fines to a host sand. The original Nerlerk sand with FC = 12% was shown to have a 4% higher ϕ'_{cs} than that of the clean sand in triaxial compression tests carried out by Sladen et al. (1985).

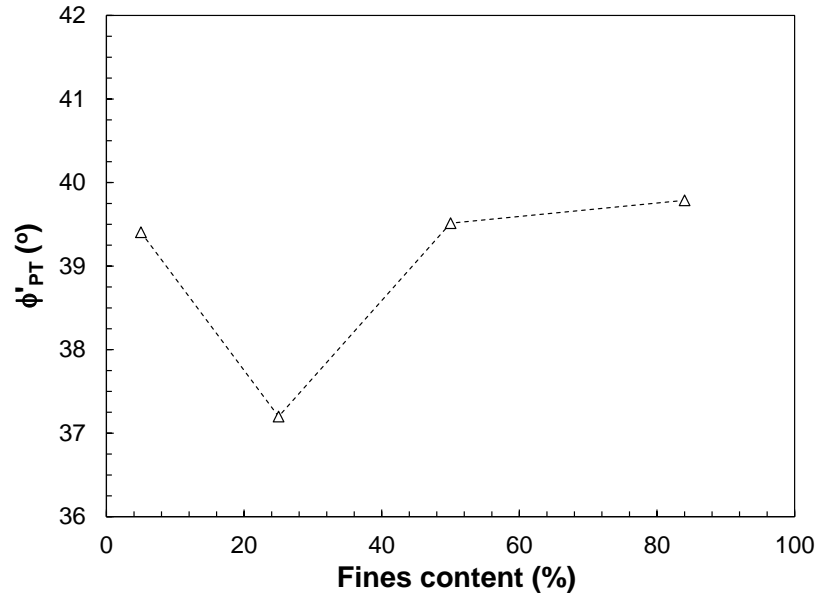


Figure 4-9: Changes of ϕ'_{PT} with FC from both isotropically- and anisotropically-consolidated specimens of this study

Critical state line

Figure 4-10 further shows the projection of critical states in the e - $\text{Log}(p')$ plane, often called the critical state line (CSL). For each FC, these data are fitted with a semi-logarithmic line with an intercept of Γ_{cs} and a slope of λ_{cs} . Several drained tests were also carried out to supplement the CSL at each FC. The final p' and void ratios (e_{cs}) reached at a shear strain of $\gamma = 25\%$ were taken as the critical states of the drained tests. Nearly the same CSLs are found from isotropically- and anisotropically-consolidated specimens during undrained or drained shearing, indicating the insignificant effects of consolidation path and drainage condition on CSL. As illustrated in Figure 4-10, clean tailings (FC = 5%) exhibit the loosest (i.e., plotted at higher void ratios) and the flattest CSL.

To better demonstrate the effect of FC on CSL, Figure 4-11 shows the changes of Γ_{cs} and λ_{cs} with FC. According to this figure, Γ_{cs} drops with increasing FC until the densest CSL ($\Gamma_{cs} = 0.78$) which occurs in the silty sand tailings (FC = 25%) as the fine particles fill-in the void spaces among the coarser sand particles. However, with further increases of FC

to 50% and 84%, the specimens' fabric transforms from a coarse- to a fine-dominant structure and the fine grains begin to push apart the sand particles, shifting the CSLs to higher void ratios. These results suggest a threshold $FC_{tr} = 25\%$ for the gold tailings studied here. The relatively higher $FC_{tr} = 50\%$ obtained by Carrera et al. (2011) for Stava tailings could be associated with their slightly plastic (plasticity index of 9.4) fine particles while those of this study were essentially non-plastic. The downward shift of the CSL also supports the higher liquefaction potential of the tailings specimens with increasing FC from 5 to 25%, and the subsequent strengthening and reduced liquefaction susceptibility at FC = 84%. On the other hand, the CSLs become progressively steeper and λ_{cs} increases with higher FC. This is not only because of the more compressible platy-shaped fine particles (Been and Jefferies 1985; Chameau and Sutterer 1994) but also the less stable fabric formed when the larger sand grains are held apart by the finer silt particles at their contact points.

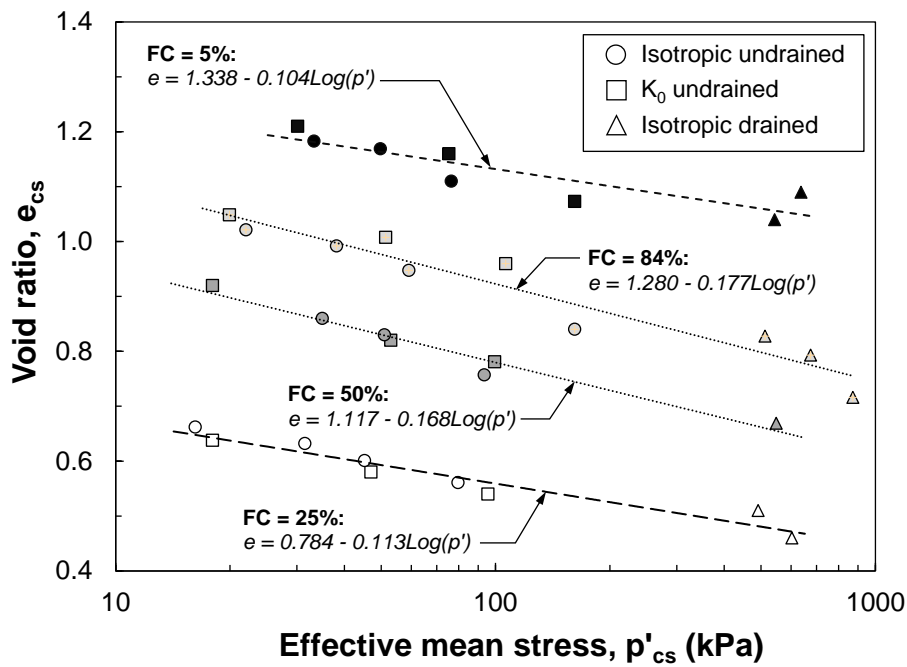


Figure 4-10: CSLs of tailings with different FC

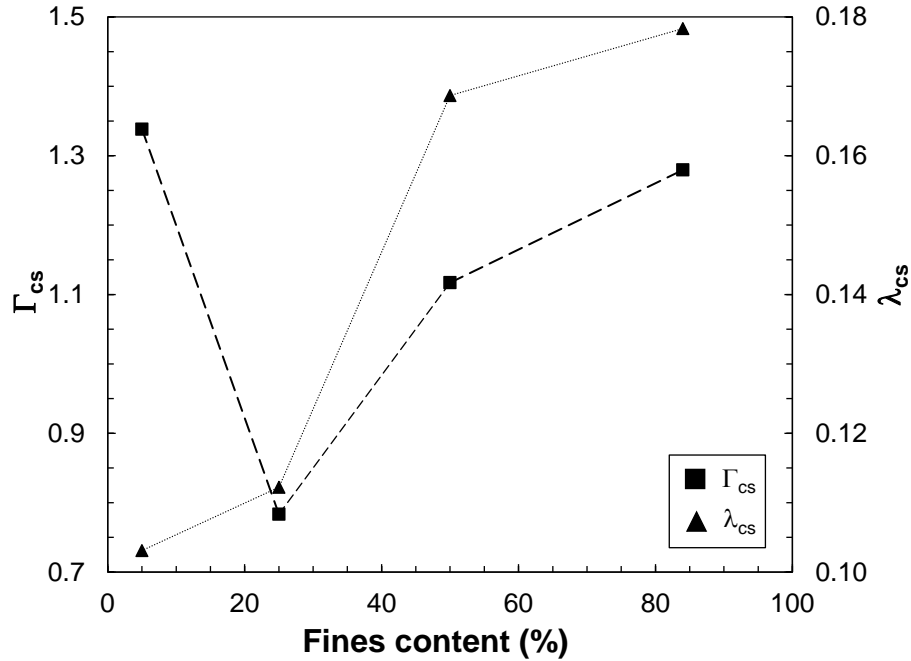


Figure 4-11: Effect of FC on Γ_{cs} and λ_{cs} of tailings examined in this study

State parameter

Using the CSLs established in Figure 4-10, the state parameter (ψ_{cs}) of each test was calculated, and summarized in Table 4-1 and Table 4-2, as the difference between the consolidation and critical state void ratios at a given p'_c (Been and Jefferies 1985). This is used in several numerical models for determining their modeling parameters (e.g. Jefferies 1993; Manzari and Dafalias 1997; Gajo and Wood 1999). Figure 4-12 and Figure 4-13 show the reductions of $s_u(\text{yield})/\sigma'_{1c}$, $s_u(\text{liq})/\sigma'_{1c}$ and ϕ'_{yield} with increasing ψ_{cs} for both isotropically- and anisotropically-consolidated specimens.

Similar to Figure 4-9 both $s_u(\text{yield})/\sigma'_{1c}$ and $s_u(\text{liq})/\sigma'_{1c}$ decrease with increasing FC from 5 to 25%. However, they subsequently increase with a further rise of FC such that those for FC = 5% & 50% fall on nearly the same $s_u(\text{yield})/\sigma'_{1c} - \psi_{cs}$ and $s_u(\text{liq})/\sigma'_{1c} - \psi_{cs}$ trends, and even exceed those of the clean tailings at FC = 84%.

Similarly, anisotropic consolidated has resulted in higher ϕ'_{yield} at a given ψ_{cs} for each FC in Figure 4-14. The lowest ϕ'_{yield} are mobilized in specimens with FC = 25% because of their denser CSL and higher ψ_{cs} values. On the other hand, while the anisotropically-consolidated specimens of tailings with FC = 5, 50 and 84% indicate a similar $\phi'_{\text{yield}} - \psi_{\text{cs}}$ trend, those subjected to isotropic consolidation show comparatively higher ϕ'_{yield} at FC = 50% than those of specimens with FC = 5 and 84%. These different observations (Figure 4-9) are artifacts of how ψ_{cs} as an index of liquefaction susceptibility follows the change of CSL with FC, which rises with increasing FC up to 25% and then drops with the addition of more fine particles.

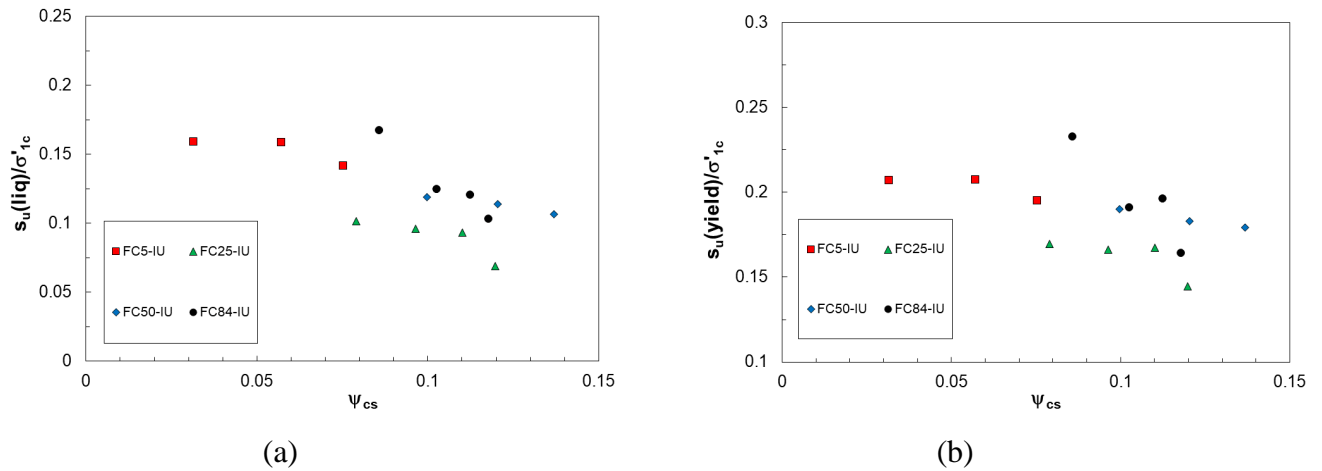


Figure 4-12: Variations of (a) $s_u(\text{yield})/\sigma'_{1c}$ and (b) $s_u(\text{liq})/\sigma'_{1c}$ with ψ_{cs} in isotropically-consolidated specimens

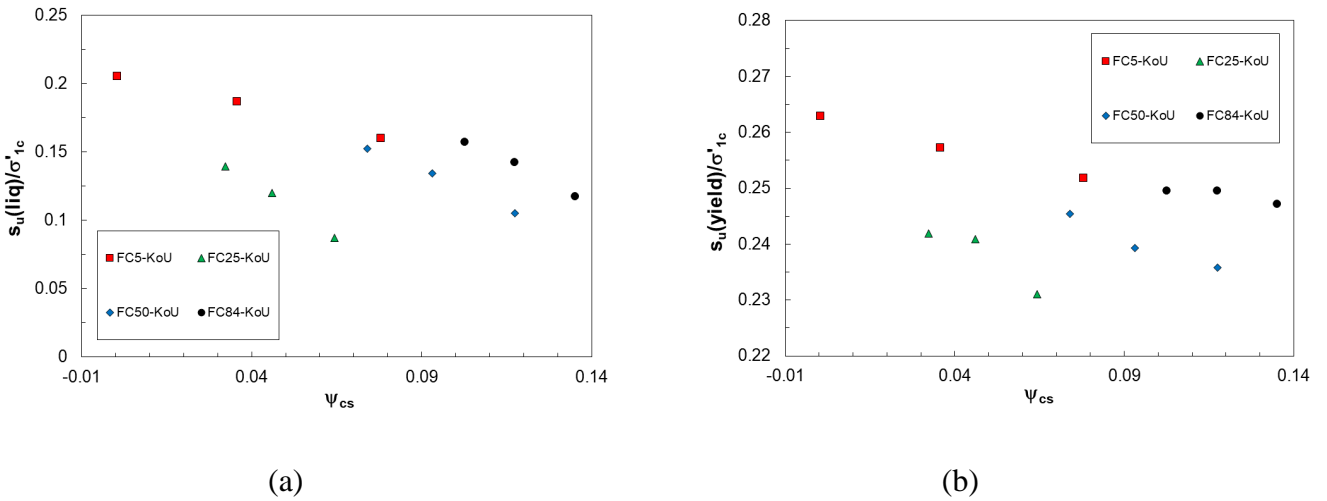


Figure 4-13: Variations of (a) $s_u(\text{yield})/\sigma'_{1c}$ and (b) $s_u(\text{liq})/\sigma'_{1c}$ with ψ_{cs} in anisotropically-consolidated specimens

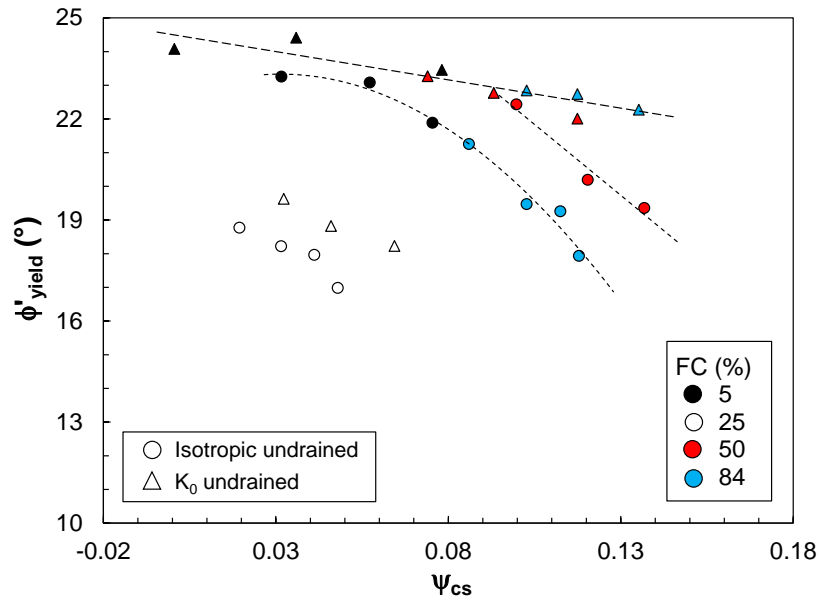


Figure 4-14: Variations of ϕ'_{yield} with ψ_{cs} for different tailings mixtures of this study

4.4.5 Effective stress unloading

Besides static liquefaction resulting from a continuous application of shear stress in an undrained condition, tailings instability can also occur from the reduction in effective

confining pressure (i.e., unloading) at a given shear stress as demonstrated in direct simple shear tests on another gold tailings by Riveros and Sadrekarimi (2020). In such stress paths, the inability of a soil specimen to carry the applied shear stress results in a run-away type failure (Chu and Leong 2002; Lade 2002). The effective stress reduction can be induced by a range of phenomena in the field, including a heavy rainfall, snowmelt, rise in phreatic surface, or lateral stress relief (Harp et al. 1990; Anderson and Sitar 1995; Olson et al. 2000; Leroueil 2001). Flow failures of the Fundao (Morgenstern et al. 2016) and the Brumadinho (Robertson et al. 2019) tailings dams in respectively 2015 and 2019 have been associated to this type of stress paths.

Instability through a reduction in effective stress was simulated here through constant deviator stress unloading (CDS) triaxial tests. As illustrated in Figure 4-15, tailings specimens were first consolidated anisotropically to certain deviator (q_c) and mean confining (p'_c) stresses, corresponding to an initial deviator stress ratio of $\eta_c = q_c/p'_c$. The effective confining pressure (p') was subsequently reduced by pumping water into the specimen to raise its pore pressure (Δu) at a rate of 1 kPa/min while sustaining the applied q_c . For the CDS experiments, e_c represent the void ratio at the end of anisotropic consolidation and prior to effective stress unloading. Three CDS tests were also carried out at unloading rates of 0.5 and 3 kPa/min to investigate the effect of unloading. Table 4-2 summarizes the CDS experiments carried out in this study. As shown in Figure 4-17(a), instability occurred in these tests as a rapid rise in the rate of ε_a , however the precise triggering of instability was identified based on Hill (1958) second-order work postulate ($d^2W = \partial\varepsilon_{vol} \times \partial p' < 0$) by tracking the change of volumetric strain (ε_{vol}) during unloading. This approach is employed by several researchers (Darve and Laouafa 2000; Sawicki and Świdziński 2010; Monkul et al. 2011) to identify the triggering of instability in axisymmetric triaxial and direct simple shear tests. According to Figure 4-17(b), the effective friction angle at the triggering of instability (ϕ'_{IL}) corresponds to the point of ε_{vol} reversal from volumetric dilation (due to unloading) to contraction (due to failure).

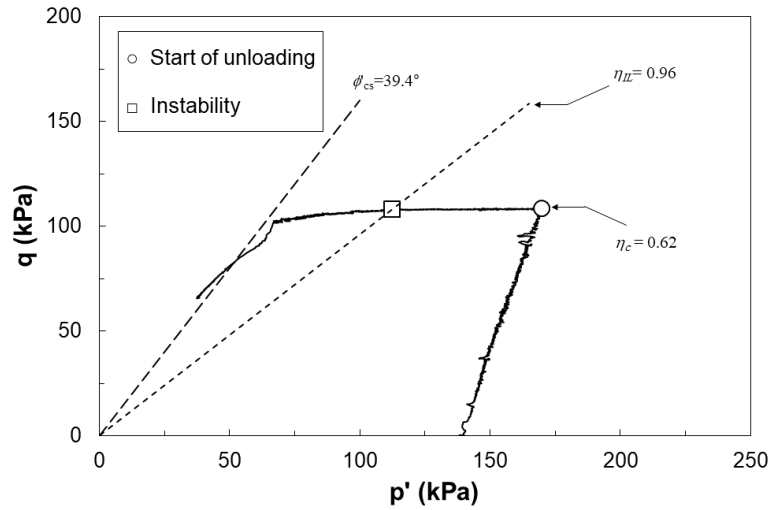


Figure 4-15: Stress path of a CDS test on a specimen with FC = 5% (CDS5-1)

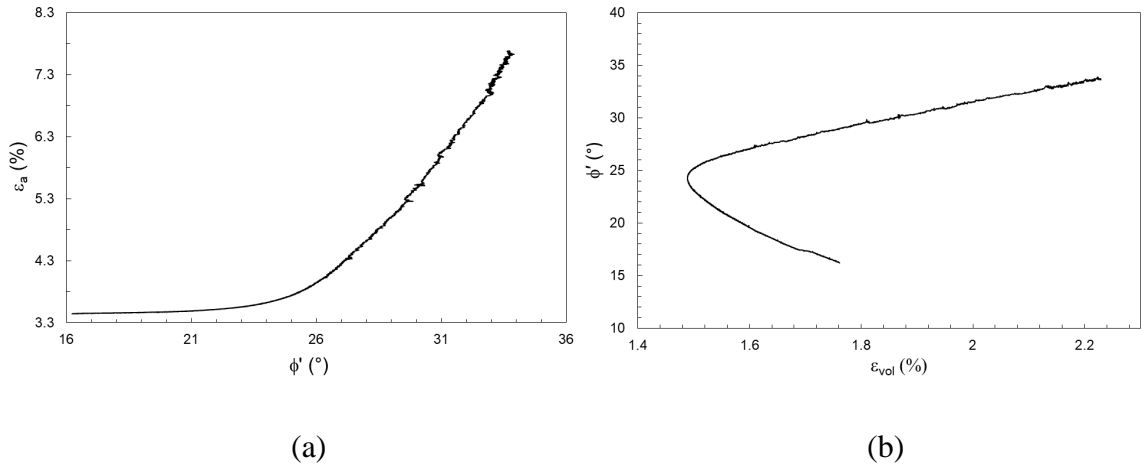
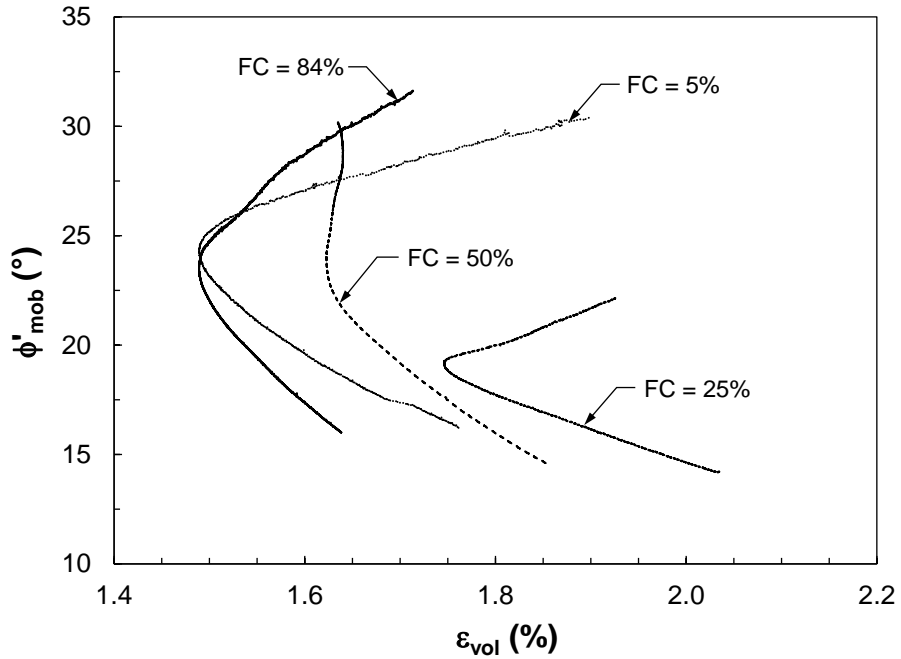


Figure 4-16: (a) ϵ_a versus mobilized ϕ' and (b) mobilized ϕ' versus ϵ_{vol} for test CDS5-1

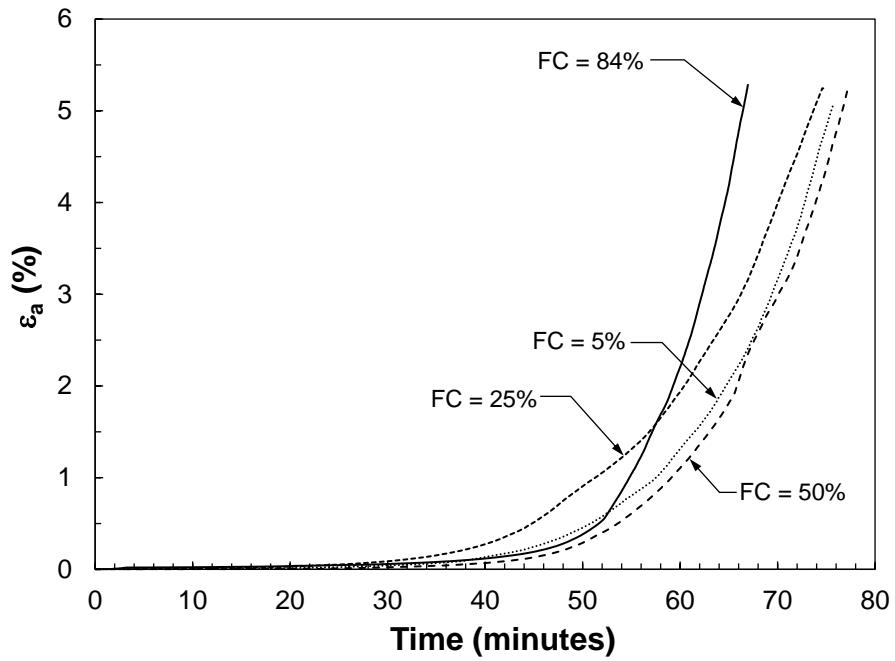
4.4.6 Effect of FC

Figure 4-17 (a) demonstrates the effect of FC on ϕ'_{yield} mobilized at the reversal of ϵ_{vol} in the CDS tests. According to this figure the ϕ'_{yield} corresponding to reversal in volumetric strain decreases noticeably when FC increases from 5% to 25%, and with any more increment in FC, increases. However, Figure 4-18 (b) indicates that FC has little impact on the triggering of instability time as ϵ_a begins to rise at nearly the same time after

unloading for different gradation subjected to unloading. Figure 4-18 shows how the mobilized friction angle changes with respect to void ratio and state parameter during CDS tests for different FC percentages.



(a)



(b)

Figure 4-17: (a) the mobilization of friction angle (ϕ'_{mob}) with volumetric strain (ϵ_{vol}) and (a) axial strain (ϵ_a) rate in CDS tests with different FC

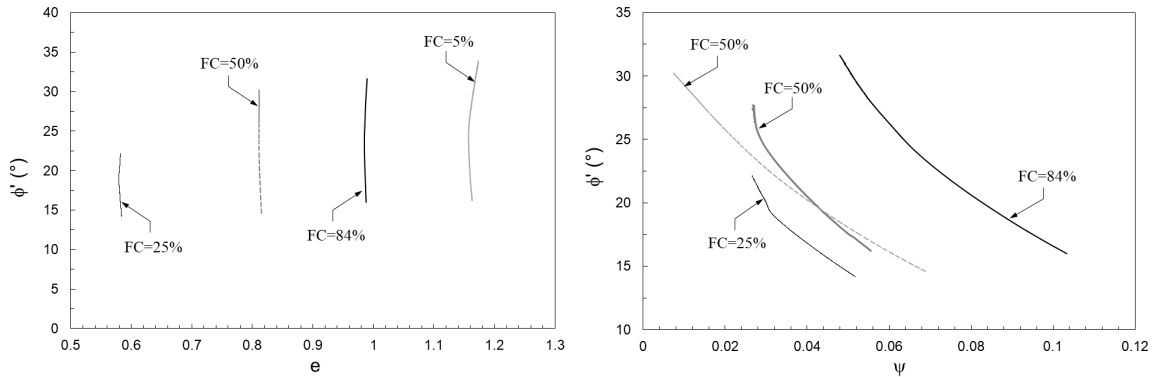


Figure 4-18: Variations of ϕ'_{yield} mobilized in the CDS tests with (a) e_c and (b) ψ_{cs}

4.4.7 Effect of stress path

As there is no $s_u(\text{yield})$ in CDS tests, the instability line (IL) is used to demarcate potentially unstable stress states from a stable condition. Several cases of flow failures in granular soil slopes have occurred due to instability (Kraft et al. 1992; Lade, 1993). The yield friction angle (ϕ'_{yield}) characterized the IL slope. These are compared with those mobilized at $s_u(\text{yield})$ of the IU and the K_oU tests in Figure 4-19, both showing reductions of ϕ'_{yield} with increasing e_c or ψ_{cs} .

According to this figure, ϕ'_{IL} mobilized in CDS and K_o -consolidation tests are generally higher than those from isotropically-consolidated specimens. As described by Imam et al. (2002), this is associated with the kinematic hardening and expansion of the yield surface when the consolidation stress ratio exceeds the corresponding ϕ'_{IL} of an isotropically-consolidated specimen. Similar increments of ϕ'_{IL} with anisotropic consolidation were

also reported by several other investigators (Prisco et al. 1995; Doanh et al. 1997; Fourie and Tshabalala 2005).

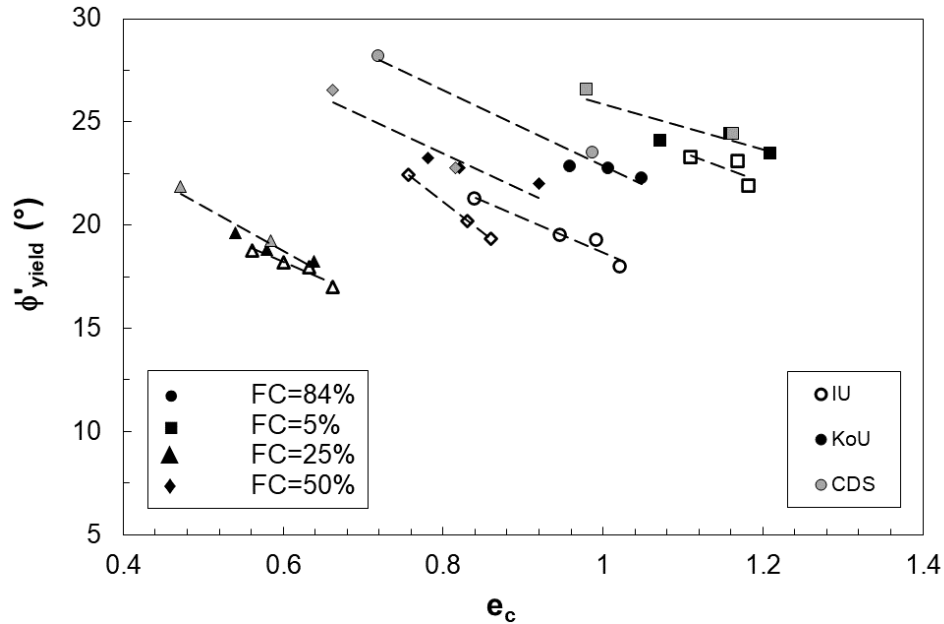


Figure 4-19: Comparisons of ϕ'_{yield} mobilized in IU, KoU and CDS tests on specimens with FC of (a) 5%, (b) 25%, (c) 50%, and (d) 84%

4.4.8 Effect of unloading rate

One of the parameters affecting failure under a CDS stress path is the rate at which the effective stress is reduced. Different studies have used different rates of effective stress unloading to examine the behavior of cohesionless soils under CDS stress paths. For example, Anderson and Sitar (1995) used a slow rate of 0.017 kPa/min, while higher rates of 0.1 and 1.0 kPa/min were applied by Lade and Pradel (1990) and Dong et al. (2016) in their triaxial tests. Several studies have further examined the effect of unloading rate on the drained instability of sands with some researchers observing a negligible effect of unloading rate (i.g. Chu et al. 2012) and others showing a small (Gajo et al. 2000) or a significant (Rabbi et al. 2019)) impact. Chu et al. (2012) found the same instability points in drained CDS triaxial tests on Singapore sand with unloading rates of 1 to 5 kPa/min. Gajo et al. (2000) observed a small reduction of ϕ'_{yield} as the rate of

effective stress reduction was increased from 0.13 to 2.5 kPa/min in drained CDS triaxial tests on Hostun sand. They attributed this decrease to the slower pore water pressure dissipation at faster unloading rates. On the other hand, a more significant reduction of ϕ'_{yield} was reported by Rabbi et al. (2019) in CDS triaxial tests on Yellow sand specimens as the unloading rate was raised from 0.2 to 5 kPa/min. Overall, no consensus has been reached regarding the effect of unloading rate on the drained instability behavior of granular materials and in particular mine tailings, warranting further investigation to address this effect.

The effect of unloading rate was examined in this study through three additional CDS tests (see Table 4-2) carried out with $\Delta u_e/\Delta t = 1$ and 3 kPa/min. As demonstrated in Figure 4-20, changes of $\Delta u_e/\Delta t$ merely shortened the time to instability while as shown in Figure 4-21 ϕ'_{yield} remained unaffected for the tailings specimens with FC = 5 and 84%. This indicates that the rate of effective stress reduction has little impact on the triggering of instability, further supporting the observations made by Wanatowski and Chu (2012) and Chu et al. (2012) in plane strain compression tests.

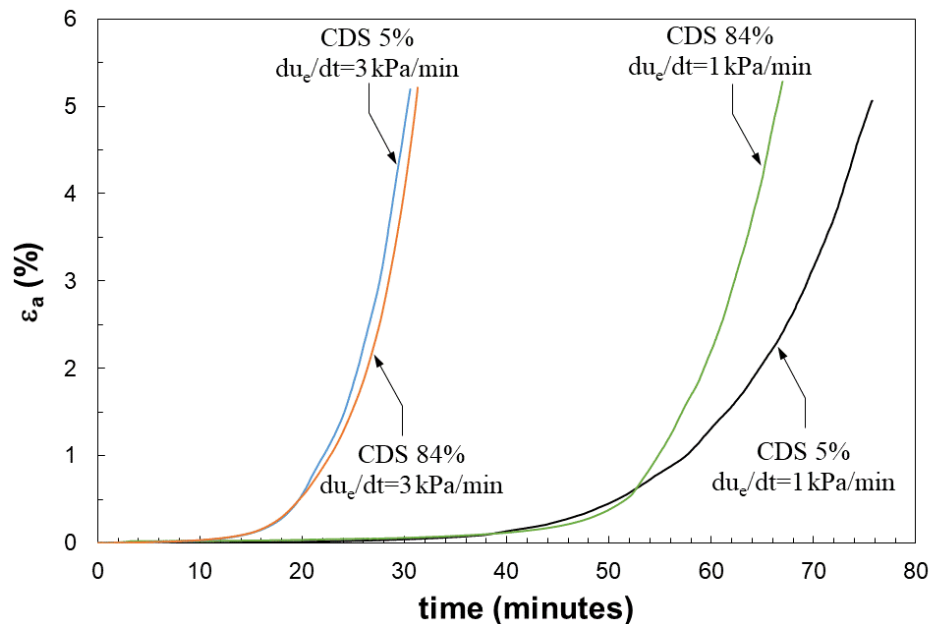


Figure 4-20: ϵ_a versus time in CDS tests with different unloading rates ($\Delta u_e/\Delta t$) for FC = 5%, and FC = 84%

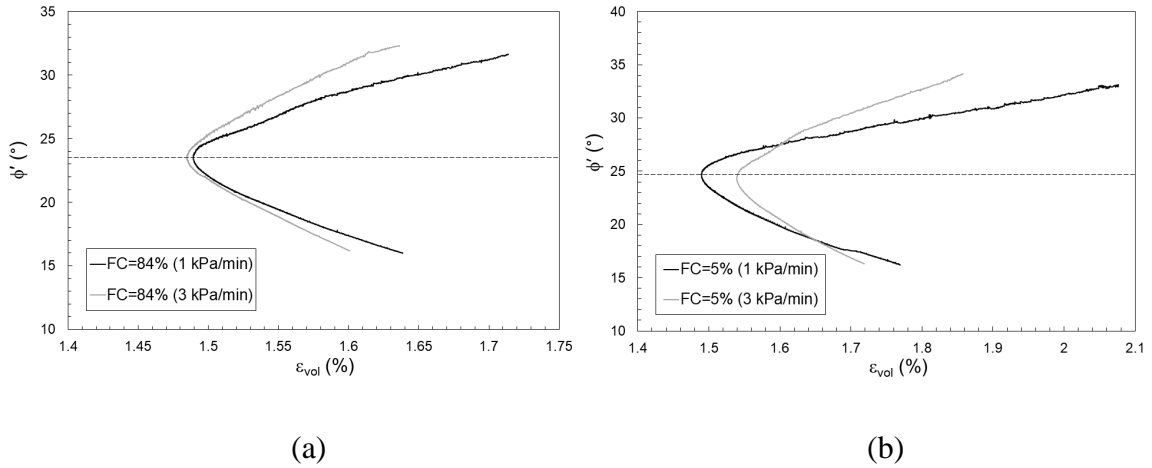


Figure 4-21: ϕ'_{mob} versus ϵ_{vol} in CDS tests with different unloading rates ($\Delta u_e/\Delta t$) for (a) FC = 5%, and (b) FC = 84%

4.5 Conclusion

Our experimental results demonstrated that liquefaction susceptibility of tailings specimens increases with the rise of FC from 5 to 25% as the tailings load-bearing structure becomes unstable due to inactive role of added fine particles. However, with further increase of FC to 84%, the density and stiffness of the fines matrix improves which results in reduced liquefaction susceptibility.

The triaxial testing results as well as the index void ratios presented in this study suggested a threshold fines content of around 25% for the examined gold tailings at which the tailings would be the most susceptible to instability and strength loss associated with undrained loading or effective stress unloading.

Note that these results correspond to the effect of non-plastic fines as plastic and non-plastic fines affect the strength and shearing behaviour of soils differently.

Chapter 5

5 Numerical modeling of a tailings impoundment using NorSand constitutive model

A two-dimensional finite element model is established in this chapter using a commercial software package to investigate the upstream construction method of a tailings dam numerically. Two different gradations of a tailings were assumed for the numerical simulation: the coarse portion and a sand-fines mixture (containing 84% fines) of the tailings. Fines tailings were considered as the waste residues to be stored in the tailings pond. The coarse portion of the material was also considered in a compacted form for the material of the containment berms. For the stored tailings with a potential susceptibility for liquefaction a critical state based model, NorSand, was used. Some parameters were derived based on available experimental results from triaxial compression tests and the rest were estimated using a calibration spreadsheet. The compacted sand tailings were modeled with an elastic-perfectly plastic behavior and the Mohr-Coulomb failure model was selected as the compacted tailings were deemed non-liquefiable. The construction scenarios consisted of different stages of placing dykes and deposition of residues. At the end, limit equilibrium slope stability analyses were coupled with the previous sections to give an insight to the factors of safety of the mentioned scenarios.

5.1 Introduction

NorSand constitutive model, initially developed and introduced by Jefferies (1993) and Jefferies and Shuttle (2005), is a critical state-based model. Such models can capture the behavior of soils by incorporating the soil's void ratio or state parameter, as a variable. Therefore, these models are considered as density dependant. Such incorporation involves the coupling of yield surface size to the void ratio. In early attempts, CamClay (Schofield and Wroth 1968), modified CamClay (Roscoe and Burland 1968) and Granta gravel models (Schofield and Wroth 1968) were presented, mostly for predicting the behavior of soils rather than sands. The reason for this division was the incapability of

these models to reproduce the liquefaction-related aspects of a loose sand's behavior, such as the observed strain softening phenomenon, yielding and flow failures. NorSand model, however, has been proved to be a versatile and yet simple model that is able to properly model dilatancy. Dilatancy is referred to the tendency of soils to change volume during shearing. This model is applicable to the soils in which particle to particle interactions are controlled by slips and contact forces. Therefore, it is suitable for granular materials as the mechanical behavior of such materials is dominated by the forces transmitted through contacts between grains, rather than bonds. The existence of a unique critical state locus in the space of q - p' - e in addition to this locus being the ultimate state of soil due to shear strain are the main ideas of NorSand model (Jefferies and Been 2019).

This model uses a range of parameters to define the full shape of the stress-strain curve. It captures the elastic stiffness, peak strength and post-peak strength loss. The “state dependency” of this model means that the behavior is constantly adjusted based on the state parameter (ψ) and mean effective stress (p').

NorSand requires eight parameters to span the entire behavior over the accessible void ratios (Shuttle and Jefferies 2010) using seven model parameters including three parameters to model soil ultimate critical state using the CSL parameters (Γ , λ , and M), two parameters for modeling the plastic hardening of the yield surface (H , N , χ), and two parameters, i.e. elastic modulus (E) and Poisson's ratio (ν), to define soil elastic behavior within the yield surface. Among the parameters which describe the yield surface, χ is a model property (typically varies between 2.5 to 4.5) that describe maximum soil dilatancy as a function of ψ . As a result of the decoupling of the size of the yield surface from void ratio, a plastic hardening modulus (H) limits the size of the yield surface and thus $s_u(\text{yield})$. Strain-softening ensues when this limit is reached and the soil subsequently accelerates to a unique critical state with further shear strain. Elasticity is modeled using a shear rigidity index ($I_r = G_{\max}/p' = 100 - 800$) and a constant Poisson's ratio, ν (0.1 – 0.3). Although ν does not vary greatly from one soil to another and it is often constant for a particular soil, I_r controls the strain at which $s_u(\text{yield})$ occurs while H controls the magnitude of the $s_u(\text{yield})$. As plastic shear strains govern soil behavior

beyond the initial loading, I_r has a relatively minor effect on the post-peak soil behavior. Using these parameters, NorSand describes soil shearing behavior moving to the critical state with shear strain in accordance with the fundamentals of the critical state soil mechanics. Shuttle and Jefferies (2010) provide further details of NorSand, its calibration procedure, evaluation, and application.

Table 5-1 summarizes the model's parameters and the range of values commonly encountered with sands. However, the 'typical' range of values for sand may not apply when modelling silt and tailings. For example, according to Shuttle and Jefferies (2010), recent testing of silt tailings in the laboratory has shown very high values of critical state strength ratio, M_{tc} . Also, the value of the dilatancy parameter χ_{tc} may also diverge from the usual sand range.

Table 5-1: NorSand model's parameters

		Typical range
CSL		
Γ	CSL's reference void ratio	0.9-1.4
λ	CSL's slope in e - $\ln(p')$ plane	0.01-0.07
Plasticity		
M_{tc}	Stress ratio at critical state in TxC	1.2-1.5
N	Volumetric coupling coefficient	0.2-0.45
H_o	Plastic hardening modulus	50-500
χ_{tc}	Dilatancy constant in TxC	2.5-4.5
Elasticity		
I_r	Dimensionless shear rigidity	100-800
ν	Poisson's ratio	0.1-0.3

This study uses the geometry and construction history of Brumadinho tailings dam. This dam suffered a sudden failure on January 25, 2019, Feijão Iron Ore Mine located in the south-west of Brumadinho town in Brazil. In less than 5 minutes, 9.7×10^6 m³ of tailings, which was about 75% of the stored tailed, was released out of the dam. An Expert Panel, Robertson et al. (2019), investigated the failure thoroughly and concluded the failure was the result of flow liquefaction within the tailings in the dam. According to them, the

construction history of the dam led to a dam that was composed of mostly loose, saturated, heavy, and brittle tailings that had high shear stresses within the downstream slope, resulting in a marginally stable dam (i.e., close to failure in undrained conditions). Their main conclusion was that the sudden strength loss, and resulting failure of the marginally stable dam, was due to a critical combination of ongoing internal strains due to creep, and a strength reduction due to loss of suction in the unsaturated zone caused by the cumulative rainfall since the end of tailings deposition, including the intense rainfall towards the end of 2018.

The purpose of this chapter is to see how the measured properties of two different gradations of a tailings used in a separate experimental program (TxC testing, shear wave velocity measurement, etc.) can be used for NorSand constitutive model in a tailings dam. The geometry of a real dam, Brumadinho dam, is used to evaluate whether the model produces reasonable results or leads to unrealistic outcomes. Prior to the mentioned assessment, another dam, Fundao tailings dam, is also modeled using the available parameters by the forensic technical team investigating its failure, to compare the results and validate the methodology.

In this study a finite element analysis software for geotechnical engineering problems, SIGMA/w® version 2021.3 in a commercially developed software package, Geo-Studio, was used to evaluate the load-deformation of a two-dimensional profile of a tailings dam. Adopting NorSand model for the stored tailings introduced liquefaction susceptibility in the scenario. Additionally, a slope stability software for performing limit equilibrium analyses, GeoStudio's SLOPE/W ® version 2021.3, was used to compute the factors of safety associated with the stress-deformation analyses.

5.2 Validation of the numerical method

In order to validate the SIGMA/W finite element analysis, the Fundao tailings dam is modeled in this section and the results are compared with what the forensic technical panel, Morgenstern et al. (2016), have presented. The deformations of a cross section

through the region in which the failure initiated (section 01 on the left abutment) are obtained and compared.

Morgenstern et al. (2016) built their elastic and Mohr-Coulomb versions of their models using version 8 of Fast Lagrangian Analysis of Continua (FLAC) finite difference software. They also used Version 6 of this software for the critical state analyses, with the NorSand constitutive model implemented as a user-defined model developed for this version of FLAC.

5.2.1 Geometry and meshing of Fundao tailings dam model

The model geometry and stratigraphy was generated in accordance with that reported by the panel (Morgenstern et al. 2016) as shown in Figure 5-1 at its final stage. The staged-construction of the dam was followed in this modeling.

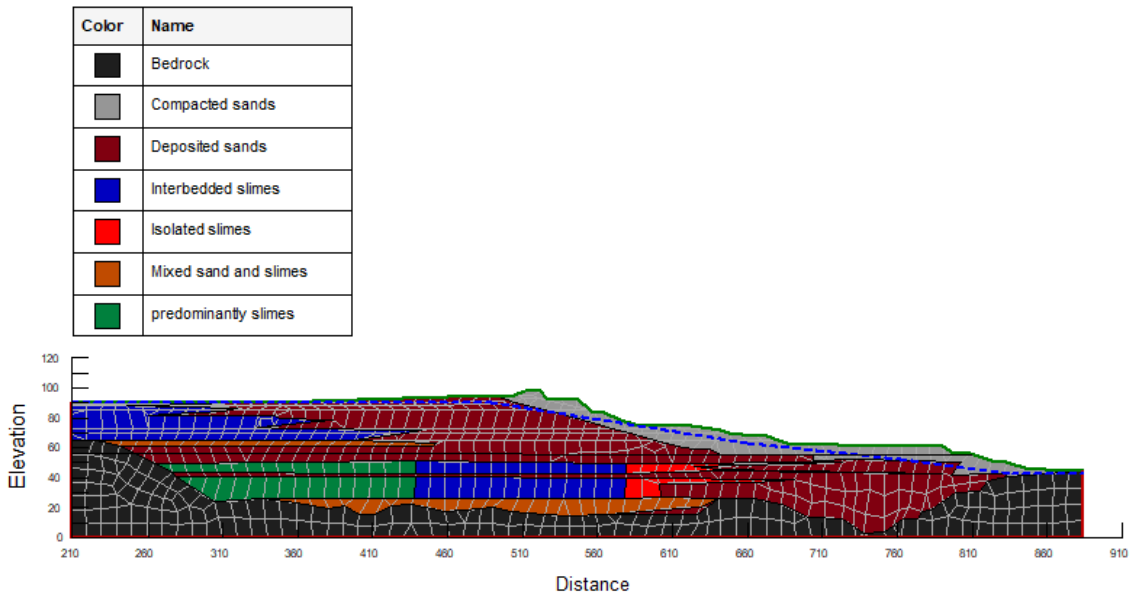


Figure 5-1. Geometry of the dam’s profile

5.2.2 Model parameters for Fundao tailings dam’s simulation

Two different models were generated and assessed in this section. The first model was entirely elastic, considering elastic behavior for all the materials. The results of this model were compared with the results of the corresponding all elastic model developed

by Morgenstern et al. (2016). They have mentioned that the purpose of the elastic 2D analysis was to identify the pattern of displacements produced by the model without the complexity of material behavior included within the Mohr-Coulomb and critical state analyses. Another scenario including the critical state based NorSand model for the deposited sand tailings was performed. In this analysis, the other materials, except for the foundation, were modeled using elastic-perfectly plastic Mohr-Coulomb model.

The parameters for Elastic, Mohr-Coulomb and NorSand models are directly derived from the panel's report (Appendix I). Trends of G versus effective vertical stress are plotted in the report for different materials of the model (Figure 5-2). Shear moduli (G) were converted to Young's moduli (E) using their elastic relationship.

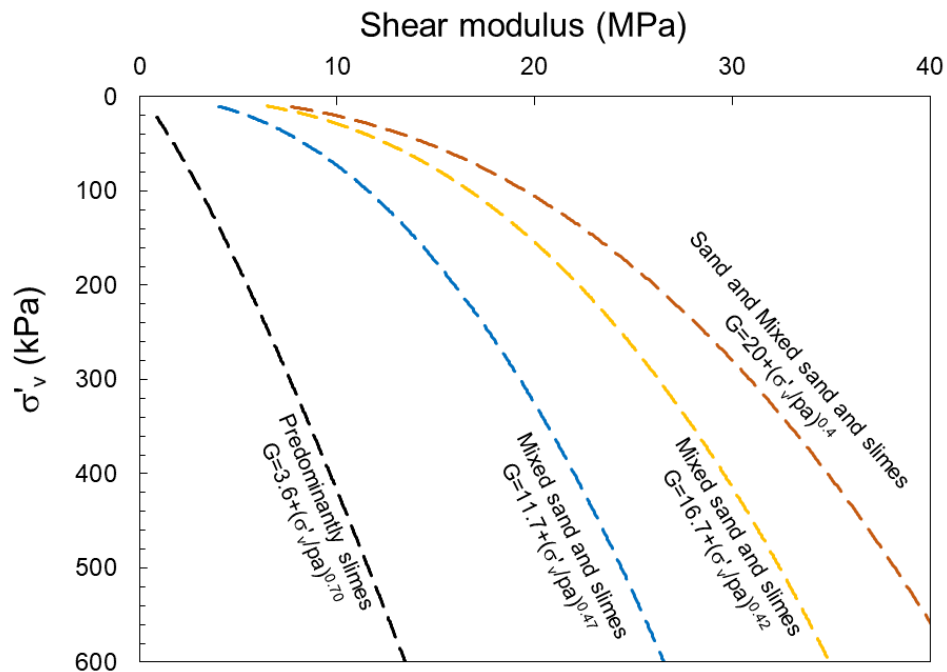


Figure 5-2. Shear modulus of different materials (Morgenstern et al. 2016)

However, defining the estimated stiffness trends increasing by effective stress in σ'_v/w resulted in very large displacements and numerical divergence. This is due to weighing effect of the low E-values for small vertical effective stresses that resulted in the

underestimation of stiffness at greater depths. Therefore, constant values of E corresponding to the 85th percentile of the stiffness were taken into account in the model. Moghaddam et al. (2020) used the same approach in modeling this dam in their finite element analysis as well.

Regarding Mohr-Coulomb analysis, the pre-implemented strain-softening Mohr-Coulomb model in SIGMA/W is an elasto-brittle-plastic model. This model considers a sudden drop in effective friction angle from an initial peak to a residual value. This is different from a strain-weakening behavior. This difference leads to unreasonable displacements comparing with the real measurements. Therefore, an elastic-perfectly plastic Mohr-Coulomb model was considered for this analysis using the same peak and residual friction angles. The critical state NorSand model was considered for the deposited sands while the fine tailings were simulated using the Mohr-Coulomb material model, similar to Morgenstern et al. (2016). The modeling parameters are shown in Table 5-2 and Table 5-3.

Table 5-2: Elastic and Mohr-Coulomb parameters for Fundao tailings dam analysis

Material	Mohr-Coulomb parameters		Elastic properties	
	ϕ' (°)	C' (kPa)	E (MPa)	ν
Compacted sands	35	5	76	0.3
Deposited sands	33	0	100	0.3
Predominantly slimes	12.4	0	18	0.3
Isolated slimes	33	0	55	0.3
Interbedded slimes	29.4	0	70	0.3
Mixed sand and slimes	23.5	5	75	0.3
Foundation	-	-	500	0.3

Table 5-3: NorSand parameters used for the deposited sands in Fundao tailings dam analysis

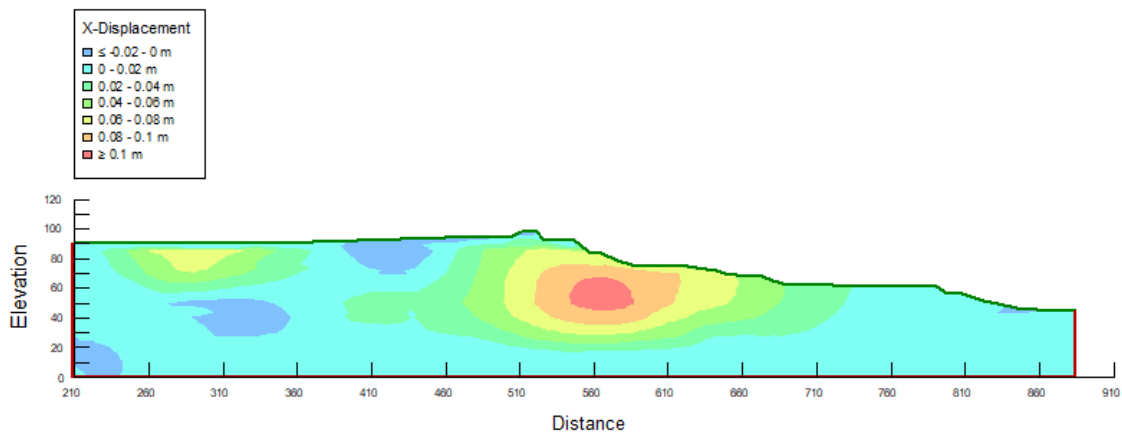
Deposited sands		
CSL		
Γ	CSL's reference void ratio	0.865
λ	CSL's slope in e-Ln(p') plane	0.024

Plasticity		
M_{tc}	Stress ratio at critical state in TxC	1.33
N	Volumetric coupling coefficient	0.38
H_o	Plastic hardening modulus	156
H_ψ	Change in hardening modulus by ψ	756
χ_{tc}	Dilatancy constant in TxC	7.2

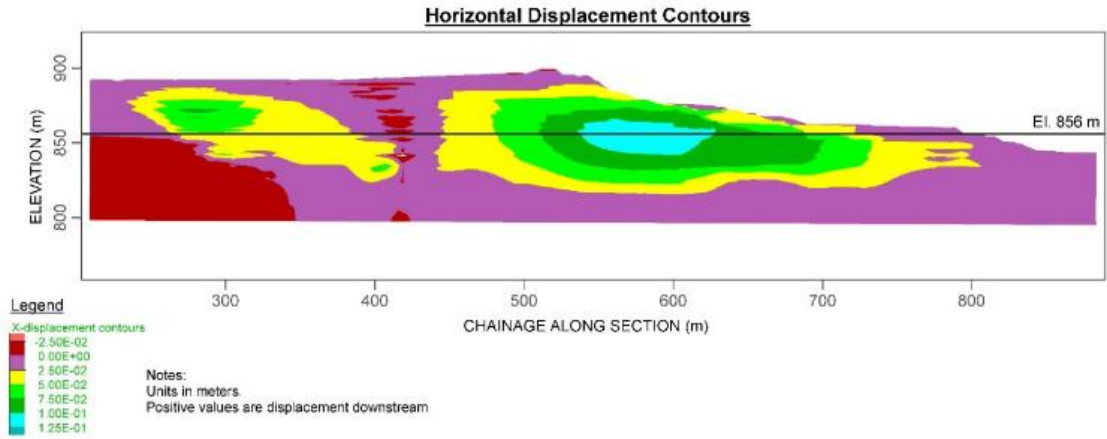
A phreatic surface was assigned with a hydrostatic pore pressure based on the piezometer water levels reported by Morgenstern et al. (2016) and considering complete saturation underneath it and zero negative pore pressure head above it. The phreatic surface is based on the piezometer monitoring data, and extrapolating the data into regions and time periods without data provided and analyzed by Morgenstern et al. (2016).

5.2.3 Results of the Fundao tailings dam's simulations

The contours of the horizontal displacement obtained from the analyses at its final stage of construction are shown in Figure 5-3 (a) for the entirely elastic model, and Figure 5-4 (a) for the second model including critical state based model for sand tailings. Additionally, the results from the forensic panel's report are shown in Figure 5-3 (b) and Figure 5-4 (b) for the first and second models, respectively.

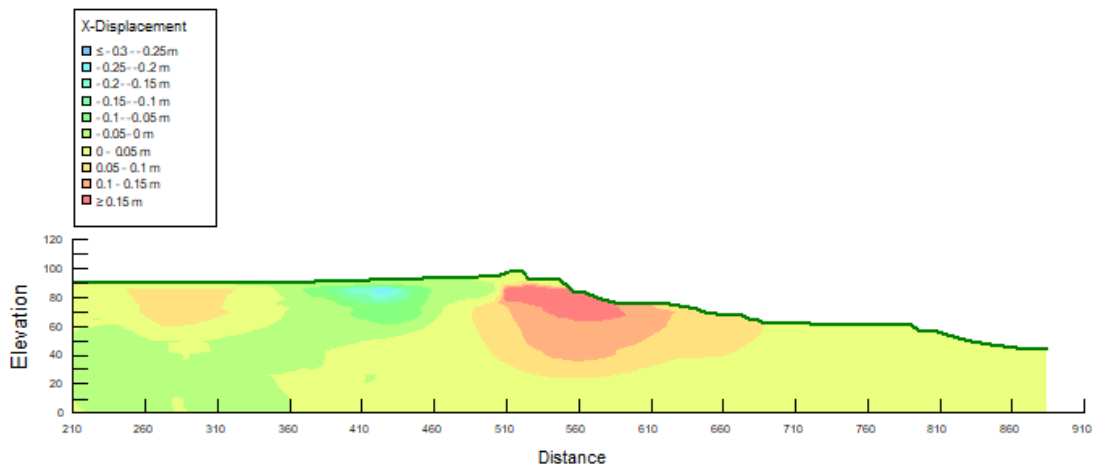


(a)

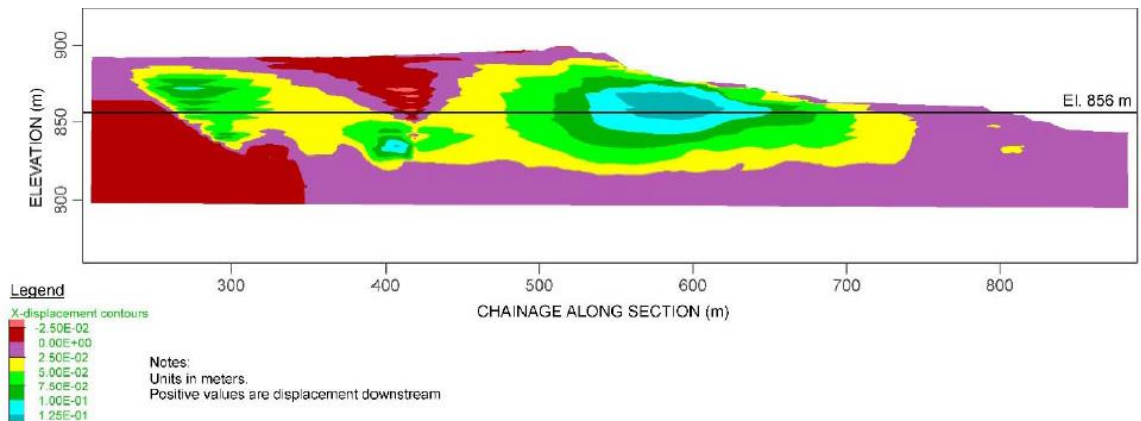


(b)

Figure 5-3. Horizontal displacement contours for the entirely elastic model obtained by (a) this study and (b) Morgenstern et al. (2016)



(a)



(b)

Figure 5-4: Horizontal displacement contours for the second model including NorSand constitutive model for sand tailings obtained by (a) this study and (b) Morgenstern et al. (2016)

Two main regions with significant horizontal displacements are obtained. One region is located towards the upstream end and the other zone is beneath the crest. The first zone towards upstream is a result of material settling. This settlement is because of the high compressibility of predominantly slimes and sliding along the interface with the foundation.

The downstream zone under the dam crest is a result of the dam's geometry. The largest horizontal displacements occur in the downstream region and concentrate in a zone that is downstream of the dike crest. The X/Y deformation vectors of the second model is also demonstrated in Figure 5-5

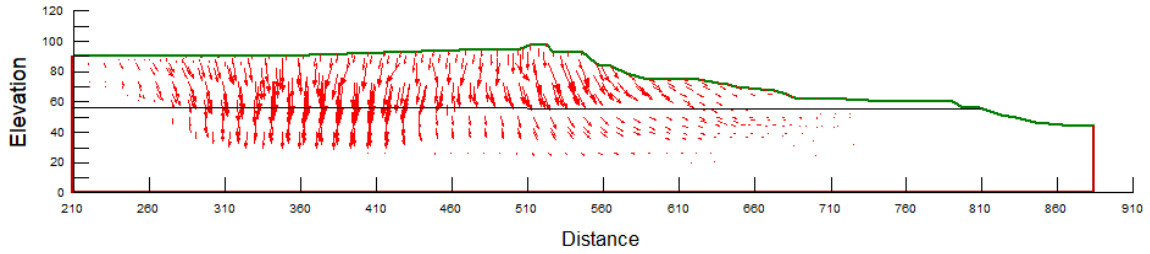
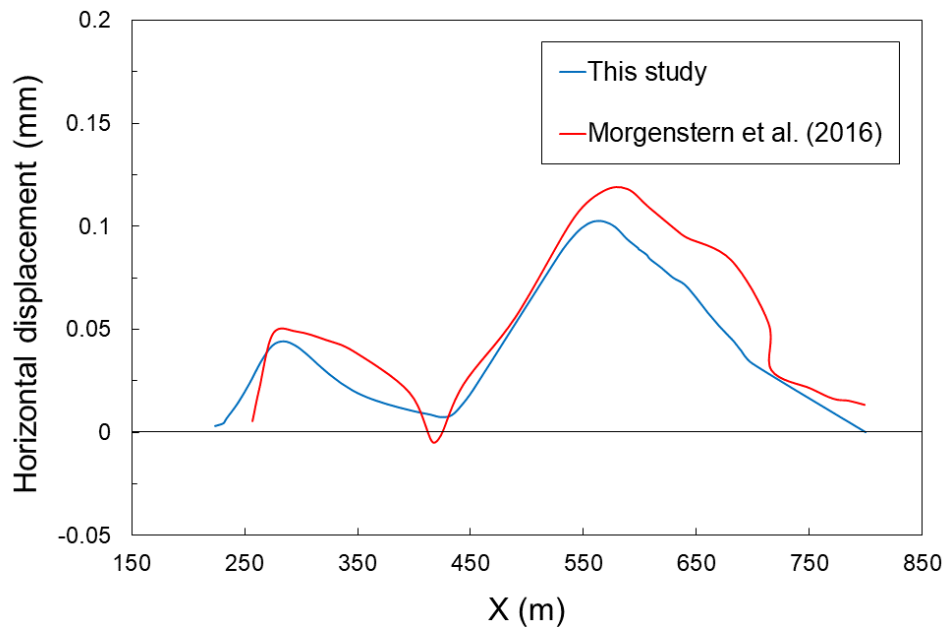
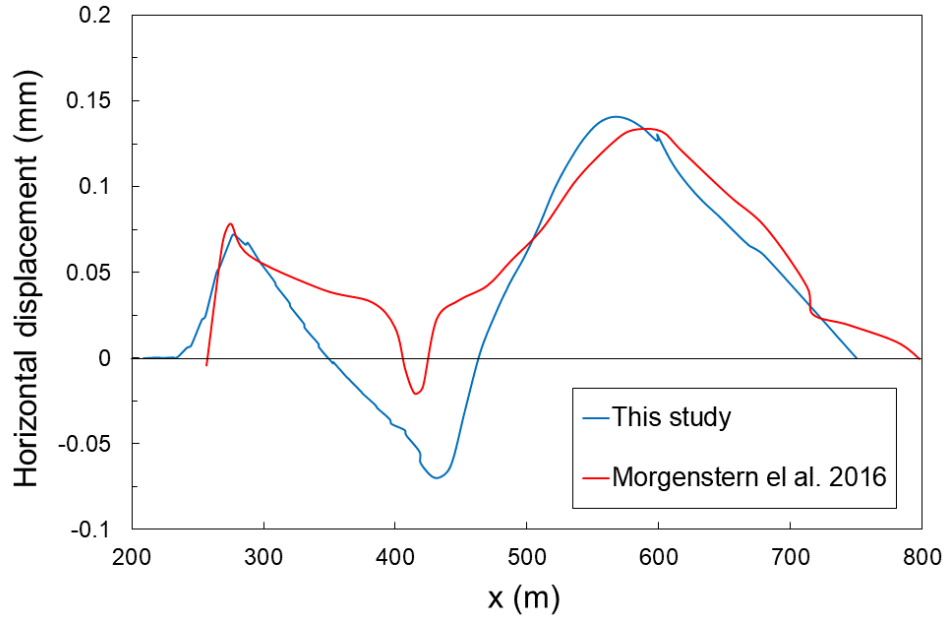


Figure 5-5. X/Y displacement vectors of the second model

To gain a better clarification on the outcomes, of the horizontal displacements of the first and second models along at El. 856 m are shown in Figure 5-6 (a) and (b), respectively. This elevation was selected by Morgenstern et al. (2016) as it includes the maximum horizontal displacement of the dam. In these figures, the results are compared with the Panel’s reported displacements. Overall, the observed trends are comparable despite some differences in the displacement contours of Figure 4. The existing differences are likely because of the different models (M/C vs strain softening) used to simulate slimes/fine tailings.



(a)



(b)

Figure 5-6. Comparisons of horizontal displacement trends at El. 856 m for (a) the first entirely elastic model and (b) the second model including NorSand model for the tailings

According to Morgenstern et al. (2016), the displacements obtained from the advanced second model, Figure 5-6 (b), implies compressive straining in the downstream direction and extension straining in the upstream direction. Extension strains result in a reduction of horizontal confinement consistent with a potential for liquefaction triggering from a lateral extrusion process.

5.3 Modeling of a tailings dam

5.3.1 Geometry and meshing

The geometry of the under-study profile is based on the Vale S.A. ("Vale") Córrego do Feijão Mine Dam I ("Dam I") in Brumadinho, Brazil, which is shown in Figure 5-7 (at its final stage). Section 1-1 of the dam, described in the Appendix H of the report by the forensic investigation report (Robertson et al. 2019) is modeled. The assigned boundary conditions are as fixed x-displacement, or roller boundaries, for the left and right sides

and fixed both x and y-displacements, or rigidly fixed, for the bottom edge. The boundary conditions are assigned to the foundation. Since the foundation is modeled as a very stiff material with high Young's modulus ($E=300$ MPa and $\nu=0.4$), the boundary conditions are expected to have no impact on the load-deformation characteristics of the tailings and berms. Horizontal displacement contours of a panel studying the failure of Brumadinho dam (Robertson et al. 2019) revealed concentrated lateral deformations within the stored tailings in the regions below and downstream from the dam crest and its vicinities.

Triangular and quadratic or mixed elements were used as the mesh property. Meshing was generated to ensure a good quality of the numerical analysis. Compatibility is maintained while mesh generation across different regions or material properties or boundary conditions. Since a complete interlocking is assumed between the compacted coarse and fine tailings, no interface is defined between them. Mesh sensitivity trials with mesh widths of 1, 2, 3, 5, and 10 m were performed to ensure that the mesh was fine enough to provide reliable results for the models used. Approximate element size of 5 m wide was used, resulting in about 2640 nodes and 2550 elements.

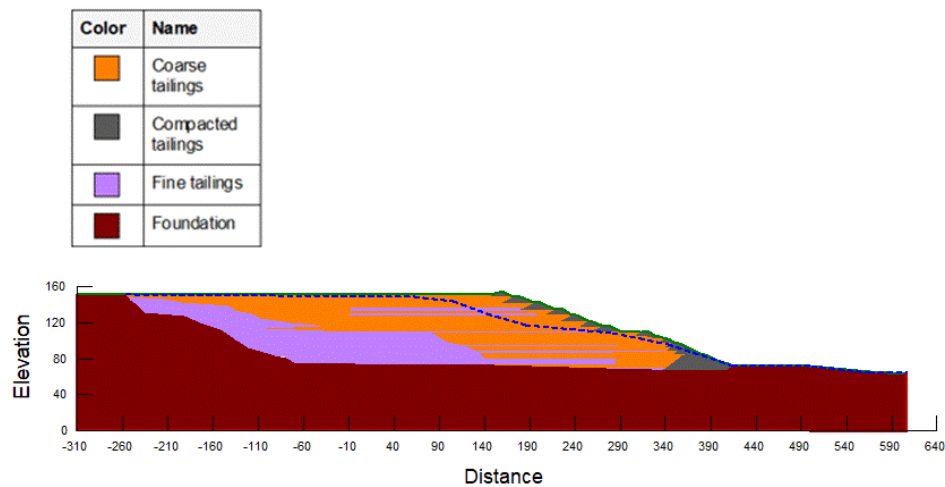


Figure 5-7: Geometry and materials of the modeled dam

5.3.2 Constitutive model selection and parameters

The tailings, both fine and coarse, were modeled using NorSand model. Any plasticity model needs to determine three fundamentals based on plasticity rules. They include the

description of yield surface, determination of flow rule and the hardening law incorporated in the model. The overall required parameters for this model are eight inputs which are divided in three groups.

Two different gradations of non-cohesive tailings (O tailings which was described in details in Chapters 2 and 3) were calibrated for this model to be used in a further simulation. The first tailings is a fine tailings with 84 percent silt content ($<75 \mu\text{m}$) mixed with sand particles. This will be the bulk slimes stored behind the simulated impoundment. The second one is the sand portion of the same tailings (with filtering fines content to a low amount of 5%). The gradation curves of both fine and coarse tailings are shown in Figure 5-8.

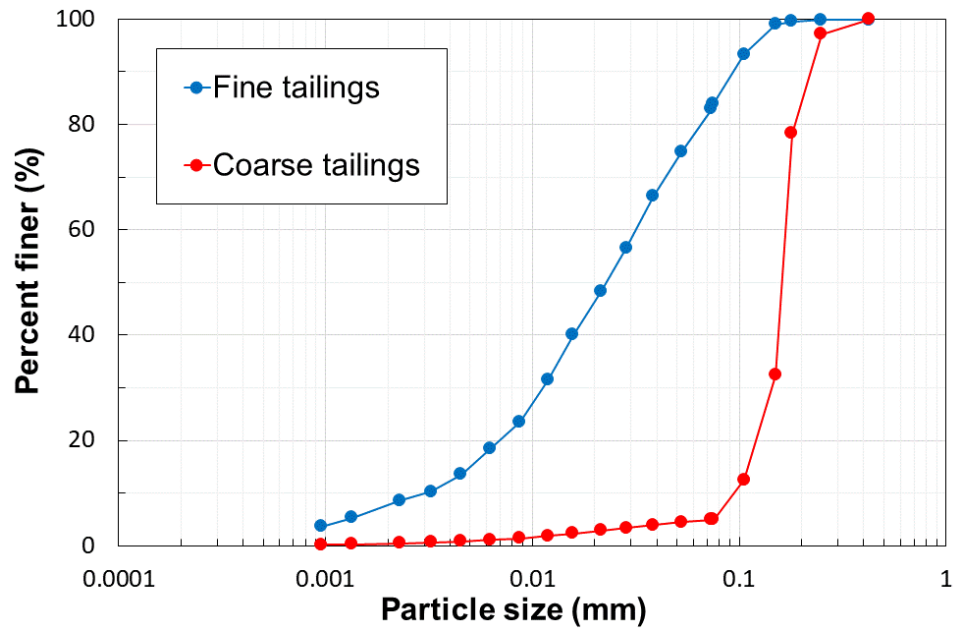


Figure 5-8: Particle size distribution curves of fine and coarse tailings

The critical state line of the coarse tailings was derived from three isotropic ($p'_c = 150 - 300 \text{ kPa}$, $D_{rc} = 72 - 80\%$) and three anisotropic ($p'_c = 85 - 310 \text{ kPa}$, $D_{rc} = 70 - 84\%$) undrained TxC tests in addition to two isotropic drained ($p'_c = 200$ and 300 kPa , $D_{rc} = 82$ and 87%) TxC tests. The fine tailings' CSL was also developed based on four isotropic ($p'_c = 160 - 600 \text{ kPa}$, $D_{rc} = 73 - 85\%$) and three anisotropic ($p'_c = 78 - 300 \text{ kPa}$, $D_{rc} = 71$

– 77%) undrained, and three isotropic drained ($p'_c = 150$ and 400 kPa, $D_{rc} = 78$ and 85%) TxC tests. These critical state lines are demonstrated in Figure 5-9.

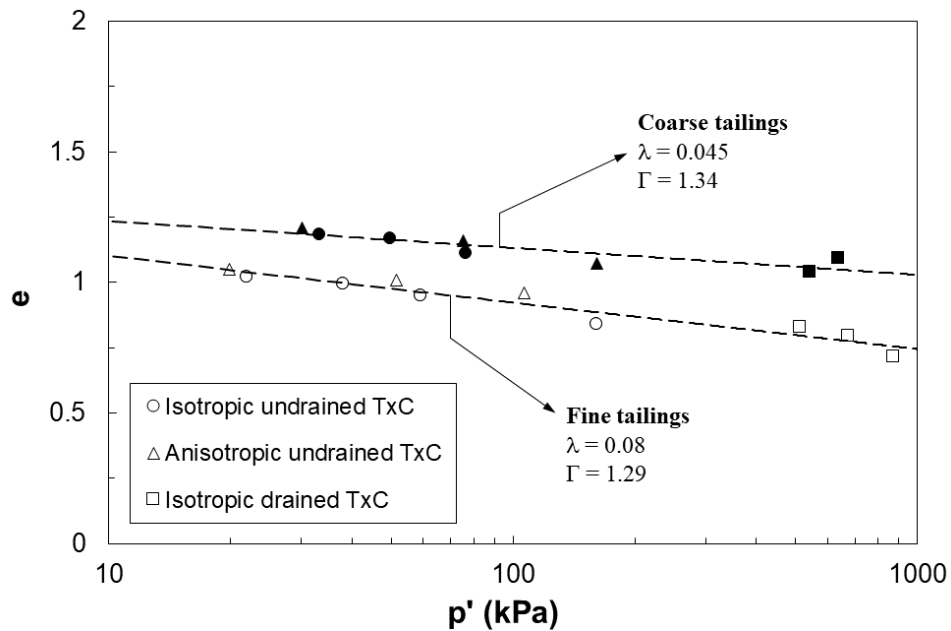


Figure 5-9: Critical state lines of the two gradations of the tailings

The results of shear wave velocity measurements using bender elements for both the gradations are brought in Figure 5-10. The shear wave velocities (V_s) were measured in moist tamped samples of the tailings using a pair of piezometric bender elements in a direct simple shear setup. They were obtained by dividing the distance between the bender element tips by the shear wave travel time through the specimen. The travel time was obtained by the peak-to-peak technique (Brignoli et al. 1996). In this technique, the time difference between the first peaks of the received wave signals were taken as the travel time. Five V_s measurements were carried out for each gradation in vertical effective stresses of 150, 200, 300, 400 and 600 kPa. The corresponding void ratios of the fine tailings were within the range of 0.92-1.02, and for the coarse tailings this range was 1.03-1.19.

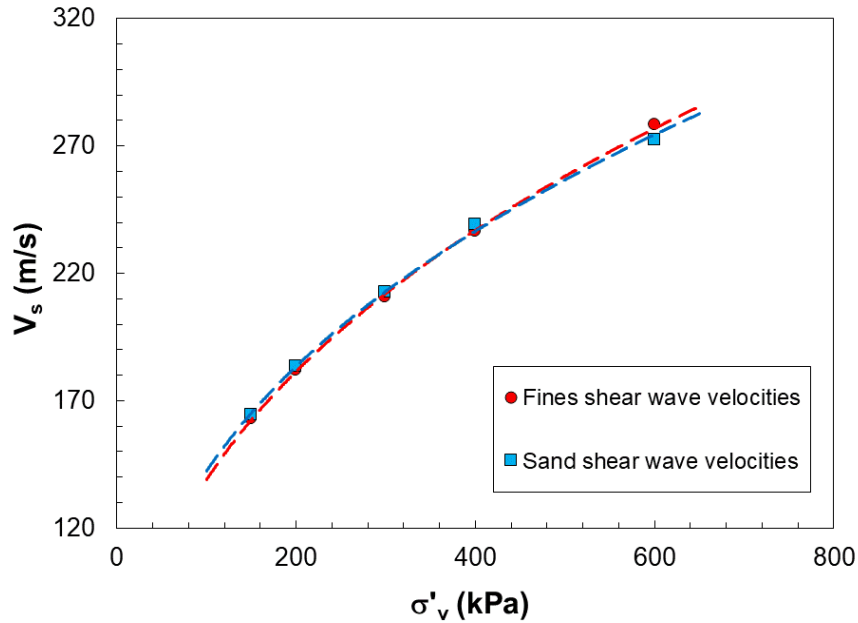


Figure 5-10: Shear wave velocities of the coarse and fine tailings

To calibrate NorSand parameters for this study, the laboratory results of a series of undrained and drained triaxial compression tests are used. The rest of the parameters were estimated by iterative numerical trial to match the experimental stress-strain and stress paths of the triaxial tests using a spreadsheet (LICENSE 1991) developed by Jefferies and Been (2019).

The results of the calibration of two undrained triaxial compression tests are shown below in Figure 5-11 for the 84% fines containing mixture. The undrained tests were performed with p'_c of 200 and 300 kPa.

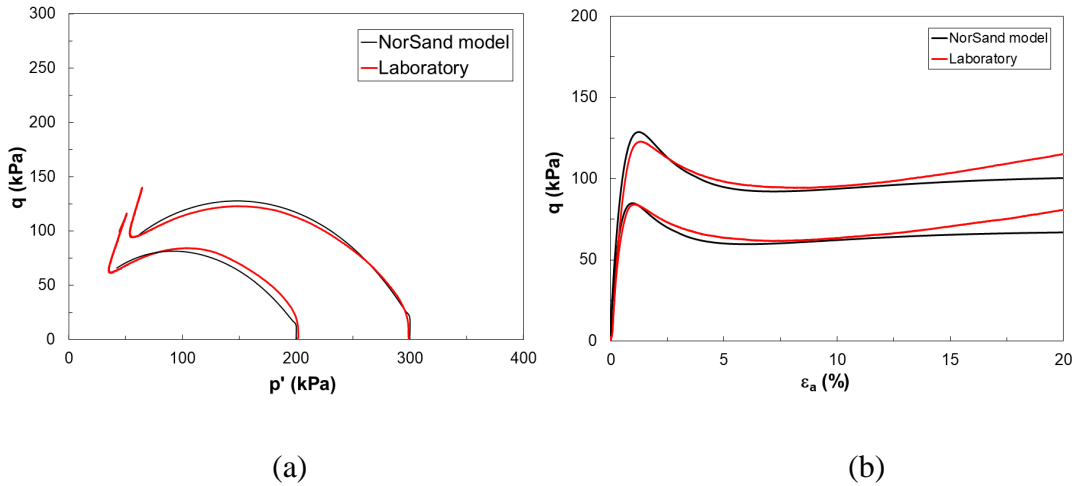


Figure 5-11: Calibration of NorSand model for the fine mixture: (a) stress paths of undrained TxC at $p'_c=200$ and 300 kPa; (b) stress-strain of undrained TxC at $p'_c=200$ and 300 kPa

Figure 5-12 further demonstrates the comparisons between the calibrated model and the experimental TxC tests data for the coarse tailings with p'_c of 200 kPa and 300 kPa.

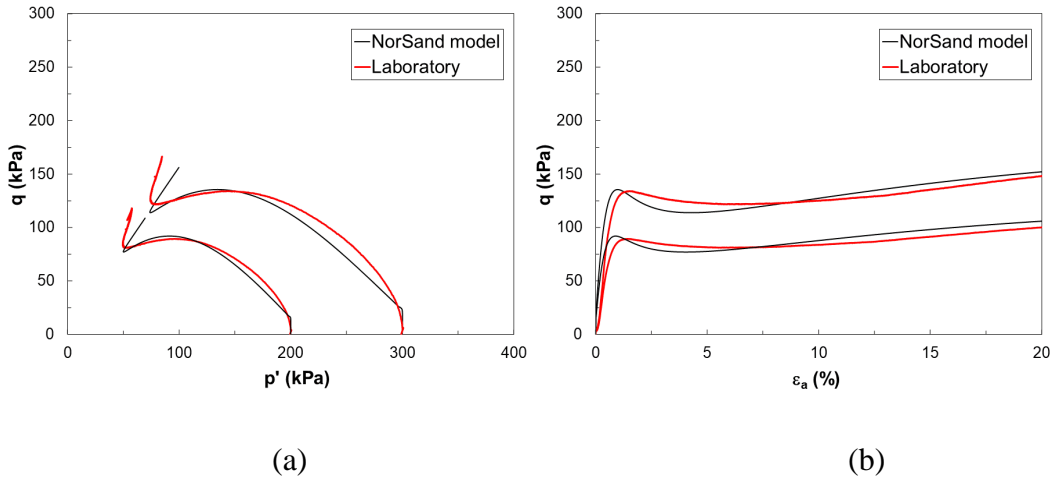


Figure 5-12: Calibration of NorSand model for the coarse tailings: (a) stress paths of undrained TxC at $p'_c=200$ and 300 kPa; (b) stress-strain of undrained TxC at $p'_c=200$ and 300 kPa

Based on the available experimental data and the estimations performed, the parameters are shown in Table 5-4. It was observed that the volumetric coupling coefficient, N , did

not seem to contribute much effect, and thus less sensitivity was considered in estimating its value. Plastic hardening modulus, H_o , change in hardening modulus by ψ , H_ψ , and Dilatancy constant, χ_{tc} , were obtained using iterative procedures.

Table 5-4: Measured and calibrated values for NorSand model

		Fine portion	Sand portion
CSL			
Γ	CSL's reference void ratio	1.292	1.34
λ	CSL's slope in e-Ln(p') plane	0.08	0.045
Plasticity			
M_{tc}	Stress ratio at critical state in TxC	1.62	1.60
N	Volumetric coupling coefficient	0.5	0.35
H_o	Plastic hardening modulus	70	35
H_ψ	Change in hardening modulus by ψ	300	1000
χ_{tc}	Dilatancy constant in TxC	6	1.5
Elasticity			
G (MPa)	Shear modulus at reference stress of 100 kPa	38	35
ν	Poisson's ratio	0.25	0.25

The containment berms on the downstream slope of the dam are assumed to consist of an elastic-perfectly plastic material following Mohr-Coulomb yielding/failure criterion. Morgenstern et al. (2016) and Robertson et al. (2019) used the same approach in their analyses and assigned Elastic-perfectly plastic behavior (Mohr-Coulomb model) to the dykes with no liquefaction potential. A small non-zero cohesion ($c=0.01$ kPa) was assigned to the material to avoid numerical difficulties.

Elastic model was assigned to the foundation with high stiffness (i.e., $E = 300$ MPa). Also, as mentioned earlier, tailings were modeled using NorSand model. However, each lift was initially placed and activated using elastic models, and after updating the levels of water table at each lift, they were switched to NorSand model and the next layer was added. This approach was taken by Robertson et al. (2019) and therefore, used in this study as well. Therefore, elastic parameters for these materials were of interest as well. The parameters used for these models are summarized in Table 5-5. The friction angles were measured using the phase transformation points of the TxC results on both fine and coarse tailings.

Table 5-5. Elastic and Mohr-Coulomb parameters

	Coarse tailings	Fine tailings	Berms	Foundation
ϕ' (°)	39.2	39.8	39.2	-
c' (kPa)	0	0	0	-
E (MPa)	55	60	55	300
ν	0.25	0.25	0.25	0.4

5.4 Results and discussions

5.4.1 Developing the dam in accordance with its construction history

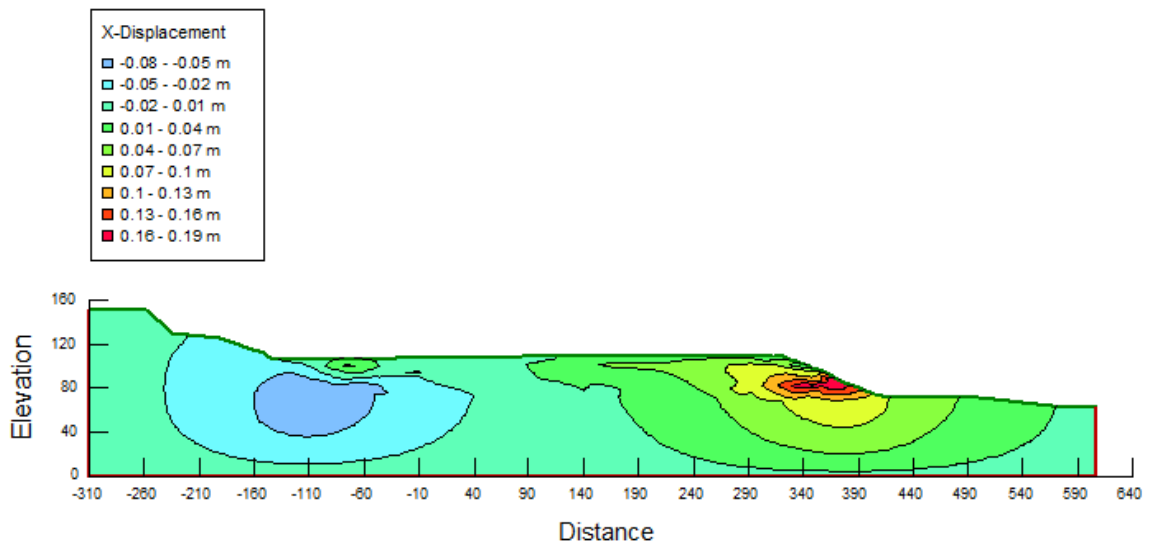
The main objective from this section was to assess the stress distribution in the tailings throughout construction and prior to failure, and comparing with the stress distributions presented by the technical panel. Afterwards, a coupled (load-displacement) LEM analysis was performed to evaluate the factor of safety of the dam at this stage. According to Robertson et al. (2019), the dam was marginally stable at this point, therefore, FOS of higher than one was expected.

The dam was constructed sequentially within 10 raising, and modeled with the same trend of construction in the simulation. Robertson et al. (2019), assumed the tailings mobilized their drained strength parameters during this stage. Therefore, drained condition was assigned to the tailings. Each lift was initially placed using elastic parameters, similar to what Robertson et al. (2019) did in their modeling. Then, the pore pressures were updated to reflect the pond and water table for that stage of construction, according to Appendix F of the Expert Panel's report. The constitutive model for that layer was then switched to the constitutive model intended for use throughout the remainder of the analysis, which is NorSand in this study. Robertson et al. (2019) used strain-weakening Mohr-Coulomb model since their use of NorSand model resulted in numerical divergencies. However, using NorSand in this study led to a model which was numerically stable. This difference is probably because of the different material properties implemented for NorSand model in this study compared to Robertson et al.

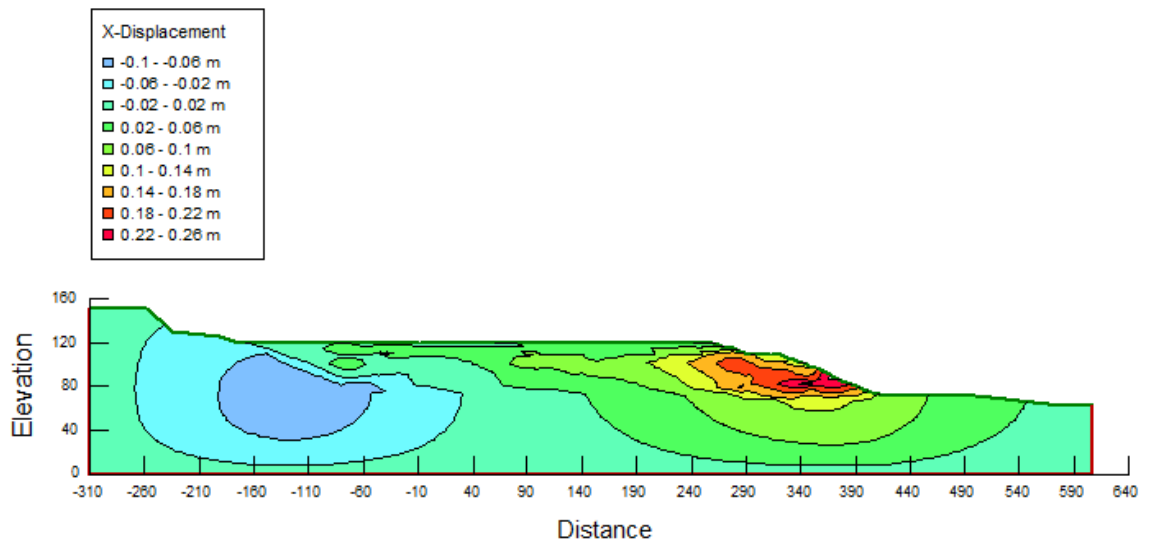
(2019). They used a high magnitude of dilatancy (χ) to capture the tailings brittle behavior in their simulations. The mentioned characteristic was the additional component of strength due to the effects of bonding between individual grains. According to them, the resulting stress-strain behavior caused numerical instabilities in the full-scale models, and preference was given to strain-weakening MC model. No such special behavior was captured in this study, and NorSand model was found to produce stable models.

Sigma/W does not allow to define stochastic variation of state parameter within the defined materials. Therefore, similar to the utilized approach by Robertson et al. (2019) in their 2D analyses, single values of ψ of +0.06 for the fine tailings and -0.02 for the coarse tailings were assigned to the tailings. They used the Robertson (2009), the Plewes et al. (1992) and the Jefferies and Been (2016) methods to estimate the state parameters of the tailings. According to them, their estimation methods showed that the ψ of the fine tailings was significantly higher than the coarse tailings. These values were assigned based on their estimation methods and to account for the looser state of the fine tailings than the sand tailings. Based on these ψ , unit weights of the fine and the coarse tailings were calculated as 19 kN/m³ and 17.3 kN/m³, respectively, which were used in the simulations.

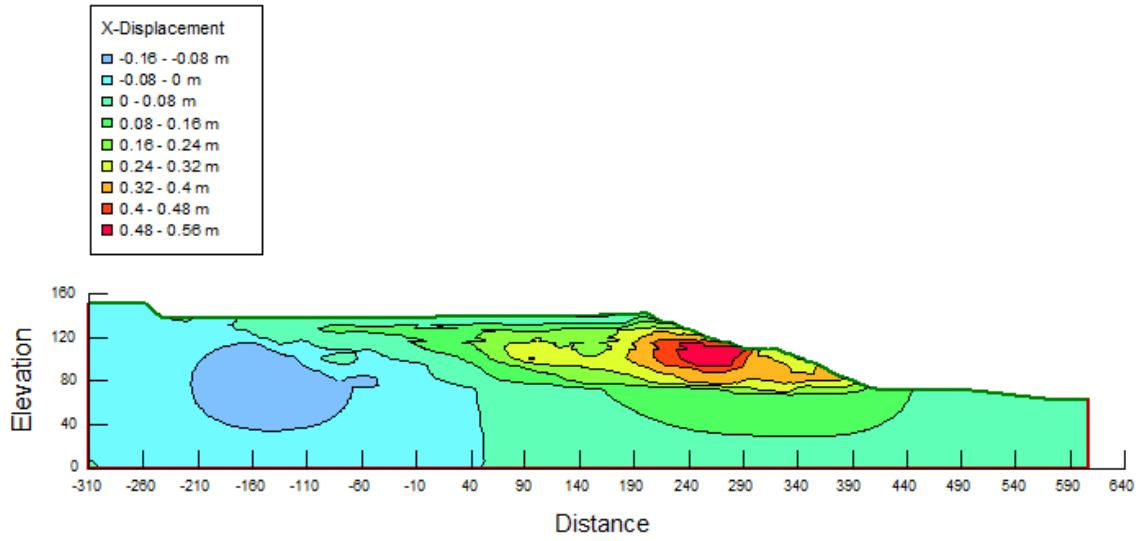
The horizontal displacement contours of the model during different construction raises are depicted in Figure 5-13. The contours of the final stage's deformation distributions presented by Robertson et al. (2019) are shown in Figure 5-14.



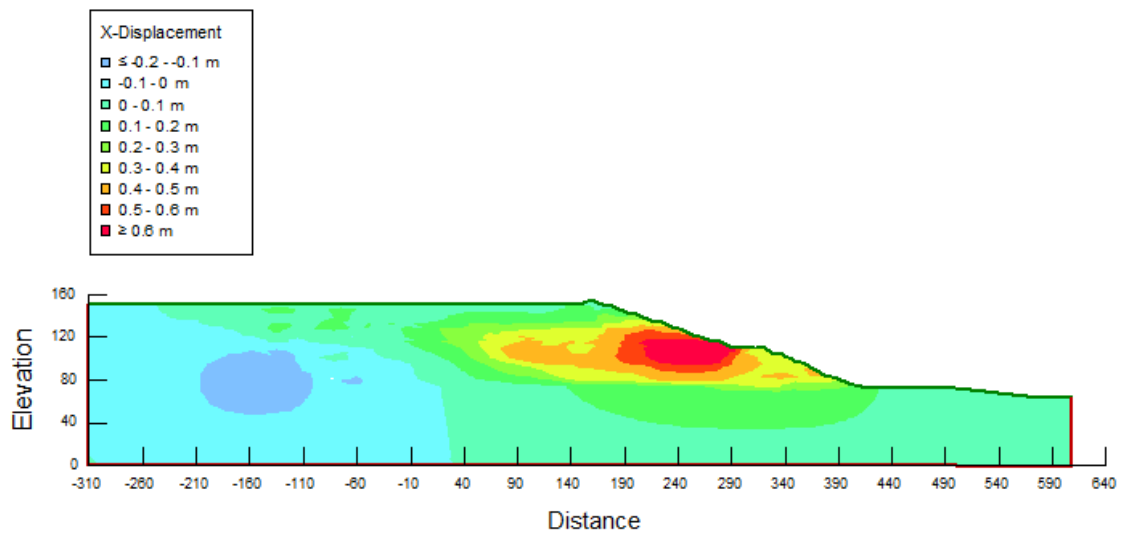
(a)



(b)



(c)



(d)

Figure 5-13. The horizontal displacement contours of (a) 3rd raising, (b) 5th raising, (c) 8th raise and (d) the final raise

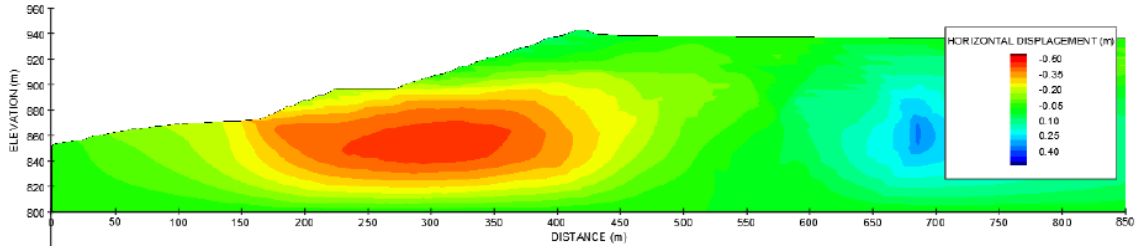
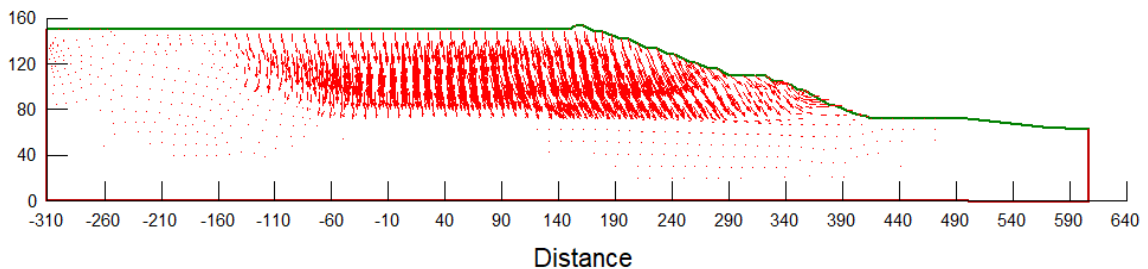


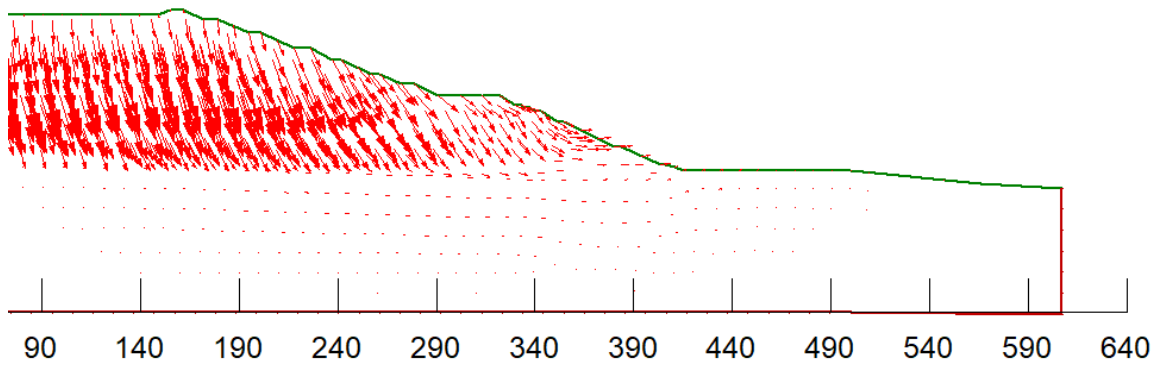
Figure 5-14. Horizontal Displacements at the end of construction Robertson et al. (2019)
(section 1-1)

These results show concentrated lateral deformations in a zone that is downstream of the crest with a maximum horizontal displacement in the order of roughly 0.75 m towards the toe of the dam. Very little deformations are observed in the upper slope. Agreeing general trends of deformations are observed in the results presented by Robertson et al. (2019) (Figure 5-13(d) and Figure 5-14) suggesting that the current model produces reasonable results. The differences between Figure 5-13(d) and Figure 5-14 are due to the different tailings' properties (i.e., iron tailings vs gold tailings) and different constitutive models (strain softening M/C vs NorSand) governing the behavior of the tailings.

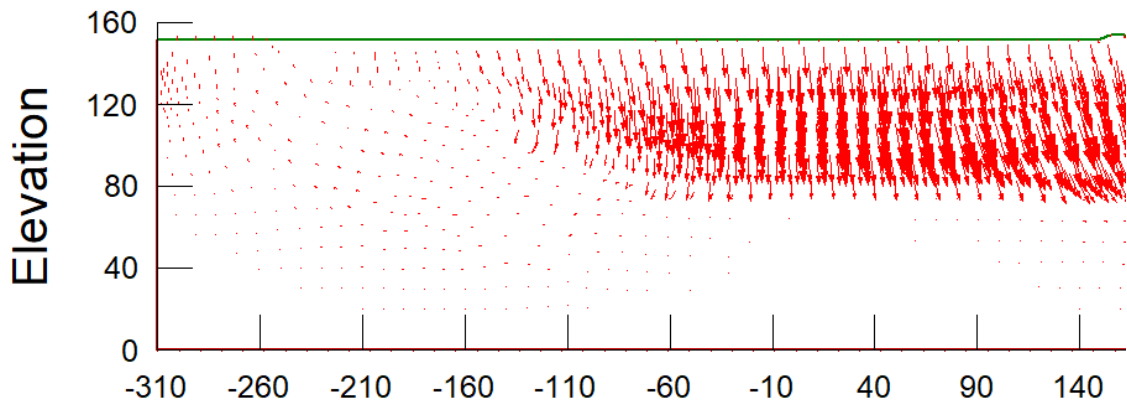
The lateral deformations in the downstream region towards the toe (compressive displacements) are a result of the dam's geometry. The slightly extensional movements in the upstream side occurred due to the tailings compression and lateral expansion. The displacement vectors are shown in Figure 5-15, depicting this trend.



(a)



(b)



(c)

Figure 5-15. X/Y displacement vectors at the end of construction (a) over all look, (b) downstream compressive deformations, and (c) upstream extensional deformations

It is established by Robertson et al. (2019) that the Brumadinho dam had high shear stresses at the end of its construction phase. The shear stress contours are shown in Figure 5-16; and the contours of η/M_{tc} of this study and Robertson et al. (2019) are shown in Figure 5-17. These figures depict high stresses generated within the body of the dam. The differences in stress ratios obtained in Figure 5-17 (a) and (b) can attribute to the selection of different constitutive models for the tailings (strain-weakening Mohr-coulomb and NorSand) as well as different material parameters.

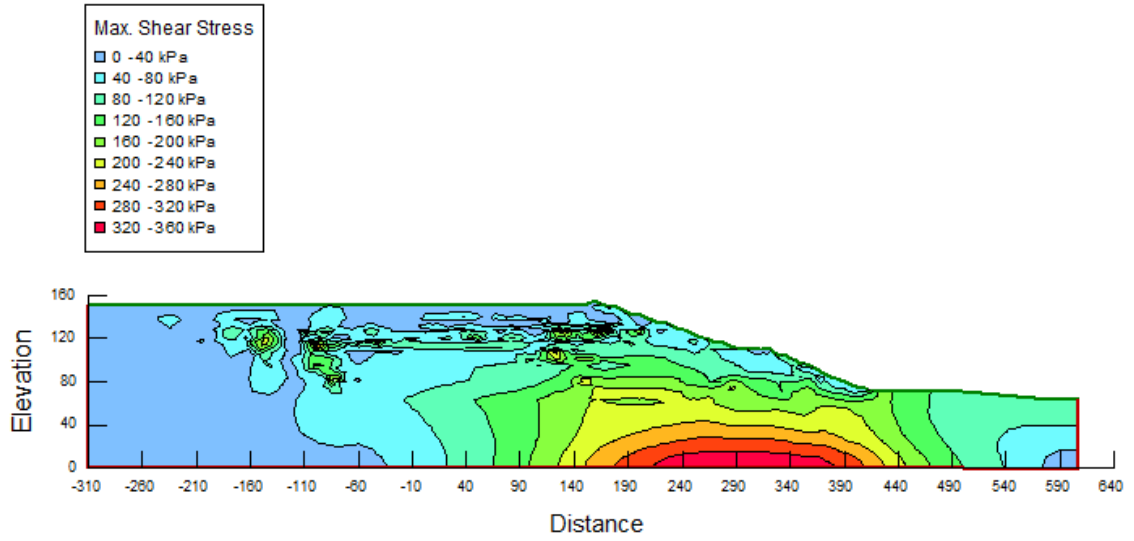
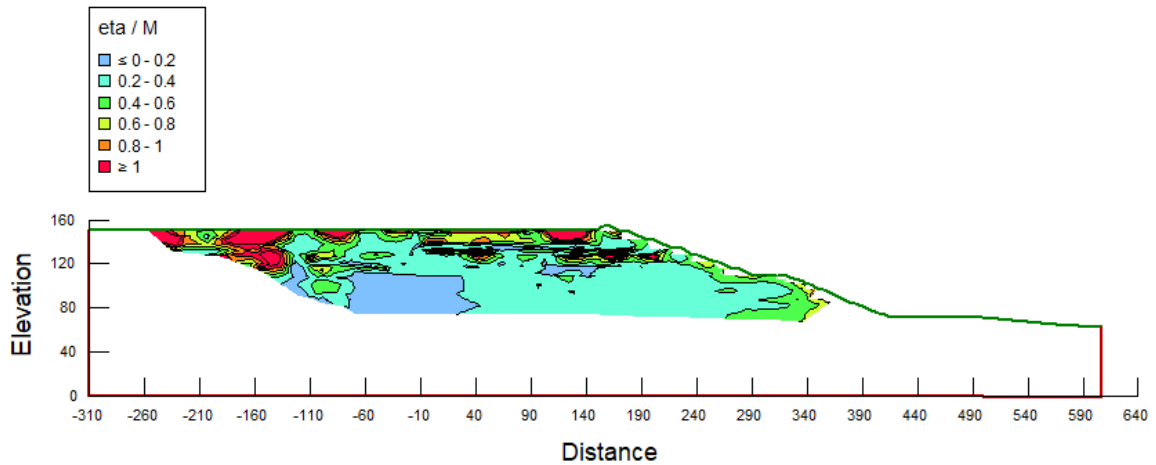
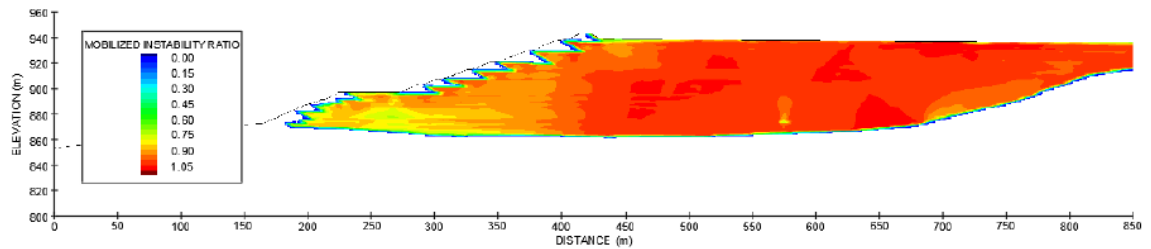


Figure 5-16: Contours of shear stresses distribution of this study



(a)



(b)

Figure 5-17: Contours of η/M_{tc} of (a) this study and (b) Robertson et al. (2019) (section 1-1)

It is also known that no localized or widespread instability was recorded during the construction period of the dam. The yielding zones (where mobilized stress ratio exceeds the yielding stress ratio) of the model at this phase are shown in Figure 5-18, illustrating very little yielding zones that most probably could produce instability of the whole dam. Coupled with this observation, a limit equilibrium analysis was performed using Slope/W by selecting Mohr-Coulomb models for the fine and coarse tailings as well as the containment berms. The same parameters shown in Table 5-5 assigned to the materials, as well as zero cohesion and 39.8° and 39.2° friction angles for fine and coarse tailings, respectively. The resultant FOS, shown in Figure 5-19, was obtained to be 2.5, confirming the stable condition of the dam.

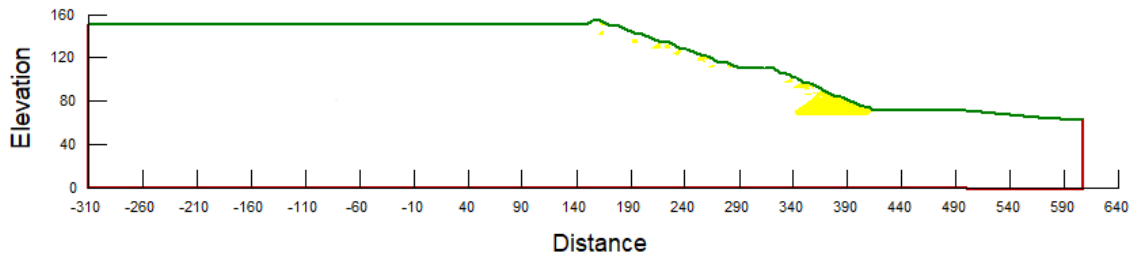


Figure 5-18. Yielding zones (colored yellow) of the model at the end of the construction

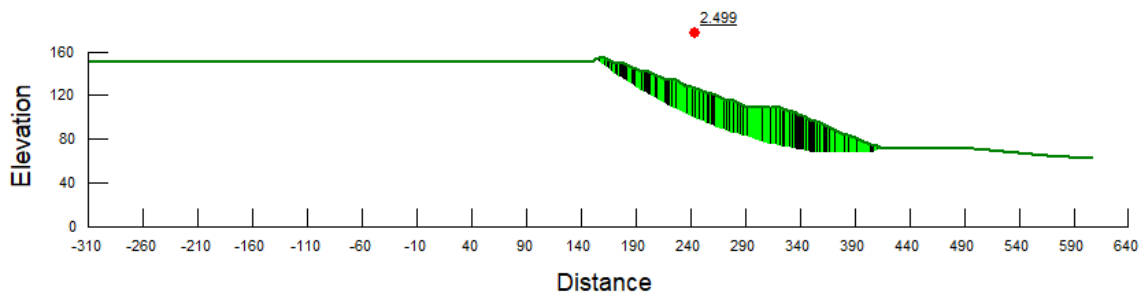


Figure 5-19. Factor of safety of the dam at the end of its construction

5.4.2 Evaluation of failure

Effect of drainage condition and strength loss in unsaturated zones

This section evaluates the effect of different conditions to see if they can result in failure of the dam. Robertson et al. (2019) concluded that the triggering mechanism was in fact the combination of strength loss of unsaturated zones as a result of cumulative rainfall, and the creep-induced internal strains.

The Expert Panel assigned undrained conditions to the stored tailings at this stage, which was done in this study as well. They simulated the strength loss of unsaturated zones by reducing strengths and reassigning the reductions to the zones above the water table. This procedure of reducing “strengths” is not possible in Sigma/W when implementing NorSand model as there is no parameter directly called strength. The unsaturated zones however, were disabled by zeroing the negative pressure head above the water table, representing the loss of suction as a

result of rainfall infiltration in unsaturated soils. The combination of drainage condition being undrained, and loss of suction in zones above water level resulted in negligible changes in x-displacement. For further clarification, the associated factor of safety for this condition was calculated. A very slight reduction, less than 15%, in factor of safety was observed (FOS=2.17, Figure 5-20), meaning the model would not become unstable with the considered scenario alone. Robertson et al. (2019) also concluded this condition alone cannot cause liquefaction and failure.

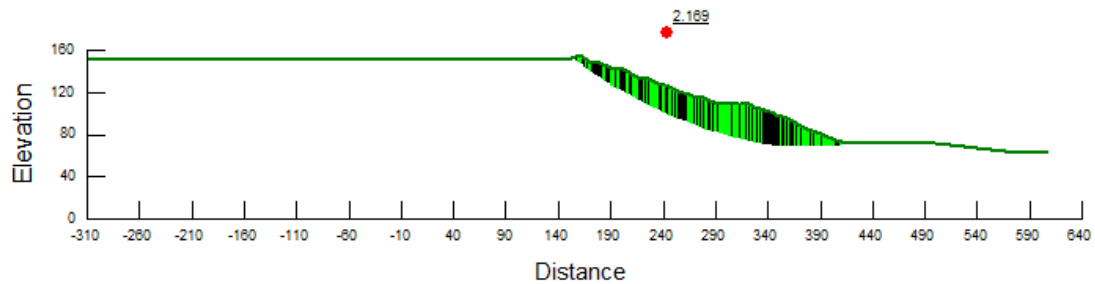


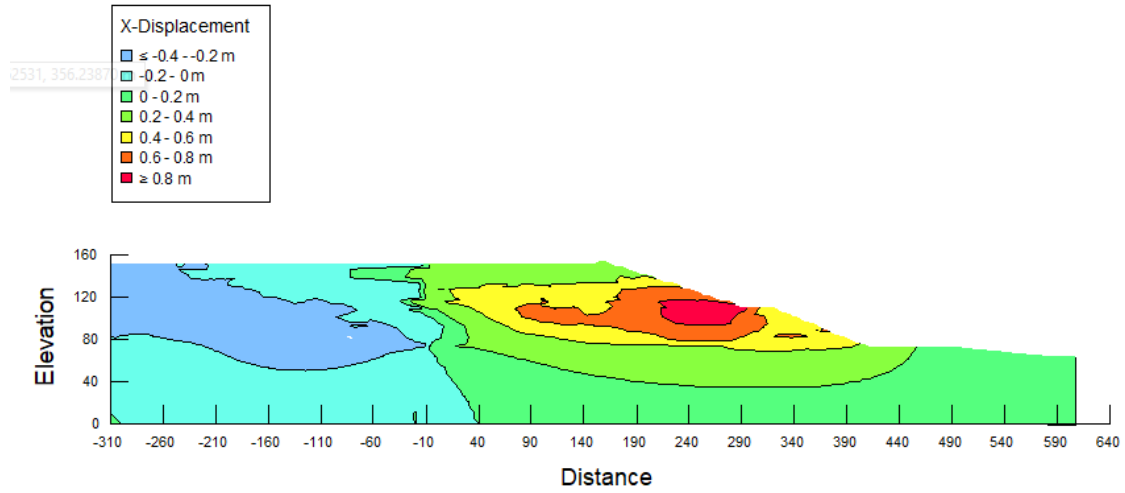
Figure 5-20. FOS of the model with zero pressure head above water level and in undrained condition

Effect of drainage condition and strength loss in unsaturated zones

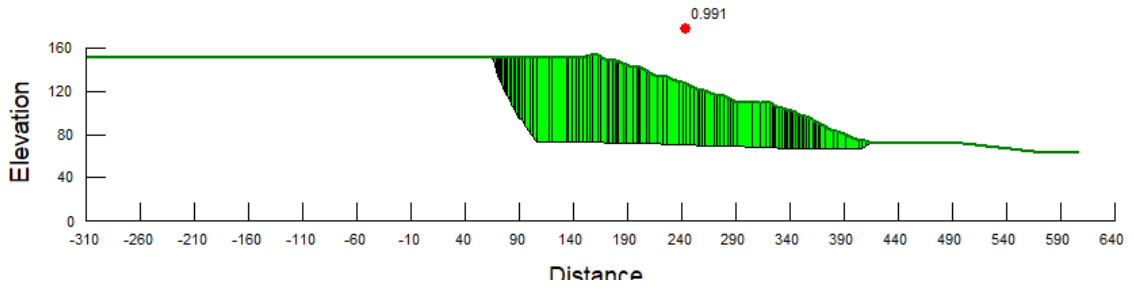
Robertson et al. (2019) associated the rainfall-induced weakening with ongoing displacements caused by creep. They modeled the creep induced displacements using an advanced method by implementing a subroutine in FLAC3D.

Such an advance method is beyond the abilities of the used software in this study, and beyond the scope of the assessments here. However, Robertson et al. (2019) reported that the addition of strength loss in unsaturated zones to a displacement of 8 to 37 cm of creep displacement recorded on the face of the dam would cause failure of the dam. Therefore, an average displacement of 15 cm was applied to the face of the modeled dam to evaluate the effect of creep-induced displacement on the dams stability. The resultant x-displacements along with its associated safety factor of less than 1 (FOS = 0.988), demonstrated in Figure 5-21 (a) and (b) respectively, demonstrate an impending failure condition. The yielding zones of the model is also shown in Figure 5-21 (c), confirming increment in these zones

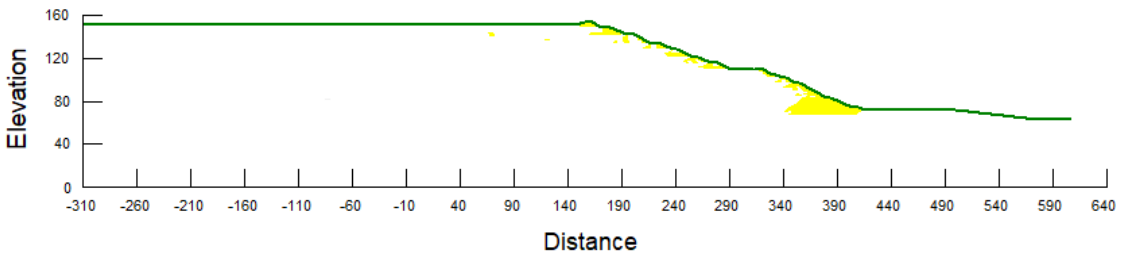
compared to Figure 5-18. Noticeable increments in shear stresses within the body of the dam (Figure 5-22 (a)) and stress ratios of η/M_{tc} (Figure 5-22b) are observed, confirming an unstable condition.



(a)

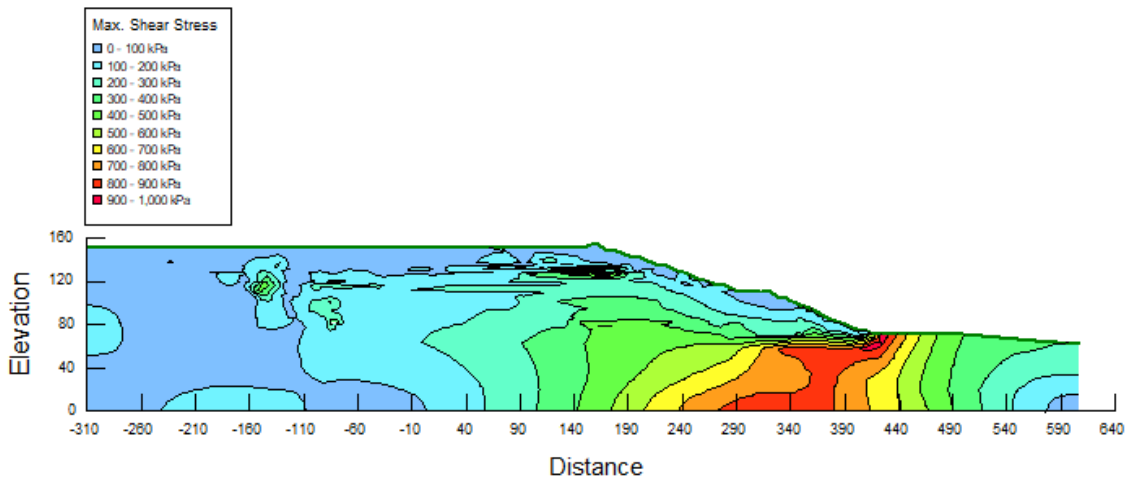


(b)

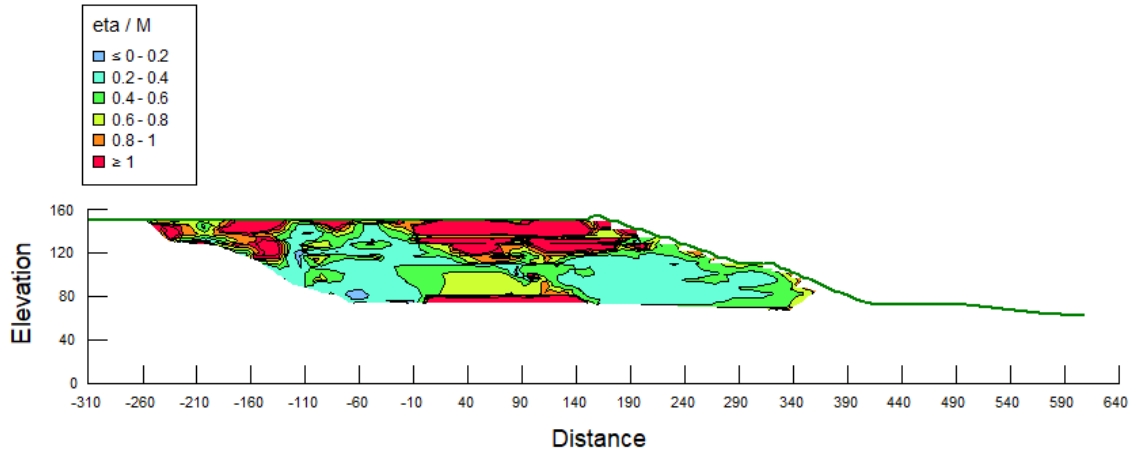


(c)

Figure 5-21. (a) x-displacement, (b) factor of safety and (c) the yielding zones of the dam after applying 15 cm deformation on its face and zeroing the suction above the water level



(a)



(b)

Figure 5-22. (a) Shear stress distribution contours and (b) η/M_{tc} contours of the dam after applying 15 cm deformation on its face and zeroing the suction above the water level

Evaluating the effect of rainfall with pore water pressure ratio (R_u) parameter

The effect of rainfall infiltration and the resulting effective stress reduction can be modeled and assessed in another way. Without applying any predefined displacements representing creep, the effect of pore water pressure is evaluated representing the effect of accumulative rainfall which was recognized as a triggering factor. This assessment was performed on the model developed at the stage of prior to failure with the zones above the piezometric line capped at 0 kPa. R_u , or pore water pressure ratio is calculated in an equation form of u/γ_z , where u is the pore-water pressure, γ is the unit weight of the soil and z is the depth below ground. The denominator (γ_z) is also known as the overburden stress. Therefore, assuming the infiltration of rainwater can cause an increase in R_u value, the associated factors of safety are computed for each case to recognize the critical case.

Figure 5-23 shows that factor of safety dramatically drops when R_u increases. It further shows that pore pressure ratio of between 0.2-0.25 results in a failure condition. The possible critical slip surfaces with some of the assigned R_u values are shown in Figure 5-24.

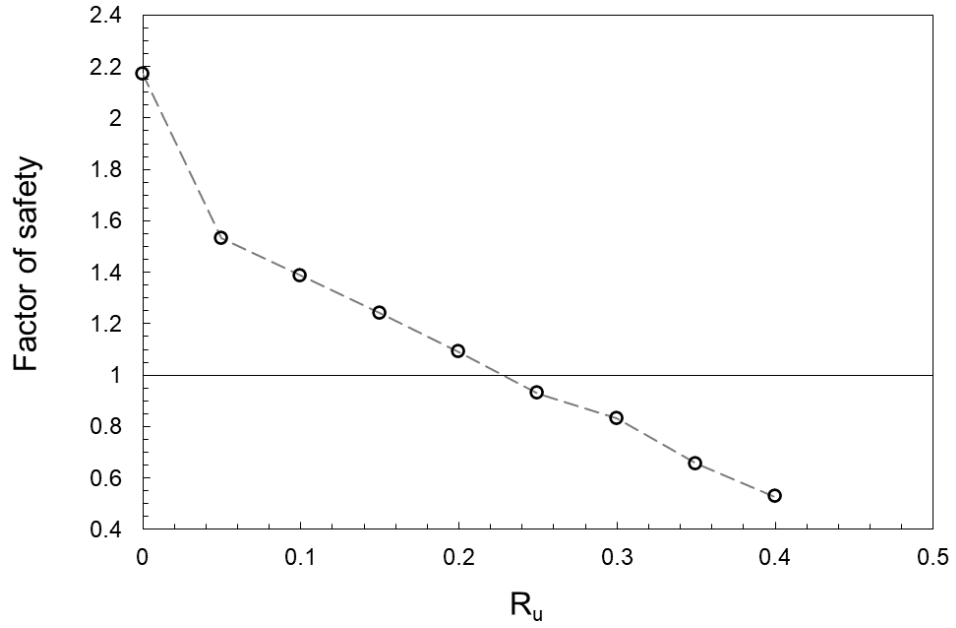
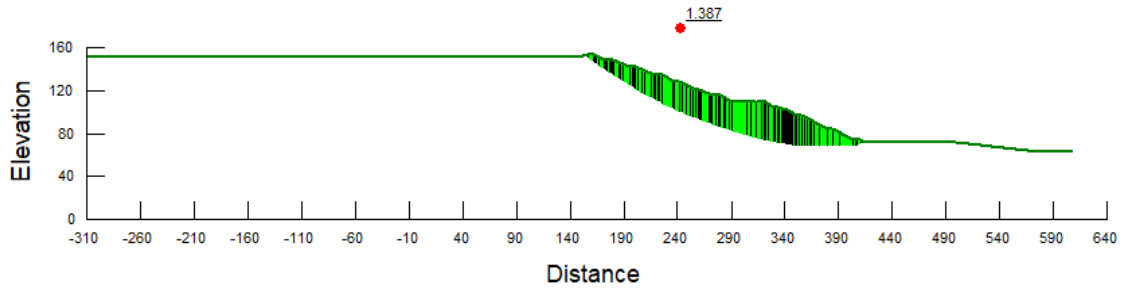
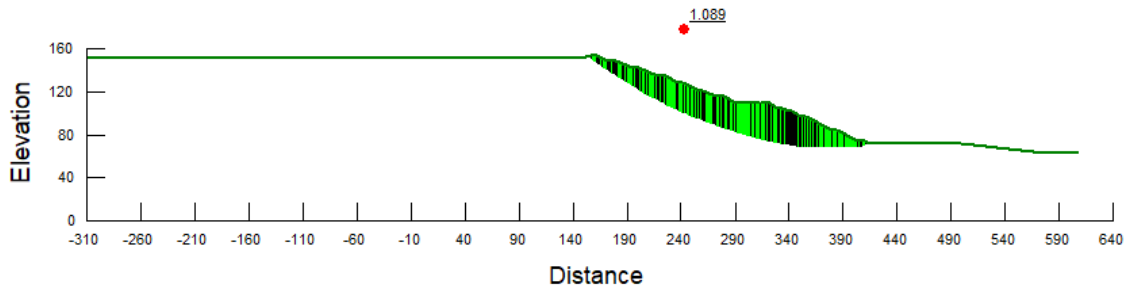


Figure 5-23. Factor of safety against pore water pressure ratio, R_u calculated from Slope/w analyses



(a)



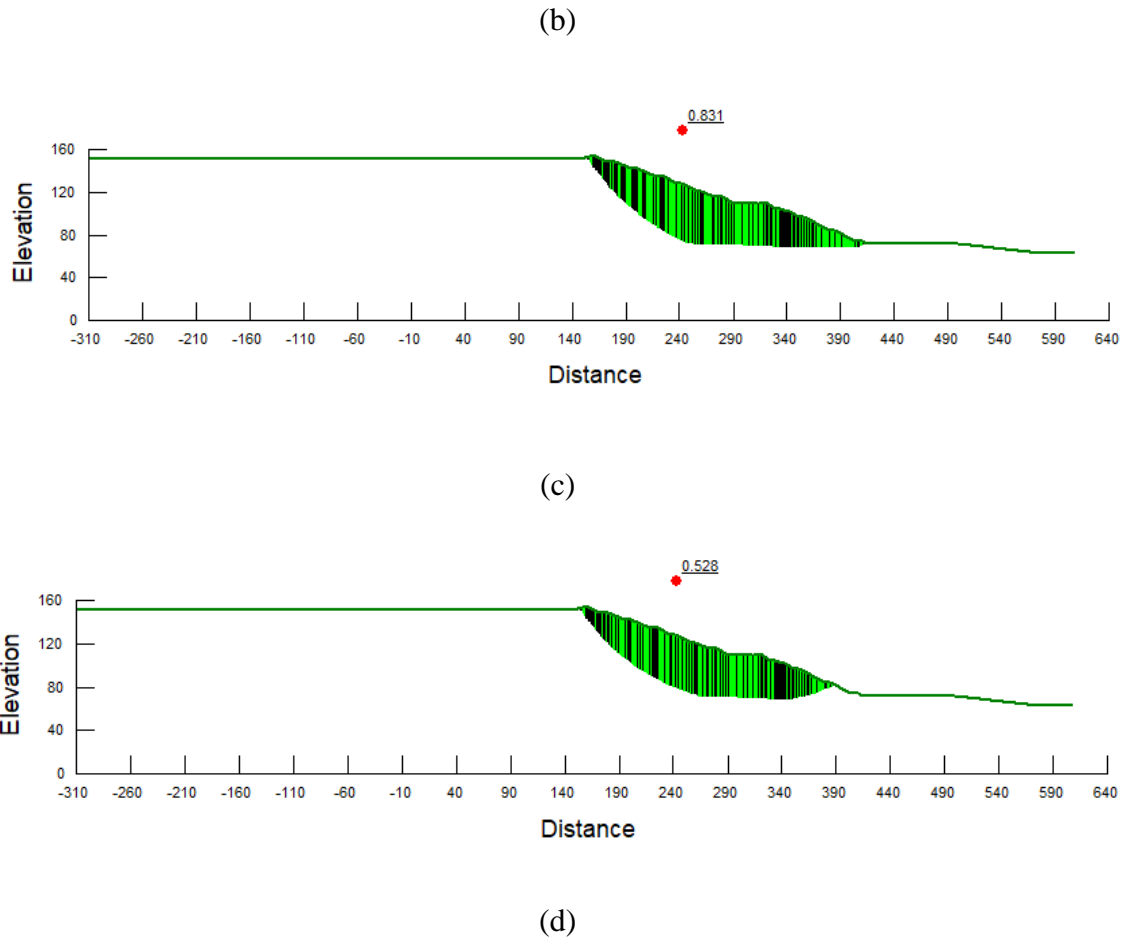


Figure 5-24. Critical slip surfaces associated with R_u values of (a) 0.1, (b) 0.2, (c) 0.3, and (d) 0.4

5.5 Conclusion

The Expert Panel of Brumadinho tailings dam was unsuccessful in using the critical state model for simulating tailings behavior, as their model did not converge. This was likely because of the high dilatancy parameter adopted by Robertson et al. (2019) for replicating the high brittle behavior of tailings. However, the NorSand model was successfully calibrated and utilized in this study with reasonable input parameters. The results show nearly comparable displacements and stress ratios to those reported by the Expert Panel. Prior to the abovementioned simulations, a model was developed simulating Fundao

tailings dam based on its construction history to verify the methodology with those presented by a technical panel investigating its failure. The load-deformation results showed a good consistency with what was described in the report. It is concluded that following the construction scenario and history of a dam's development is crucial in numerical modeling of tailings dams.

Based on the same methodology, Brumadinho tailings dam was developed. The model was generated based on the properties of two different gradations of a tailings. The modeled materials were considered to have liquefaction susceptibility by assigning NorSand model. The resultant model showed reasonable outcomes. This was confirmed by comparing the general trends of displacements with similar results presented by a technical panel who investigated the failure of the dam. The deformations mainly concentrated in two regions. LEM analyses were performed to compute the factors of safety coupled with the load-deformation analyses. Sensitivity of the model against pore-water pressure ratio, R_u , was evaluated to see how the dam is prone to the increment of this parameter, for example due to rainfall.

Chapter 6

6 Conclusions

Chapter 2 of this study examined the instability and critical state behavior of a gold mine tailings under compression and extension modes of shearing. Most specimens were prepared by moist tamping because of the higher liquefaction potential of such specimens compared to those prepared by pluviation through air or deposited as a slurry. Difference in the behavior type (limited liquefaction vs complete liquefaction) led to separate critical state lines (CSL) in specimens subjected to different modes of shearing, with a slightly looser CSL from specimens sheared only in extension compared those sheared in compression. Undrained triggering and post-liquefaction shear strength ratios (normalized by the consolidation vertical stress) as well as friction angles at the triggering of instability decreased with increasing consolidation void ratio and critical state parameter in both modes of shearing. These strength parameters were found to be greater in specimens consolidated anisotropically and then shear in the same direction (i.e., CKCU, EKEU) compared those subjected to isotropic consolidation or undergoing loading reversal from consolidation to shearing (i.e., CKEU tests). This was attributed to the enhanced interlocking and stiffer fabric of particles shearing and consolidated in the same direction compared to when they were disengaged by a change in the loading direction. Friction angles mobilized at phase transformation were also found to be a function of the loading direction and increased from 18° to 38° in respectively extension and compression loadings for the same consolidation mode. Tailings specimens subjected to undrained extensional shearing exhibited lower undrained strength ratios and friction angles, as well as higher brittleness compared to those sheared in compression. Unique trends were found between brittleness index (IB) and the maximum excess pore pressure ratio (ru_{max}) for specimens subjected to a certain consolidation and shearing direction. For a given shearing mode, these trends indicated relatively lower ru_{max} generation in anisotropically-consolidated specimens compared to those subjected to isotropic consolidation for inducing a certain IB. In summary, loading direction in consolidation and shearing were observed to have profound effects on the mobilized friction angle,

critical state line, brittleness and undrained shear strengths of tailings and this should be accounted for in analyzing the occurrence of liquefaction and stability of tailings dams. It was finally demonstrated that gold tailings often present looser (i.e., located at higher void ratios) CSLs and higher instability and post-liquefaction shear strengths than those of natural sands and silts.

In chapter 3 the drained instability of coarse and fine gold mine tailings under lateral stress relief and undrained loading paths were examined through a comprehensive series of triaxial compression tests. Instability was observed in tailings specimens subjected to effective stress unloading at a constant deviator stress (CDS) as a rapid increase in shear strain. The triggering of instability was subsequently determined based on the sign of the second-order work increment. The effective stress paths of these specimens ultimately reached the failure line of the undrained tests. In undrained loading, instability occurred as a reduction in shear resistance following the exceedance of a peak yield strength. Irrespective of the stress path and drainage condition, similar stress ratios were mobilized at the triggering of instability in specimens consolidated to the same initial stress anisotropy. Among the different parameters examined in this study, density (void ratio) and anisotropic consolidation were found to have the strongest effects on the onset of instability and static liquefaction with the triggering strength increasing with increasing density and initial deviator stress ratio. This resulted in the anisotropically-consolidated specimens exhibiting greater liquefaction triggering shear strengths compared to the isotropically-consolidated samples. Note that this doesn't mean that a steeper tailings dam would be more resistant to static liquefaction as the shear stress increment (from the initial to the instability condition) required to triggering instability reduced in anisotropically-consolidated specimens. Furthermore, as a result of their more angular particle shapes, higher fines content, and denser fabric, greater liquefaction-triggering and post-liquefaction shear strengths were mobilized in the finer tailings than those of the coarse tailings. Other than inducing instability faster, increasing the unloading rate from 0.1 to 3.0 kPa/min had little effect on the CDS stress path and the mobilized stress ratio at the triggering of instability. For each tailings, trendlines were established between undrained triggering and post-liquefaction shear strength ratios as well as the deviator

stress ratio at the triggering of instability with consolidation void ratio (e_c) and the state parameter (ψ_{cs}). Finally, irrespective of the drainage condition and consolidation history, unique critical state lines were established for each tailings studied here, with that of the finer tailings being denser (at lower void ratios) and steeper than the critical state line of the coarse tailings.

The results of Chapter 4 demonstrated that liquefaction susceptibility of tailings specimens increases with the rise of FC from 5 to 25% as the tailings load-bearing structure becomes unstable due to inactive role of added fine particles. However, with further increase of FC to 84%, the density and stiffness of the fines matrix improves which results in reduced liquefaction susceptibility. The triaxial testing results as well as the index void ratios presented in this study suggested a threshold fines content of around 25% for the examined gold tailings at which the tailings would be the most susceptible to instability and strength loss associated with undrained loading or effective stress unloading.

In chapter 5 NorSand model was successfully calibrated and utilized in this study with reasonable input parameters and modeling results show nearly comparable displacements and stress ratios to those reported by an expert panel. Before the abovementioned simulations, a model was developed simulating Fundao tailings dam based on its construction history to verify the results with those presented by a technical panel investigating its failure. The load-deformation results showed a good consistency with what was described in the report. It is concluded that following the construction scenario and history of a dam's development is crucial in numerical modeling tailings dams.

References

- Agurto-Detzel, H., Bianchi, M., Assumpção, M., Schimmel, M., Collaço, B., Ciardelli, C., Barbosa, J.R., and Calhau, J. 2016. The tailings dam failure of 5 November 2015 in SE Brazil and its preceding seismic sequence. *Geophysical Research Letters*, **43**(10): 4929–4936. Wiley Online Library.
- Al-Tarhouni, M., Simms, P., and Sivathayalan, S. 2011. Cyclic behaviour of reconstituted and desiccated–rewet thickened gold tailings in simple shear. *Canadian Geotechnical Journal*, **48**(7): 1044–1060. NRC Research Press.
- Alarcon-Guzman, A., Leonards, G.A., and Chameau, J.L. 1988. Undrained monotonic and cyclic strength of sands. *Journal of Geotechnical Engineering*, **114**(10): 1089–1109. American Society of Civil Engineers.
- de Alba, P., and Ballesterro, T.P. 2008. Effect of fines on sand residual strength after liquefaction. *In Geotechnical Earthquake Engineering and Soil Dynamics IV*. pp. 1–11.
- Altun, S., and Goktepe, A.B. 2006. Evaluation of Static Liquefaction Susceptibility of Sands with Triaxial Test. *In GeoCongress 2006: Geotechnical Engineering in the Information Technology Age*. pp. 1–4.
- American Society for Testing and Materials (ASTM), D.-14. 2014. Standard test methods for specific gravity of soil solids by water pycnometer.
- Amini, F., and Qi, G.Z. 2000. Liquefaction testing of stratified silty sands. *Journal of geotechnical and geoenvironmental engineering*, **126**(3): 208–217. American Society of Civil Engineers.
- Anderson, S.A., and Riemer, M.F. 1995. Collapse of saturated soil due to reduction in confinement. *Journal of geotechnical engineering*, **121**(2): 216–220. American Society of Civil Engineers.

- Anderson, S.A., and Sitar, N. 1995. Analysis of rainfall-induced debris flows. *Journal of Geotechnical Engineering*, **121**(7): 544–552. American Society of Civil Engineers.
- ASTM, D. 2000. 4253. Standard Test Methods for Maximum Index Density and Unit Weight of Soils Using a Vibratory Table. ASTM International,.
- ASTM, D. 2007. Standard test method for particle-size analysis of soils. West Conshohocken, PA.
- Ayoubian, A., and Robertson, P.K. 1998. Void ratio redistribution in undrained triaxial extension tests on Ottawa sand. *Canadian geotechnical journal*, **35**(2): 351–359. NRC Research Press Ottawa, Canada.
- Bahadori, H., GHALANDARZADEH, A., and Towhata, I. 2008. Effect of non plastic silt on the anisotropic behavior of sand. *Soils and foundations*, **48**(4): 531–545. The Japanese Geotechnical Society.
- Baziar, M.H., and Dobry, R. 1995. Residual strength and large-deformation potential of loose silty sands. *Journal of geotechnical engineering*, **121**(12): 896–906. American Society of Civil Engineers.
- Been, K., and Jefferies, M.G. 1985. A state parameter for sands. *Géotechnique*, **35**(2): 99–112. Thomas Telford Ltd.
- Belkhatir, M., Missoum, H., Arab, A., Della, N., and Schanz, T. 2011. Undrained shear strength of sand-silt mixture: Effect of intergranular void ratio and other parameters. *KSCE Journal of Civil Engineering*, **15**(8): 1335–1342. Springer.
- Vanden Berghe, J.-F., Ballard, J.-C., Jewell, R.A., Pirson, M., and Reh, U. 2009. Importance of shear stress anisotropy and bottom drainage on tailings dam stability: a case history. *In Proceedings of the 17th International Conference on Soil Mechanics and Geotechnical Engineering (Volumes 1, 2, 3 and 4)*. IOS Press. pp. 1626–1629.
- Bhanbhro, R. 2014. Mechanical Properties of Tailings: Basic Description of a Tailings

Material from Sweden. Luleå tekniska universitet.

- Bishop, A.W. 1971. Shear strength parameters for undisturbed and remolded soil specimens. *In* Roscoe Memorial Symp.,(1971). pp. 3–58.
- Bishop, A.W. 1973. The stability of tips and spoil heaps. *Quarterly Journal of Engineering Geology and Hydrogeology*, **6**(3–4): 335–376. Geological Society of London.
- Bishop, A.W., and Henkel, D.J. 1962. The measurement of soil properties in the triaxial test.
- Bobei, D.C., Lo, S.R., Wanatowski, D., Gnanendran, C.T., and Rahman, M.M. 2009. Modified state parameter for characterizing static liquefaction of sand with fines. *Canadian Geotechnical Journal*, **46**(3): 281–295. NRC Research Press.
- Bouckovalas, G.D., Andrianopoulos, K.I., and Papadimitriou, A.G. 2003. A critical state interpretation for the cyclic liquefaction resistance of silty sands. *Soil Dynamics and Earthquake Engineering*, **23**(2): 115–125. Elsevier.
- Boukpeti, N., Mróz, Z., and Drescher, A. 2002. A model for static liquefaction in triaxial compression and extension. *Canadian geotechnical journal*, **39**(6): 1243–1253. NRC Research Press Ottawa, Canada.
- Brand, E.W. 1981. Some thoughts on rain-induced slope failures. *Proc. 10th ICSMFE*, 1981, **3**: 373–376.
- Brignoli, E.G.M., Gotti, M., and Stokoe, K.H. 1996. Measurement of shear waves in laboratory specimens by means of piezoelectric transducers. *Geotechnical testing journal*, **19**(4): 384–397. ASTM International.
- Carraro, J.A.H., Bandini, P., and Salgado, R. 2003. Liquefaction resistance of clean and nonplastic silty sands based on cone penetration resistance. *Journal of geotechnical and geoenvironmental engineering*, **129**(11): 965–976. American Society of Civil Engineers.

- Carraro, J.A.H., Prezzi, M., and Salgado, R. 2009. Shear strength and stiffness of sands containing plastic or nonplastic fines. *Journal of geotechnical and geoenvironmental engineering*, **135**(9): 1167–1178. American Society of Civil Engineers.
- Carrera, A., Coop, M.R., and Lancellotta, R. 2011. Influence of grading on the mechanical behaviour of Stava tailings. *Géotechnique*, **61**(11): 935–946. Thomas Telford Ltd.
- Casagrande, A. 1936. Characteristics of cohesionless soils affecting the stability of slopes and earth fills. *J. Boston Society of Civil Engineers*, **23**(1): 13–32.
- Castro, G. 1969. Liquefaction of sands. ph. D. Thesis, Harvard Soil Mech.,.
- Chameau, J.-L., and Sutterer, K. 1994. Influence of fines in liquefaction potential and steady state considerations. *In International conference on soil mechanics and foundation engineering*. pp. 183–184.
- Chang, N.-Y., Hsieh, N.-P., Samuelson, D.L., and Horita, M. 1982. Effect of Frequency on Liquefaction Potential of Saturated Monterey No. O Sand. *In Computational Methods and Experimental Measurements*. Springer. pp. 433–446.
- Chang, N., Heymann, G., and Clayton, C. 2011. The effect of fabric on the behaviour of gold tailings. *Géotechnique*, **61**(3): 187–197. Thomas Telford Ltd.
- Cherif Taiba, A., Mahmoudi, Y., Belkhatir, M., Kadri, A., and Schanz, T. 2018. Experimental characterization of the undrained instability and steady state of silty sand soils under monotonic loading conditions. *International Journal of Geotechnical Engineering*, **12**(5): 513–529. Taylor & Francis.
- Chien, L.-K., Oh, Y.-N., and Chang, C.-H. 2002. Effects of fines content on liquefaction strength and dynamic settlement of reclaimed soil. *Canadian Geotechnical Journal*, **39**(1): 254–265. NRC Research Press Ottawa, Canada.
- Cho, G.-C., Dodds, J., and Santamarina, J.C. 2007. Closure to “Particle Shape Effects on Packing Density, Stiffness, and Strength: Natural and Crushed Sands” by Gye-Chun

- Cho, Jake Dodds, and J. Carlos Santamarina. Journal of geotechnical and geoenvironmental engineering, **133**(11): 1474. American Society of Civil Engineers.
- Cho, G.C., Dodds, J., and Santamarina, J.C. 2004. Particle shape effects on packing density. Stiffness and Strength of Natural and Crushed Sands-Internal Report, Georgia Institute of Technology, 33pp.
- Chu, J., and Leong, W.K. 2002. Effect of fines on instability behaviour of loose sand. Geotechnique, **52**(10): 751–755. Thomas Telford Ltd.
- Chu, J., Leong, W.K., Loke, W.L., and Wanatowski, D. 2012. Instability of loose sand under drained conditions. Journal of Geotechnical and Geoenvironmental Engineering, **138**(2): 207–216. American Society of Civil Engineers.
- Chu, J., Leroueil, S., and Leong, W.K. 2003. Unstable behaviour of sand and its implication for slope instability. Canadian Geotechnical Journal, **40**(5): 873–885. NRC Research Press.
- Chu, J., and Wanatowski, D. 2008. Instability conditions of loose sand in plane strain. Journal of Geotechnical and Geoenvironmental Engineering, **134**(1): 136–142. American Society of Civil Engineers.
- Chung, E.K.F. 1985. Effects of stress path and prestrain history on the undrained monotonic and cyclic loading behaviour of saturated sand. University of British Columbia.
- Cloud Jr, P.E. 1964. Geology: Stratigraphy and Sedimentation. By WC Krumbein and LL Sloss. Freeman, San Francisco, ed. 2, 1963. 676 pp. Illus. \$10.50. Science, **143**(3602): 124–125. American Association for the Advancement of Science.
- Colliat-Dangus, J.L., Desrues, J., and Foray, P. 1988. Triaxial testing of granular soil under elevated cell pressure. *In* Advanced triaxial testing of soil and rock. ASTM International.
- Daouadji, A., AlGali, H., Darve, F., and Zeghloul, A. 2010. Instability in Granular

- Materials: Experimental Evidence of Diffuse Mode of Failure for Loose Sands. *Journal of Engineering Mechanics*, **136**(5): 575–588. American Society of Civil Engineers (ASCE). doi:10.1061/(asce)em.1943-7889.0000101.
- Darve, F., and Laouafa, F. 2000. Instabilities in granular materials and application to landslides. *Mechanics of Cohesive-frictional Materials: An International Journal on Experiments, Modelling and Computation of Materials and Structures*, **5**(8): 627–652. Wiley Online Library.
- Doanh, T., Ibraim, E., and Matiotti, R. 1997. Undrained instability of very loose Hostun sand in triaxial compression and extension. Part 1: experimental observations. *Mechanics of Cohesive-frictional Materials: An International Journal on Experiments, Modelling and Computation of Materials and Structures*, **2**(1): 47–70. Wiley Online Library.
- Dobry, R., and Alvarez, L. 1967. Seismic failures of Chilean tailings dams. *Journal of Soil Mechanics & Foundations Div.*,
- Dong, Q., Xu, C., Cai, Y., Juang, H., Wang, J., Yang, Z., and Gu, C. 2016. Drained instability in loose granular material. *International Journal of Geomechanics*, **16**(2): 4015043. American Society of Civil Engineers.
- Drucker, D.C. 1957. A definition of stable inelastic material. BROWN UNIV PROVIDENCE RI.
- Eckersley, D. 1990. Instrumented laboratory flowslides. *Geotechnique*, **40**(3): 489–502. Thomas Telford Ltd.
- Enomoto, T. 2019. Liquefaction and post-liquefaction properties of sand-silt mixtures and undisturbed silty sands. *Soils and Foundations*, **59**(6): 2311–2323. Elsevier.
- Finge, Z., Doanh, T., and Dubujet, P. 2006. Undrained anisotropy of Hostun RF loose sand: new experimental investigations. *Canadian geotechnical journal*, **43**(11): 1195–1212. NRC Research Press.

- Foray, P., Balachowski, L., and Colliat, J.-L. 1998. Bearing capacity of model piles driven into dense overconsolidated sands. *Canadian Geotechnical Journal*, **35**(2): 374–385. NRC Research Press Ottawa, Canada.
- Fourie, A.B., Blight, G.E., and Papageorgiou, G. 2001. Static liquefaction as a possible explanation for the Merriespruit tailings dam failure. *Canadian Geotechnical Journal*, **38**(4): 707–719. NRC Research Press Ottawa, Canada.
- Fourie, A.B., and Papageorgiou, G. 2001. Defining an appropriate steady state line for Merriespruit gold tailings. *Canadian Geotechnical Journal*, **38**(4): 695–706. NRC Research Press.
- Fourie, A.B., and Tshabalala, L. 2005. Initiation of static liquefaction and the role of K_0 consolidation. *Canadian geotechnical journal*, **42**(3): 892–906. NRC Research Press.
- Fukushima, S., and Tatsuoka, F. 1984. Strength and deformation characteristics of saturated sand at extremely low pressures. *Soils and Foundations*, **24**(4): 30–48. The Japanese Geotechnical Society.
- Gajo, A., and Piffer, L. 1999. The effects of preloading history on the undrained behaviour of saturated loose sand. *Soils and Foundations*, **39**(6): 43–53. The Japanese Geotechnical Society.
- Gajo, A., Piffer, L., and De Polo, F. 2000. Analysis of certain factors affecting the unstable behaviour of saturated loose sand. *Mechanics of Cohesive-frictional Materials: An International Journal on Experiments, Modelling and Computation of Materials and Structures*, **5**(3): 215–237. Wiley Online Library.
- Gajo, A., and Wood, M. 1999. Severn–Trent sand: a kinematic-hardening constitutive model: the q – p formulation. *Géotechnique*, **49**(5): 595–614. Thomas Telford Ltd.
- Gennaro, V. De, Canou, J., Dupla, J.C., and Benahmed, N. 2004. Influence of loading path on the undrained behaviour of a medium loose sand. *Canadian Geotechnical Journal*, **41**(1): 166–180. NRC Research Press.

- Gens, A. 1982. Stress-strain characteristics of a low plasticity clay. PhD. Thesis, Imperial College of Science and Technology, University of London.
- Georgiannou, V.N. 1988. The behaviour of clayey sands under monotonic and cyclic loading. Imperial College London (University of London).
- Ghionna, V.N., and Porcino, D. 2006. Liquefaction resistance of undisturbed and reconstituted samples of a natural coarse sand from undrained cyclic triaxial tests. *Journal of Geotechnical and Geoenvironmental Engineering*, **132**(2): 194–202. American Society of Civil Engineers.
- Guo, P. 2010. Effect of density and compressibility on K_0 of cohesionless soils. *Acta Geotechnica*, **5**(4): 225–238. Springer.
- HANZAWA, H. 1980. Undrained strength and stability analysis for a quick sand. *Soils and Foundations*, **20**(2): 17–29. The Japanese Geotechnical Society.
- Harp, E.L., Wells, W.G., and Sarmiento, J.G. 1990. Pore pressure response during failure in soils. *Geological Society of America Bulletin*, **102**(4): 428–438. Geological Society of America.
- Hill, R. 1958. A general theory of uniqueness and stability in elastic-plastic solids. *Journal of the Mechanics and Physics of Solids*, **6**(3): 236–249. Elsevier.
- Høeg, K., Dyvik, R., and Sandbækken, G. 2000. Strength of undisturbed versus reconstituted silt and silty sand specimens. *Journal of geotechnical and geoenvironmental engineering*, **126**(7): 606–617. American Society of Civil Engineers.
- Huang, A.B., and Huang, Y.T. 2007. Undisturbed sampling and laboratory shearing tests on a sand with various fines contents. *Soils and foundations*, **47**(4): 771–781. Elsevier.
- Hyodo, M., Tanimizu, H., Yasufuku, N., and Murata, H. 1994. Undrained cyclic and monotonic triaxial behaviour of saturated loose sand. *Soils and foundations*, **34**(1):

19–32. The Japanese Geotechnical Society.

IMAM, S.M.R., Morgenstern, N.R., Robertson, P.K., and CHAN, D.H. 2002. Yielding and flow liquefaction of loose sand. *Soils and Foundations*, **42**(3): 19–31. The Japanese Geotechnical Society.

Ishihara, K. 1993. Liquefaction and flow failure during earthquakes. *Geotechnique*, **43**(3): 351–451. Thomas Telford Ltd.

Ishihara, K., Tatsuoka, F., and Yasuda, S. 1975. Undrained deformation and liquefaction of sand under cyclic stresses. *Soils and foundations*, **15**(1): 29–44. The Japanese Geotechnical Society.

Ishihara, K., Yasuda, S., and Yoshida, Y. 1990. Liquefaction-induced flow failure of embankments and residual strength of silty sands. *Soils and Foundations*, **30**(3): 69–80. The Japanese Geotechnical Society.

Jafarzadeh, F., Javaheri, H., Sadek, T., and Wood, D.M. 2008. Simulation of anisotropic deviatoric response of Hostun sand in true triaxial tests. *Computers and Geotechnics*, **35**(5): 703–718. Elsevier.

Jantzer, I., Bjelkevik, A., and Pousette, K. 2008. Material properties of Tailings from Swedish mines. *In Nordiska Geoteknikermötet: 03/09/2008-06/09/2008*. Norsk Geoteknisk Forening. pp. 229–235.

Jefferies, M., and Been, K. 2015. *Soil liquefaction: a critical state approach*. CRC press.

Jefferies, M., and Been, K. 2016. *Soil Liquefaction: A Steady State Approach*. CRC Press, Taylor and Francis Group, LLC, Boca Raton.

Jefferies, M., and Been, K. 2019. *Soil liquefaction: a critical state approach*. CRC press.

Jefferies, M.G. 1993. Nor-Sand: a simple critical state model for sand. *Géotechnique*, **43**(1): 91–103. Thomas Telford Ltd.

Jefferies, M.G., and Shuttle, D.A. 2005. NorSand: Features, calibration and use. *In Soil*

- Constitutive Models: Evaluation, Selection, and Calibration. pp. 204–236.
- Johansson, L. 1990. Geomechanical properties of tailings: a study of backfill materials for mines. Luleå tekniska universitet.
- Kato, S., Ishihara, K., and Towhata, I. 2001. Undrained shear characteristics of saturated sand under anisotropic consolidation. *Soils and Foundations*, **41**(1): 1–11. The Japanese Geotechnical Society.
- Keyhani, R., and Haeri, S.M. 2013. Evaluation of the effect of anisotropic consolidation and principle stress rotation on undrained behavior of silty sands. *Scientia Iranica*, **20**(6): 1637–1653. Sharif University of Technology.
- Khoa, H.D.V., Georgopoulos, I.O., Darve, F., and Laouafa, F. 2006. Diffuse failure in geomaterials: Experiments and modelling. *Computers and Geotechnics*, **33**(1): 1–14. Elsevier.
- Kossoff, D., Dubbin, W.E., Alfredsson, M., Edwards, S.J., Macklin, M.G., and Hudson-Edwards, K.A. 2014. Mine tailings dams: characteristics, failure, environmental impacts, and remediation. *Applied Geochemistry*, **51**: 229–245. Elsevier.
- Kuerbis, R., Negussey, D., and Vaid, Y.P. 1988. Effect of gradation and fines content on the undrained response of sand. *Geotechnical special publication*, (21): 330–345. American Society of Civil Engineers (ASCE).
- Kuerbis, R., and Vaid, Y.P. 1988. Sand sample preparation-the slurry deposition method. *Soils and Foundations*, **28**(4): 107–118. The Japanese Geotechnical Society.
- Kwa, K.A., and Airey, D.W. 2017. Effects of fines on liquefaction behaviour in well-graded materials. *Canadian Geotechnical Journal*, **54**(10): 1460–1471. NRC Research Press.
- Ladd, R.S. 1978. Preparing test specimens using undercompaction. *Geotechnical Testing Journal*, **1**(1): 16–23. ASTM International.

- Lade, P. V. 1992. Static instability and liquefaction of loose fine sandy slopes. *Journal of Geotechnical Engineering*, **118**(1): 51–71. American Society of Civil Engineers.
- Lade, P. V. 1993. Initiation of static instability in the submarine Nerlerk berm. *Canadian Geotechnical Journal*, **30**(6): 895–904. NRC Research Press Ottawa, Canada.
- Lade, P. V. 2002. Instability, shear banding, and failure in granular materials. *International journal of solids and structures*, **39**(13–14): 3337–3357. Elsevier.
- Lade, P. V, Nelson, R.B., and Ito, Y.M. 1987. Nonassociated flow and stability of granular materials. *Journal of Engineering Mechanics*, **113**(9): 1302–1318. American Society of Civil Engineers.
- Lade, P. V, and Pradel, D. 1990. Instability and plastic flow of soils. I: Experimental observations. *Journal of engineering mechanics*, **116**(11): 2532–2550. American Society of Civil Engineers.
- Lade, P. V, and Yamamuro, J.A. 1997. Effects of nonplastic fines on static liquefaction of sands. *Canadian Geotechnical Journal*, **34**(6): 918–928. NRC Research Press.
- Lashkari, A., Karimi, A., Fakharian, K., and Kaviani-Hamedani, F. 2017. Prediction of undrained behavior of isotropically and anisotropically consolidated Firoozkuh sand: instability and flow liquefaction. *International Journal of Geomechanics*, **17**(10): 4017083. American Society of Civil Engineers.
- Lee, K.L. 1965. Triaxial compressive strength of saturated sand under seismic loading conditions. University of California, Berkeley.
- LePoudre, D.C. 2015. Examples, statistics and failure modes of tailings dams and consequences of failure. *In Proceedings of the 2015 Canadian Dam Association Conference*, Mississauga, Ontario, Canada.
- Leroueil, S. 2001. Natural slopes and cuts: movement and failure mechanisms. *Géotechnique*, **51**(3): 197–243. Thomas Telford Ltd.

- Li, X.S., and Dafalias, Y.F. 2000. Dilatancy for cohesionless soils. *Geotechnique*, **50**(4): 449–460. Thomas Telford Ltd.
- LICENSE, G.N.U.L.G.P. 1991. GNU Lesser General Public License.
- Lo, S.R., Rahman, M.D., and Bobei, D. 2008. Limited flow behaviour of sand with fines under monotonic and cyclic loading. *In Geotechnical Engineering for Disaster Mitigation and Rehabilitation*. Springer. pp. 201–209.
- Lottermoser, B.G. 2010. Mine Wastes: Characterization, treatment and environmental impacts. *Mine Wastes: Characterization, Treatment and Environmental Impacts*.
- Lourenço, S.D.N., Wang, G.-H., and Chu, J. 2011. Aspects of sand behaviour by modified constant shear drained tests. *Environmental Earth Sciences*, **62**(4): 865–870. Springer.
- Manzari, M.T., and Dafalias, Y.F. 1997. A critical state two-surface plasticity model for sands. *Geotechnique*, **47**(2): 255–272. Thomas Telford Ltd.
- Matiotti, R., Ibraim, E., and Doanh, T. 1995. Undrained behaviour of very loose Hostun RF sand in triaxial compression and extension. *In Numerical models in geomechanics*. pp. 119–124.
- McPhail, G.I., and Wagner, J.C. 1987. Disposal of residues. *The Extractive Metallurgy of Gold in South Africa*, The Chamber of Mines of South Africa, **2**: 655–707.
- Mesri, G., and Hayat, T.M. 1993. The coefficient of earth pressure at rest. *Canadian geotechnical journal*, **30**(4): 647–666. NRC Research Press Ottawa, Canada.
- Mitchell, J.K., and Soga, K. 2005. *Fundamentals of soil behavior*. John Wiley & Sons New York.
- Mittal, H.K., and Hardy, R.M. 1977. Geotechnical aspects of a tar sand tailings dyke. *In Geotechnical Practice for Disposal of Solid Waste Materials*. ASCE. pp. 327–347.
- Mittal, H.K., and Morgenstern, N.R. 1975. Parameters for the design of tailings dams.

- Canadian Geotechnical Journal, **12**(2): 235–261. NRC Research Press Ottawa, Canada.
- Miura, S., and Toki, S. 1982. A sample preparation method and its effect on static and cyclic deformation-strength properties of sand. *Soils and foundations*, **22**(1): 61–77. The Japanese Geotechnical Society.
- Moghaddam, R., Riveros, G., and Farhangi, S. (n.d.). A Finite Element Analysis of the Fundão Dam Failure.
- Monkul, M.M., Etminan, E., and Şenol, A. 2017. Coupled influence of content, gradation and shape characteristics of silts on static liquefaction of loose silty sands. *Soil Dynamics and Earthquake Engineering*, **101**: 12–26. Elsevier.
- Monkul, M.M., Yamamuro, J.A., and Lade, P. V. 2011. Failure, instability, and the second work increment in loose silty sand. *Canadian Geotechnical Journal*, **48**(6): 943–955. NRC Research Press.
- Morgenstern, N.R., Vick, S.G., Viotti, C.B., and Watts, B.D. 2016. Fundão tailings dam review panel report on the immediate causes of the failure of the Fundão dam. Cleary Gottlieb Steen & Hamilton LLP, New York,.
- Muhammad, K. 2013. Case history-based analysis of liquefaction in sloping ground. University of Illinois at Urbana-Champaign.
- Murthy, T.G., Loukidis, D., Carraro, J.A.H., Prezzi, M., and Salgado, R. 2007. Undrained monotonic response of clean and silty sands. *Géotechnique*, **57**(3): 273–288. Thomas Telford Ltd.
- Naeini, S.A., and Baziar, M.H. 2004. Effect of fines content on steady-state strength of mixed and layered samples of a sand. *Soil Dynamics and Earthquake Engineering*, **24**(3): 181–187. Elsevier.
- Ni, Q., Tan, T.S., Dasari, G.R., and Hight, D.W. 2004. Contribution of fines to the compressive strength of mixed soils. *Géotechnique*, **54**(9): 561–569. Thomas

Telford Ltd.

- Olson, S.M. 2002. Liquefaction analysis of level and sloping ground using field case histories and penetration resistance. Mid-America Earthquake Center CD Release 02-02,.
- Olson, S.M., and Mattson, B.B. 2008. Mode of shear effects on yield and liquefied strength ratios. Canadian geotechnical journal, **45**(4): 574–587. NRC Research Press.
- Olson, S.M., and Stark, T.D. 2002. Liquefied strength ratio from liquefaction flow failure case histories. Canadian Geotechnical Journal, **39**(3): 629–647. NRC Research Press.
- Olson, S.M., and Stark, T.D. 2003a. Yield strength ratio and liquefaction analysis of slopes and embankments. Journal of Geotechnical and Geoenvironmental Engineering, **129**(8): 727–737. American Society of Civil Engineers.
- Olson, S.M., and Stark, T.D. 2003b. Use of laboratory data to confirm yield and liquefied strength ratio concepts. Canadian Geotechnical Journal, **40**(6): 1164–1184. NRC Research Press Ottawa, Canada.
- Olson, S.M., Stark, T.D., Walton, W.H., and Castro, G. 2000. 1907 static liquefaction flow failure of the north dike of Wachusett dam. Journal of Geotechnical and Geoenvironmental engineering, **126**(12): 1184–1193. American Society of Civil Engineers.
- Omar, T., and Sadrekarimi, A. 2015. Specimen size effects on behavior of loose sand in triaxial compression tests. Canadian Geotechnical Journal, **52**(6): 732–746. NRC Research Press.
- Papadopoulou, A., and Tika, T. 2008. The effect of fines on critical state and liquefaction resistance characteristics of non-plastic silty sands. Soils and foundations, **48**(5): 713–725. Elsevier.

- Park, J., and Santamarina, J.C. 2017. Revised soil classification system for coarse-fine mixtures. *Journal of Geotechnical and Geoenvironmental Engineering*, **143**(8): 4017039. American Society of Civil Engineers.
- Pitman, T.D., Robertson, P.K., and Segoo, D.C. 1994. Influence of fines on the collapse of loose sands. *Canadian Geotechnical Journal*, **31**(5): 728–739. NRC Research Press Ottawa, Canada.
- Plewes, H.D., Davies, M.P., and Jefferies, M.G. 1992. CPT based screening procedure for evaluating liquefaction susceptibility. *In Proceedings of the 45th Canadian Geotechnical Conference*, Toronto, Ont. pp. 1–9.
- Prisco, C. di, Matioti, R., and Nova, R. 1995. Theoretical investigation of the undrained stability of shallow submerged slopes. *Géotechnique*, **45**(3): 479–496. Thomas Telford Ltd.
- Qiu, Y., and Segoo, D.C. 2001. Laboratory properties of mine tailings. *Canadian Geotechnical Journal*, **38**(1): 183–190. NRC Research Press.
- Rabbi, A.T.M.Z., Rahman, M.M., and Cameron, D. 2019. Critical state study of natural silty sand instability under undrained and constant shear drained path. *International Journal of Geomechanics*, **19**(8): 4019083. American Society of Civil Engineers.
- Rabbi, A.T.M.Z., Rahman, M.M., and Cameron, D.A. 2018. Undrained behavior of silty sand and the role of isotropic and K_0 consolidation. *Journal of Geotechnical and Geoenvironmental Engineering*, **144**(4): 4018014. American Society of Civil Engineers.
- Reid, D., Fanni, R., Koh, K., and Orea, I. 2018. Characterisation of a subaqueously deposited silt iron ore tailings. *Géotechnique Letters*, **8**(4): 278–283. Thomas Telford Ltd.
- Riemer, M.F., and Seed, R.B. 1997. Factors affecting apparent position of steady-state line. *Journal of geotechnical and geoenvironmental engineering*, **123**(3): 281–288.

American Society of Civil Engineers.

Riveros, G.A., and Sadrekarimi, A. 2019. Static liquefaction analysis of the Fundão dam failure. *In Sustainable and Safe Dams Around the World*. CRC Press. pp. 3354–3367.

Riveros, G.A., and Sadrekarimi, A. 2020. Static Liquefaction Behaviour of Gold Mine Tailings. *Canadian Geotechnical Journal*, (ja).

Robertson, P.K. 2009. Interpretation of cone penetration tests—a unified approach. *Canadian geotechnical journal*, **46**(11): 1337–1355.

Robertson, P.K., de Melo, L., Williams, D.J., and Ward Wilson, G. 2019. Report of the expert panel on the technical causes of the failure of Feijão Dam I. Prepared for Vale Ltd, **12**.

Robertson, P.K., Melo, L., Williams, D.J., and Wilson, G.W. 2020. Report of the Expert Panel on the Technical Causes of the Failure of Feijão Dam I.

Rock, A.C.D.-18 on S. and. 2006. Standard test methods for minimum index density and unit weight of soils and calculation of relative density. ASTM International.

Rock, A.C.D.-18 on S. and. 2011. Standard test method for consolidated undrained triaxial compression test for cohesive soils. ASTM International.

Rodriguez, J. 2013. Importance of the particle shape on mechanical properties of soil materials. Luleå tekniska universitet.

Roscoe, K., and Burland, J.B. 1968. On the generalized stress-strain behaviour of wet clay.

Roscoe, K.H., Schofield, An., and Wroth, andC P. 1958. On the yielding of soils. *Geotechnique*, **8**(1): 22–53. Thomas Telford Ltd.

Rowe, P.W., and Barden, L. 1964. Importance of free ends in triaxial testing. *Journal of Soil Mechanics & Foundations Div*, **90**(Proc. Paper 3753).

- Sadrekarimi, A. 2009. Development of a new ring shear apparatus for investigating the critical state of sands. University of Illinois at Urbana-Champaign.
- Sadrekarimi, A. 2013. Influence of state and compressibility on liquefied strength of sands. *Canadian geotechnical journal*, **50**(10): 1067–1076. NRC Research Press.
- Sadrekarimi, A. 2016. Static liquefaction analysis considering principal stress directions and anisotropy. *Geotechnical and Geological Engineering*, **34**(4): 1135–1154. Springer.
- Sadrekarimi, A. 2020. Forewarning of Static Liquefaction Landslides. *Journal of Geotechnical and Geoenvironmental Engineering*, **146**(9): 4020090. American Society of Civil Engineers.
- Sadrekarimi, A., and Olson, S.M. 2011. Yield strength ratios, critical strength ratios, and brittleness of sandy soils from laboratory tests. *Canadian Geotechnical Journal*, **48**(3): 493–510. NRC Research Press.
- Salgado, R., Bandini, P., and Karim, A. 2000. Shear strength and stiffness of silty sand. *Journal of geotechnical and geoenvironmental engineering*, **126**(5): 451–462. American Society of Civil Engineers.
- Santana, T., and Candeias, M. 2015. K₀ Measurement in a Sand Using Back Volume Change. *Soils and Rocks, São Paulo*, **38**(1): 3–8.
- Sasitharan, S., Robertson, P.K., Segoo, Dc., and Morgenstern, N.R. 1993. Collapse behavior of sand. *Canadian Geotechnical Journal*, **30**(4): 569–577. NRC Research Press.
- Sawicki, A., and Świdziński, W. 2010. Modelling the pre-failure instabilities of sand. *Computers and Geotechnics*, **37**(6): 781–788. Elsevier.
- Schnaid, F., Bedin, J., Viana da Fonseca, A.J.P., and de Moura Costa Filho, L. 2013. Stiffness and strength governing the static liquefaction of tailings. *Journal of Geotechnical and Geoenvironmental Engineering*, **139**(12): 2136–2144. American

Society of Civil Engineers.

- Schofield, A.N., and Wroth, P. 1968. Critical state soil mechanics. McGraw-hill London.
- Seed, H.B. 1987. Design problems in soil liquefaction. *Journal of Geotechnical Engineering*, **113**(8): 827–845. American Society of Civil Engineers.
- Shahsavari Goughari, M. 2012. Effect of initial shear stress direction and stress history on the undrained behaviour of sands under triaxial loading. Carleton University.
- Shuttle, D., and Jefferies, M. 2010. Norsand: description, calibration, validation and applications. *In Geo-frontiers congress 2005–Soil constitutive models: evaluation, selection, and calibration*. pp. 204–236.
- Skopek, P., Morgenstern, N.R., Robertson, Pk., and Segoo, D.C. 1994. Collapse of dry sand. *Canadian Geotechnical Journal*, **31**(6): 1008–1014. NRC Research Press.
- Sladen, J.A., D'hollander, R.D., and Krahn, J. 1985. The liquefaction of sands, a collapse surface approach. *Canadian geotechnical journal*, **22**(4): 564–578. NRC Research Press.
- Sottile, M., Kerguelen, A., and Sfriso, A. 2019. A comparison of procedures for determining the state parameter of silt-like tailings. *In The 17th african regional conference on soil mechanics and geotechnical engineering*. pp. 1–5.
- Stark, T.D., and Mesri, G. 1992. Undrained shear strength of liquefied sands for stability analysis. *Journal of Geotechnical Engineering*, **118**(11): 1727–1747. American Society of Civil Engineers.
- Taylor, D.W. 1948. Fundamentals of soil mechanics. LWW.
- Terzaghi, K., Peck, R.B., and Mesri, G. 1996. Soil mechanics in engineering practice. John Wiley & Sons.
- Thevanayagam, S. 1998. Effect of fines and confining stress on undrained shear strength of silty sands. *Journal of Geotechnical and Geoenvironmental Engineering*, **124**(6):

479–491. American Society of Civil Engineers.

Thevanayagam, S., Ravishankar, K., and Mohan, S. 1997. Effects of fines on monotonic undrained shear strength of sandy soils. *Geotechnical testing journal*, **20**(4): 394–406. ASTM International.

Thevanayagam, S., Shenthan, T., Mohan, S., and Liang, J. 2002. Undrained fragility of clean sands, silty sands, and sandy silts. *Journal of geotechnical and geoenvironmental engineering*, **128**(10): 849–859. American Society of Civil Engineers.

Torres-Cruz, L.A., and Santamarina, J.C. 2020. The critical state line of nonplastic tailings. *Canadian Geotechnical Journal*, **57**(10): 1508–1517. NRC Research Press 1840 Woodward Drive, Suite 1, Ottawa, ON K2C 0P7.

Vaid, Y.P., Chung, E.K.F., and Kuerbis, R.H. 1990. Stress path and steady state. *Canadian Geotechnical Journal*, **27**(1): 1–7. NRC Research Press Ottawa, Canada.

Vaid, Y.P., and Sivathayalan, S. 1996. Static and cyclic liquefaction potential of Fraser Delta sand in simple shear and triaxial tests. *Canadian Geotechnical Journal*, **33**(2): 281–289. NRC Research Press.

Vaid, Y.P., and Sivathayalan, S. 2000. Fundamental factors affecting liquefaction susceptibility of sands. *Canadian Geotechnical Journal*, **37**(3): 592–606. NRC Research Press.

Vaid, Y.P., Sivathayalan, S., and Stedman, D. 1999. Influence of specimen-reconstituting method on the undrained response of sand. *Geotechnical Testing Journal*, **22**(3): 187–195. ASTM International.

Vaid, Y.P., and Thomas, J. 1995. Liquefaction and postliquefaction behavior of sand. *Journal of Geotechnical Engineering*, **121**(2): 163–173. American Society of Civil Engineers.

Verdugo, R., and Ishihara, K. 1996. The steady state of sandy soils. *Soils and*

- foundations, **36**(2): 81–91. The Japanese Geotechnical Society.
- Vermeulen, N.J. 2007. The composition and state of gold tailings. University of Pretoria.
- Vick, S.G. 1990. Planning, design, and analysis of tailings dams. BiTech Publishers Ltd.
- Wanatowski, D., and Chu, J. 2012. Factors affecting pre-failure instability of sand under plane-strain conditions. *Géotechnique*, **62**(2): 121–135. Thomas Telford Ltd.
- Wanatowski, D., Chu, J., and Gan, C.L. 2009. Compressibility of Changi sand in K0 consolidation. *Geomech. Eng.*, **1**(3): 241–257.
- Wanatowski, D., Chu, J., and Loke, W.L. 2010. Drained instability of sand in plane strain. *Canadian Geotechnical Journal*, **47**(4): 400–412. NRC Research Press.
- Wang, G., and Sassa, K. 2000. Undrained Shear Behavior of Silty Soils in Ring-Shear Tests. *In* ISRM International Symposium. International Society for Rock Mechanics and Rock Engineering.
- Yamamuro, J.A., and Covert, K.M. 2001. Monotonic and cyclic liquefaction of very loose sands with high silt content. *Journal of geotechnical and geoenvironmental engineering*, **127**(4): 314–324. American Society of Civil Engineers.
- Yamamuro, J.A., and Lade, P. V. 1996. Drained sand behavior in axisymmetric tests at high pressures. *Journal of Geotechnical Engineering*, **122**(2): 109–119. American Society of Civil Engineers.
- Yamamuro, J.A., and Lade, P. V. 1997. Static liquefaction of very loose sands. *Canadian Geotechnical Journal*, **34**(6): 905–917. NRC Research Press Ottawa, Canada.
- Yamamuro, J.A., and Lade, P. V. 1998. Steady-state concepts and static liquefaction of silty sands. *Journal of geotechnical and geoenvironmental engineering*, **124**(9): 868–877. American Society of Civil Engineers.
- Yang, S.L., Sandven, R., and Grande, L. 2006. Steady-state lines of sand–silt mixtures. *Canadian Geotechnical Journal*, **43**(11): 1213–1219. NRC Research Press Ottawa,

Canada.

- Yoshimine, M., Ishihara, K., and Vargas, W. 1998. Effects of principal stress direction and intermediate principal stress on undrained shear behavior of sand. *Soils and Foundations*, **38**(3): 179–188. Elsevier.
- Yoshimine, M., Robertson, P.K., and Wride, C.E. 2001. Undrained shear strength of clean sands to trigger flow liquefaction: Reply. *Canadian geotechnical journal*, **38**(3): 654–657. NRC Research Press Ottawa, Canada.
- Zhu, J.-H., and Anderson, S.A. 1998. Determination of shear strength of Hawaiian residual soil subjected to rainfall-induced landslides. *Géotechnique*, **48**(1): 73–82. Thomas Telford Ltd.
- Zlatovic, S., and Ishihara, K. 1997. Normalized behavior of very loose non-plastic soils: effects of fabric. *Soils and foundations*, **37**(4): 47–56. The Japanese Geotechnical Society.
- Zlatović, S., and Ishihara, K. 1995. On the influence of nonplastic fines on residual strength. *In* First International Conference on Earthquake Geotechnical Engineering. pp. 239–244.

Curriculum Vitae

Name:	Amir reza Fotovvat
Post-secondary Education and Degrees:	Amirkabir University of Technology (Tehran Polytechnic) Tehran, Iran 2011-2015 B.Sc. (Civil and Environmental Engineering) Amirkabir University of Technology (Tehran Polytechnic) Tehran, Iran 2015-2017 M.Sc. (Geotechnical Engineering) The University of Western Ontario London, Ontario, Canada 2018-2022 Ph.D. (Geotechnical Engineering)
Honours and Awards:	Western Graduate Research Scholarship 2018-2022
Related Work Experience	Teaching Assistant The University of Western Ontario 2018-2022 Research and Teaching Assistant Amirkabir University of Technology (Tehran Polytechnic) Tehran, Iran 2015-2017 Junior Geotechnical Engineer GHD May 2022-present
Publications	Fotovvat, A. R., & Sadrekarimi, A. (2022). Instability of a Gold Mine Tailings Subjected to Different Stress Paths. (<i>ASCE Journal of Geotechnical and Geoenvironmental Engineering</i> , 148(5), 04022020). Fotovvat, A. R., & Sadrekarimi, A. (2022). Instability of Gold Mine Tailings subjected to Undrained and Drained Unloading Stress Paths. Accepted in <i>Géotechnique</i> .